ANALYSIS OF GLARE LAMINATES UNDER LOW VELOCITY IMPACT

A Thesis Submitted in

Partial Fulfillment of the Requirements for the Degree of

Doctor of Philosophy

by

Sasanka Kakati
(Roll no: 186103032)

under the guidance of

Dr Debabrata Chakraborty

DEPARTMENT OF MECHANICAL ENGINEERING

INDIAN INSTITUTE OF TECHNOLOGY GUWAHATI

GUWAHATI-781039, ASSAM, INDIA

June 2023


भारतीय प्रौद्योगिकी संस्थान गुवाहाटी
Indian Institute of Technology Guwahati

Dedicated to my parents.....

DECLARATION

I declare that,

a. the work contained in this thesis is original and has been done by me under the guidance of my supervisor.

b. the work has not been submitted to any other Institute for any degree or diploma.

c. I have followed the guidelines provided by the Institute in preparing the thesis.

d. I have conformed to the norms and guidelines given in the Ethical Code of Conduct of the Institute.

e. wherever I have used materials (data, theoretical analysis, figures and text) from other sources, I have given due credit to them by citing them in the text of the thesis and giving their details in the references. Further, I have taken permission from the copyright owners of the sources, wherever necessary.

Sasanka Kakati

Department of Mechanical Engineering
Indian Institute of Technology Guwahati
Guwahati, Assam, India, 781039

CERTIFICATE

This is to certify the thesis entitled "**Analysis of GLARE laminates under low velocity impact**", submitted by **Sasanka Kakati** (186103032) to the Department of Mechanical Engineering, Indian Institute of Technology Guwahati, for the award of the degree of Doctor of Philosophy, is a record of an original research work carried out under my supervision and guidance. The work in this thesis has not been submitted elsewhere for the award of any other degree or diploma.

June 2023
IIT Guwahati

(Debabrata Chakraborty)
Professor
Department of Mechanical Engineering
Indian Institute of Technology Guwahati
Guwahati-781039, Assam, India

Acknowledgements

First and foremost I would like to express my sincere gratitude to my supervisor, Prof. Debabrata Chakraborty for guiding me and mentoring me throughout the entire period of my research work. I am extremely grateful to my supervisor for his valuable advice, providing critical insight based on his knowledge and experience in this field which has benefitted me immensely in carrying out my research work.

I also take this opportunity to express my sincere gratitude to Doctoral Committee members Prof. Rajiv Tiwari and Prof. Pankaj Biswas from the Department of Mechanical Engineering and Prof. Anjan Dutta from the Department of Civil Engineering for their valuable suggestions at various stages of my research work. I am also grateful to the former and present heads of the Department of Mechanical Engineering for providing a congenial academic and research environment for research work.

I sincerely acknowledge the infrastructural facilities provided by Indian Institute of Technology and financial support provided by the Ministry of Education (MoE) during the entire period of the doctoral research work. I sincerely acknowledge the computational facility provided by the Department of Mechanical Engineering to carry out my research work smoothly.

I would like to thank my lab members Pran Jyoti Saikia, Chukka Atchuta Rao, Nibir Saha and Sai Kumar for their valuable inputs and also to Krishna Murthy Pabbu, Lalit Kumar, Avneesh Kumar, Sukanya Phukan, Rajdeep Ghosh, including all my lab members for their support and maintaining a friendly working environment. I am also grateful to Dixita, Parthajit, Pratim, Debajit, Faladrum, Ritam, Nabajyoti, Nayan, Upasana, Sanghamitra, Juri, and many more who encouraged me through their unabated support throughout my work.

Last but by no means the least, I express my sincere gratitude and heartfelt love to my mother Mrs. Triveni Choudhury for her patience, understanding, love and constant support in accomplishing my goal and in remembrance of my late father Mr. Bhumidhar Kakati, I convey my gratitude and love to him.

There are many more persons who helped me in many ways and whose names elude me at this moment of time. I extend my gratitude to them.

Last, but not the least, I shall always be grateful to God for giving me the strength and blessing me with opportunities throughout my life.

June 2023 **Sasanka Kakati**

Abstract

Superior impact properties of glass aluminium reinforced epoxy (GLARE) have led to their usage in impact prone structures such as aircraft fuselage, wings and cargo panels. However, these advanced laminated structures are also susceptible to impact induced damages, especially under low velocity impact (LVI) where the damages are sub-surface and barely visible. Finite element analysis (FEA) enables a more in-depth study of the complex nature of the response and damages due to arbitrary LVIs. This dissertation thus presents the FEA of GLARE under LVI, evaluating the response of the target and the associated damage due to LVI. A complete 3D finite element (FE) formulation has been developed using 3D layered solid elements to evaluate the contact impact response of GLARE subjected to arbitrary (normal and oblique) LVIs. A transient dynamic FE code has been developed incorporating the Newmark-β method and implementing suitable normal and tangential contact models for accurate determination of the contact responses and the associated interfacial delamination damages. An important aspect of the present FE modelling is the incorporation of an adjustable contact stiffness based on the impactor to plate mass ratio which is critical for accurate evaluation of the contact response and correctly predicting the associated damages. Influence of important parameters like properties and geometry of the GLARE laminate and the impactor along with the trajectory of the impact on the contact impact response and the delamination damages have been investigated. Results from the present work show that besides the size and geometry of the impactor, the trajectory of the impactor relative to the target and the coefficient of friction between them also significantly influence the contact response as well as the evolution of delamination at the interfaces. Further, for multiple impacts, the interval between the successive impacts greatly influences the magnitude of contact force as well as delamination at the fibre-metal interfaces. The presence of discontinuities in the form of cut-outs or open holes (due to functional requirements) in the GLARE laminate significantly influences how delamination grows around these locations due to increased stress concentrations under impact loads. Results from the analysis of LVI show that the pitch of the cut-outs and their size and shape has significant influence on the evolution of delamination, especially at the metal/composite interfaces.

Table of contents

List of figures

List of tables

Nomenclature

List of symbols

$[C]$: Material stiffness matrix

$\left[\bar{C}\right]$: Transformed stiffness matrix

$[S]$: Material compliance matrix

$[D]$: Bending stiffness matrix

$[T]$: Transformation matrix

$[l]$: Direction cosine matrix

E : Young's modulus

E^* : Effective contact modulus of the impactor target system

G : Shear modulus

G^* : Effective rigidity modulus of the impactor target system

x-y-z : Global axes

1-2-3 : Local axes

$[R]$: Reuter matrix

N_i : Shape functions

$[J]$: Jacobian

$x_i,\ y_i,\ z_i$: Global coordinates of the n^{th} node

$u,\ v,\ w$: Displacement components along x, y and z

$[B]$: Strain-displacement matrix

$\{d\}$: Displacement vector

$\{\dot{d}\}$: Velocity vector

$\{\ddot{d}\}$: Acceleration vector

$\left[I^c\right]$: Matrix consisting of incompatible modes

$[K_e]$: Element stiffness matrix

$\{F\}$: Load vector

$[M_e]$: Element mass matrix

$[\hat{K}]$: Effective stiffness matrix

$\{\hat{F}\}$: Effective force vector

f_N : Normal contact force

f_T : Tangential contact force

k_c^{eff} : Effective contact stiffness

T : Thickness of the solid element

t_k : Thickness of k^{th} layer

m^o : Impactor mass

m_p : Plate mass

m_p^* : Plate areal mass density

$\vec{v}^o$: Impactor velocity

R^o : Impactor radius

v_n^o : Normal component of impactor velocity

v_t^o : Tangential component of impactor velocity

t : Time

Δt : Time step

ΔT : Time delay between two impacts

L : Cylinder half length

r : Cylinder radius

b_o : Cylinder half width

R_2 : Radius of curvature of indented surface

X_T : Longitudinal tensile strength

X_C : Longitudinal compressive strength

Y_T : Transverse tensile strength

Y_C : Transverse compressive strength

S : Shear strength

Greek symbols

$\sigma_1,\ \sigma_2,\ \sigma_3$: Normal stress components along material/local axes

$\sigma_x,\ \sigma_y,\ \sigma_z$: Normal stress components along global/local axes

$\tau_{12},\ \tau_{23},\ \tau_{13}$: Shear stress components along material axes

$\tau_{xy},\ \tau_{yz},\ \tau_{xz}$: Shear stress components along global axes

θ	:	Angle between two directions
$\varepsilon_1,\ \varepsilon_2,\ \varepsilon_3$	:	Normal strain components along material axes
$\varepsilon_x,\ \varepsilon_y,\ \varepsilon_z$	:	Normal strain components along global axes
$\gamma_{12},\ \gamma_{23},\ \gamma_{13}$	:	Shear strain components along material/local axes
$\gamma_{xy},\ \gamma_{yz},\ \gamma_{xz}$	:	Shear strain components along global/local axes
ν	:	Poisson's ratio
ξ, η, μ	:	Natural coordinates
μ_f	:	Coefficient of friction
α	:	Normal indentation by impactor
δ	:	Tangential displacement of impactor
β	:	Contact area radius

Chapter 1

Introduction

This chapter briefly introduces the present research work investigated in this thesis by taking a quick glimpse at the early usage of the composite materials and their evolution to advanced hybrid polymer composites available today. The chapter highlights the applications of fibre reinforced polymer (FRP) laminates in modern aviation, their advantages and drawbacks, and the need for incorporating advanced hybrid fibre metal laminates (FMLs) such as GLARE. It also stresses on the necessity to investigate the threats these laminated structures pose in the advent of impact-induced loadings.

1.1. Composite materials: Overview

It is the innate nature of humankind to aspire for progress which has led to ground breaking discoveries and scientific advancements to achieve the modern world of the present. This very nature had led to their quest to search for different materials, their urge to combine various constituents with a sole purpose: to have a material which is more robust than its constituents like the straw reinforced mud walls by the Egyptians dating back to 1500 B.C. These can be termed as composite materials, and they have been in existence since time immemorial. The word 'composite' originated from the Latin word *compositus,* meaning "placed together", past participle of the word *componere*, formed from "com+ponere", which means "together + to place". Composite materials are engineered or naturally occurring materials that consist of two or more constituent materials having notably different physical or chemical properties which remain separate and distinct within the structure. Typically in a composite material, one is the reinforcing phase in the form of continuous or short fibres, particulates, or in the form of flakes embedded in a continuous media called the matrix phase.

Therefore, these could be classified based on the type of the reinforcement as particulate, flake or fibre composite or based on the type the matrix material used such as metal matrix, ceramic matrix, carbon or polymer matrix. **Figure 1.1** shows the typical classification of composite materials. In practice, these composites are used in their usable structural forms which are capable of bearing designed loads for practical applications in the form of laminates, sandwich panels or other hybrid forms.

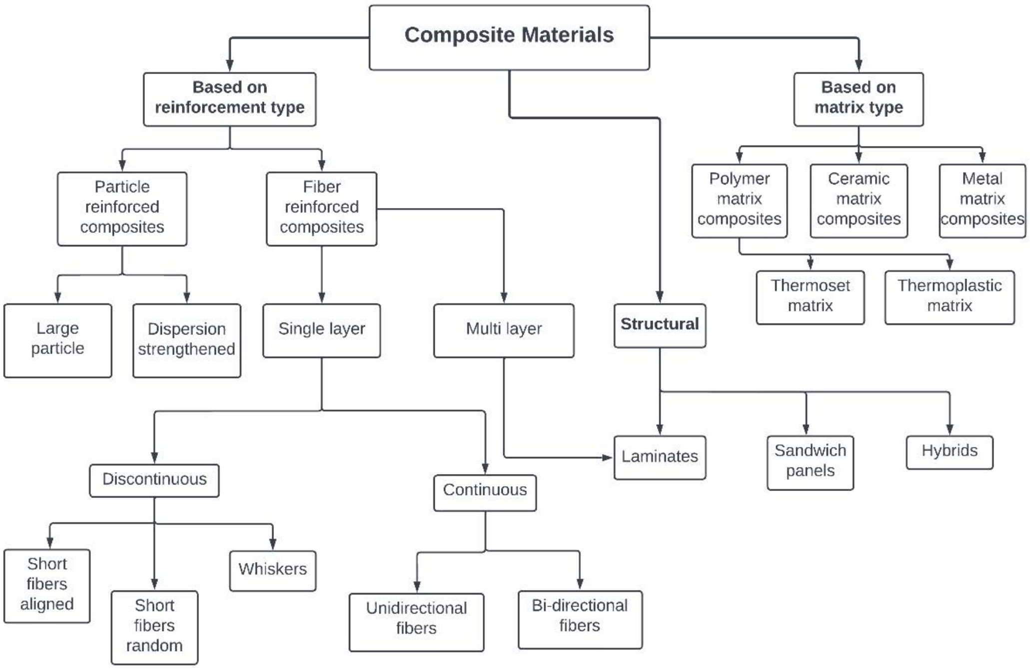

Figure 1.1: Classification of composites

Numerous applications of composite materials can be found in typical day-to-day objects like sports equipment, in the construction of houses and structures where the concrete is reinforced with metal bars. With passing time and technological advancements, there has been a scientific and structured approach towards developing and manufacturing modern composite materials for numerous applications. In recent times, the polymer composites have become popular material over traditional materials because of their customisable properties which permits to achieve the desired strength and stiffness to suit a particular application. The design flexibility provided by these polymer composites in terms of forming continuous complex shapes along with better fatigue properties and environmental resistance have made it a material of choice for advanced aerospace applications.

1.2. Fibre reinforced polymer composites

The era of modern composites began in the mid-1930s with the development of polymer resins and glass fibres. With the demand for superiority in military aviation and increasing commercial travel, a significant thrust was seen in developing polymer composites reinforced with different fibres. Fibre reinforced polymer (FRP) composites, as shown in **Figure 1.2**, are polymer matrices reinforced by long or short fibres. Long fibre composites have continuous fibres unlike the short fibres which are discontinuous. The discontinuous fibres may be aligned or present in random orientations.

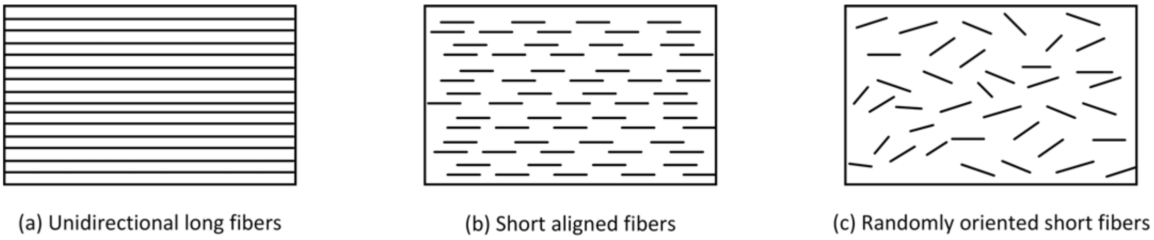

Figure 1.2: Different fibre types in an epoxy matrix

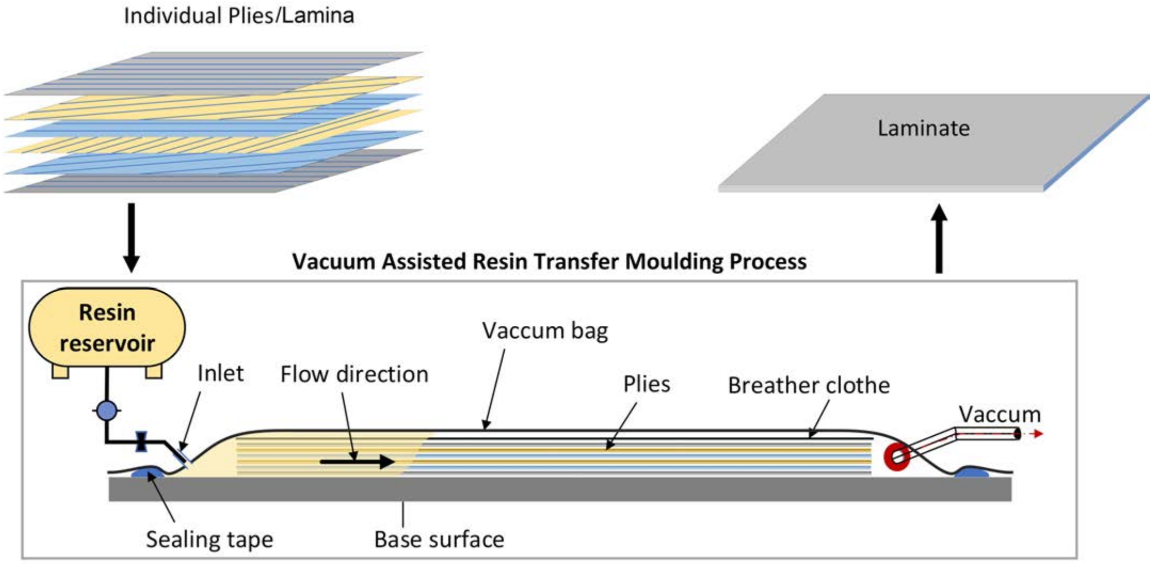

Figure 1.3: Making of a composite laminate

In general, the fibre reinforced polymers have highest strength in the direction of the fibre and the least in the transverse direction. FRP composites, which usually comprise of carbon, glass or aramid fibres embedded in a polymer matrix of thermosetting plastics or epoxy resins are used to form laminates by stacking a number of individual lamina. Large numbers of fibres are bonded in a particular direction by resins forming a lamina. A laminate formed by stacking several such lamina can serve various purposes depending on the objective. The unidirectional fibres in a lamina may be oriented at different angles and these different lamina having different fibre orientations are stacked together in a particular sequence forming a laminate as shown in **Figure 1.3** to achieve the desired strength and stiffness requirements for an application. A rising demand of their usage is seen owing to their higher stiffness and strengths in addition to lower weights compared to the conventional metal alloys. In addition, polymer materials exhibit better thermal and vibration properties and also have better tolerance to environmental degradation from erosion or corrosion. The FRP composites have significantly transformed the aerospace, automotive and marine industries and there has been a continuous effort to make advanced composites more durable, cost effective and markedly less resource intensive to make their production environment friendly.

1.3. FRP composites in aviation

The aviation industry is one of the ever-growing sectors catering to the transportation of commercial or military payloads. The fuselage is the main section of the aircraft which houses the passengers or the goods and commodities to transport and is subjected to various loading conditions. The aluminium and titanium alloys, high-strength steels and composites have been the most commonly used commercial aircraft structural materials and it accounts for more than 90% of the airframe weight. Due to their low densities and excellent strength, aluminium alloys have been a common choice for aircraft structures because of their ease of application and moderate cost [1]. In the past two decades, significant progress has been made in the design and selection of materials for the construction of aircraft components like the fuselage, aircraft wings, door panels, turbine blades etc., driven by the need to reduce carbon emissions, to become more efficient and at the same time maintain the structural integrity for flight safety.

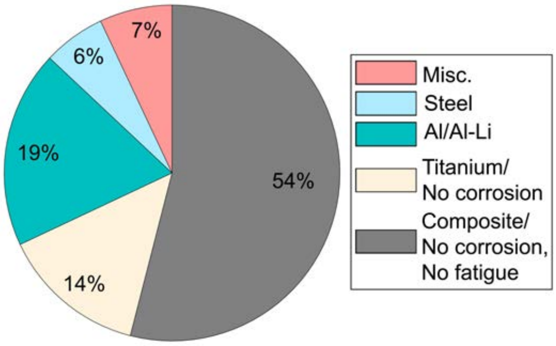

Figure 1.4: Composition of materials in A350 [2]

Figure 1.5: A Sukhoi SU-30MKI combat aircraft

A constant aim to reduce weight and cut operational costs has led to using composites in the aviation sector. Airbus A310 introduced in the 1980s, was the first commercial aeroplane to implement composite components extensively. The use of the composite vertical stabilizer in Airbus A310 made it about 400 kg lighter than the previously used aluminium vertical stabilizers [3]. **Figure 1.4** [2] shows the application of different materials in the Airbus A350, and evidently, the use of composites in the commercial aircraft industry is significant. The extensive use of laminated fibre composites is also seen in modern military aircrafts owing to the demands for superior structural performance. These laminated composites generally comprise of unidirectional fibres of high specific modulus (like Kevlar, carbon and glass fibres) which have high strength, better fatigue performance, good resistance to corrosion and the anisotropic properties of the laminates can be used to tailor for specific strength and stiffness requirements. The reduction in the structural mass, especially in the combat aircrafts (refer **Figure 1.5**), benefit them immensely in their performance, particularly in their acceleration, climb rate, range and maximum payload [4,5]. Another material of choice which have garnered major interest in the aviation industry since the last few decades are the fibre metal laminates (FMLs). These advanced hybrid composites typically used in the aerospace sector have seen a major breakthrough in terms of the weigh-saving aspects in addition to improved mechanical characteristics.

1.4. Fibre Metal Laminates: A new generation of hybrid materials

Although the polymer composite materials have proved to be advantageous over conventional alloys, they are liable to damage during initial manufacturing. The laminated composites may suffer from interfacial delamination due to weak interface strengths, low ductility compared to aluminium alloys, and mainly poor impact properties and residual strengths whereas the aluminium alloys are susceptible to fatigue crack growth and environmental exposure [6]. More importantly, the low impact strength of laminated composites make them undergo significant damage when subjected to LVIs in the form of both intra-laminar as well as interlaminar damage modes. Fibre and matrix failure and debonding between fibre and matrix are the intra-laminar damage incurred by such laminates while the inter-laminar damage is characterised by delamination between adjacent plies. When these laminates are subjected to impacts at higher velocities, they are more likely to undergo damage in the form of perforation and penetration. These are major causes of concern in the aviation industry which compromise the safety and overall structural stability of the aircraft.

The need for lighter and yet high strength and reliable material has been the driving force for the development of hybrid structural material called as fibre metal laminates (FMLs) which comprise of two key constituents viz. laminated composites and metal alloys. A typical FML is shown in **Figure 1.6** where fibre reinforced composite prepreg layers stacked alternately between thin metal layers. The load bearing aspects are superior in case of the

FMLs and their improved impact resistance can be attributed to the presence of outer metal alloy layer. At the same time it also inherits the fibre dominated properties such as excellent fatigue characteristics and improved specific strength/stiffness such that these FMLs possess the required desirable characteristics of their individual components.

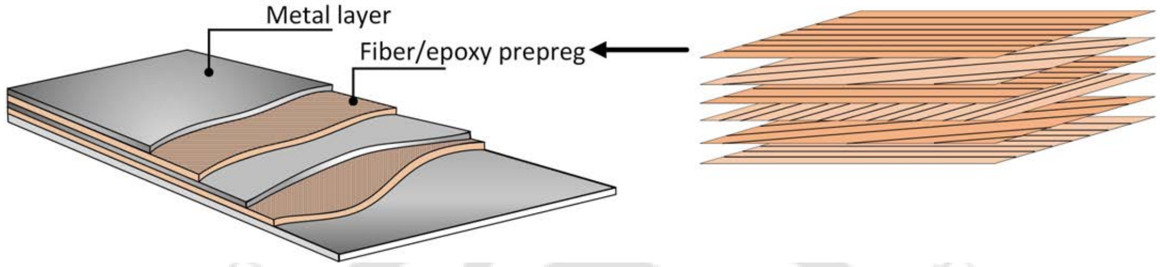

Figure 1.6: Fibre metal laminate

1.4.1. Development of FMLs

The metals currently used in FMLs include aluminium, titanium or magnesium, and the fibre-reinforced layer is either a glass, carbon or Kevlar fibre reinforced composite laminate [7]. Commercially available FMLs are glass laminate aluminium reinforced epoxy (GLARE), which consists of high strength glass fibres, aramid reinforced aluminium (ARALL) and carbon fibre reinforced aluminium (CARALL) laminates.

The development of FMLs can be tracked back to the early 1980s witnessed by the introduction of ARALL which found promising use in aircraft structures. ARALL is a first generation FML introduced by the Faculty of Aerospace Engineering at the Delft University of Technology in the Netherlands in 1978 and it consists of uniaxial or biaxial aramid fibres alternately placed between 0.2 mm - 0.4 mm thick aluminium alloys [8]. Different variations of these were fabricated but ALCOA Company was the first to manufacture commercially available standardised ARALL [9,10]. Two trade variants, ARALL 1 and ARALL 2 were standardised, with the former having aluminium 7075 layers while aluminium 2024 layers were present in ARALL 2 in the as-cured condition [11]. But several critical problems emerged with ARALL variants like low interface strengths including fibre failure under tension-compression fatigue loading and moisture adsorption. CARALL offered certain advantages over ARALL owing to its higher specific modulus and high stiffness carbon fibres for crack bridging thereby lowering the crack growth rates. But the limited range in their failure strain and galvanic corrosion between the carbon fibres and aluminium sheets in moist environment proved to be a negative aspect for these FMLs [12–14].

1.5. GLARE: The second generation FMLs

GLARE consisting of high-strength glass fibre reinforced laminates placed alternately between monolithic aluminium layers are the second generation FMLs developed in the late 1980s. They were first developed in Delft University of Technology and patent was filed by AKZO on October 14th 1987 naming Roebroeks and Vogelesang as the inventors [15]. These hybrid laminates were developed with an aim to be used as primary structural components and coming to the present day, they have found extensive use in the fuselage structure of modern day aircrafts. GLARE FMLs are lightweight and offer better damage tolerance characteristics, compared to its individual constituents thereby making them gain considerable interest in the aerospace industry.

1.5.1. GLARE codes and standardisation

The typical layups of GLARE laminates are shown in **Figure 1.7** which consists of S2-glass/FM94 epoxy composite plies alternately placed between 2024-T3 aluminium layers [16]. The diameter of the S2-glass fibres is approximately 10 μm and they are embedded in FM94 epoxy adhesive to form lamina of nominal thickness ranging between 0.125 mm - 0.132 mm with an average fibre volume fraction of 59%−62%. GLARE has six standardised grades, all having unidirectional glass fibres embedded in epoxy forming prepregs which are placed in different orientations between the aluminium alloy sheets. Such different layups enable tailoring their properties to meet the structure specific requirements. The different GLARE grades are summarised in **Table 1.1** [16–18].

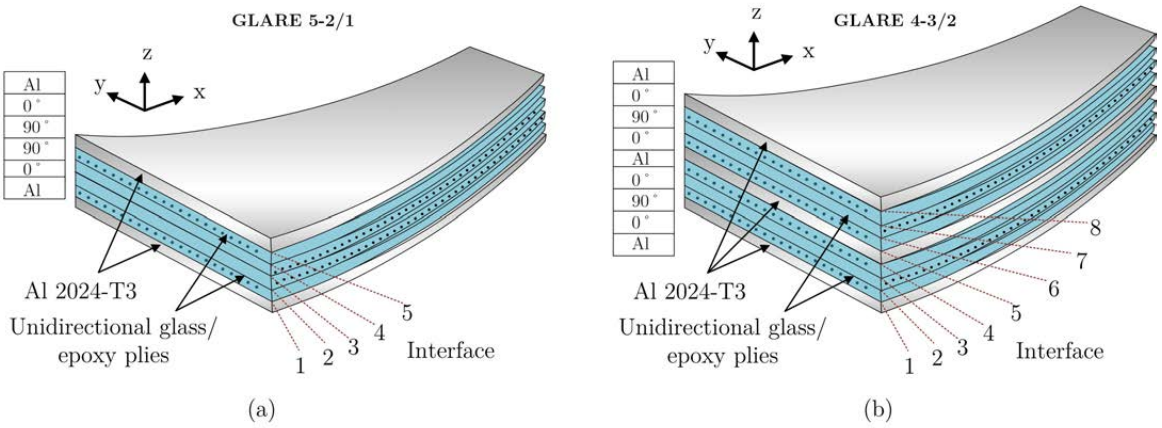

(a)

(b)

Figure 1.7: GLARE 5-2/1 and GLARE 4-3/2

For any commercial production of a material with different grades, a standardised naming convention needs to be implemented for the ease of identification and suitability of a particular variant with its intended use. A coding system to name GLARE laminates is followed. For example, if a laminate is defined as GLARE 4A-3/2-0.4, it implies the following:

- The word GLARE implying a glass aluminium reinforced epoxy FML.
- 4A: Layup of the S2-glass fibre/FM94 epoxy plies are in the order [0°/90°/0°] and having Al-alloy 2024-T3 as the metal layers.
- 3/2: Three aluminium layers bonded alternatively with two layers of glass/epoxy prepregs.
- 0.4: The thickness of aluminium alloy sheets are 0.4 mm.

Table 1.1: Different standard GLARE grades [16–18]

GLARE grade		**Prepreg orientation in each composite layer**	**Aluminium sheet**		**Main favourable characteristics**
Main	**Sub**		**Alloy**	**Thickness (mm)**	
GLARE 1	—	0/0	7475-T761	0.3-0.4	Fatigue, strength, yield stress
GLARE 2	GLARE 2A	0/0	2024-T3	0.2-0.5	Fatigue, strength
	GLARE 2B	90/90	2024-T3	0.2-0.5	Fatigue, strength
GLARE 3	—	0/90	2024-T3	0.2-0.5	Fatigue, strength
GLARE 4	GLARE 4A	0/90/0	2024-T3	0.2-0.5	Fatigue, strength in 0° direction
	GLARE 4B	90/0/90	2024-T3	0.2-0.5	Fatigue, strength in 90° direction
GLARE 5	—	0/90/90/0	2024-T3	0.2-0.5	Impact
GLARE 6	GLARE 6A	+45/-45	2024-T3	0.2-0.5	Shear, off-axis properties
	GLARE 6B	-45/+45	2024-T3	0.2-0.5	Shear, off-axis properties

1.5.2. Characteristic properties and applications

GLARE FMLs developed primarily for aircraft applications are superior to aluminium alloys in terms of resistance to fatigue crack growth and damage. The fibre layers present between the metal layers act as crack bridging mechanism in the direction of loading in the event of fatigue crack thereby reducing the stress intensity at the crack tip and arresting the crack growth as shown in **Figure 1.8**.

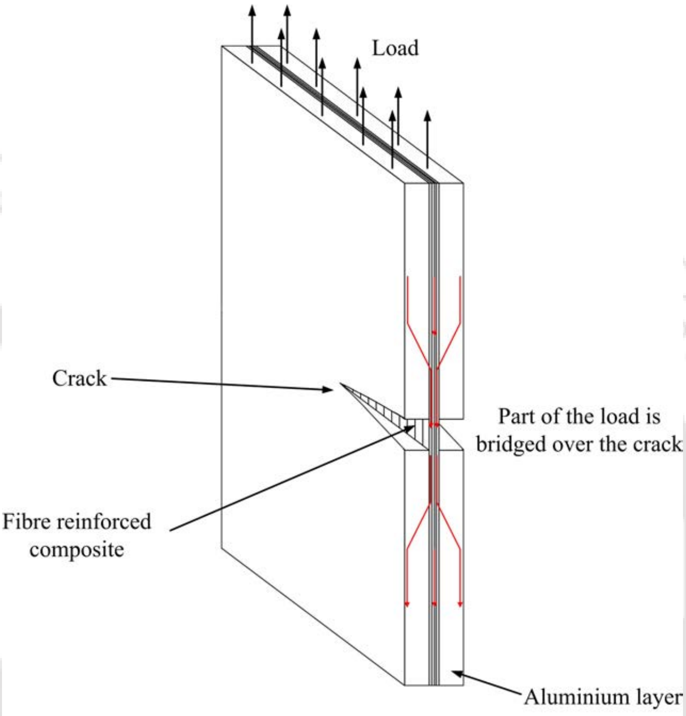

Figure 1.8: Illustration of crack bridging mechanism by intact fibres

GLARE panels used in fuselage of aircrafts (refer **Figure 1.9**) proved better in terms of improved ability to sustain higher shear stresses, burn through resistance and particularly superior impact resistance [19] which is common in day to day operations due to dropping of objects or bird strikes during flights. GLARE have proved to be superior in comparison to monolithic aluminium in many aspects along with easier inspection for damages [20]. Some of the important characteristics are as follows [15,19,21]:

- The GLARE grades with biaxial fibre layers are better compared to the individual aluminium 2024-T3 layers and S2-glass/FM94 epoxy fibre composites.
- At high strain rates (bird strikes, hailstorms), GLARE exhibits improved impact behaviour. Visible dents formed on the outer aluminium layers make the inspection easier.
- There is almost 10% reduction in specific weight of GLARE as compared to aluminium.

- Better damage tolerance compared to aluminium and composites. Loss in strength due to fatigue damage is significantly small. Compared to the fatigue behaviour of aluminium alloys, the glass/epoxy laminates significantly improve the fatigue behaviour of the overall GLARE laminates.
- The repairing of GLARE laminates can be done in the same way as done for aluminium alloys.
- Machining of GLARE can be done using the same tools and following the similar processes as for aluminium alloys.
- GLARE 5 in particular is specially developed for impact resistance and outperforms aluminium alloys in terms of impact performances.
- GLARE grades have improved fire resistance compared to aluminium alloys and also show good performance in corrosive environment.

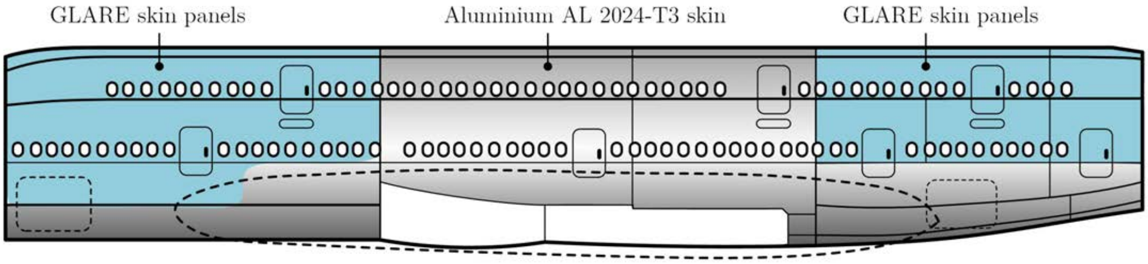

Figure 1.9: GLARE skin panels on Airbus A380 fuselage(reproduced from Assler and Telgkamp [22])

1.5.3. Impact induced damage: A critical concern

Impact can be termed as the process of deformation and failure during the collision between two objects. In most cases, the event of an impact occurs between a foreign object and a target structure with the latter being the concern of analysis. Based on the characteristic properties discussed in **Section 1.5.2**, GLAREs have found several applications, especially in the aerospace sector. As already discussed, the superior fatigue and damage properties of GLARE has made it suitable for its application in the fuselage, upper and lower wings of the aircrafts. The aircraft floors and cargo doors which are liable to impact damage due to falling of tools and human contacts necessitates the use of GLARE for improved flight experience. During take-off or landing, runway debris and flying tyre parts due to tyre burst can cause noticeable damage to the lower fuselage structure. As shown in **Figure 1.10**, approximately 68% of impacts occur around the passenger and cargo doors [23].

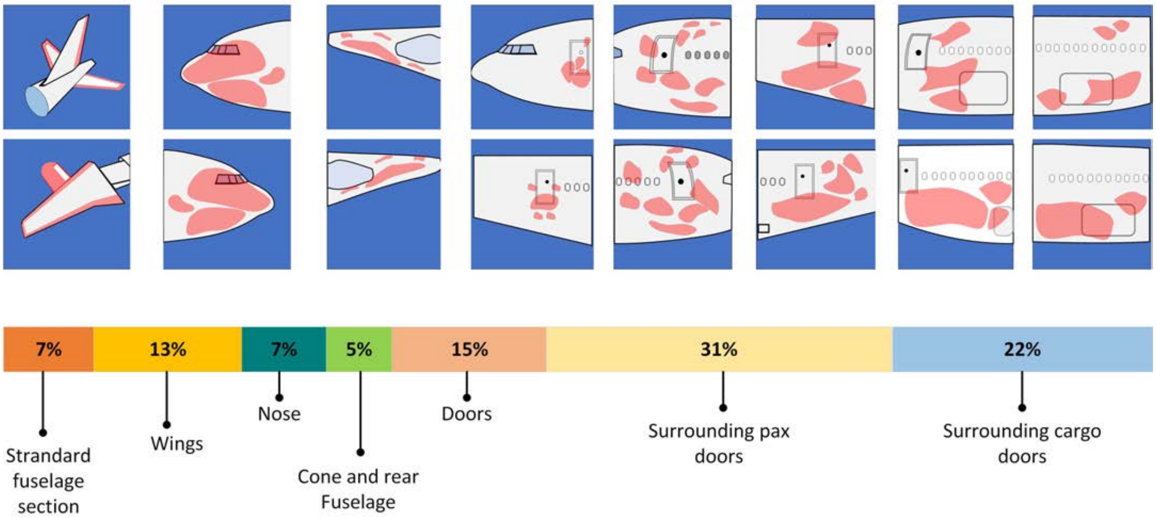

Figure 1.10: Impacts sites by percentage on the Airbus A320 (reproduced from FAST#48[23])

Damage due to impact is a major issue for the safety of operations as it reduces the structural integrity and safety of operations. In the recent years the increase in the use of drones in irregular manner have posed a cause of concern for the safe operation of the aircrafts increasing the vulnerability of their unwanted collisions [24]. A concerning aspect involving impact events on FMLs is their susceptibility to damage when subjected to low or high velocity impacts. In most high velocity impacts (HVIs) the damages are clearly visible due to the through the thickness perforations or cracks appearing near the impact site unlike the case for LVIs. In most LVI events, the barely visible impact damage (BVID) of composite laminates can be a concerning issue [25], as it can grow undetected depending on the event of future loadings which may be well under the critical limit. Consequently, the damage experienced by such hybrid structures on account of dynamic load due to impact is complex in nature involving various failure modes as illustrated in **Figure 1.11** [26] which shows a cross-sectional view of a symmetric quadrant of a typical impactor-target system. As seen the typical damage associated with GLARE on account of impact is by local indentation of the outer aluminium layer followed by delamination and matrix cracking. With higher energies of impact, the rear aluminium failure can occur by cracking and the impactor penetration may occur.

Primary failure due to impact damage has been an increasing concern, especially in the current aviation scenario where the use of composites has seen a significant increase. It has been reported that in the fuselage repairs of seventy-one Boeing 747, at least 13% of 688 repairs were related to damages caused by impacts [27]. Due to the ductile nature of the outer aluminium layer there is indentation at the impact site during LVI at lower energies which enables easier inspection for damage [28,29]. But in reality, this estimate can be much higher since impact damages are repaired when visible cracks are formed or when the dent depth exceeds the maximum limit and hence their repair may be oversighted. This makes the critical analysis of LVI an important area of study since internally delamination may occur, thereby significantly compromising the flight safety.

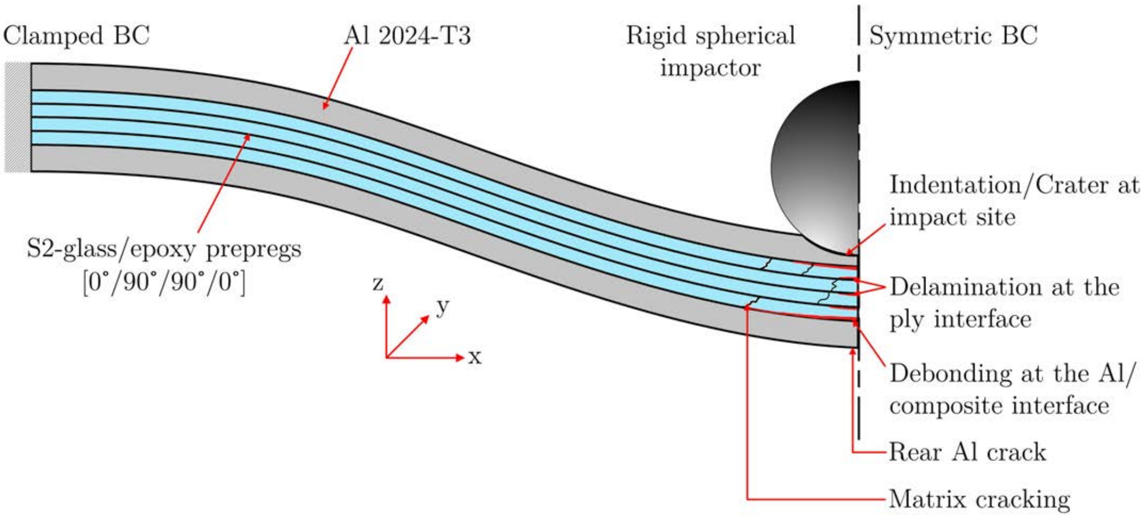

Figure 1.11: Typical failure modes in a FML due to LVI

1.6. Motivation for present research

The damage due to impacts have become one of the critical area of concern for aircraft structures. The FMLs like GLARE often find their use in thin-walled structures, making them susceptible to impacts at lower and higher velocities. As discussed previously, the different scenarios pertaining to these are hailstorms, bird strikes, runaway debris and more recently unwarranted flying of drones and other human actions. There are well documented reports of bird strikes on planes [30]. Such accidental impact events by foreign objects have been a constant cause of concern because of their nature to evade visual detection in most of the cases when subjected to LVIs.

In order to investigate the damage of such advanced composite materials like GLARE FMLs, it is necessary to have systematic and in-depth insight on their structural response and the associated local effects in the vicinity of the impact site to accurately estimate the damage sustained by them. An effective approach to analyse the effect of impact on such structures is to study two main aspects of impact, viz. the resistance to impact damage and the impact damage tolerance. Impact damage resistance of a structure is its response to impact and the damage incurred by it because of impact. On the other hand, when the study is associated with the impact damage tolerance, it mainly deals with the strength and stability of the structure with existing impact damage. This forms the motivation in investigating the impact damage resistance of GLARE structures when subjected to LVI. Since, it is not always feasible to conduct experiments due to material and economic constraints, a full 3D finite element simulation to investigate the dynamic responses to assess the damage on account of LVI on GLARE and to study the influence of the important parameters on such damage could be a worthy area of investigation.

1.6.1. Research scope

High energy impacts can lead to through the thickness perforation and cracks and under such events complete replacement of the part becomes necessary if not repairable by use of composite patches. The impacts occurring at low energies may result in surface damage and internal delamination which is difficult to assess in case of composites but are visible in FMLs due to the occurrence of surficial dents. But in case of BVID, although the impact site damage may not be readily inspectable, damage of the inner layers in the form of delamination, matrix or fibre cracking may occur. Therefore, a critical and thorough analysis of such impact events is of utmost concern. Works can be undertaken to study the LVI on GLARE which might lead to significant internal damage in the form of delamination of these structures with barely visible external damage. GLARE being a highly favoured material for many impact prone structures as well as their better fatigue responses and residual strengths makes it an interesting material for the study of its responses subjected to LVI. Therefore, the study of LVI on these material for use in aircraft structures is necessary to assess their impact responses based on the impactor mass, type and to predict their failure and performance under such situations.

In general, the impacts occurring in real scenarios can be arbitrary, simultaneously impacting at different trajectories, giving rise to complexity in analysing the impact phenomena. This necessarily entails the need to implement a robust numerical finite element (FE) model capable of modelling impact on such GLARE structures. To obtain practically viable response of the target on account of LVI, the different physical parameters affecting the impact needs to be investigated. These parameters can be geometry based like the target size and the shape and size of the impactor. In addition to the impactor trajectory and impacting velocity the material based parameters like the different stacking sequence on impact responses needs to be explored to have an in-depth understanding of the LVI phenomenon on GLARE. More importantly, the contact model for such complex dynamic analysis needs to be properly implemented in the FE model taking note of the different critical parameters like the contact stiffness, mesh refinement, and a stable time step that can have significant influence on the analysis. Therefore, investigating the effect of these influential parameters such as target panel size, stacking sequence, ply orientation, the sequence of the occurring impacts, impactor mass, impact location and impactor trajectory on the impact response could be of critical importance.

This study of LVI on GLARE provides the opportunity to investigate the impact response and their damage resistance concerning the primary aircraft materials, i.e. aluminium and composite plies. Based on the FE analysis, the impact resistance of the different GLARE layups can be estimated along with the extent to which they incur damage to help the design engineers to optimise these FML panels for better serviceability.

Chapter 2

Review of literature

In spite of their various advantages over metals, it is inherent of any laminated composite structures to underperform and be susceptible to impact loads compared to metals. This led to the thrust in developing FMLs which show better impact performance compared to bare composite laminates. The present chapter gives a comprehensive overview of the published works on the impact induced response of fibre metal laminates (FMLs) subjected to low-velocity impacts. It is aimed to identify the progress in the experimental and numerical investigations to assess the low-velocity impact on FMLs and GLARE in particular. The limitations faced and the need for continuing research on certain areas of dynamic responses and impact induced failure of FMLs subjected to LVI are ascertained.

2.1. Introduction

The fibre metal laminates (FMLs) emanate from the need for advanced hybrid structures comprising of metals and composite plies to achieve better characteristic properties in terms of structural strength and durability. In the last two decades, there has been a steady growth in the use of advanced hybrid composites like the FMLs, especially in the aerospace sector, to meet the demands for lighter yet durable and strong structures. Using lower-density materials and reducing the thickness; for example, reducing the thickness of the aircraft fuselage can significantly cut operating costs. The fatigue and damage properties of GLARE have made it suitable for its application in the fuselage and upper and lower wings of an aircraft. Also, considering a lighter and thinner GLARE panel compared to conventional aluminium alloy reduces the structure's overall weight. But, a concerning aspect of such thin walled structures is their susceptibility to impacts on account of runaway debris, hails, bird strikes, dropping of tools during maintenance etc. which might cause damage of these laminated structures [31,32], thereby necessitating the need for in-depth analysis of such impact events and makes it a critical area of research. In the subsequent sections, published works in this area are discussed.

2.2. Impact behaviour of FMLs

The study of impact on composite structures has been an interesting area of investigation since the early 1980s by many researchers. The articles on the dynamic analyses of laminated composite targets on account of impact and subsequent analysis of their failure are documented in literature [32–34]. The impact loading can generally be demarcated into low-velocity impacts (LVIs) and high-velocity impacts (HVIs). The LVIs are of more critical in the sense that the internal damages due to LVI are not easily observable from outside, unlike the HVIs where there is laminate penetration and fibre breakage. The range of LVI is generally limited to 10 m/s, although it is also defined in some literature to be associated with matrix cracking and delamination initiation [35,36] which is more common at low impact energies.

There is a considerable amount of work available investigating the impact responses of GLARE and other FMLs in general [37–41] concerning with the normal contact of the impactor on the target. However, in practical applications, the impactor's trajectory of incidence can be arbitrary relative to the target causing complex response of the structure. The FMLs being a combination of metal layers and composite plies, the different combination of the metals and composite plies can vary their out-of-plane responses when subjected to impacts. In FMLs the global dynamic response is dominated by the constituent metal [42–44] and depending on the ductility of the metal layers the damage patterns vary when subjected to impact loadings [45,46]. These can cause complex damage modes such as indentation and cratering of the outer aluminium layer (elastic-plastic behaviour of the outer metal layer) at the impact site, matrix cracking and delamination of the inner composite plies. Furthermore, there is an increased tendency of debonding at the fibre-metal interfaces owing to the anisotropic nature of the composite plies and difference in the strains between the ductile metal layer and the composite plies. This makes delamination a critical damage mode which can significantly affect the post impact behaviour of the FMLs [47]. For targets having the same aerial density, the impact performance of GLARE is at par or superior by almost 15% compared to monolithic aluminium alloys in terms of minimum cracking energy[31]. For impacts at higher velocities (HVIs in the order of 100 m/s), GLARE outperforms conventional aluminium alloys and GLARE 5 was reported to have an increase in the ballistic limit by 15% [45,48].

2.3. Experimental investigations of LVI on FMLs

There are several factors affecting the low-velocity impact response of FMLs which can be classified as material-based or geometry based-parameters. The material-based parameters relate to the type of metal layers and their thickness, stacking sequence, type of fibres, metal to fibres volume ratio and bonding of the interfaces. Geometry-based parameters are the effects of pre or post stretching of the FMLs, size of the specimen to be tested, mass and velocity of the impactor and impactor geometry. The geometry of the impactor can be varied according to the requirement of the test. The specimen to be tested is clamped at all sides or circumferentially for testing specimens with circular clamped conditions and the impact between the impactor and the clamped specimen takes place normally. The energy of the impact can be varied by adjusting the drop height.

Sun et al. [49] carried out indentation tests on 0° and 90° ARALL 2 laminates having a 3/2 configuration to characterise their impact damage and to investigate their residual strength. It was reported that the strength in the transverse direction remained insensitive to impact damage while that in the fibre direction showed a reduction as impact velocity is increased beyond a range. The permanent local indentation caused by the impactor after impact can be used to determine the residual strength.

The resistance to impact damage of the FMLs over other materials like aluminium and other composites were studied through static indentation and low-velocity impact tests on clamped specimens. It was observed that the dent depth for GLARE was similar to that of monolithic aluminium. ARALL and CARALL always showed fibre critical failure, whereas GLARE showed fibre critical behaviour for only the unidirectional variants. The damage size for the FMLs were small compared to that for conventional composites [31,50]. The effect of prestress of the FMLs on the impact response was also studied.

2.3.1. Effect of constituent material parameters

In the analysis of FMLs, the properties of the material constituents play a critical role in determining their impact and fatigue performances. Therefore the FMLS can be classified based on their constituent materials and structural arrangements like their stacking configurations, type of the metal and composite prepreg layers tailored as per the required application [51,52].

2.3.1.1. Metal layer

The proper selection of the metal layers is important so that the stresses at the metal composite interfaces are not extreme due to the difference in their material properties. Besides

GLARE, ARALL [31,49,53] and CARALL [54–56] FMLs have seen numerous investigations pertaining to impact, fatigue and strength characteristics. Furthermore, magnesium (Mg) and titanium (Ti) bases FMLs have also been studied [7,41,57,58].

In the studies investigating the characteristics of CARALL laminates the problem of galvanic corrosion is observed for the aluminium layers when paired with carbon fibre prepregs [13]. It was observed from the findings of published literature [31,59,60] that the grade of the aluminium alloys and their thickness along with their stacking configuration played an important role in determining the mechanical properties and impact behaviour of GLARE and FMLs in general.

Magnesium (Mg) was reported to be suitable for FML owing to its lower density, superior corrosion resistance and better specific perforation resistance compared to aluminium (Al) based FMLs [7]. But the brittle nature of Mg based FMLs resulted in lower impact resistance than Al based alloys [57]. Also, the problem of galvanic corrosion was observed in the case of Mg alloy and carbon fibre based FMLs [61]. For high temperature applications like in the fuselage of supersonic flights, the fuselage temperature rises to as high as 350 ˚F (177 ˚C) and at such temperature range, creeping may occur in aluminium and magnesium alloys owing to their lower melting points [62]. This has led to exploring the titanium based FMLs due to their higher melting point (1668 ˚C) [63] and impact resistance at elevated temperatures [64,65].

In the analysis of LVI on titanium based glass fibre reinforced polymer FMLs (Ti/GFRP) the presence of titanium layers restricted the matrix crack growth and delamination but at the advent of crack on the non-impacted, the delamination growth was seen to be rapid [63]. Furthermore, the relatively lower ductility of the high strength titanium alloy compared to high strength Al 2024 T3 alloys could lead to poor impact resistance and provide no improvement in the impact resistance [66].

Aluminium based FMLs have found widespread use because of the lower cost of the aluminium alloys and their easier machinability along with favourable strength properties. Two types of aluminium alloys viz. Al 2024–T3 and Al 7075–T6 or (7475-T6) are most commonly used as the metal constituent GLARE or FMLs in general. The 2024 grade alloys of aluminium are more ductile and comparatively stiffer compared to the 7075 grade which are more brittle [67]. This results in lower energy until failure for Al 7075–T6 compared to Al 2024–T3 owing to smaller area under the stress-strain curve and it can have significant influence on the impact performance as more energy is absorbed by plastic deformation in case of Al 2024–T3 alloys. Therefore GLARE FMLs having 2024–T3 grade aluminium layers can provide more resistance to impact induced damages compared to 7075–T6 grades [68].

2.3.1.2. Fibre system and architecture

The type of fibre and the fibre architecture also influence the impact response of the laminate. The fibres play an important role in improving the fatigue performance on a FML by keeping a check on the fatigue crack growth. Some of the commonly used fibres are aramid, carbon and glass fibres which are used to make composite prepregs [69].

Carbon fibres have high specific strengths and stiffness but are relatively brittle compared to glass fibres [70]. Although the glass fibres are comparatively low in strength and stiffness but the glass fibres have a larger area under the stress-strain curve and therefore higher strain to failure. This makes the glass fibres a favourable substitute for impact prone structures and their easy availability and lower cost compared to the high cost carbon fibres further reinforces their preferentiality.

In the investigation for the impact resistance of bare fibre reinforced composite laminates, a considerably larger area under the stress-strain curve for aramid and glass fibre based laminates were reported compared to that of carbon fibre based laminates [71]. Also, the carbon fibre reinforce polymer laminates (CFRP) fail by brittle fracture while the E-glass composite laminates fail gradually by interlaminar delamination and other subsequent damage modes. There are other variants of glass fibres which have high strengths and have been used in FMLs such as in GLARE. They are referred to as R-glass and the glass fibres having the highest tensile strengths is S2-glass which are rich in magnesium-aluminium-silica and have approximately 50% higher tensile strength compared to E-glass. They find their application in the aerospace sector because of their high strength, high temperature resistance and inertness to environmental factors [72].

Of late, new interests have been garnered into exploring the fibre architectures of the composite plies. In most of the conventional cases, unidirectional prepregs and 2D plain woven fabrics are commonly used. The unidirectional plies have excellent in-plane properties and their use is seen in the manufacturing of the aircraft wings, tail fins and fuselages. In these plies, there are no transverse fibres and most of the out of plane loads due to impact are borne by the matrix material which can cause delamination at the ply interfaces even when there is no failure in the top and bottom layers of the composite laminate [73]. Stress concentration sites occur due to the crimping of the yarns, causing the in-plane properties of the 2D woven or bidirectional composites to be lower [74].

In recent times, laminates with 3D woven composites have drawn the interest of aerospace sector for their excellent mechanical properties in the thickness direction. The laminates with 3D fibre fabrics were found to have better resistance to repeated impact loads [75]. Several experimental investigations on the LVI and HVI performances of laminates having yarns in 1D, 2D and 3D have been carried out [76–83].

2.3.1.3. Matrix media

The matrix media also plays a significant role in determining the impact behaviour. The role of the matrix in a fibre reinforced polymer composite is to keep the fibres aligned and stabilized and assist in the load transfer between the fibres and across the interfaces. The matrix constituent can either be thermosetting or thermoplastic. Although the thermosetting matrix material such as epoxies are widely used, the thermoplastic matrix materials like polyetheretherketone (PEEK) has seen some positive response in the manufacturing of composites subjected to impacts.

The impact characteristics of the thermoplastic composites and thermosetting composites have been explored investigating the influence of the matrix type on impact resistance. It was observed that the thermoplastic composites performed better because of their ability to absorb a significant amount of impact energy without undergoing extensive damage [84,85]. These result in the thermoplastic composite laminates to incur lesser extent of interlaminar delamination compared to thermosetting composite laminates. But the thermosetting epoxy resins are extensively used in the making of FRP composites because in addition to the ease of impregnating the fibre systems they have superior mechanical characteristics, better temperature performances and superior strength and stiffnesses compared to thermoplastic matrix systems. Furthermore, there is a fuzziness in the research area exploring the impact response of both these matrix systems and as a result the preferentiality of the thermosetting matrix based composites are still strong and the use of thermoplastic matrix based composites are limited to special impact applications.

Vlot [68] reported that the LVI resistance of the ARALL FMLs having thermoplastic matrix material are lower compared to the thermosetting matrix based ARALL. This may be attributed to the higher temperature required for curing thermoplastic material based FMLs which results in the Al 2024–T3 alloys to lose some ductility and also leads to the development of unfavourable internal stresses during the manufacturing process. These negatively influence the energy absorbing capacity and hence the impact performance of the outer aluminium layers. Also, the crack length of the ARALL with thermoplastic matrix system was found to be larger compared to that of thermosetting matrix based ARALL although the first cracking energy for both the ARALL variants were found to be in close range.

2.3.2. Effect of stacking configurations

There are numerous literature exploring the effect of stacking sequence of laminated composites and FMLs on impact performances [58,86–92]. It is evident that the tendency for interlaminar delamination at the interfaces of plies having differently oriented fibres or different material properties is more. The interlaminar fracture toughness can be improved by selecting an optimized stacking sequence and interface properties which can effectively improve the impact resistance and damage tolerance. In exploring the delamination for the different stacking sequence, Wang et al. [93] concluded that the accurate estimation of interlaminar delamination is a key factor in estimating the damage tolerance of laminated composites.

Khoramishad and Tofighi [94] investigated the effect of the adhesive layer material, their thickness and the number of metal layers on the LVI response. It was observed that the metal layer elastic modulus and yield strength significantly influenced the contact duration and contact force magnitude. Yaghoubi and Liaw [91] observed in their ballistic impact analysis of GLARE 5 FMLs that the layup and orientation influenced the contact resistance and the contour of the damage pattern. In their observed results, it was found that the specimen having $[0/90]_S$ lay-up orientation, dissipated the most energy compared to quasi-isotropic or unidirectional panels.

Liu and Liaw [67] conducted a number of LVI tests to investigate the impact responses of GLARE 2 and GLARE 3 FMLs with respect to unidirectional and cross-ply glass fibers respectively. It was observed that for similar thickness, GLARE 3 having cross-ply prepregs were superior to GLARE 2 when subjected to LVI. In the works of Laliberté et al. [95], GLARE 5-2/1 configuration was found to have relatively higher impact resistance compared to other configurations. Many works have been carried out investigating the superior impact behaviour of GLARE 5 FMLs and its suitability in aircraft fuselage, cargo floors and wing skins [45,96]. This can be attributed to a greater number of glass/epoxy layers in GLARE 5.

Zohreh and Taheri [58] stressed the significance of weight and material cost in their works studying the influence of stacking sequence on LVI responses of 3D woven fibreglass based FML. In line with the weight saving aspects along with lesser dissimilar material interfaces, a GLARE 5-2/1 configuration may be regarded more suitable compared to other configurations. Seyed et al. [88] analysed the low-velocity impact of GLARE 5-3/2 FMLs considering unidirectional, quasi-isotropic, angled and cross ply orientations. It was observed that the impact properties were affected by stacking sequence.

2.3.3. Effect of metal volume fraction

In FMLs, the change in the stacking configurations considering different combination of fibre metal layups may change the metal volume fraction (MVF) because of the change in the number of metal layers and composite plies along with the change in the thickness of the metal layers. Sadighi et al. [41] investigated the influence of the MVF on the impact resistance of GLARE 5–3/2 and observed that the impact resistance improved with the increase of the metal thickness. In their analysis, it was observed that upon normalising the maximum impact forces with respect to the laminate weight, the specific maximum impact force for the GLARE plate having slightly thinner aluminium layer was more compared to that for the GLARE plate having thicker aluminium layer.

Vlot and Krull [97] observed that increasing the S2-glass/epoxy content improved the impact damage resistance of the FMLs. GLARE FML showed approximately 15% better minimum cracking energy compared to monolithic aluminium for impact at lower velocities (10m/s). Zhu and Chai [98] investigated the quasi-static and low-velocity impact responses of unidirectional and woven glass fibre-reinforced aluminium FMLs having 2/1 and 2/2 configurations. It was reported that the maximum load showed no change with variation in MVF but the GLARE laminates having unidirectional fibres showed better stiffness and failure strengths. Khoramishad et al. [99] observed the increasing the MVF of a particular metal in a metal laminate could cause the laminate to inherit the impact characteristics of that particular metal material. This can be of significant importance while modelling a FML from designers' viewpoint in tuning their effective structural properties when subjected to LVI.

Laiberté et al. [100] compared the low-velocity impact responses of GLARE 3-2/1, 4-2/1 and 5-2/1 laminates and observed that GLARE 5-2/1 had the highest impact damage resistance compared to the other configurations owing to more number of S2-glass/epoxy layers and its greater volume fraction of fibres.

2.3.4. Effect of total thickness

In the analysis of LVI or any quasi-static loading of a particular laminated plate, the maximum deflection attained is significantly influenced by its total thickness. A thicker plate will undergo a lesser extent of deflection compared to a thinner plate of the same material [68]. Seyed and Liaw [45] investigated the ballistic impact behaviour of GLARE 5 FMLs having different configurations and observed that the overall thickness and configuration of the specimen significantly affects the maximum contact force developed. In addition, the impactor response at 50m/s was found to vary in a parabolic trend with respect to MVF and specimen thickness. Although the perforation resistance and the maximum force increases for GLARE with increase in the overall thickness, the specific perforation energy more or less remains the same over the thickness range considered [101]. The thinner laminates owing to their lower inertia responds quickly to the incoming impact compared to a thicker laminate [97]. The efficient membrane deformation of a thinner plate results in higher specific cracking energy compared to a thicker plate when subjected to LVI. Similar observations were reported by Liaw and Liu [18] while examining the thickness effect of the GLARE 5 panels by increasing the number of layers which resulted in a parabolic variation of the minimum cracking energy with respect to the panel thickness.

Seyed et al. [102] investigated the LVI responses of GLARE 5 panels having different thicknesses and reported that the failure modes changed depending on the thickness of the plate. The main failure modes being fibre critical failure and aluminium critical failure depending on the plate thickness, it was observed that for the thinner GLARE 5-2/1 plates, post delamination/debonding the aluminium layer on the non-impacting site failed by cracking. But in the case of GLARE 5-3/2, failure occurred mainly by debonding on the non-impacting side and fibre breakage and fracture of the aluminium layers followed. With further increase of the panel thickness as in case of GLARE 5-5/4 and 6/5 configurations, the failure on account of delamination occurred at relatively lower energies of impact. Fan et al. [103] observed that with increasing thickness of the GLARE laminates, the perforation energy showed an increasing trend and increasing the thickness of the composite layers significantly enhanced the resistance to perforation.

2.3.5. Effect of hybridisation

There are limited literature on studies investigating the effect of hybridisation of GLARE by incorporating carbon/glass fibre or Kevlar-49/glass composite layers on their LVI responses. Some of the literatures investigated the effect of such hybridisations on the mechanical behaviour of these FMLs [104,105]. Kevlar/epoxy laminates are popular in the military and aerospace applications due to its better impact characteristics [106–108] and their hybridisation with aluminium layers investigating the tensile impact behaviours at high strain rates are reported in a few literatures [109,110]. It was observed that the stacking sequence of the aluminium layers significantly affected the energy absorbed during impact. Moreover, exploring the weight saving aspects, hybrid laminates can result in further reduction in the overall weight of the structure and improve the structural performances. In recent developments, the hybridisation of different fibres are reported and a few articles on carbon-glass fibre hybrid FMLs have been published [104,111,112].

2.3.6. Effect of geometrical parameters

2.3.6.1. Target geometry

Geometrical parameters like specimen geometry, impactor mass and velocity influences the impact response of the FMLs. The influence of target geometry on the low-velocity impact response of a glass fibre reinforced polyester composite has been investigated by Cantwell [113]. It was observed that the extent of damage varied directly with the force generated during impact. Furthermore, the extents of the damage-force for the larger and smaller sized GFRP plates lied in a narrow band and were similar in nature.

From the LVI analysis of GLARE panels, Fan et al. [114] observed that the initial load-displacement slope and the maximum contact force decreased upon increasing the target size. The larger sized plate resulted in reduced flexural stiffness making it more flexible and as a result reacts quicker to the impact and incur a lesser extent of damage. Seyed et al. [88] observed a similar trend in their study of GLARE 5 FMLs. It was observed that the damage patterns and the impact behaviour were invariant to the specimen geometry but changes are observed when the outer perimeter of the target geometry was changed from square to circular. This was attributed to the relative anisotropy of the specimen with respect to its clamping.

Laliberté et al. [115] also investigated the effect of the geometry of the fixture on the LVI response of GLARE by considering square and circular fixture geometries. It was observed that the square specimens showed corner deformations unlike in case of the circular specimens and hence the specimen fixture needs to be carefully selected as it can affect the damage evolution within the laminate.

2.3.6.2. Impactor parameters

The effect of increasing impact energy on the impact damage of FMLs and bare laminates is a generic conclusion which is commonly reported in many literatures [45,113,116]. But increasing the impactor mass and velocity alone individually will result in different impact responses. In the analysis of LVI on laminated composite specimens, it was observed that for impactor masses much higher than the mass of the target, the LVI responses were similar to quasi static response whereas it is wave controlled for small mass impacts unaffected by the plate size and boundary conditions [117].

It has been observed that the damage incurred by the target with a projectile having a smaller tip diameter is more compared to an impactor having a larger tip diameter [118,119].

With the smaller diameter impactor, the damage was localised and extent of delamination was more with cracks appearing on the non-impacted side aluminium layer which primarily dissipated the impact energy. But a larger diameter impactor caused a global deformation of the target GLARE plate and lesser extent of delamination indicating that a large amount of energy was absorbed by global plate deformation. Similar observations were made by Sevkat et al. [120] regarding changing the impactor geometry which caused a change in the peak impact force attained during an impact event.

In the LVI tests of carbon fibre reinforced aluminium (CARALL) FMLs and bare carbon fibre reinforced polymer (CFRP) laminates conducted by Bienias et al. [121], it was observed that in the impact energy range of 1.5 J-2.5 J, delamination is a prevailing form of damage which is also observed at the fibre/metal interfaces.

From the discussed literature, it can be emphasised that delamination damage occurring at the interfaces will differ based on the loading history as the delamination at the interfaces is influenced by the generated contact force as well as by the plate strains which influences the stresses developed at the interfaces. This highlights the importance of relative mass of impactor to target on the dynamic response as well as the damage pattern experienced by a laminated structure on account of impact.

2.3.6.3. Cut-outs and discontinuities

In many cases, open holes are present in a structure required for riveting and also cut-outs are made in the panels to allow for access to inner components such as wires and for carrying out scheduled repair and maintenance of inner assemblies. The presence of open holes in the form of cut-outs can have adverse effect on the integrity of a structure when subjected to impact loadings. Such cut-outs in a laminated composite can cause stress concentration regions around the hole peripheries making the FML prone to delamination when subjected to LVIs. Moreover, in case of aircraft structures, the fuselage is supported by frames and stringers joined to the outer skin by riveting [122].

Santos et al. [123] experimentally investigated the effect of the distance between the impact point and the hole cutout on the fatigue strength of a glass/poxy laminate subjected impact. It was observed that at larger offset distance of the impact point from the circular cutout, the contact point deflection decreases but the maximum contact force increases. The damage accumulation near the impact site and the circular hole upon repeated impacts resulted in a decrease in elastic energy. Similar analysis was done by Ortiz et al. [124], investigating the effect of drilled holes on the aluminium layers of GLARE and being subjected to LVI. Holes were drilled on the aluminium layers to create flow paths to impregnate the inner composite preforms. It was observed that the holes in close proximity to the impact zone resulted in cracks propagating through the hole boundary and along the flow path.

Jain and Mittal [125] observed that maximum stress concentration occurred under transverse static loading at the hole boundary for plates with a central circular hole. Such discontinuities in the form of cut-outs or open holes can significantly influence the way delamination grows around these locations due to increased stress concentrations under transverse loads on account of LVIs. Therefore, it is crucial to study the LVI response of such panels having open holes or any such discontinuities and accurately estimate the underlying delamination at the interfaces such that it enables the prompt repair/replacement of components preventing catastrophic accidents.

2.3.7. Effect of temperature, preloading and post stretching

It is well established that the prestressing of metallic alloys can affect their mechanical behaviour, significantly affecting the overall properties of FMLs [126]. Vlot [27,127] investigated the effect of the initial prestress of ARALL on the LVI behaviour and observed that upon impact, the cack length of the outer aluminium layer increased at higher initial prestress. In addition, the damage shape changed with the preload as the crack tended to remain perpendicular to the preload direction instead of bending towards the fibre direction.

Homan [128] analytically modelled the effect of curing on GLARE laminates as the curing process induces residual thermal stresses on the individual components during cooling on account of their different thermal coefficients. This causes tension of the aluminium layers and compression of the glass fibre/epoxy layers, thus resulting in the preloading of the GLARE laminates.

The effect of post stretching of these GLARE laminates is seen by the reversal of the internal stress states [31,129] causing a favourable compressive (crack closing) stress on the aluminium layers and tensile stress in the glass fibres. But the residual stresses have minor influence on the impact characteristics of FMLs, as reported in the literatures of Roeder and Sun [130] and Morinière et al. [96]. In addition, the effect of temperature was experimentally studied by Badawy [131] on GFRP composites and observed that the thermal strains could change the GFRP composite failure mode from fibre pull-out to fibre breakage when increasing the exposure temperature.

Hirai et al. [132] studied the low energy impact response of glass/epoxy composites. It is seen that there is a degradation of the mechanical strength of the resin at elevated temperature which increases the damage extent of the composite. Similar observations were made by Chow et al. [133] on the LVI response of GLARE. It was observed that the elevated temperatures increased the permanent energy absorption with reduced impactor rebound for non-penetrating impacts, and the load-bearing capacity of the GLARE dropped by 5% to 10% for every 20˚C rise in temperature.

2.4. Numerical investigations of LVI on FMLs

During LVI on FMLs, there is a high possibility of damage beyond the visible dents and perforation which are challenging to detect, limiting the possibility of physical inspection. Also, the production of these hybrid laminated components requires high expertise and the processes involved need to be properly monitored to ensure the final product's quality which increases the production cost. In addition, the experimental investigations may lead to wastage of material and time, thereby increasing the expenses. Therefore, the need for conducting numerical simulations have taken a positive thrust since the complexity of physically analysing the critical damage modes can be simplified by numerical investigations. To overcome these limitations, researchers have adopted analytical methods as well as numerical techniques for more in-depth and robust analysis of FMLs under LVI.

2.4.1. Finite element analysis of LVI on FMLs

A number of work associated with the numerical analyses of the impact responses of composites are available [75,134–136]. User developed FE codes and commercial software like ABAQUS, LS-DYNA have been extensively used to predict the impact responses and damage in composite laminates. These numerical analyses have been extended to the low-velocity impact analysis of FMLs and are presented here.

Tsartsaris et al. [137] modelled GLARE laminates using shell elements where the delamination was modelled using a contact tie-break formulation. Seo et al. [138] did finite element analysis for low-velocity impact response of GLARE laminates (refer **Figure 2.1**) and emphasised the use of three-dimensional solid elements (C3D8R) over continuum shell elements (SC8R) for accurate estimation of delamination as it depends on the out of plane stress states of the consecutive layers. This necessitates incorporating all the six components of stress and a three dimensional failure model in order to accurately simulate the damage and failure of these FML composites. **Figure 2.2** shows the meshed geometry of the impactor and a half section of the circular clamped GLARE plate used for numerical analysis of LVI by Seo et al. [138]. The impactor was modelled as a perfectly rigid body with motion only in the vertical direction while the layers of the GLARE target was modelled by using hexahedral solid elements. It was reported that the slight deviation in contact duration between the experimental and numerical analyses was due to the small amount of clearance between the clamps and the specimen, prolonging the impact duration in case of the experimental examination. Sadighi et al. [41] also concluded the same regarding the use of three dimensional solid elements for accurate modelling of the interfaces of the FMLs subjected to impact loading to correctly predict the low-velocity impact responses.

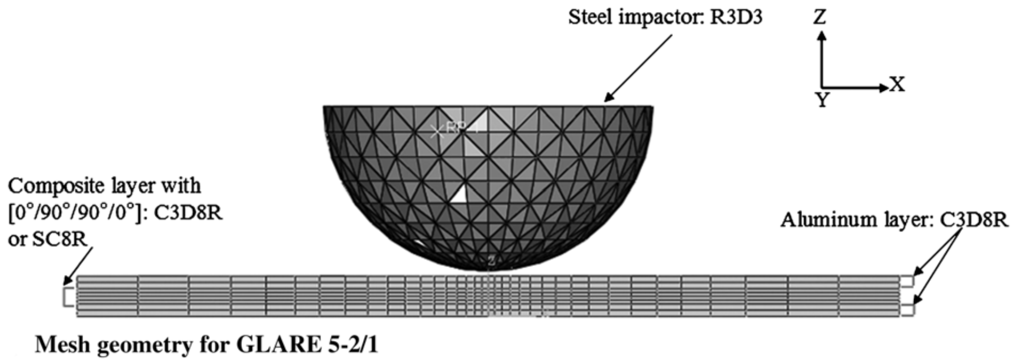

Figure 2.1: Finite element model geometry of LVI on GLARE [138]

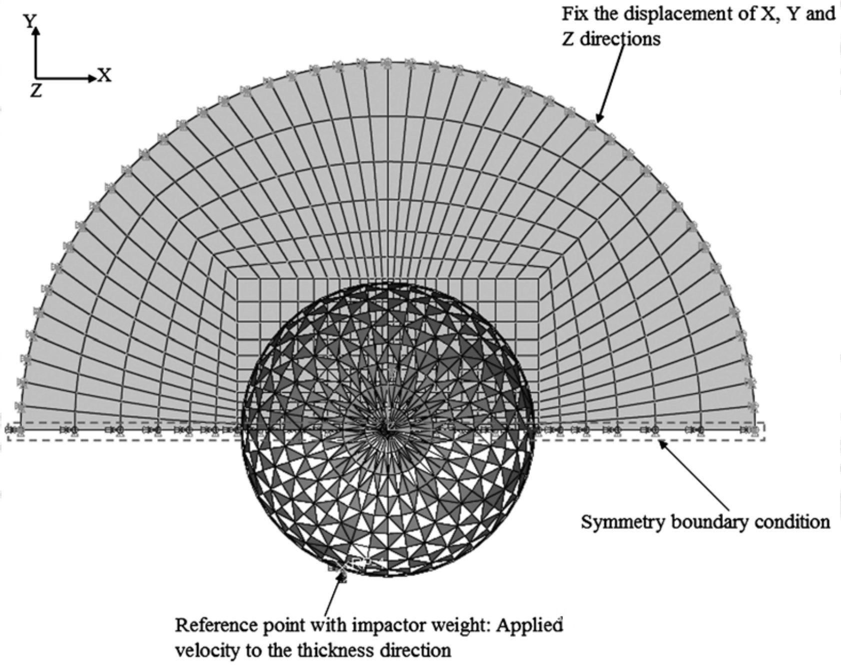

Figure 2.2: Boundary conditions of finite element model geometry [138]

Fan et al. [139] did FE analysis for low-velocity impact on GLARE laminates to understand the effects of target size, impactor size and impact location. The aluminium layers were modelled as elasto-plastic material considering shear and tensile failure to simulate damage in the aluminium layers and the woven glass fibres as orthotropic elastic material considering Hashin's failure criteria for damage initiation.

Liu et al. [118] used the commercial finite element code LS-DYNA to simulate the impact responses of circular GLARE laminates and observed close approximations with experimental results. The interface between the aluminium and glass/epoxy was modelled using the tie-break interface option in LS-DYNA to simulate delamination. It was seen that severe local damages were incurred with smaller indenters whereas the larger indenters resulted in extensive global deformation of the GLARE specimens.

In recent times, the incorporation of user defined subroutines in explicit/dynamics analysis of impact on composites have enabled to model the damage progressions of laminates in a more accurate manner [140–143] and evaluate their compression after impact (CAI) performances.

Zhang et al. [144] implemented the Johnson–Cook model for aluminium and implemented a VUMAT subroutine for GFRP based on Hashin's criteria using bi-linear traction separation law for the cohesive interfaces. Investigating the energy dissipation mechanisms of GLARE during LVI and its relationship with the dynamic responses and the damages, it was observed that although the aluminium cracking on account of LVI is critical in nature but the delamination between the rear GFRP and aluminium interface remained indifferent. Delamination was observed to take place even in the absence of aluminium cracking which makes delamination a critical cause of concern. In this regard, optimisation of GLARE configurations may be done, given the significance of delamination on compression after impact performance.

Yao et al. [145] investigated the behaviour of CARALL FMLs under multiple central impacts with the net energy being same. They reported that the sequence of the multiple impacts governed the extent of damage of the layers and an improvement of the stiffness after the first impact was attributed to the strain hardening of the aluminium layers with stiffness reduction in subsequent impacts. It was also observed that the extent of delamination is closely related to the magnitude of impact energy, the impact energy divisions and their sequence. Some recent computational works on the LVI analysis of FMLs and composites along with important observations are tabulated in **Table 2.1**.

Table 2.1: Numerical investigations of LVI

Source	Key aspects of modelling	Interests/Observations
[144]	• Johnson–Cook model for aluminum • Hashin's criteria and exponential damage evolution law based VUMAT subroutine for GFRP and bi-linear traction–separation cohesive zone model	• Importance of delamination on CAI performance. • Role of Al on the damage evolution and rebounding processes.

[146]	• 2D Hashin and 3D Hashin VUMAT models are used to analyse and compare each composite layer • Johnson cook model describes the aluminium layer.	• Failure forms of CARALL under the tensile loading mainly show aluminium layer fracture, fibre pull-out and fracture, and matrix tensile fracture. • The 3D Hashin model more accurately revealed the failure mechanisms.
[143]	• The plies of the finite element model are created using 3D deformable solid elements. • 3D Hashin criteria and a surface-based cohesive behavior to capture the delamination between the plies.	• A unit cell representation is used to calculate the homogenized elastic properties of the non-crimp fabric plies. • A numerical model of the CAI specimen is developed
[147]	• A progressive damage finite element model is developed using VUMAT. • The Hou failure criteria are applied to simulate the intra-layer damage, while the cohesive zone model is adopted to describe the inter-layer damage.	• For both single and repeated impact, the impact response parameters vary linearly with thickness for the chosen plates. • The dominant damage mode changes from intra- laminar damage to inter-laminar damage as the thickness increases. • The repeated impact does not change the internal damage mode, but only causes the slight expansion of damaged region.
[133]	• Using explicit nonlinear code LS-DYNA. • Johnson-Cook model for aluminium, Chang- Chang failure criteria for GFRP and cohesive zone model for delamination.	• The temperature ranged from 30 to 110 ◦ C has proven to significantly affect FML impact characteristics through load-displacement and final deflection responses.
[148]	• Two models of elastic damage, i.e. ductile and Johnson-Cook damage models. • C3D8R elements – reduced integration for the polymer laminates. • 3D Hashin's criteria (VUMAT subroutine).	• For high strain-rates, Johnson-Cook damage model showed a lower mismatch compared to the ductile damage model.

[149]	• Using LS-DYNA • A 3D model for GLARE accommodating the volumetric cohesive interfaces. • Lagrangian smoothed particles populated the projectile.	• The mismatch in bending stiffness of sub-laminates led to large interface failure by mode-I loading. • The gelatin projectile considered allowed a greater dissipation of the projectile kinetic energy in the projectile fragmentation.
[150]	• The Johnson-Cook model for the aluminium layers. • A search algorithm IAAGSS [151] is applied to search fracture plane for Puck criteria.	• Delamination is found to be the dominant damage mode compared to intralaminar damage. • The delamination at the Al/composite interface is more serious than that between composite layers.
[152]	• 3D Hashin failure criterion (using VUMAT).	• Effect of repeated impacts on the global mechanical responses. • Exploring the effect of repeated impacts on damage characteristics and delamination at the interfaces.

2.4.2. Analytical modelling of LVI on FMLs

The dynamic response of FMLs is influenced by the metal layers [43,45] and the stacking sequence and nature of fibre significantly influence the damage pattern [153]. As the FMLs consists of different combinations of metals and composites, their global behaviour subjected to impacts need careful attention during modelling [42]. More importantly, a model developed to analyse thin specimen may not be applicable to thick specimen [116]. Thus, the analytical modelling of such systems can be complex and careful interpretation of the dynamic behaviour needs to be done to accurately model their dynamic responses on account of LVI.

The analytical methods to analyse the impact response of composites have been reported by many researchers [154–157]. Abrate [42] classified the available solution models for impact into four categories viz. spring-mass models, energy balance models, complete models and impact on infinite plate.

Shivakumar et al. [155] neglected the transverse shear deformation of the circular laminated plates and considered the plate to deform axi-symmetrically under axi-symmetric load. Their analysis was based on minimisation of the total potential energy and von Kármán strain displacement relations. The analytical results for damage areas obtained by suitable failure criteria were in close agreement with experimental results. A large array of elements was accounted in their model as each ply was represented by a single layer of elements. In their analysis the ply failure was evaluated using the Tsai-Wu criterion and the underlying damage modes (fibre splitting and fibre failure only) were checked using the maximum stress criterion. From their analysis it was observed that the damage initiated at the bottom-most ply with the extent of damage being larger for the bottom ply and the target plate size influenced the splitting failure thresholds.

Ramkumar and Chen [154] took into account the transverse shear deformation using Mindilin's plate theory and the analytically predicted results were seen to compare satisfactorily with those obtained by experimental results as well as the finite element solutions for low-velocity impact. Pang et al. [156] predicted the contact duration, force, indentation and displacement considering a spring-mass model for impact of a hemispherical impactor on laminated composite plates by implementing Hertz contact law between the impactor and the composite plate.

There are a few studies investigating the low-velocity impact response of FMLs based on the analytical methods. Vlot [68] made significant contribution on the low-velocity impact response of FMLs. The first impact model proposed by Vlot [68] was based on the linear elastic analysis. In this model, a clamped rectangular or circular specimen was modelled by considering it as a spring-mass system having a constant stiffness and an equivalent mass. The contact between the impactor and the plate was assumed to be rigid. In addition, the bending stiffness of the plate was assumed to be constant for deflections smaller than plate thickness.

The second impact model of Vlot [68] assumed the Hertzian contact law between the impactor and clamped plate during the low-velocity impact. The plate was modelled by two springs in series viz. a non-linear one with the Hertzian contact stiffness and a linear one for the bending stiffness of the plate. As the impact process involves the energy transformation between the impactor and the plate, the governing equation was obtained by using the conservation of energy.

In the third model again by Vlot [68], an elasto-plastic deformation was incorporated considering a quasi-static loading and assuming an axis-symmetric dent shape of the specimen. The elasto-plastic material was assumed to have a bilinear effective stress-strain curve, which was described by the Young's modulus, yield stress and strain hardening coefficient.

Caprino et al. [158] assumed a simple second order polynomial curve representing the load variation with respect to displacement during both loading and rebound phase of a GLARE laminate in the developed semi-empirical low-velocity impact model. The model was developed to predict the quasi-static response of the structure. But validity of the developed model was observed only until there is a sudden discontinuity attributed to sudden load drop. So, this model is limited only for initial design stage until the point of first significant failure.

Payeganeh et al. [159] investigated the low-velocity impact response of FMLs and importance of the parameters such as layup configuration, mass and velocity of the impactor and the aspect ratio of the plate. The governing equations of the composite plate was solved analytically using the first order shear deformation theory and Fourier series method. The impactor-plate interaction was modelled with a two degree of freedom spring mass system and Choi's linearized Hertzian contact model [160] was used in the low-velocity impact analysis. Bikakis [37] also modelled the low-velocity impact response of thin circular GLARE plates considering a linearized spring-mass model.

Asaee and Taheri [161] developed an analytical model to predict the low-velocity impact responses of 3D fibre metal laminates. In the developed analytical model based on the Hertzian contact law, the energy is assumed to dissipate through shear, bending and indentation contact mechanics by using an energy balance approach. The integrity of the developed analytical model was ascertained by comparing the results with the numerical and experimental results.

2.5. Oblique LVI on GLARE

Most of the works investigating the low-velocity impact response of FRP composite structures and FMLs have considered a normal impact of the projectile on the target. Works regarding oblique low-velocity impact (OLVI) on laminated composite structures and FMLs are limited. Experimental studies reporting the actual contact forces during oblique impact have been less common as compared to the normal drop weight impact tests carried out on the specimens. However, in practical applications, the impactor's trajectory of incidence can be arbitrary relative to the target. Although numerous works are done on studying the oblique impact between bodies incorporating different contact models [162–167], only a few literatures are available on OLVI on laminated structures in general and GLAREs in particular [168–172] investigating their dynamic responses and the associated interfacial delamination.

Neogi et al. [173] investigated the low-velocity impact behaviour of a simply supported composite hypar shell roof under oblique impact, considering modified Hertzian contact law, for different impact velocities and impact angle. They reported a reduction in contact force with an increase in obliquity. Moreover, higher the impactor velocity, larger was the observed contact force but the force died down to zero relatively faster which was attributed to the rapid elastic rebound of the impactor.

Mao et al. [172] developed a new analytical oblique impact contact model to predict the nonlinear dynamic response and damage propagation of FRP laminated plates under low-velocity impact. The contact model utilised Hertzian contact law for calculation of normal contact force and the theory of Mindlin and Deresiewicz [174] for calculation of tangential contact force which were iteratively calculated simultaneously during the impacting process. In the oblique impact of elastic spheres without adhesion, the normal and tangential contact force-displacement relations was modelled based on the theories of Hertz and Mindlin and Deresiewicz respectively [175,176].

Thornton et al. [177] compared the alternate contact force models for the oblique impact of an elastic sphere on a planar target and based on their analysis it was reported that the tangential force needed to be updated incrementally as the tangential stiffness changed with the varying normal force while considering a non-linear contact model.

Bikakis [178] conducted finite element analysis using ANSYS software to predict the static response of thin circular clamped GLARE laminated plates, subjected to frictional oblique indentation at the centre. The derived analytical formulae predicted the GLARE plate indentation load and strain energy as a function of the displacement of the indentor, the friction coefficient, and the indentation direction which were in good agreement with the numerical results.

Meybodi et al. [179] modelled OLVI on GLARE by considering two types of boundary conditions for the impactor viz. constrained, for a constant impact angle between the impactor and target during and after the contact, and free, in the case rotation of the impactor and change in angle with respect to the target is likely to occur. The effect of the considered boundary conditions and the impact angle on the contact force and energy absorption were studied.

Yao et al. [171] investigated the oblique successive impact behaviour of CARALL and observed that the damage tolerance improved with increasing obliquity of impact. In case of repetitive impacts, the strain hardening of the outer aluminium layer led to an increase in the stiffness of the FML after first impact and a rise in the contact force is seen. After first impact, delamination and matrix damage were observed to be the main damage modes occurring in the FML and similar damage modes were seen during the second impact event. These were difficult to detect since no evident metal cracks were observed on the FML surface during the first two impacts. With further subsequent impacts, no increase in the stiffness is seen due to severe damage of the composite plies and damage accumulation of the metal cracks on the outer aluminium layers. Delamination damage was seen to be a critical damage mode which generated from the shear stresses due to stiffness mismatch at the metal/composite interfaces.

Li et al. [180] also studied the low-velocity impact response and damage of GLARE laminates under single and repeated impacts at different impact angles. A cohesive zone model was utilised to analyse the delamination at the interfaces of aluminium and composite layers implementing a user defined material subroutine in VUMAT to simulate the damage behaviour of the composites. From the investigations of LVI at different obliquities, the dynamic response was found to vary with the obliquity of impact. It was observed that although the error percentage of 3D Hashin criteria was less compared to 2D Hashin, but the efficiency of the 3D Hashin model was found to be less compared to the 2D Hashin model. Furthermore, subjected to repetitive impacts, the interfaces of the plies having differently oriented fibres are most susceptible and delamination is most likely to occur.

From the literature it is evident that although there are works investigating the dynamic responses due to OLVI, the investigations regarding OLVI of GLARE and FMLs in general is limited and there is a scope for further study of the dynamic responses and associated damage mechanisms on account of OLVI on such FML structures.

2.6. Summary and prospective research areas

In this chapter, a brief review of the experimental, analytical and numerical analyses done to assess the impact behaviour of FMLs was presented. GLARE has seen a positive rise in application since its inception, especially in the aerospace industry because of its superior impact and fatigue properties. An impact can either be low-velocity impact (LVI) or high-velocity impact (HVI), characterised by the nature and mode of damage to the target. The LVIs are more critical in the sense that the internal damages due to LVI are not readily observable, unlike in the case of HVIs.

The numerical investigations concerning the LVI analysis have seen a growing trend since the last ten to fifteen years owing to the development of computational capacity and commercial FEA software. Although studies regarding the LVI analyses of FMLs, including GLARE, have been done numerically in the last couple of years, detailed insight into the damage initiation and its progression is still of significant concern. To obtain a practically viable response of the target due to LVI, different physical parameters (target size, impactor shape and size and stacking sequence) affecting the impact need to be investigated. The advantage of the numerical analyses can be highlighted by the minimisation of material wastage and, more importantly, the scope to have a detailed insight into the complex damage and failure patterns of the FMLs, which is difficult to observe by experimental investigations. To date, numerical analyses regarding the LVI behaviour of GLARE are not plenty.

In most of the available literature, the impact responses of GLARE and other FMLs are concerned with the normal contact of the impactor on the target. However, impacts in real scenarios could be arbitrary, simultaneously impacting at different trajectories, giving rise to complexity in analysing the impact phenomena. The study of impacts occurring at an obliquity is still in its infancy, and there is limited literature on oblique LVIs on laminated structures and GLAREs in particular. The study of oblique LVIs requires separate modelling of the normal and tangential contact responses to ensure the correctness in evaluating the stresses and assessing the damages, indicating the complexity of their analyses.

Delamination is a major cause of failure during LVIs where the damages are barely visible at the surface, but, delamination at the inner interfaces may initiate, posing a significant concern for the structure's safety. Most of the failure analyses are concerned with the ply by ply failure of the individual plies. Cohesive elements have been used at the interfaces to model the damage based on the traction separation laws. Still, the accurate prediction of the stresses at the interfaces to accurately predict the interfacial delamination is a necessary concern. From the reviewed literature, it can be emphasised that delamination damage occurring at the interfaces will differ based on the loading history, as the delamination at the interfaces is influenced by the generated contact force and the plate strains which affect the stresses developed at the interfaces.

Most of the works reported on LVI of GLARE and FMLs, in general, are performed by experimental tests and FE simulations and are based on high ratios of impactor to plate mass, resulting in a quasi-static response. It can be concluded that not much work is reported in exploring the influence the impactor-plate mass ratio and how it could influence the contact coefficient between the impactor and a GLARE target of finite dimensions. In order to get a detailed insight into the influence of the impactor-plate mass ratio on the dynamic responses of the GLARE plate, it is first necessary to evaluate the contact stiffness conforming the two cases of low and high mass impacts, as the dynamic responses will be different pertaining to both the cases. The accurate evaluation of the contact stiffness at the impact location is of critical importance for correctly predicting the impact response of the plate since the peak contact force, as well as the impact duration, is influenced by the contact stiffness. However, no such work has been reported, especially for thin GLARE laminate where the contact stiffness has been adjusted based on the impactor's mass relative to the plate, taking account of the plate geometry.

The presence of discontinuities in the form of through holes or cut-outs can significantly influence the impact responses, and further investigations can be done to study their effect. Of late, using hybrid configurations has seen a rising interest and exploring the hybridisation of FMLs like GLARE with different materials are still limited. Exploring the same could be an interesting area in terms weight saving and structural stability aspects.

Even though commercial FE packages could be used to carry out FE modelling and analysis of contact impact problems, there are certain pertaining issues which needs to be addressed in the analysis of LVI on GLARE structures as follows

- In implicit solver, rigid body motions are not allowed and all parts need to be connected to the ground in all directions. Therefore, for impact analysis, Abaqus/Explicit solver needs to be used to perform the analysis for a rigid body impact on the target plate as reported in many literatures. In most of the FE packages/solvers, especially for explicit analysis, when the material model for each layer changes, they cannot be grouped together and therefore layers having different material models need to be modelled separately with solid or shell elements.
- The adjustment of the contact stiffness for different impactor to plate mass ratios is an important aspect for accurate evaluation of the impact response and damage evolution under low velocity impact which is not readily available in commercial FE packages.

This necessitates the need for the development of a robust FE code for accurate contact impact analysis of GLARE.

2.7. Objectives of the present work

Based on the summary of the literature, research gap and the prospective research issues discussed, the present work implements a 3D FE code to investigate the low-velocity impact (LVI) behaviour of GLARE with the following objectives:

i. **To perform 3D FE analysis of normal LVI on GLARE considering the following:**

  - Evaluation of a modified effective contact stiffness considering
    - the effect of plate geometry
    - the effective out-of-plane plate stiffness and
    - the influence of the impactor mass.

- Implementation of appropriate contact models for spherical and cylindrical LVI.
- Evaluation of interfacial stresses and delamination at the interfaces.

ii. **To investigate the influence of geometrical and material parameters on LVI responses and delamination of GLARE considering the following:**

- Influence of plate and impactor dimensions.
- Influence of metal volume fraction, total plate thickness and stacking configuration.
- Influence of hybridisation of GLARE by using inner Kevlar/epoxy layers.

iii. **To incorporate oblique low-velocity impact (OLVI) analysis of GLARE into the 3D FE code for investigating the impact response, addressing the following:**

- The effect of the obliquity of impact.
- The combined effect of the obliquity of impact, coefficient of friction, and impactor size.
- The interfacial delamination due to OLVI.

iv. **To investigate the LVI response and interfacial delamination of a GLARE plate having cut-outs considering the following:**

- The effect of impact offset on a GLARE plate having a central through-the-thickness cut-out.
- The effect of size, shape, and relative positions of the cut-outs in a GLARE plate having more than one cut-outs.

v. **To perform 3D FE analysis of multiple normal and oblique LVIs on GLARE and study the effects of the following factors:**

- The time interval between two LVIs.
- Multiple LVIs on a plate having a central cut-out.
- The relative positions of the two LVIs.
- The relative trajectories of the impactors in case of multiple OLVIs.

vi. **To study the effects of repeated LVIs on GLARE, focusing on the following:**

- The effect of impactor mass.
- The effect of the impact energy divisions on the damages.

Chapter 3

Theoretical formulations

The GLARE FMLs are hybrid laminated composites having inner glass/epoxy plies alternately placed between the aluminium layers. The presence of anisotropic composite prepregs in such laminates makes it necessary to understand the complexities in their constitutive relations, unlike the isotropic materials. This chapter starts with the lamina level analysis, considering the basic concepts of mechanics of composite materials, material orthotropy and their constitutive relations and then proceeds to the finite element modelling of GLARE using 3-D eight-noded solid elements for analysis of low-velocity impact on GLARE target considering both normal as well as oblique impacts.

3.1. Stress-strain relationship

3.1.1. Generalised Hooke's law

The generalised Hooke's law in 3D for any material model can be written in terms of the strains, ε_{kl} and the stresses, σ_{ij}, related by a fourth order tensor C_{ijkl} comprising of the material elastic constants as

$$\sigma_{ij} = C_{ijkl}\varepsilon_{kl} \tag{3.1.a}$$

The stress-strain relationship in Eq. (3.1.a) is invertible, yielding

$$\varepsilon_{ij} = S_{ijkl}\sigma_{kl} \tag{3.1.b}$$

S_{ijkl} are the compliance coefficients of the fourth order tensor $[S]$ which is the inverse of the stiffness matrix $[C]$. Expanding Eq. (3.1.a), results in 9 equations, each with 9 unknowns, with a total of 81 unknown elastic constants. The symmetry of the stress tensor, σ_{ij}, allows the reduction of unknowns in the stiffness matrix $[C]$ to 36. The stiffness matrix being symmetric, the 36 unknowns are further reduced to 21 independent constants for the case of a linear elastic anisotropic material. In matrix form, the stiffness matrix for an anisotropic material having no material property symmetry can be written as:

$$\begin{Bmatrix} \sigma_1 \\ \sigma_2 \\ \sigma_3 \\ \tau_{12} \\ \tau_{23} \\ \tau_{31} \end{Bmatrix} = \begin{bmatrix} C_{11} & C_{12} & C_{13} & C_{14} & C_{15} & C_{16} \\ C_{12} & C_{22} & C_{23} & C_{24} & C_{25} & C_{26} \\ C_{13} & C_{23} & C_{33} & C_{34} & C_{35} & C_{36} \\ C_{14} & C_{24} & C_{34} & C_{44} & C_{45} & C_{46} \\ C_{15} & C_{25} & C_{35} & C_{45} & C_{55} & C_{56} \\ C_{16} & C_{26} & C_{36} & C_{46} & C_{56} & C_{66} \end{bmatrix} \begin{Bmatrix} \varepsilon_1 \\ \varepsilon_2 \\ \varepsilon_3 \\ \gamma_{12} \\ \gamma_{23} \\ \gamma_{31} \end{Bmatrix} \tag{3.2}$$

The six stress components (Eq. (3.2)) at a point can be visualised to be acting on a vanishingly small rectangular parallelepiped having sides △x, △y and △z as shown in **Figure 3.1**. The reference coordinate axes x-y-z along with the local coordinate axes 1-2-3 are chosen to be parallel to the edges of this rectangular parallelepiped.

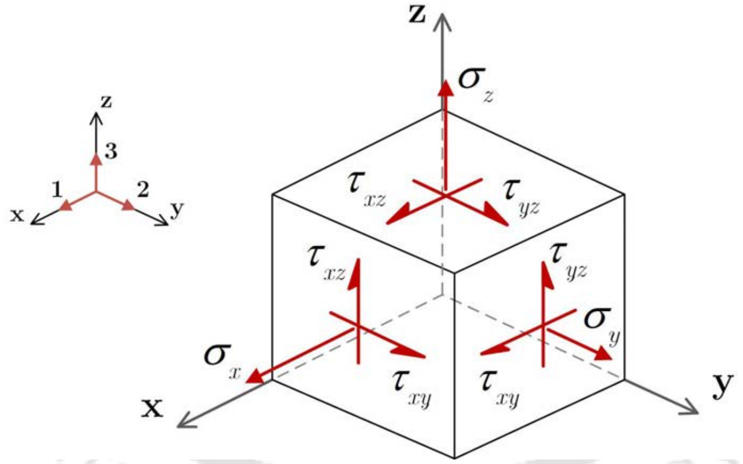

Figure 3.1: 3D stress at a point

3.1.2. Material model for GLARE laminates

In the present analysis of laminated composites, the material model is generally considered to be orthotropic. In the case of the GLARE laminates, a similar approach is taken where the inner S2-glass-epoxy plies are modelled considering the orthotopic material model and the outer aluminium layers are modelled as isotropic (refer **Figure 3.2**). Furthermore, the interfaces between the individual layers are considered to be perfectly bonded.

In discussing the mechanics of fibre reinforced material, it is convenient to use an orthogonal coordinate system that has one axis aligned with the fibre direction. The study of the stress-strain response of a single layer is same as to determining the relations between the stresses applied to the bounding surfaces of the layer as a whole. The effect of fibre reinforcement is uniformly spread over the whole volume of the material and adopting a macromechanical approach it can be assumed that the two-material fibre-matrix system can be replaced by an equivalent single homogeneous material thus making its analysis easier. It is to be noted that this single material may not have same properties in all directions. A local coordinate system 1-2-3 as shown in **Figure 3.1** is aligned along the reference axes x-y-z implying that the fibres are aligned along the global x-direction. In the analysis of the fibre-reinforced polymer (FRP) plies, they can be generally categorised under the class of orthotropic materials. An orthotropic material as shown in **Figure 3.2(a)** has three mutually perpendicular planes of material property symmetry. This reduces the [C] matrix to comprise of 12 non-zero elastic constants and 9 independent elastic constants such that the stress-strain relations when the global coordinates are aligned with the local (material) axes are

$$\begin{Bmatrix} \sigma_1 \\ \sigma_2 \\ \sigma_3 \\ \tau_{12} \\ \tau_{23} \\ \tau_{31} \end{Bmatrix} = \begin{bmatrix} C_{11} & C_{12} & C_{13} & 0 & 0 & 0 \\ C_{12} & C_{22} & C_{23} & 0 & 0 & 0 \\ C_{13} & C_{23} & C_{33} & 0 & 0 & 0 \\ 0 & 0 & 0 & C_{44} & 0 & 0 \\ 0 & 0 & 0 & 0 & C_{55} & 0 \\ 0 & 0 & 0 & 0 & 0 & C_{66} \end{bmatrix} \begin{Bmatrix} \varepsilon_1 \\ \varepsilon_2 \\ \varepsilon_3 \\ \gamma_{12} \\ \gamma_{23} \\ \gamma_{31} \end{Bmatrix} \tag{3.3}$$

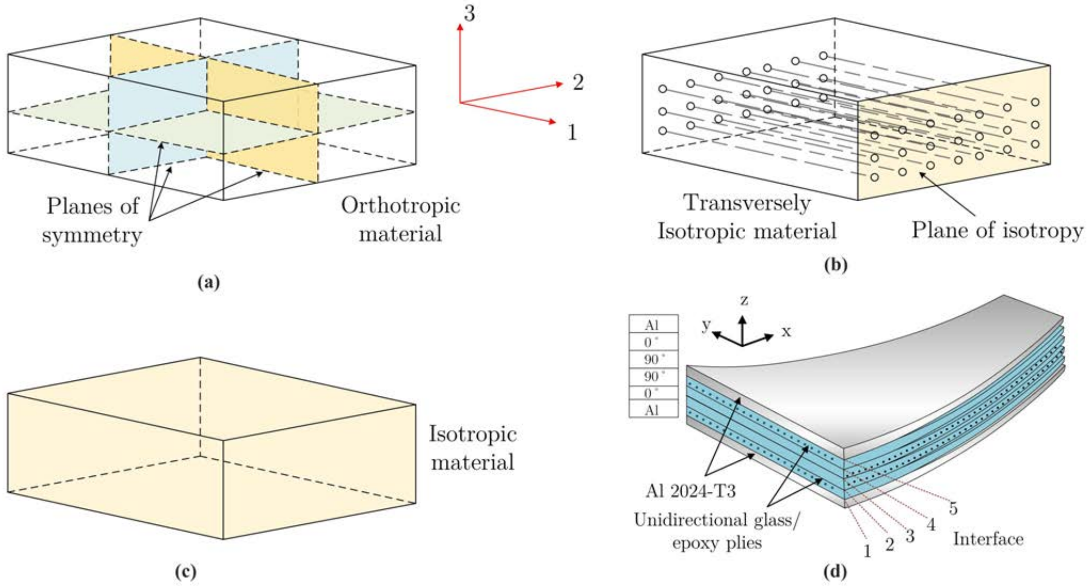

Figure 3.2: Material models (a) Orthotropic (b) Transversely isotropic and (c) Isotropic and (d) a typical GLARE having two different material models

Given the material properties E_1, E_2, E_3, ν_{12}, ν_{23}, ν_{13}, G_{12}, G_{23} and G_{13}, the terms of [C] matrix can be computed. The relation among the material properties is illustrated by Maxwell-Betti reciprocal theorem [181] which gives

$$\frac{\nu_{12}}{E_1}=\frac{\nu_{21}}{E_2};\quad \frac{\nu_{13}}{E_1}=\frac{\nu_{31}}{E_3};\quad \frac{\nu_{23}}{E_2}=\frac{\nu_{32}}{E_3} \tag{3.4}$$

Therefore, the constant terms can be evaluated by the following relations

$$\begin{aligned}
&C_{11}=\frac{1-\nu_{23}\nu_{32}}{E_2E_3\Delta};C_{22}=\frac{1-\nu_{13}\nu_{31}}{E_1E_3\Delta};C_{33}=\frac{1-\nu_{12}\nu_{21}}{E_1E_2\Delta};C_{12}=C_{21}=\frac{\nu_{21}+\nu_{23}\nu_{31}}{E_2E_3\Delta};\\
&C_{13}=C_{31}=\frac{\nu_{31}+\nu_{21}\nu_{32}}{E_2E_3\Delta};C_{23}=C_{32}=\frac{\nu_{32}+\nu_{12}\nu_{31}}{E_1E_3\Delta};\\
&C_{44}=G_{12};C_{55}=G_{23};C_{66}=G_{31}
\end{aligned} \tag{3.5}$$

$$\text{where } \Delta=\frac{1-\nu_{12}\nu_{21}-\nu_{23}\nu_{32}-\nu_{13}\nu_{31}-2\nu_{21}\nu_{32}\nu_{13}}{E_1E_2E_3}$$

A transversely isotropic material is one with physical properties which are symmetric about an axis that is normal to a plane of isotropy of an orthotropic body as shown in **Figure 3.2(b)** where plane 2-3 is the plane of isotropy. This transverse plane has infinite planes of symmetry and thus, within this plane, the material properties are the same in all directions. As seen in **Figure 3.2(b)**, the plane 2-3 is a plane of material isotropy owing to the unidirectional fibre reinforcements being in a repeating pattern. This transverse isotropy results in the properties in the two directions perpendicular to the fibre (plane 2-3) to be equal such that $E_2=E_3$, $\nu_{12}=\nu_{13}$ and $G_{12}=G_{13}$ thereby reducing the number of independent constants to five. Therefore, the constitutive relations can be written as

$$\begin{Bmatrix}\sigma_1\\ \sigma_2\\ \sigma_3\\ \tau_{12}\\ \tau_{23}\\ \tau_{31}\end{Bmatrix}=\begin{bmatrix}C_{11}&C_{12}&C_{12}&0&0&0\\ C_{12}&C_{22}&C_{23}&0&0&0\\ C_{12}&C_{23}&C_{22}&0&0&0\\ 0&0&0&\frac{(C_{22}-C_{23})}{2}&0&0\\ 0&0&0&0&C_{55}&0\\ 0&0&0&0&0&C_{55}\end{bmatrix}\begin{Bmatrix}\varepsilon_1\\ \varepsilon_2\\ \varepsilon_3\\ \gamma_{12}\\ \gamma_{23}\\ \gamma_{31}\end{Bmatrix} \tag{3.6}$$

If every plane is a plane of elastic symmetry, the material is referred as isotropic, and the elastic material parameters are independent of the orientation of the coordinate system (**Figure 3.2(c)**). For an isotropic material, there are only two independent stiffness (or compliance) coefficients and the material properties being same in all directions gives

$$E_1 = E_2 = E_3 = E, \;\; \nu_{12} = \nu_{13} = \nu_{23} = \nu, \;\; G_{12} = G_{13} = G_{23} = G \tag{3.7.a}$$

where

$$G = \frac{E}{2(1+\nu)} \tag{3.7.b}$$

Therefore, there are only two independent engineering constants and the constitutive relations can be written as

$$\begin{Bmatrix} \sigma_1 \\ \sigma_2 \\ \sigma_3 \\ \tau_{12} \\ \tau_{23} \\ \tau_{31} \end{Bmatrix} = \begin{bmatrix} C_{11} & C_{12} & C_{12} & 0 & 0 & 0 \\ C_{12} & C_{11} & C_{12} & 0 & 0 & 0 \\ C_{12} & C_{12} & C_{11} & 0 & 0 & 0 \\ 0 & 0 & 0 & \frac{(C_{11}-C_{12})}{2} & 0 & 0 \\ 0 & 0 & 0 & 0 & \frac{(C_{11}-C_{12})}{2} & 0 \\ 0 & 0 & 0 & 0 & 0 & \frac{(C_{11}-C_{12})}{2} \end{bmatrix} \begin{Bmatrix} \varepsilon_1 \\ \varepsilon_2 \\ \varepsilon_3 \\ \gamma_{12} \\ \gamma_{23} \\ \gamma_{31} \end{Bmatrix} \tag{3.8.a}$$

Where

$$C_{11} = \frac{E(1-\nu)}{(1-2\nu)(1+\nu)}, \;\; C_{12} = \frac{\nu E}{(1-2\nu)(1+\nu)} \;\; \text{and} \;\; \frac{C_{11}-C_{12}}{2} = G \tag{3.8.b}$$

3.2. Transformation relations

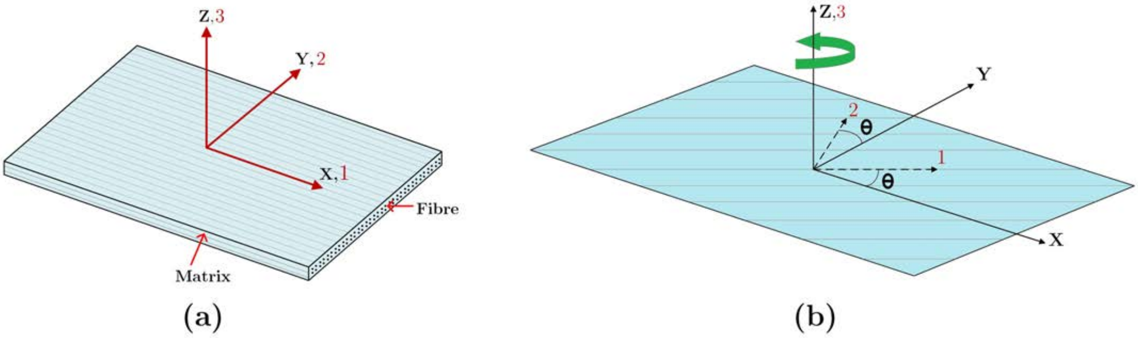

Figure 3.3: (a) Lamina with unidirectional fibres (b) Material axes 1-2-3 aligned along the fibre direction at an angle θ w.r.t. global x-y-z axes

A single lamina of unidirectional fibres is shown in **Figure 3.3(a)** where the local and global axes aligned, the axis-1 is aligned with the fibre direction and axis-2 is in the plane of the lamina and perpendicular to the fibre direction and the axis-3 is perpendicular to the plane of the lamina. For isotropic materials the material constants do not change on changing of the coordinates but for orthotropic materials the constants are given in a particular direction and on changing the coordinate axes the properties will not remain the same in the global space. The transformation relations find its application when the ply-material axes do not coincide with the global coordinate axes. As shown in **Figure 3.3(b)**, the x-y-z system is taken as the global coordinate system and 1-2-3 are the material (or local) axes aligned along the fibre direction of the lamina and both are orthogonal coordinate systems. The ply axes initially coinciding with the global axes are given a rotation of angle θ about z-axis in the counter-clockwise direction such that axis-3 is coincident with the z-axis. The rotation is assumed to be positive when the fibres rotate anticlockwise with respect to positive x-axis.

From **Figure 3.3(b)** it is to be noted that for a pure rotation θ given to the material axis-3, the angles made by axis-1 and axis-2 w.r.t. the x-axis and y-axis is θ. This results in the direction cosine matrix $\left[l\right]$ to be evaluated as

$$\begin{array}{c|ccc} & \mathrm{x} & \mathrm{y} & \mathrm{z} \\ \hline 1 & \cos(\theta) & \cos(270+\theta) & \cos(90) \\ 2 & \cos(90+\theta) & \cos(\theta) & \cos(90) \\ 3 & \cos(90) & \cos(90) & \cos(0) \end{array} \tag{3.9.a}$$

$$\Rightarrow \begin{bmatrix} l_1 & m_1 & n_1 \\ l_2 & m_2 & n_2 \\ l_3 & m_3 & n_3 \end{bmatrix} = \begin{bmatrix} \cos(\theta) & \sin(\theta) & 0 \\ -\sin(\theta) & \cos(\theta) & 0 \\ 0 & 0 & 1 \end{bmatrix} \tag{3.9.b}$$

Therefore, the 6×6 transformation matrix is given by $\left[T\right]$ as

$$\left[T\right] = \begin{bmatrix} l^2{}_1 & m^2{}_1 & n^2{}_1 & 2l_1m_1 & 2m_1n_1 & 2n_1l_1 \\ l^2{}_2 & m^2{}_2 & n^2{}_2 & 2l_2m_2 & 2m_2n_2 & 2n_2l_2 \\ l^2{}_3 & m^2{}_3 & n^2{}_3 & 2l_3m_3 & 2m_3n_3 & 2n_3l_3 \\ l_1l_2 & m_1m_2 & n_1n_2 & m_1l_2+m_2l_1 & m_1n_2+m_2n_1 & n_1l_2+n_2l_1 \\ l_2l_3 & m_2m_3 & n_2n_3 & m_2l_3+m_3l_2 & m_2n_3+m_3n_2 & n_2l_3+n_3l_2 \\ l_3l_1 & m_3m_1 & n_3n_1 & m_3l_1+m_1l_3 & m_3n_1+m_1n_3 & n_3l_1+n_1l_3 \end{bmatrix} \tag{3.10}$$

Substituting the values from Eq. (3.9), for a pure rotation θ about z-axis,

$$\left[T\right] = \begin{bmatrix} \cos^2\theta & \sin^2\theta & 0 & 2\sin\theta\cos\theta & 0 & 0 \\ \sin^2\theta & \cos^2\theta & 0 & -2\sin\theta\cos\theta & 0 & 0 \\ 0 & 0 & 1 & 0 & 0 & 0 \\ -\sin\theta\cos\theta & \sin\theta\cos\theta & 0 & \cos^2\theta-\sin^2\theta & 0 & 0 \\ 0 & 0 & 0 & 0 & \cos\theta & -\sin\theta \\ 0 & 0 & 0 & 0 & \sin\theta & \cos\theta \end{bmatrix} \tag{3.11}$$

The transformation of the stress vector from global x-y-z axes to local 1-2-3 axes are related by $\left[T\right]$ using the tensor transformation laws are as follows

$$\begin{Bmatrix} \sigma_1 \\ \sigma_2 \\ \sigma_3 \\ \tau_{12} \\ \tau_{23} \\ \tau_{31} \end{Bmatrix} = \left[T\right] \begin{Bmatrix} \sigma_x \\ \sigma_y \\ \sigma_z \\ \tau_{xy} \\ \tau_{yz} \\ \tau_{zx} \end{Bmatrix} \tag{3.12}$$

In case of the strain transformations, $\left[T\right]$ can be similarly used to evaluate the transformed strains from global x-y-z axes to local 1-2-3 axes as follows

$$\begin{Bmatrix} \varepsilon_1 \\ \varepsilon_2 \\ \varepsilon_3 \\ \dfrac{\gamma_{12}}{2} \\ \dfrac{\gamma_{23}}{2} \\ \dfrac{\gamma_{31}}{2} \end{Bmatrix} = \left[T\right] \begin{Bmatrix} \varepsilon_x \\ \varepsilon_y \\ \varepsilon_z \\ \dfrac{\gamma_{xy}}{2} \\ \dfrac{\gamma_{yz}}{2} \\ \dfrac{\gamma_{zx}}{2} \end{Bmatrix} \tag{3.13}$$

But, in the strain transformation, to avoid the additional step of halving the shear strains prior to tensor transformation and doubling the corresponding values later to get the net engineering strains, a Reuter matrix $\left[R\right]$ is introduced such that

$$\begin{Bmatrix} \varepsilon_1 \\ \varepsilon_2 \\ \varepsilon_3 \\ \gamma_{12} \\ \gamma_{23} \\ \gamma_{31} \end{Bmatrix} = \left[R\right] \begin{Bmatrix} \varepsilon_1 \\ \varepsilon_2 \\ \varepsilon_3 \\ \dfrac{\gamma_{12}}{2} \\ \dfrac{\gamma_{23}}{2} \\ \dfrac{\gamma_{31}}{2} \end{Bmatrix} \tag{3.14}$$

and

$$\begin{Bmatrix} \varepsilon_x \\ \varepsilon_y \\ \varepsilon_z \\ \gamma_{xy} \\ \gamma_{yz} \\ \gamma_{zx} \end{Bmatrix} = \left[R\right] \begin{Bmatrix} \varepsilon_x \\ \varepsilon_y \\ \varepsilon_z \\ \dfrac{\gamma_{xy}}{2} \\ \dfrac{\gamma_{yz}}{2} \\ \dfrac{\gamma_{zx}}{2} \end{Bmatrix} \tag{3.15}$$

where the Reuter matrix $\left[R\right]$ is given by

$$\left[R\right] = \begin{bmatrix} 1 & 0 & 0 & 0 & 0 & 0 \\ 0 & 1 & 0 & 0 & 0 & 0 \\ 0 & 0 & 1 & 0 & 0 & 0 \\ 0 & 0 & 0 & 2 & 0 & 0 \\ 0 & 0 & 0 & 0 & 2 & 0 \\ 0 & 0 & 0 & 0 & 0 & 2 \end{bmatrix} \tag{3.16}$$

Using Eq. (3.13-3.16), the strain transformation is given as

$$\begin{Bmatrix} \varepsilon_1 \\ \varepsilon_2 \\ \varepsilon_3 \\ \gamma_{12} \\ \gamma_{23} \\ \gamma_{31} \end{Bmatrix} = \left[R\right]\left[T\right]\left[R\right]^{-1} \begin{Bmatrix} \varepsilon_x \\ \varepsilon_y \\ \varepsilon_z \\ \gamma_{xy} \\ \gamma_{yz} \\ \gamma_{zx} \end{Bmatrix} \tag{3.17}$$

Thus, the strain transformation matrix is

$$\left[\bar{T}\right] = \left[R\right]\left[T\right]\left[R\right]^{-1} \tag{3.18}$$

$$\Rightarrow \left[\bar{T}\right] = \begin{bmatrix} \cos^2\theta & \sin^2\theta & 0 & \sin\theta\cos\theta & 0 & 0 \\ \sin^2\theta & \cos^2\theta & 0 & -\sin\theta\cos\theta & 0 & 0 \\ 0 & 0 & 1 & 0 & 0 & 0 \\ -2\sin\theta\cos\theta & 2\sin\theta\cos\theta & 0 & \cos^2\theta - \sin^2\theta & 0 & 0 \\ 0 & 0 & 0 & 0 & \cos\theta & -\sin\theta \\ 0 & 0 & 0 & 0 & \sin\theta & \cos\theta \end{bmatrix} \tag{3.19}$$

Therefore, the strain transformation from global x-y-z axes to local 1-2-3 axes is

$$\{\varepsilon\}_{123} = \left[\bar{T}\right]\{\varepsilon\}_{xyz} \tag{3.20}$$

From Eq. (3.3), Eq. (3.12) and Eq. (3.20), the stresses and strains in the global coordinates can be written as

$$\{\sigma\}_{xyz} = \left[T\right]^{-1}\left[C\right]\left[\bar{T}\right]\{\varepsilon\}_{xyz} \tag{3.21}$$

From Eq. (3.21), the matrix comprising of the transformed stiffness components is given by $\left[\bar{C}\right]$ such that

$$\{\sigma\}_{xyz} = \left[\bar{C}\right]\{\varepsilon\}_{xyz} \tag{3.22.a}$$

where

$$\left[\bar{C}\right] = \left[T\right]^{-1}\left[C\right]\left[\bar{T}\right] \tag{3.22.b}$$

3.3. Finite element formulation

In the analysis of complex geometry and structures, it is often easier to analyse when these structures are discretised into simpler forms having a definite number of degrees of freedoms (DOFs). This enables the model based numerical approximations or simulations of actual physical structures and has resulted in the development and use of finite element methods (FEM) in structural mechanics. In the present analysis of GLARE laminates, eight-noded solid elements are used to discretise the physical model into the finite element model. The use of these three dimensional finite elements enables the accurate modelling of the physical solid structures and implement the boundary conditions for both forces and displacements in a more realistic manner. The next subsection describes the attributes of eight-noded solid elements for linear elastic problems.

3.3.1. Eight-noded solid element

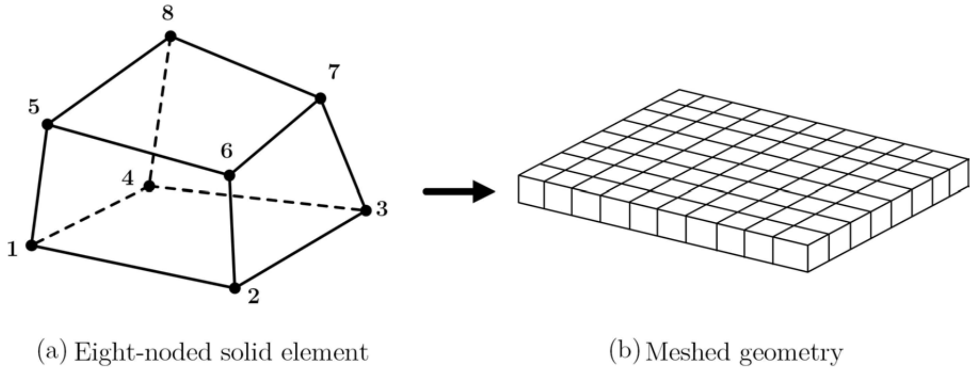

(a) Eight-noded solid element (b) Meshed geometry

Figure 3.4: (a) Eight-noded solid element and (b) meshed geometry

The three dimensional finite element in consideration is the eight noded hexahedron informally known as brick element. These eight-noded solid elements have eight corners with three faces meeting at each corner as can be seen in **Figure 3.4(a)** and used to generate regular meshes as shown in **Figure 3.4(b)**. The elements can be refined to form a finer mesh improving the accuracy of the analysis.

3.3.2. Isoparametric formulations

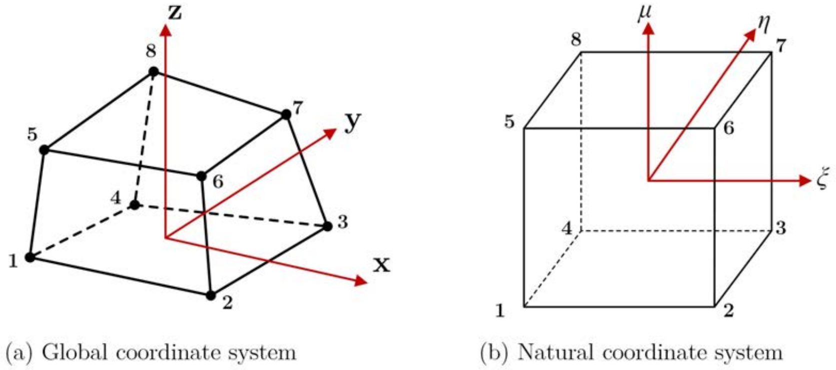

(a) Global coordinate system (b) Natural coordinate system

Figure 3.5: (a) Global and (b) Natural coordinate systems

The term isoparametric implies the use of the same shape functions (or interpolation functions) to define the element's geometric shape as well as the displacements within the element. Isoparametric element equations are formed using a natural coordinate system that is defined by element geometry and not by the element orientation in the global coordinate system. This method can be used to transform the natural coordinates of a point to the Cartesian (global) coordinate system and vice versa. The global and natural coordinate systems are shown in **Figure 3.5**. The use of isoparametric formulations enable the solid elements to have non-rectangular shapes making them versatile and applicable for use is the analysis of various complex structures. The shape functions for defining the geometry and variation of displacement within the element is given by [182]

$$\begin{aligned}
N_1 &= \frac{1}{8}(1-\xi)(1-\eta)(1-\mu) & N_5 &= \frac{1}{8}(1+\xi)(1-\eta)(1+\mu) \\
N_2 &= \frac{1}{8}(1+\xi)(1-\eta)(1-\mu) & N_6 &= \frac{1}{8}(1+\xi)(1-\eta)(1+\mu) \\
N_3 &= \frac{1}{8}(1+\xi)(1+\eta)(1-\mu) & N_7 &= \frac{1}{8}(1+\xi)(1+\eta)(1+\mu) \\
N_4 &= \frac{1}{8}(1-\xi)(1+\eta)(1-\mu) & N_8 &= \frac{1}{8}(1-\xi)(1+\eta)(1+\mu)
\end{aligned} \tag{3.23}$$

In concise form, the shape functions can be written as

$$N_i = \frac{1}{8}\left(1+\xi\xi_i\right)\left(1+\eta\eta_i\right)\left(1+\mu\mu_i\right) \qquad i = 1,2,3.....8 \tag{3.24}$$

where ξ, η, μ are the natural coordinates in the interval [-1,1] and ξ_i, η_i, μ_i are the values corresponding to the i^{th} node given in **Table 3.1**. The geometry of the element can be expressed by the interpolation functions as follows

$$\begin{Bmatrix} x \\ y \\ z \end{Bmatrix} = \begin{Bmatrix} N_1x_1 + N_2x_2 + ... + N_8x_8 \\ N_1y_1 + N_2y_2 + ... + N_8y_8 \\ N_1z_1 + N_2z_2 + ... + N_8z_8 \end{Bmatrix} = \sum_{i=1}^{n=8} N_i \begin{Bmatrix} x_i \\ y_i \\ z_i \end{Bmatrix} \tag{3.25}$$

where x_i, y_i, z_i are the global coordinates of the n^{th} node of the element. In a similar manner, the variation of the displacement within the element can be expressed using the same interpolation functions as

$$\begin{Bmatrix} u \\ v \\ w \end{Bmatrix} = \sum_{i=1}^{n=8} N_i \begin{Bmatrix} u_i \\ v_i \\ w_i \end{Bmatrix} \tag{3.26}$$

Table 3.1: Nodal coordinates in natural coordinate system

Node	ξ_i	η_i	μ_i	Node	ξ_i	η_i	μ_i
1	-1	-1	-1	5	-1	-1	$+1$
2	$+1$	-1	-1	6	$+1$	-1	$+1$
3	$+1$	$+1$	-1	7	$+1$	$+1$	$+1$
4	-1	$+1$	-1	8	-1	$+1$	$+1$

3.3.3. Jacobian matrix

The relationship between the derivatives of the shape functions in the global coordinates and the natural coordinates is given by the Jacobian matrix. The Jacobian matrix is a square matrix and is given by

$$\left[J\right] = \begin{bmatrix} \frac{\partial x}{\partial \xi} & \frac{\partial y}{\partial \xi} & \frac{\partial z}{\partial \xi} \\ \frac{\partial x}{\partial \eta} & \frac{\partial y}{\partial \eta} & \frac{\partial z}{\partial \eta} \\ \frac{\partial x}{\partial \mu} & \frac{\partial y}{\partial \mu} & \frac{\partial z}{\partial \mu} \end{bmatrix} \tag{3.27}$$

Using Eq. (3.25) for x, y and z, the Jacobian matrix for an element can be computed as

$$[J] = \sum_{i=1}^{8} \begin{bmatrix} x_i \dfrac{\partial N_i}{\partial \xi} & y_i \dfrac{\partial N_i}{\partial \xi} & z_i \dfrac{\partial N_i}{\partial \xi} \\ x_i \dfrac{\partial N_i}{\partial \eta} & y_i \dfrac{\partial N_i}{\partial \eta} & z_i \dfrac{\partial N_i}{\partial \eta} \\ x_i \dfrac{\partial N_i}{\partial \mu} & y_i \dfrac{\partial N_i}{\partial \mu} & z_i \dfrac{\partial N_i}{\partial \mu} \end{bmatrix} \tag{3.28}$$

And the inverse of Jacobian is represented by

$$[J]^{-1} = \begin{bmatrix} J_{11}^* & J_{12}^* & J_{13}^* \\ J_{21}^* & J_{22}^* & J_{23}^* \\ J_{31}^* & J_{32}^* & J_{33}^* \end{bmatrix} \tag{3.29}$$

The derivatives in global coordinates are related to the derivatives in natural coordinates by the Jacobian as

$$\begin{Bmatrix} \dfrac{\partial}{\partial x} \\ \dfrac{\partial}{\partial y} \\ \dfrac{\partial}{\partial z} \end{Bmatrix} = [J]^{-1} \begin{Bmatrix} \dfrac{\partial}{\partial \xi} \\ \dfrac{\partial}{\partial \eta} \\ \dfrac{\partial}{\partial \mu} \end{Bmatrix} = \begin{bmatrix} J_{11}^* & J_{12}^* & J_{13}^* \\ J_{21}^* & J_{22}^* & J_{23}^* \\ J_{31}^* & J_{32}^* & J_{33}^* \end{bmatrix} \begin{Bmatrix} \dfrac{\partial}{\partial \xi} \\ \dfrac{\partial}{\partial \eta} \\ \dfrac{\partial}{\partial \mu} \end{Bmatrix} \tag{3.30}$$

3.3.4. Strain-displacement matrix

In a displacement based formulation for linear elastic analysis, the strains are obtained from the first order derivatives of the displacements in the global coordinates. The components of strain in the global coordinates for a general eight-noded solid element can be computed from the displacements as

$$\begin{Bmatrix} \varepsilon_x \\ \varepsilon_y \\ \varepsilon_z \\ \gamma_{xy} \\ \gamma_{yz} \\ \gamma_{zx} \end{Bmatrix} = \begin{Bmatrix} \dfrac{\partial u}{\partial x} \\ \dfrac{\partial v}{\partial y} \\ \dfrac{\partial w}{\partial z} \\ \dfrac{\partial v}{\partial x} + \dfrac{\partial u}{\partial y} \\ \dfrac{\partial w}{\partial y} + \dfrac{\partial v}{\partial z} \\ \dfrac{\partial u}{\partial z} + \dfrac{\partial w}{\partial x} \end{Bmatrix} = \begin{Bmatrix} u,_x \\ v,_y \\ w,_z \\ v,_x + u,_y \\ w,_y + v,_z \\ u,_z + w,_x \end{Bmatrix} \tag{3.31}$$

Using Eq. (3.30)

$$\begin{bmatrix} \dfrac{\partial u}{\partial x} & \dfrac{\partial v}{\partial x} & \dfrac{\partial w}{\partial x} \\ \dfrac{\partial u}{\partial y} & \dfrac{\partial v}{\partial y} & \dfrac{\partial w}{\partial y} \\ \dfrac{\partial u}{\partial z} & \dfrac{\partial v}{\partial z} & \dfrac{\partial w}{\partial z} \end{bmatrix} = \begin{bmatrix} J_{11}^{*} & J_{12}^{*} & J_{13}^{*} \\ J_{21}^{*} & J_{22}^{*} & J_{23}^{*} \\ J_{31}^{*} & J_{32}^{*} & J_{33}^{*} \end{bmatrix} \begin{bmatrix} \dfrac{\partial u}{\partial \xi} & \dfrac{\partial v}{\partial \xi} & \dfrac{\partial w}{\partial \xi} \\ \dfrac{\partial u}{\partial \eta} & \dfrac{\partial v}{\partial \eta} & \dfrac{\partial w}{\partial \eta} \\ \dfrac{\partial u}{\partial \mu} & \dfrac{\partial v}{\partial \mu} & \dfrac{\partial w}{\partial \mu} \end{bmatrix} \tag{3.32}$$

Using Eq. (3.32), Eq. (3.31) can be written as

$$\{\varepsilon\}_{6\times1} = \left\{u,_{x}\right\}_{6\times1} = [\bar{J}^{*}]_{6\times9}\{u,_{\xi}\}_{9\times1} \tag{3.33}$$

Eq. (3.33) in matrix form can be written as

$$\begin{Bmatrix} u,_{x} \\ v,_{y} \\ w,_{z} \\ v,_{x}+u,_{y} \\ w,_{y}+v,_{z} \\ u,_{z}+w,_{x} \end{Bmatrix} = \begin{bmatrix} J_{11}^{*} & 0 & 0 & J_{12}^{*} & 0 & 0 & J_{13}^{*} & 0 & 0 \\ 0 & J_{21}^{*} & 0 & 0 & J_{22}^{*} & 0 & 0 & J_{23}^{*} & 0 \\ 0 & 0 & J_{31}^{*} & 0 & 0 & J_{32}^{*} & 0 & 0 & J_{33}^{*} \\ J_{21}^{*} & J_{11}^{*} & 0 & J_{22}^{*} & J_{12}^{*} & 0 & J_{23}^{*} & J_{13}^{*} & 0 \\ 0 & J_{31}^{*} & J_{21}^{*} & 0 & J_{32}^{*} & J_{22}^{*} & 0 & J_{33}^{*} & J_{23}^{*} \\ J_{31}^{*} & 0 & J_{11}^{*} & J_{32}^{*} & 0 & J_{12}^{*} & J_{33}^{*} & 0 & J_{13}^{*} \end{bmatrix} \begin{Bmatrix} u,_{\xi} \\ v,_{\xi} \\ w,_{\xi} \\ u,_{\eta} \\ v,_{\eta} \\ w,_{\eta} \\ u,_{\mu} \\ v,_{\mu} \\ w,_{\mu} \end{Bmatrix} \tag{3.34}$$

Using Eq. (3.26), the $\left\{u,_{\xi}\right\}_{9\times1}$ part of Eq. (3.32) can be expanded as

$$\left\{u,_{\xi}\right\}_{9\times1} = \left[G\right]_{9\times24}\{d_{a}\}_{24\times1} \tag{3.35}$$

where

$$\left[G\right] = \left[\begin{matrix} N_{1},_{\xi} & 0 & 0 & N_{2},_{\xi} & 0 & 0 & N_{3},_{\xi} & 0 & 0 & N_{4},_{\xi} & 0 & 0 & \cdots \\ 0 & N_{1},_{\xi} & 0 & 0 & N_{2},_{\xi} & 0 & 0 & N_{3},_{\xi} & 0 & 0 & N_{4},_{\xi} & 0 & \cdots \\ 0 & 0 & N_{1},_{\xi} & 0 & 0 & N_{2},_{\xi} & 0 & 0 & N_{3},_{\xi} & 0 & 0 & N_{4},_{\xi} & \cdots \\ N_{1},_{\eta} & 0 & 0 & N_{2},_{\eta} & 0 & 0 & N_{3},_{\eta} & 0 & 0 & N_{4},_{\eta} & 0 & 0 & \cdots \\ 0 & N_{1},_{\eta} & 0 & 0 & N_{2},_{\eta} & 0 & 0 & N_{3},_{\eta} & 0 & 0 & N_{4},_{\eta} & 0 & \cdots \\ 0 & 0 & N_{1},_{\eta} & 0 & 0 & N_{2},_{\eta} & 0 & 0 & N_{3},_{\eta} & 0 & 0 & N_{4},_{\eta} & \cdots \\ N_{1},_{\mu} & 0 & 0 & N_{2},_{\mu} & 0 & 0 & N_{3},_{\mu} & 0 & 0 & N_{4},_{\mu} & 0 & 0 & \cdots \\ 0 & N_{1},_{\mu} & 0 & 0 & N_{2},_{\mu} & 0 & 0 & N_{3},_{\mu} & 0 & 0 & N_{4},_{\mu} & 0 & \cdots \\ 0 & 0 & N_{1},_{\mu} & 0 & 0 & N_{2},_{\mu} & 0 & 0 & N_{3},_{\mu} & 0 & 0 & N_{4},_{\mu} & \cdots \end{matrix}\right. \tag{3.36}$$

$$\left.\begin{matrix}
\cdots N_{5,\xi} & 0 & 0 & N_{6,\xi} & 0 & 0 & N_{7,\xi} & 0 & 0 & N_{8,\xi} & 0 & 0 \\
\cdots 0 & N_{5,\xi} & 0 & 0 & N_{6,\xi} & 0 & 0 & N_{7,\xi} & 0 & 0 & N_{8,\xi} & 0 \\
\cdots 0 & 0 & N_{5,\xi} & 0 & 0 & N_{6,\xi} & 0 & 0 & N_{7,\xi} & 0 & 0 & N_{8,\xi} \\
\cdots N_{5,\eta} & 0 & 0 & N_{6,\eta} & 0 & 0 & N_{7,\eta} & 0 & 0 & N_{8,\eta} & 0 & 0 \\
\cdots 0 & N_{5,\eta} & 0 & 0 & N_{6,\eta} & 0 & 0 & N_{7,\eta} & 0 & 0 & N_{8,\eta} & 0 \\
\cdots 0 & 0 & N_{5,\eta} & 0 & 0 & N_{6,\eta} & 0 & 0 & N_{7,\eta} & 0 & 0 & N_{8,\eta} \\
\cdots N_{5,\mu} & 0 & 0 & N_{6,\mu} & 0 & 0 & N_{7,\mu} & 0 & 0 & N_{8,\mu} & 0 & 0 \\
\cdots 0 & N_{5,\mu} & 0 & 0 & N_{6,\mu} & 0 & 0 & N_{7,\mu} & 0 & 0 & N_{8,\mu} & 0 \\
\cdots 0 & 0 & N_{5,\mu} & 0 & 0 & N_{6,\mu} & 0 & 0 & N_{7,\mu} & 0 & 0 & N_{8,\mu}
\end{matrix}\right]_{9\times24}
\begin{Bmatrix} u_1 \\ v_1 \\ w_1 \\ u_2 \\ v_2 \\ w_2 \\ \vdots \\ \vdots \\ u_8 \\ v_8 \\ w_8 \end{Bmatrix}_{24\times1}$$

By using Eq. (3.31-3.36), the strain-displacement matrix $\left[B_a\right]$ is obtained which relates the displacement and strains as

$$\{\varepsilon\}_{6\times1} = [B_a]_{6\times24}\{d_a\}_{24\times1} \tag{3.37.a}$$

$$\text{where} \qquad \left[B_a\right]_{6\times24} = \left[\bar{J}^*\right]_{6\times9}\left[G\right]_{9\times24} \tag{3.37.b}$$

In case of a general brick element, $\left[B_a\right]$ can be considered as a combination of eight submatrices of size 6×3 as follows

$$\left[B_a\right] = \left[\left[B_1\right] \vdots \left[B_2\right] \vdots \left[B_3\right] \vdots \left[B_4\right] \vdots \left[B_5\right] \vdots \left[B_6\right] \vdots \left[B_7\right] \vdots \left[B_8\right]\right]_{6\times24} \tag{3.38.a}$$

and the values of $\left[B_i\right]$ at the i^{th} node becomes

$$\left[B_i\right] = \begin{bmatrix} N_{i,x} & 0 & 0 \\ 0 & N_{i,y} & 0 \\ 0 & 0 & N_{i,z} \\ N_{i,y} & N_{i,x} & 0 \\ 0 & N_{i,z} & N_{i,y} \\ N_{i,z} & 0 & N_{i,x} \end{bmatrix} \tag{3.38.b}$$

3.3.4.1. Incompatible modes

In case of the fully integrated linear elastic hexahedral solid elements, they tend to be overly stiff resulting in the problem of shear locking due to the development of spurious shear strains. This deters the ability to produce accurate results, especially in simulating cases where the structure is subjected to pure bending. The motivation for the incorporation of incompatible modes in the displacement variation within the element is to adequately simulate the flexural response when subjected to out-of-plane loads. This was introduced in the year 1973 by Wilson et al. [183] to improve the bending behaviour of lower order plane and solid elements. These additional displacement modes have quadratic expressions and are functions of type

$$I_1^c = \left(1-\xi^2\right);\ I_2^c = \left(1-\eta^2\right);\ I_3^c = \left(1-\mu^2\right) \tag{3.39}$$

These incompatible modes are associated with linear shear and normal strains and remain deactivated at the nodes of the eight-noded solid element. From Eq. (3.26), the variation of displacement considering the incompatible modes can be written as

$$\begin{Bmatrix} u \\ v \\ w \end{Bmatrix} = \sum_{i=1}^{n=8} N_i \begin{Bmatrix} u_i \\ v_i \\ w_i \end{Bmatrix} + \left[I^c\right]_{3\times9} \{\psi\}_{9\times1} \tag{3.40}$$

Expanding,

$$\begin{Bmatrix} u \\ v \\ w \end{Bmatrix} = \sum_{i=1}^{n=8} N_i \begin{Bmatrix} u_i \\ v_i \\ w_i \end{Bmatrix} + \begin{bmatrix} I_1^c & I_2^c & I_3^c & 0 & 0 & 0 & 0 & 0 & 0 \\ 0 & 0 & 0 & I_1^c & I_2^c & I_3^c & 0 & 0 & 0 \\ 0 & 0 & 0 & 0 & 0 & 0 & I_1^c & I_2^c & I_3^c \end{bmatrix} \begin{Bmatrix} \psi_1 \\ \psi_2 \\ \psi_3 \\ \vdots \\ \psi_9 \end{Bmatrix} \tag{3.41}$$

In the present displacement formulation, with the addition of the incompatible displacement modes, the strains are evaluated in a similar manner as

$$\{\varepsilon\}_{6\times1} = [B]_{6\times33} \{d\}_{33\times1} \tag{3.42.a}$$

where

$$\{d\}^T = [u_1\ v_1\ w_1\ u_2\ v_2\ w_2 \ldots\ldots u_8\ v_8\ w_8\ \psi_1\ \psi_4\ \psi_7\ \psi_2\ \psi_5\ \psi_8\ \psi_3\ \psi_6\ \psi_9]$$

Eq. (3.42.a) can be written as

$$\{\varepsilon\} = \sum_{i=1}^{8} [B_i]\{d_i\} + [I^{c'}]\{\psi'\} \tag{3.42.b}$$

or

$$\{\varepsilon\} = [B_a]\{d_a\} + [I^{c'}]\{\psi'\} \tag{3.42.c}$$

where

$$\{d_i\}^T = [u_i\ v_i\ w_i]$$

$$\{\psi'\}^T = [\psi_1\ \psi_4\ \psi_7\ \psi_2\ \psi_5\ \psi_8\ \psi_3\ \psi_6\ \psi_9]$$

The components of $[I^{c'}]$ contain the differentiation of $[I^c]$ with respect to x, y and z in the global coordinates. With the incompatible displacement modes, the displacement derivatives as in Eq. (3.30) with respect to global x, y and z becomes

$$\begin{bmatrix} \frac{\partial u}{\partial x} & \frac{\partial v}{\partial x} & \frac{\partial w}{\partial x} \\ \frac{\partial u}{\partial y} & \frac{\partial v}{\partial y} & \frac{\partial w}{\partial y} \\ \frac{\partial u}{\partial z} & \frac{\partial v}{\partial z} & \frac{\partial w}{\partial z} \end{bmatrix} = \begin{bmatrix} J^*_{11} & J^*_{12} & J^*_{13} \\ J^*_{21} & J^*_{22} & J^*_{23} \\ J^*_{31} & J^*_{32} & J^*_{33} \end{bmatrix} \left\{ \begin{bmatrix} \frac{\partial u}{\partial \xi} & \frac{\partial v}{\partial \xi} & \frac{\partial w}{\partial \xi} \\ \frac{\partial u}{\partial \eta} & \frac{\partial v}{\partial \eta} & \frac{\partial w}{\partial \eta} \\ \frac{\partial u}{\partial \mu} & \frac{\partial v}{\partial \mu} & \frac{\partial w}{\partial \mu} \end{bmatrix} + \begin{bmatrix} -2\xi\psi_1 & -2\xi\psi_4 & -2\xi\psi_7 \\ -2\eta\psi_2 & -2\eta\psi_5 & -2\eta\psi_8 \\ -2\mu\psi_3 & -2\mu\psi_6 & -2\mu\psi_9 \end{bmatrix} \right\} \tag{3.43}$$

and $[I^{c\prime}]$ can be written as

$$[I^{c\prime}] = \left[\begin{array}{ccc:ccc:ccc} -2\xi J^*_{11} & 0 & 0 & -2\eta J^*_{12} & 0 & 0 & -2\mu J^*_{13} & 0 & 0 \\ 0 & -2\xi J^*_{21} & 0 & 0 & -2\eta J^*_{22} & 0 & 0 & -2\mu J^*_{23} & 0 \\ 0 & 0 & -2\xi J^*_{31} & 0 & 0 & -2\eta J^*_{32} & 0 & 0 & -2\mu J^*_{33} \\ -2\xi J^*_{21} & -2\xi J^*_{11} & 0 & -2\eta J^*_{22} & -2\eta J^*_{12} & 0 & -2\mu J^*_{23} & -2\mu J^*_{13} & 0 \\ 0 & -2\xi J^*_{31} & -2\xi J^*_{21} & 0 & -2\eta J^*_{32} & -2\eta J^*_{22} & 0 & -2\mu J^*_{33} & -2\mu J^*_{23} \\ -2\xi J^*_{31} & 0 & -2\xi J^*_{11} & -2\eta J^*_{32} & 0 & -2\eta J^*_{12} & -2\mu J^*_{33} & 0 & -2\mu J^*_{13} \end{array} \right] \tag{3.44}$$

$$\Rightarrow [I^{c\prime}] = \Big[\underset{6\times3}{[B_9]} \;\vdots\; \underset{6\times3}{[B_{10}]} \;\vdots\; \underset{6\times3}{[B_{11}]} \Big] = [B_d]$$

Therefore, the strain-displacement matrix in Eq. (3.42.a) now constitutes 11 submatrices as

$$[B] = [\underbrace{[B_1] \vdots [B_2] \vdots [B_3] \vdots [B_4] \vdots [B_5] \vdots [B_6] \vdots [B_7] \vdots [B_8]}_{[B_a]} \;\; \underbrace{[B_9] \vdots [B_{10}] \vdots [B_{11}]}_{[B_d]}] \tag{3.45}$$

3.3.5. Stiffness matrix

3.3.5.1. Principle of virtual work

An effective method for solving a range of structural mechanics problem is by the principle of virtual work. The virtual work may be caused by true force moving through imaginary displacements or vice versa. Thus, the principle of virtual work can be categorised as

(i) Principle of virtual forces

(ii) Principle of virtual displacements

The compatibility conditions are established by the principle of virtual forces. The principle of virtual displacements provides the conditions of equilibrium and is used in the displacement-based model of the finite element technique. External virtual work is the work done by an actual load moving through imaginary displacements in a structure. These loads include both the load distributed over the entire surface and the entire volume. Thus, the virtual work done by the external force is

$$\delta W_E = \int_\Gamma \{\delta u \quad \delta v \quad \delta w\} \begin{Bmatrix} F_{\Gamma x} \\ F_{\Gamma y} \\ F_{\Gamma z} \end{Bmatrix} d\Gamma + \int_\Omega \{\delta u \quad \delta v \quad \delta w\} \begin{Bmatrix} F_{\Omega x} \\ F_{\Omega y} \\ F_{\Omega z} \end{Bmatrix} d\Omega \tag{3.46}$$

where, δu, δv and δw are the components of the virtual displacements in x, y and z direction respectively. $\{F_\Gamma\}$ are the surface forces and $\{F_\Omega\}$ are the body forces. In the above equation, the integration is carried out over the entire surface in the first term and over the entire volume in the second term. The above expression can be rewritten as

$$\delta W_E = \int_\Gamma \{\delta d\}^T \{F_\Gamma\} d\Gamma + \int_\Omega \{\delta d\}^T \{F_\Omega\} d\Omega \,; \; \{d\}^T = [u \;\; v \;\; w] \tag{3.47}$$

For the three dimensional stress-strain conditions, there are six components of stresses and six strain components. Therefore, the virtual internal work can be expressed as

$$\delta U = \int_\Omega \{\delta \varepsilon\}^T \{\sigma\} d\Omega \tag{3.48}$$

According to the principle of virtual work, the work done by external forces due to the virtual displacement of a body in equilibrium is equal to the work done by the internal forces for the virtual internal displacement. Thus, Eq. (3.47) is equal to Eq. (3.48) and can be related as follows

$$\int_\Omega \{\delta \varepsilon\}^T \{\sigma\} d\Omega = \int_\Gamma \{\delta d\}^T \{F_\Gamma\} d\Gamma + \int_\Omega \{\delta d\}^T \{F_\Omega\} d\Omega \tag{3.49}$$

3.3.5.2. Variational principle

Variational formulation is the generalized method of forming the element stiffness matrix and load vector using the variational principle of solid mechanics. For a three dimensional structural problem, $[B]$ relates the strains and displacements by Eq. (3.42). Again, the stresses can be computed in terms of the obtained strains by the constitutive relationship matrix $[C]$ as given in Eq. (3.3) in case of orthotropic materials and Eq. (3.8) in case of isotropic materials. Since [B] is independent of displacements, the strains due to the virtual displacements can be written as

$$\{\delta \varepsilon\} = [B]\{\delta d\} \tag{3.50}$$

Using Eq. (3.48) in Eq. (3.47)

$$\int_\Omega [[B]\{\delta d\}]^T [C][B]\{d\} d\Omega = \int_\Gamma \{\delta d\}^T \{F_\Gamma\} d\Gamma + \int_\Omega \{\delta d\}^T \{F_\Omega\} d\Omega \tag{3.51.a}$$

$$\{\delta d\}^T \int_\Omega [B]^T [C][B]\{d\} d\Omega = \{\delta d\}^T \int_\Gamma \{F_\Gamma\} d\Gamma + \{\delta d\}^T \int_\Omega \{F_\Omega\} d\Omega \tag{3.51.b}$$

The variation of displacements being arbitrary, Eq. (3.49) can be written as

$$\int_{\Omega} \underbrace{[B]^T[C][B]d\Omega}_{[K_e]}\{d\} = \underbrace{\int_{\Gamma}\{F_{\Gamma}\}d\Gamma + \int_{\Omega}\{F_{\Omega}\}d\Omega}_{\{F_e\}} \tag{3.52.a}$$

i.e.
$$[K_e]\{d\} = \{F_e\} \tag{3.52.b}$$

where $[K_e]$ is the element stiffness matrix and $\{F_e\}$ is the load vector.

3.3.6. Numerical integration

The integration of the stiffness matrix for the eight-noded isoparametric solid element is carried out in the natural coordinate system i.e. ξ, η, μ as

$$[K_e] = \int_{-1}^{1}\int_{-1}^{1}\int_{-1}^{1}[B(\xi,\eta,\mu)]^T[C][B(\xi,\eta,\mu) \mid J \mid d\xi d\eta d\mu \tag{3.53}$$

The numerical integration applied to evaluate the stiffness matrix is done by the Gauss Quadrature method using 2×2×2 integration for linear eight-noded solid elements. Within the element, eight sampling points also known as gauss points are used (**Table 3.2**), all having associated weights equal to 1. A solid element in natural coordinates and the eight gauss points are shown in **Figure 3.6**.

Table 3.2: Gauss points

GP	ξ	η	μ
I	−0.5774	−0.5774	−0.5774
II	+0.5774	−0.5774	−0.5774
III	+0.5774	+0.5774	−0.5774
IV	−0.5774	+0.5774	−0.5774
V	−0.5774	−0.5774	+0.5774
VI	+0.5774	−0.5774	+0.5774
VII	+0.5774	+0.5774	+0.5774
VIII	−0.5774	+0.5774	+0.5774

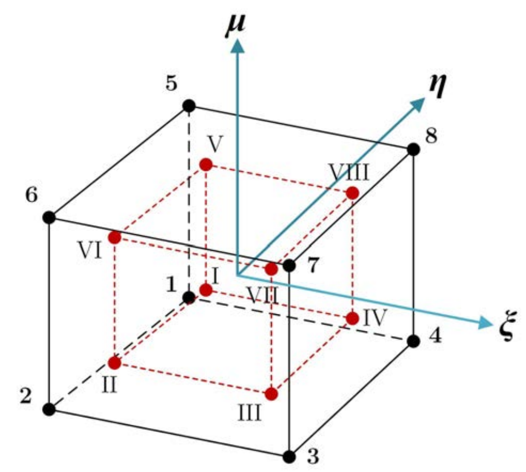

Figure 3.6: Solid element in natural coordinates and the eight gauss points

Therefore, in the evaluation of $[K_e]$, considering the 2×2×2 sampling points, the integral in Eq. (3.53) becomes

$$\underset{33\times 33}{[\mathrm{K}_e]} = \sum_{i=I}^{VIII}\sum_{j=I}^{VIII}\sum_{k=I}^{VIII} f(\xi_i, \eta_j, \mu_k) w_i w_j w_k \tag{3.54}$$

where

$$f(\xi,\eta,\mu)=[B(\xi,\eta,\mu)]^T[C][B(\xi,\eta,\mu)]\,|\,J\,|;$$

$$w_i=w_j=w_k=1\;\forall i,j,k\in[I,VIII]$$

3.3.7. Static condensation

The element stiffness matrix obtained using Eq. (3.54) is of size 33×33 due to the additional incompatible modes. In practice, these nodeless DOFs do not connect with the adjoining elements and can be condensed before the assembly of the elements and only those coefficients that multiply element boundary DOFs are assembled in the global stiffness matrix. The incompatible modes and the DOFs associated with these additional terms can be eliminated using the method of static condensation to get the condensed stiffness matrix of size 24×24 corresponding to the external nodes of the element. This is done by sub-structuring the element stiffness matrix $[K_e]$ by reordering the relevant coefficients corresponding to the external DOFs, $\{d_r\}$ associated with the nodes, and the nodeless DOFs, $\{d_c\}$, for the incompatible modes to obtain

$$\begin{bmatrix}[k_{rr}] & [k_{rc}]\\ [k_{cr}] & [k_{cc}]\end{bmatrix}\begin{Bmatrix}\{d_r\}\\ \{d_c\}\end{Bmatrix}=\begin{Bmatrix}\{F_r\}\\ \{F_c\}\end{Bmatrix} \tag{3.55}$$

where $\{F_c\}=\{0\}$ (3.56.a)

$$[k_{rr}]=\int_{-1}^{1}\int_{-1}^{1}\int_{-1}^{1}[B_a]^T[C][B_a]\,|\,J\,|\,d\xi d\eta d\mu \tag{3.56.b}$$

$$[k_{rc}]=\int_{-1}^{1}\int_{-1}^{1}\int_{-1}^{1}[B_a]^T[C][B_d]\,|\,J\,|\,d\xi d\eta d\mu \tag{3.56.c}$$

$$[k_{cr}]=\int_{-1}^{1}\int_{-1}^{1}\int_{-1}^{1}[B_d]^T[C][B_a]\,|\,J\,|\,d\xi d\eta d\mu \tag{3.56.d}$$

$$[k_{cc}]=\int_{-1}^{1}\int_{-1}^{1}\int_{-1}^{1}[B_d]^T[C][B_d]\,|\,J\,|\,d\xi d\eta d\mu \tag{3.56.e}$$

Solving the lower partition of Eq. (3.55) for $\{d_c\}$ and using Eq. (3.56.a) gives

$$\{d_c\}=-[k_{cc}]^{-1}[k_{cr}]\{d_r\} \tag{3.57}$$

Substituting the expression for $\{d_c\}$ from Eq. (3.57) in the upper partition of Eq. (3.55) to get

$$\begin{aligned}&[k_{rr}]\{d_r\}-[k_{rc}][k_{cc}]^{-1}[k_{cr}]\{d_r\}=\{F_r\}\\ \Rightarrow\;&\underbrace{\left([k_{rr}]-[k_{rc}][k_{cc}]^{-1}[k_{cr}]\right)}_{[\bar{K}_e]}\{d_r\}=\underbrace{\{F_r\}}_{\{\bar{F}\}}\end{aligned} \tag{3.58}$$

Therefore, the stiffness matrix $[\bar{K}_e]$ is of size 24×24 and $\{\bar{F}\}$ is the condensed load vector corresponding to the condensed element such that $[\bar{K}_e]\{d_c\} = \{\bar{F}\}$. The condensed elemental stiffness matrix and the force vector are assembled to produce the global equations and can be written as

$$[K]\{d\} = \{F\} \tag{3.59}$$

3.3.8. Eight-noded layered solid element

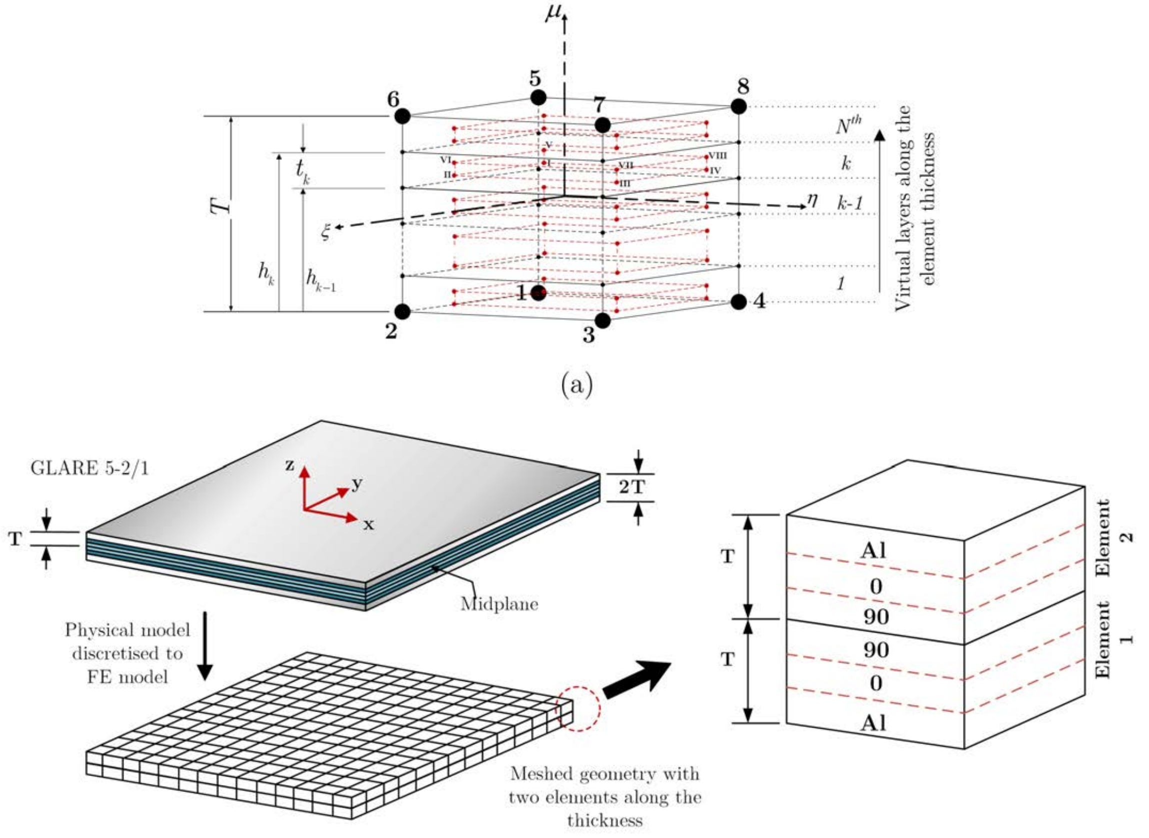

(a)

(b)

Figure 3.7: (a) A *N*-layered solid element (b) A GLARE 5-2/1 plate meshed using layered solid elements

Using layered elements significantly reduces the computational demand in the analysis of laminated structures as discussed in the works of Jones et al. [184]. As shown in **Figure 3.7**, for a solid element having N layers of individual thicknesses t_k, the total thickness of the element can be written as

$$T = \sum_{k=1}^{N} t_k = \sum_{k=1}^{N} h_k - h_{k-1} \tag{3.60}$$

In the evaluation of the elemental stiffness matrix as in Eq. (3.53), along the thickness direction taking $h \in [0, T]$ and changing the limits of μ from (-1,1) to (0, *T)* leads to

$$\begin{aligned} h &= \frac{T}{2}(1+\mu) \\ \Rightarrow \mu &= \frac{2}{h} - 1 \\ \Rightarrow d\mu &= \frac{2}{T}dh \end{aligned} \tag{3.61}$$

Substituting the value of $d\mu$ in Eq. (3.53) gives

$$[K_e] = \frac{2}{T}\int_{-1}^{1}\int_{-1}^{1}\int_{0}^{T} f(\xi,\eta,\mu)d\xi d\eta dh \tag{3.62}$$

Integrating separately over each layer of thickness t_k, the integral becomes

$$[K_e] = \frac{2}{T}\int_{-1}^{1}\int_{-1}^{1}\sum_{k=1}^{N}\int_{h_{k-1}}^{h_k} f(\xi,\eta,\mu)d\xi d\eta dh \tag{3.63}$$

Changing back the limits of integration,

$$[K_e] = \frac{2}{T}\int_{-1}^{1}\int_{-1}^{1}\sum_{k=1}^{N}\frac{t_k}{2}\int_{-1}^{1} f(\xi,\eta,\mu)d\xi d\eta d\mu \tag{3.64}$$

The above integral can be evaluated numerically using Gauss Quadrature scheme discussed in **Section 3.3.6**.

3.3.9. Elemental mass matrix

For the finite element analysis of dynamic impact problems, the mass matrix is needed to be paired with the stiffness matrix and the mass matrix can be evaluated either by the method of direct mass lumping or the variational method. In the present variational formulation, the same shape functions as used in the evaluation of the elemental stiffness matrix is used to give the consistent mass matrix as

$$[M_e] = \int_{-1}^{1}\int_{-1}^{1}\int_{-1}^{1} \rho[N]^T[N]\,|\,J\,|\,d\xi d\eta d\mu \tag{3.65}$$

where ρ is the density of the element. In a similar way to the evaluation of the stiffness matrix of a layered element, the mass matrix can also be evaluated as

$$[M_e] = \frac{2}{T}\int_{-1}^{1}\int_{-1}^{1}\sum_{k=1}^{N}\frac{t_k}{2}\int_{-1}^{1} g(\xi,\eta,\mu)d\xi d\eta d\mu \tag{3.66}$$

where $g(\xi,\eta,\mu) = \rho[N]^T[N]\,|\,J\,|$

3.4. Modelling of low-velocity impact on GLARE

A rectangular GLARE FML plate having sides $a \times b$ and thickness h, clamped on all sides is subjected to a low-velocity impact (LVI) by an arbitrary rigid impactor of mass m^o with a velocity $\vec{v}^o$ as shown in **Figure 3.8**. Furthermore, impacts by impactors having different geometries can occur at different trajectories relative to the target and multiple impacts can occur at arbitrary times. On account of such LVIs, it is desired to evaluate the transient dynamic response of the target plate and evaluate the contact forces using appropriate contact laws for accurate estimation of the stresses developed within the GLARE FML.

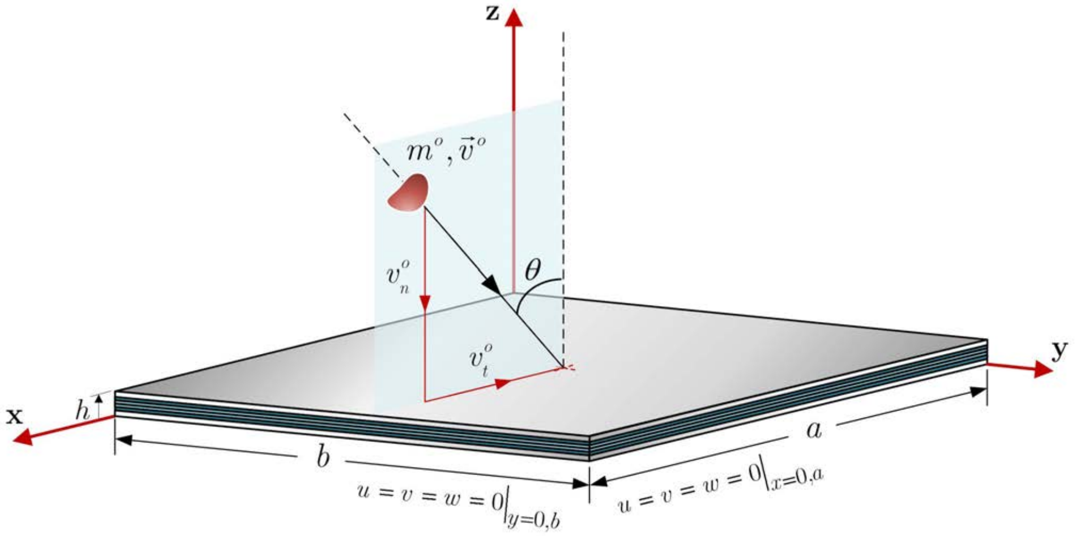

Figure 3.8: Clamped GLARE plate subjected to LVI

3.4.1. Governing equations for impact analysis

After evaluating the global mass matrix $[M]$ and the global stiffness matrix $[K]$ and neglecting damping effects, the governing equation due to a transient force $\{F\}$ can be written as [173]

$$[M]\{\ddot{d}\}^{t+\Delta t} + [K]\{d\}^{t+\Delta t} = \{F\}^{t+\Delta t} \tag{3.67}$$

where $\{d\}$ is the displacement vector and its subsequent time derivatives $\{\dot{d}\}$ and $\{\ddot{d}\}$ denote velocity and acceleration respectively. Now, using the Newmark-β integration method [185], Eq. (3.67) can be written as

$$[\hat{K}]\{d\}^{t+\Delta t} = \{\hat{F}\}^{t+\Delta t} \tag{3.68}$$

where the effective stiffness matrix $[\hat{K}]$ and the effective force vector $\{\hat{F}\}$ are computed as

$$
\begin{aligned}
[\hat{K}] &= \frac{1}{\phi \Delta t^2}[M]+[K] \\
\{\hat{F}\} &= \{H\}^t + \{F\}^{t+\Delta t} \\
\{H\}^t &= [M]\left(\frac{1}{\phi \Delta t^2}\{d\}^t + \frac{1}{\phi \Delta t}\{\dot{d}\}^t + \frac{1-2\phi}{2\phi}\{\ddot{d}\}^t \right)
\end{aligned}
\tag{3.69}
$$

Neglecting the effects of preload, Eq. (3.68) can be written as

$$[\hat{K}]\{d\}^{t+\Delta t} = \{H\}^t + \{P\}^{t+\Delta t} \tag{3.70}$$

where $\{P\}$ is the force vector comprising of the concentrated loads. The displacement vector $\{d\}$ is the net contribution of the displacements due to the force $\{H\}$ and contact force $\{P\}$ and can be written as [186]

$$\{d\}^{t+\Delta t} = \{d\}_H^{t+\Delta t} + \{d\}_P^{t+\Delta t} \tag{3.71}$$

Eq. (3.70) and Eq. (3.71) gives [186]

$$[\hat{K}]\{d\}^{t+\Delta t} = [\hat{K}]\{d\}_H^{t+\Delta t} + [\hat{K}]\{d\}_P^{t+\Delta t} \tag{3.72}$$

where $\{d\}_H$ is the displacement due to force $\{H\}$ and $\{d\}_P$ is the displacement due to the concentrated loads $\{P\}$. Considering a general case of the impactor striking arbitrarily along a certain plane (x-z plane as shown in **Figure 3.8**) at an obliquity θ with respect to the normal, the vector $\{d\}$, $\{d\}_H$ and $\{d\}_P$ in Eq. (3.72) can be decoupled into vectors containing normal and tangential components as

$$[\hat{K}]\{d_N\}^{t+\Delta t} = [\hat{K}]\{d_N\}_H^{t+\Delta t} + [\hat{K}]\{d_N\}_P^{t+\Delta t} \tag{3.73.a}$$

$$[\hat{K}]\{d_T\}^{t+\Delta t} = [\hat{K}]\{d_T\}_H^{t+\Delta t} + [\hat{K}]\{d_T\}_P^{t+\Delta t} \tag{3.73.b}$$

such that

$$\{d\} = \{d_N\} + \{d_T\} \tag{3.74.a}$$

$$\{d\}_H = \{d_N\}_H + \{d_T\}_H \tag{3.74.b}$$

$$\{d\}_P = \{d_N\}_P + \{d_T\}_P \tag{3.74.c}$$

The vectors $\{U\}_N$ and $\{U\}_T$ are taken having their concerned degree of freedom components equal to −1 only in the contact force directions viz. normal and tangential direction respectively while rest being zero. Taking the scalar point force along the normal direction to be f_N and that along the tangential direction to be f_T at a particular instant $t+\Delta t$, the displacement due to the concentrated loads becomes [186]

$$[\hat{K}]\{d\}_P^{t+\Delta t} = f_N^{t+\Delta t}\{U\}_N + f_T^{t+\Delta t}\{U\}_T \tag{3.75}$$

Using Eq. (3.72 and 3.73)

$$[\hat{K}]\{d_N\}_P^{t+\Delta t} = f_N^{t+\Delta t}\{U\}_N \tag{3.76.a}$$

$$[\hat{K}]\{d_T\}_P^{t+\Delta t} = f_T^{t+\Delta t}\{U\}_T \tag{3.76.b}$$

For unit contact forces ($f_N^{t+\Delta t}$=1 and $f_T^{t+\Delta t}$=1), Eq. (3.76) becomes

$$[\hat{K}]\{d_N\}_{P_U}^{t+\Delta t} = \{U\}_N \tag{3.77.a}$$

$$[\hat{K}]\{d_T\}_{P_U}^{t+\Delta t} = \{U\}_T \tag{3.77.b}$$

Using Eq. (3.75-3.77),

$$\{d\}_P^{t+\Delta t} = f_N^{t+\Delta t}\{d_N\}_{P_U}^{t+\Delta t} + f_T^{t+\Delta t}\{d_T\}_{P_U}^{t+\Delta t} \tag{3.78}$$

Substituting the value of $\{d\}_P^{t+\Delta t}$ in Eq. (3.71) yields

$$\{d\}^{t+\Delta t} = \{d\}_H^{t+\Delta t} + f_N^{t+\Delta t}\{d_N\}_{P_U}^{t+\Delta t} + f_T^{t+\Delta t}\{d_T\}_{P_U}^{t+\Delta t} \tag{3.79}$$

For an impactor of mass m^o and having a velocity $\vec{v}^o$, the position of the impactor at time $t+\Delta t$ can be evaluated by using Newton's second law to obtain the instantaneous position along the normal and tangential directions as

$$\alpha_S^{t+\Delta t} = \int_0^{t+\Delta t} v_n^o \; dt + \int_0^{t+\Delta t}\int_0^{t+\Delta t} \frac{f_N}{m^o} \; dt \; dt \tag{3.80.a}$$

$$\delta_S^{t+\Delta t} = \int_0^{t+\Delta t} v_t^o \; dt + \int_0^{t+\Delta t}\int_0^{t+\Delta t} \frac{f_T}{m^o} \; dt \; dt \tag{3.80.b}$$

where α_S and δ_S are the displacement components of the centre of the impactor along the normal (z-direction) and tangential (x-direction) direction respectively. Similarly, v_n^o and v_t^o are the components of $\vec{v}^o$ along the normal and tangential direction respectively. The magnitude of the contact forces due to impact needs to be evaluated prior to the plate motion being analysed. The evaluation of these contact forces ($f_N^{t+\Delta t}$ and $f_T^{t+\Delta t}$) depends on the impactor's position relative to the target. They are governed by the contact laws appropriately selected according to the geometry of the impactor and the target and the nature of the contact. These are discussed in the subsequent sections.

3.4.2. Normal impact by a rigid spherical impactor

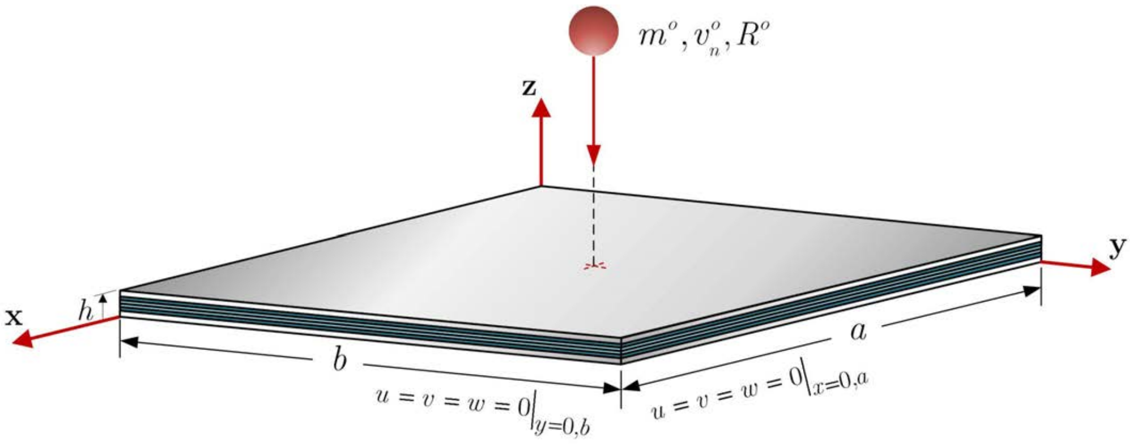

Figure 3.9: Normal impact by a rigid spherical impactor on a clamped GLARE plate

As shown in **Figure 3.9**, the GLARE plate having mass m_p is considered to be clamped on all sides and impacted by a rigid spherical impactor of mass m^o normally at the centre. If the target plate's centre displacement at the impact location in the normal direction is $\delta_{NC}^{t+\Delta t}$, then the relative displacement of the centre of the impactor to the plate centre gives the normal indentation as

$$\alpha^{t+\Delta t} = \alpha_S^{t+\Delta} - \delta_{NC}^{t+\Delta} \tag{3.81}$$

where

$$\delta_{NC}^{t+\Delta t} = \left(\delta_{NC}^{t+\Delta t}\right)_H + f_N^{t+\Delta t}\left(\delta_{NC}^{t+\Delta t}\right)_{P_U} \tag{3.82}$$

For normal contact between the spherical impactor and a transversely isotropic half space, the contact force during loading can be obtained by using the Hertzian contact law [186] as

$$f_N^{t+\Delta t} = \begin{cases} k_c^{eff}\left(\alpha^{t+\Delta t}\right)^{3/2}, & loading \\ f_N^{\max}\left[\dfrac{\alpha^{t+\Delta t} - \alpha_o}{\alpha_{\max} - \alpha_o}\right]^{2.5}, & unloading \end{cases} \tag{3.83}$$

where k_c^{eff} is the modified Hertz contact stiffness or the effective contact stiffness, α_o is the permanent indentation which may be indented during loading/unloading and $\alpha_{\max}$ is the maximum indentation due to the maximum contact force $f_N^{\max}$. The value of α_o is decided by the following conditions governed by critical indentation α_{cr} as

$$\alpha_o = \begin{cases} 0 & ,\alpha_{\max} < \alpha_{cr} \\ \alpha_{\max}\left[1-\left(\dfrac{\alpha_{cr}}{\alpha_{\max}}\right)^{2/5}\right] & ,\alpha_{\max} \geq \alpha_{cr} \end{cases} \tag{3.84}$$

where α_{cr} depends on the shear strength S, of the top layer of the GLARE plate, radius of the rigid impactor, R^o and effective contact modulus, E^*, and is given by [187]

$$\alpha_{cr} = \frac{2.72S^2\pi^2R^o}{E^{*2}} \tag{3.85}$$

where

$$E^* = \left[\frac{1-\upsilon_i^2}{E_i}+\frac{1}{E'_{yy}}\right]^{-1} \tag{3.86}$$

E'_{yy} is generally taken as the effective elastic modulus in the transverse direction and E_i and υ_i are the Young's modulus and Poisson's ratio of the impactor respectively. In the present case of GLARE, considering a weight φ equal to the cubic ratio of the thickness of the top aluminium layer to the total thickness of the target plate, the value of E'_{yy} is computed [188] as

$$E'_{yy} = E_{2ply} + (E_{Al} - E_{2_{ply}})\varphi \tag{3.87}$$

3.4.2.1. Evaluation of the effective contact stiffness

To appropriately analyse the contact impact problem, taking into account the effects of the impactor to plate mass ratios as well as the plate dimensions, an accurate estimation of the effective contact stiffness is required. In case of moderate indentation by small mass spherical impactor of radius R^o where boundary conditions have a very little influence during the course of their short impact times, the contact stiffness k_l between the spherical impactor and the plate is given by [189]

$$k_l = \frac{4}{3}\sqrt{R^o}E^* \tag{3.88}$$

For the case of a larger mass impactor striking the plate at lower velocities, the contact response of the plate is similar to quasi-static response and accordingly the contact stiffness would differ. For longer duration impacts as in the case of impactors whose mass is intermediate $(0.2 \leq m^o/m_p \leq 3)$ and considerably higher than the target mass, the calculation of the contact stiffness may turn out to be a complicated task [190]. Generally for impactors having masses much higher than the plate mass, as reported by Bucinell et al. [191], the contact can be modelled with a linearized spring. For a smooth sphere of radius R^o contacting a smooth planar half space with a concentrated contact load P, the normal approach/indentation α is given by [192]

$$\alpha^3 = \left(\frac{3P}{4E^*}\right)^2 \frac{1}{R^o} \tag{3.89}$$

Therefore, the linearized contact stiffness for a quasi-static loading in case of impactors with much higher masses can be computed as

$$k_h = \frac{dP}{d\alpha} = (6PR^o E^{*2})^{1/3} \tag{3.90}$$

Another way to evaluate the linearized contact stiffness k_d is by considering the impactor mass m^o and initial velocity v_n^o [191] as

$$k_d = 1.502\left(\frac{m^o v_n^o}{2}\right)^{1/5} k_l^{4/5} \tag{3.91}$$

For evaluating the linearized stiffness by Eq. (3.90), the load may not be known apriori. Considering the spring having stiffness k_d to be compressed by the critical thickness α_{cr}, a factor r_k is defined which takes into account the excess or deficiency in the relative energy of the impactor to the energy stored in the spring, and the critical contact load P_o is evaluated as

$$P_o = (r_k)^{1/5} k_l \alpha_{cr}^{3/2} \tag{3.92}$$

where

$$r_k = \frac{\frac{1}{2} m^o (v_n^o)^2}{\frac{1}{2} k_d \alpha_{cr}^2} \tag{3.93}$$

The value of k_h is finally evaluated by putting the obtained value of P_o in Eq. (3.90). But, the linearization of the contact stiffness impairs the capture of the complete motion. A mobility ratio χ is defined in Eq. (3.94) such that χ tending to zero would imply an elastic impact with the rebound velocity tending to initial velocity and with higher values of χ, the response will be more prolonged as in the case of large mass quasi-static LVIs and its value is calculated as [193]

$$\chi = \frac{k_l^{2/5} {m^{o}}^{3/5} {v^{o}}^{1/5}}{8\sqrt{m_p^{*} D^{*}}} \tag{3.94}$$

where m_p^* is the target plate areal mass density and D^* is the effective plate stiffness defined by the components of the bending stiffness matrix, $[D]$ as

$$D^{*} = \left(D_{12} + 2D_{66} + \sqrt{D_{11}D_{22}}\right)\Big/2 \tag{3.95}$$

Evidently, a simple closed form expression for evaluating the effective contact stiffness k_c^{eff} is necessary as the target may not be ideally assumed to be an infinite half space and the influence of the boundary conditions and target dimensions needs to be taken into account relative to the impactor. A semi-empirical relation for the contact coefficient k_c^{eff} obtained by curve fitting can be written as

$$k_c^{eff} = \begin{cases} k_l / [1 + \Phi\chi^{1/5}(\log_{10}(5m^o / m_p))^2]\ , & m^o / m_p \geq 1/5 \\ k_l\ , \quad m^o / m_p < 1/5 & \end{cases} \tag{3.96}$$

where Φ is a constant based on the plate geometry and $1 \leq \Phi \leq 3$. The evaluation of the effective contact stiffness is done by taking note of the impactor/plate mass ratio as well as ratio of the plate mobility to contact mobility. The expression in Eq. (3.96) is obtained by curve fitting such that the effective contact stiffness tends to the higher limiting end in case of LVIs by smaller mass impactors and towards an asymptotic lower limit associated with quasi-static response in case of higher mass impactors as in this regime the dynamics of the contact is significantly dominated by the structural response. For small mass impactors having mass less than one-fifth of the plate mass, $\Phi = 0$. In many practical cases, the stresses would be high at the contact location exceeding the yield limit resulting in yielding of the surface near the contact during impact by a rigid impactor. For low energy impacts by smaller mass impactors at lower velocities which are mostly in the elastic region, the regime of analysis can be limited to elastic-plastic limits and the loading/unloading for non-adhesive contact can be computed satisfactorily by Eq. (3.83). But in case of metals there is yielding even at lower velocities due to higher contact stresses. To avoid overprediction of the peak contact force, a proper elastic-plastic contact considering the effect of local permanent deformation is assumed. Therefore, during loading when the indentation exceeds the yield limit, the contact force is computed as [187]

$$f_{\substack{N\\ \text{loading}}}^{t+\Delta t} = k_c^{eff}\alpha_{cr}^{3/2} + k_p(\alpha^{t+\Delta t} - \alpha_{cr}) \;\;,\;\; \alpha > \alpha_{cr} \;\;,\;\; \textit{elastic - plastic loading} \tag{3.97.a}$$

$$f_{\substack{N\\ (\text{elastic})\\ \text{unloading}}}^{t+\Delta t} = f_N^{\max}\left[\frac{\alpha^{t+\Delta t} - \alpha_o}{\alpha_{\max} - \alpha_o}\right]^{3/2} \;\;,\;\; \textit{elastic unloading,} \tag{3.97.b}$$

$$\alpha_o = \alpha_{\max}\left[1 - \frac{\alpha_{cr}}{\alpha_{\max}}\left(\frac{2\alpha_{\max}}{\alpha_{cr}} - 1\right)^{1/2}\right] \tag{3.97.c}$$

where k_p is the stiffness in the linear part of the elastic-plastic loading phase and can be ideally taken as

$$k_p = 1.5k_c^{eff}\sqrt{\alpha_{cr}} \tag{3.98}$$

The contact force is calculated either by Eq. (3.83) or (3.97) by substituting the value of α and implementing the Newton-Raphson method to minimise the error in the evaluation of the contact force. Subsequently, the plate displacement is obtained using Eq. (3.79) and using Newmark-β method, the velocity and acceleration at time $t + \Delta t$ is evaluated. This procedure is repeated for each time step to obtain the displacements, strains and stresses.

3.4.3. Oblique impact by a rigid spherical impactor

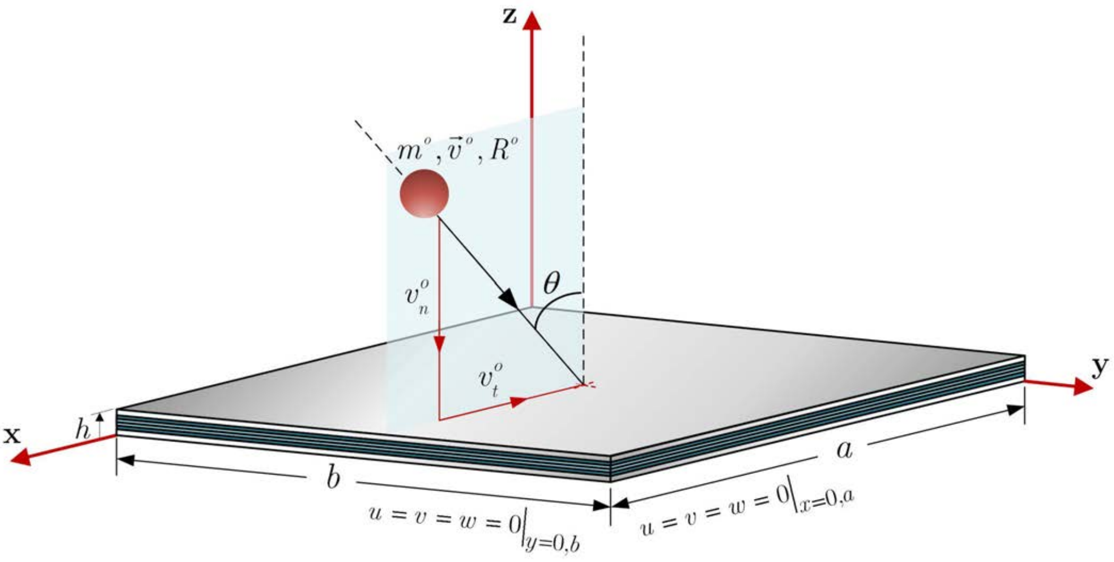

Figure 3.10: Oblique impact by a steel sphere on a clamped GLARE plate

In the case of oblique low-velocity impact (OLVI), the normal component (f_N) and the tangential component (f_T) of the contact force need to be evaluated simultaneously. As discussed in **Sections 3.4.2-3.4.3**, Hertzian force-displacement relation is used to evaluate the normal contact force and the tangential contact force is computed by using the theory of

Mindlin and Deresiewicz [176,177]. As shown in **Figure 3.10**, the target GLARE plate is considered to be clamped on all sides and impacted by a rigid spherical impactor of mass m^o at the centre along the x-z plane at an arbitrary angle of incidence θ with respect to the plate normal. A flowchart showing the basic steps for the study of OLVI is shown in **Figure 3.11**.

3.4.3.1. Tangential contact force-displacement relations

Considering the coefficient of friction between the contacting surfaces to be μ_f, for a constant normal force, the inherent nature of the tangential force is to cause partial slip over the part of the contact area when $f_T < \mu_f f_N$ and this slip region develops and grows inward until rigid body sliding commences at the instance when $f_T \geq \mu_f f_N$. At time $t + \Delta t$, updating the normal contact force f_N and the normal indentation α, the contact area radius β is evaluated as

$$\beta = \sqrt{R^o \alpha} \tag{3.99}$$

The tangential force $f_T^{t+\Delta t}$ at time $t + \Delta t$ is evaluated by an incremental approach by first calculating the value of Δf_T using the newly obtained values of f_N and β. The tangential incremental displacement $\Delta\delta$ is related to the incremental values of the normal and tangential contact forces and is given by [177,194]

$$\Delta\delta = \frac{1}{8G^*\beta}\left(\pm\mu_f \Delta f_N + \frac{\Delta f_T \mp \mu_f \Delta f_N}{\lambda}\right) \tag{3.100}$$

except for the situation when

$$\left|\Delta\delta\right| < \frac{\mu_f \Delta f_N}{8G^*\beta} \text{ for } \Delta f_N > 0 \tag{3.101}$$

where μ_f is the coefficient of friction between the two bodies and the value of G^* is evaluated in terms of the Poisson's ratios and shear moduli of the impactor and the top layer as

$$G^* = \left[\frac{2-\upsilon_i}{G_i} + \frac{2-\upsilon_{Al}}{G_{Al}}\right]^{-1} \tag{3.102}$$

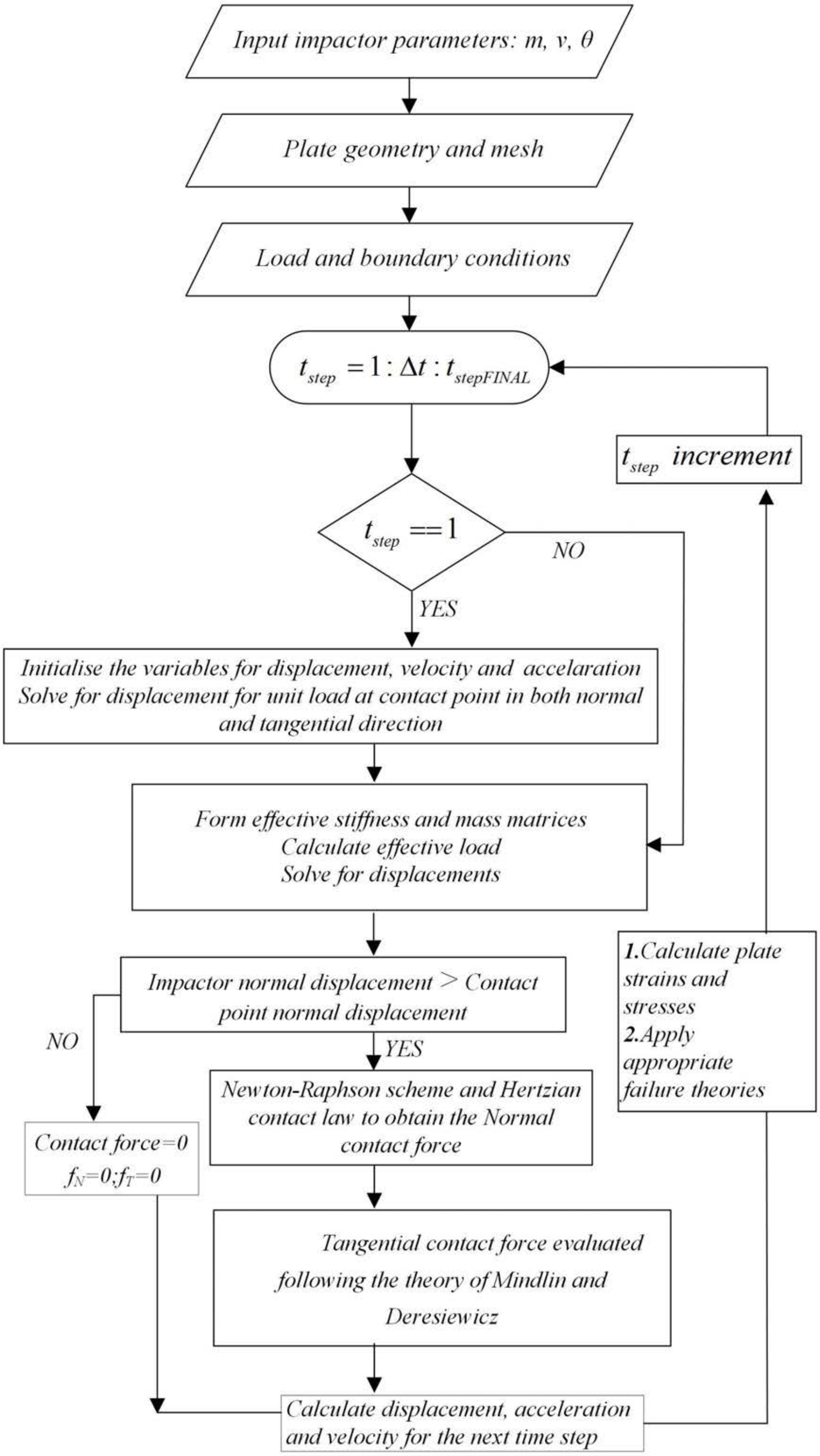

Figure 3.11: Basic steps for the study of oblique low-velocity impact

Rearranging Eq. (3.100), the tangential stiffness is computed as

$$k_t = \frac{\Delta f_T}{\Delta \delta} = 8G^* \beta\lambda \pm \mu_f \left(1-\lambda\right)\frac{\Delta f_N}{\Delta \delta} \tag{3.103}$$

where the negative sign is invoked only during the unloading phase and the value of λ is evaluated as

$$\lambda^3 = \begin{cases} 1-\dfrac{f_T^{t+\Delta t}+\mu_f \Delta f_N}{\mu_f f_N^{t+\Delta t}} & \Delta\delta > 0 \quad (loading) \quad (3.104.a) \\ 1-\dfrac{f_T^{*}-f_T^{t+\Delta t}+2\mu_f \Delta f_N}{2\mu_f f_N^{t+\Delta t}} & \Delta\delta < 0 \quad (unloading) \quad (3.104.b) \\ 1-\dfrac{f_T^{t+\Delta t}-f_T^{**}+2\mu_f \Delta f_N}{2\mu_f f_N^{t+\Delta t}} & \Delta\delta > 0 \quad (Re\,loading) \quad (3.104.c) \end{cases}$$

The parameters f_T^* and f_T^{**} correspond to the load reversal points and are continuously updated as

$$f_T^* = f_T + \mu_f \Delta f_N \quad \text{and} \quad f_T^{**} = f_T^* - \mu_f \Delta f_N \tag{3.105}$$

In Eq. (3.103), the value of λ is set to 1 until the following condition is satisfied [194]

$$8G^*\beta \sum \Delta\delta > \mu_f \sum \Delta f_N \tag{3.106}$$

In a similar way as for the evaluation of the normal contact force, after finding the tangential incremental displacement of the impactor $\Delta\delta$ and using Eq. (3.103-3.104), the tangential force is obtained using the Newton-Raphson method. Then the plate displacement, velocity and acceleration are obtained by Newmark-β integration scheme. This process is repeated at every time step to obtain the displacements and subsequently the strains and stresses.

3.4.4. Normal impact by a rigid cylindrical impactor

In the analysis of LVI by rigid cylindrical impactor, the contact between the impactor and the flat target occurs along the length of the cylinder in the form of a line as shown in **Figure 3.12**. The cylindrical impactor of length $2L$, radius r and mass m^o strikes the target GLARE plate normally along its length such that the loading can be considered as a line load acting over a narrow strip on the impact location. For a smooth cylinder in contact with a plane, Hertzian pressure distribution is assumed over the contact length, and the Hertzian half-width of the contact area is assumed to be uniform along the contact length.

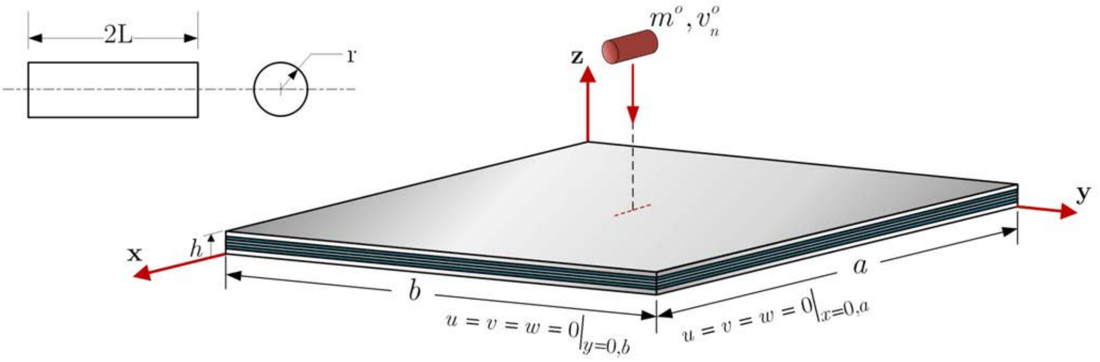

Figure 3.12: LVI by a rigid cylindrical impactor

The narrow strip in the x-y plane is assumed to have a half width b_o and length $2L$, and if α is the depression at the centre of the contact area, then the contact force at $t+\Delta t$ is evaluated as [192,195,196]

$$f_N = \frac{\pi L E^* \alpha}{1.193145 + \ln\left(\dfrac{L}{b_o}\right)} \tag{3.107}$$

For a cylindrical line impactor of radius r, Young's modulus E_i and Poisson's ratio υ_i contacting a transversely isotropic half space of transverse modulus E'_{yy}, the value of the half-width b_o is given by

$$b_o = \left(\frac{4 f_N r}{\pi E^*}\right)^{1/2} \tag{3.108}$$

The value of E^* is evaluated in a similar manner as discussed in **Section 3.4.2**. Using Eq. (3.79-3.81), the contact force during loading can be evaluated as

$$f_N^{t+\Delta t} = \frac{\pi L E^*}{1.193145 + \ln\left(\dfrac{L}{b_o}\right)} \left(\begin{array}{r} \displaystyle\int_0^{t+\Delta t} v_n^o dt + \int_0^{t+\Delta t}\int_0^{t+\Delta t} \frac{f_N}{m^o}\, dt\;\; dt \\ -(\delta_{NC}^{t+\Delta t})_H - f_N^{t+\Delta t}(\delta_{NC}^{t+\Delta t})_{P_U} \end{array} \right) \tag{3.109}$$

In general, the target plate might undergo some extent of permanent indentation α_o during loading/unloading decided by the critical indentation α_{cr}. Considering the centre of the contact location of the cylindrical impact, the value of α_o is

$$\alpha_o = \begin{cases} 0 & , \alpha_{\max} < \alpha_{cr} \\ \alpha_{\max}\left[1 - \left(\dfrac{\alpha_{cr}}{\alpha_{\max}}\right)^{2/5}\right] & , \alpha_{\max} \geq \alpha_{cr} \end{cases} \tag{3.110}$$

where $\alpha_{\max}$ is the value corresponding to the maximum contact force. Therefore, the contact force during unloading can be written as

$$f_N^{t+\Delta t} = \frac{\pi L E^*}{1.193145 + \ln\left(\frac{L}{b_o}\right)} \left(\int_0^{t+\Delta t} v_n^o dt + \int_0^{t+\Delta t}\int_0^{t+\Delta t} \frac{f_N}{m^o}\, dt\ dt - (\delta_{NC}^{t+\Delta t})_H - f_N^{t+\Delta t}(\delta_{NC}^{t+\Delta t})_{P_U} - \alpha_o \right) \tag{3.111}$$

The contact force is evaluated using Eq. (3.109) or Eq. (3.111) by substituting the value of α and implementing the Newton-Raphson method the error in the evaluation of the contact force is minimised. This is repeated at every time step and the plate displacement, velocity and acceleration at time $t + \Delta t$ is evaluated and then the strains and stresses.

3.4.5. Modelling LVI by multiple impactors

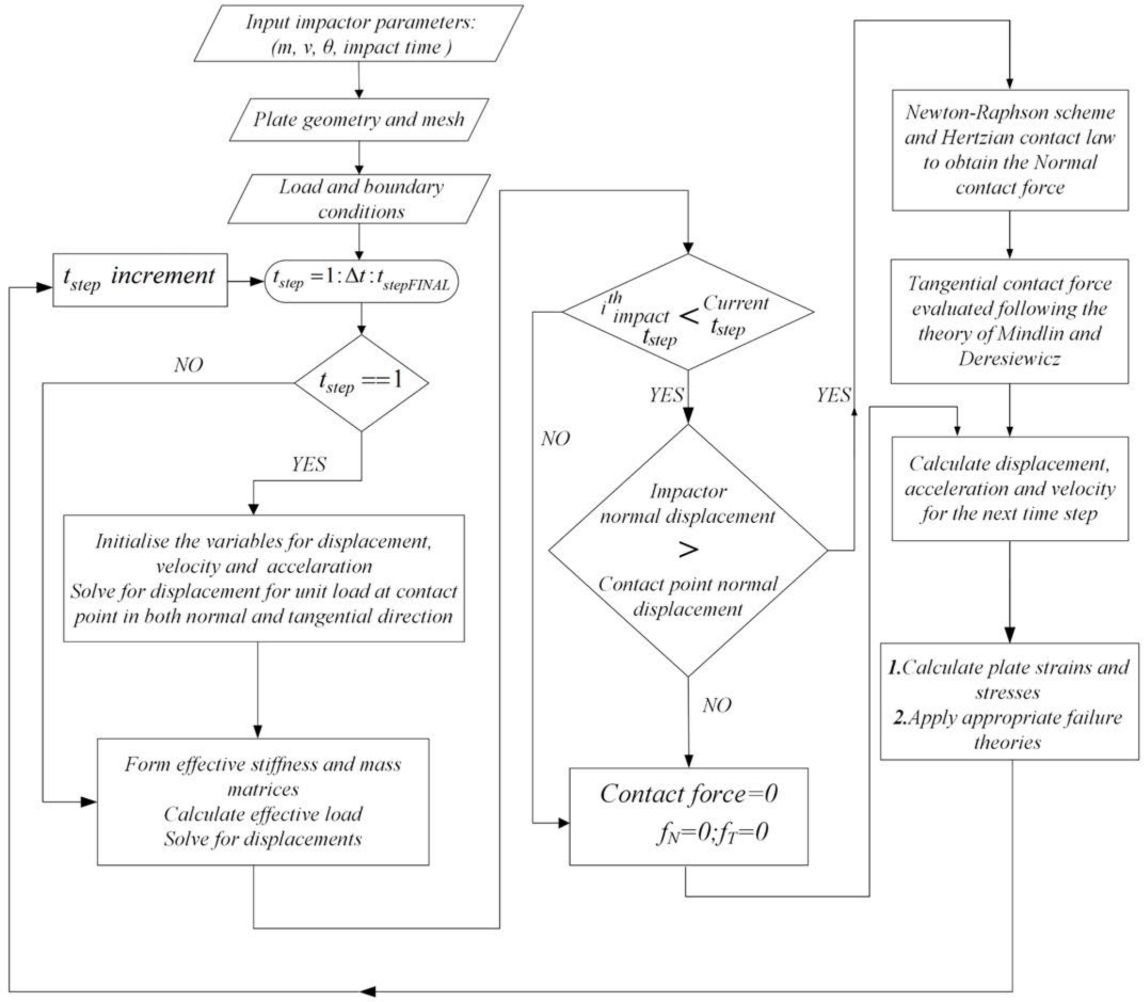

Figure 3.13: Analysis of multiple LVI on GLARE

The FE code is extended to incorporate multiple impactors of arbitrary masses and velocities hitting the GLARE plate surface at different locations at arbitrary time intervals.

Proceeding in a similar way as discussed in the preceding sections, in the analysis of multiple LVIs by n numbers of rigid impactors, the displacement vector in Eq. (3.79) becomes

$$\{d\}^{t+\Delta t} = \{d\}_H^{t+\Delta t} + \sum_{i=1}^{n} f_{Ni}^{t+\Delta t}\{d_{Ni}\}_{P_U}^{t+\Delta t} + f_{Ti}^{t+\Delta t}\{d_{Ti}\}_{P_U}^{t+\Delta t} \tag{3.112}$$

The respective contact loads of the concerned i^{th} impactor is set to zero until the cumulative time step of the particular impactor is greater than or equal to the mentioned impacting time and the position of the individual impactors are calculated using Eq. (3.80). The individual impactors can be of arbitrary geometries (spherical or cylindrical) and the contact laws needs to be appropriately selected for the analysis of multiple LVIs. Based on the present formulation of LVI, the flowchart in **Figure 3.13** presents the analysis of multiple impacts on GLARE.

3.4.6. Transformation to nodal stresses

After computing the displacements, the strains and stresses are computed at the gauss points. In order to accurately predict the delamination at the ply interfaces, these stresses need to be correctly interpolated to the ply interfaces. The nodes being located at the ply surface, the gauss point stresses are transformed to nodal stresses by the least square formulation given by Hinton and Campbell [197] as

$$\sigma_i' = [\underline{\Lambda}]\sigma_j \qquad i = 1,2,...,8; j = I, II, ..., VIII \tag{3.113}$$

where σ'_i and σ_j are the nodal and gauss point stresses respectively. $[\underline{\Lambda}]$ is the transformation matrix for converting the gaussian stresses to nodal stresses for an eight-noded brick element and is given by

$$[\underline{\Lambda}] = \begin{bmatrix} \sum_{j=I}^{VIII} N_1(\xi_j,\eta_j,\mu_j)N_1(\xi_j,\eta_j,\mu_j) & \cdots & \cdots & \sum_{j=I}^{VIII} N_1(\xi_j,\eta_j,\mu_j)N_8(\xi_j,\eta_j,\mu_j) \\ \sum_{j=I}^{VIII} N_2(\xi_j,\eta_j,\mu_j)N_1(\xi_j,\eta_j,\mu_j) & \cdots & \cdots & \sum_{j=I}^{VIII} N_2(\xi_j,\eta_j,\mu_j)N_8(\xi_j,\eta_j,\mu_j) \\ : & : & : & : \\ : & : & : & : \\ \sum_{j=I}^{VIII} N_8(\xi_j,\eta_j,\mu_j)N_1(\xi_j,\eta_j,\mu_j) & \cdots & \cdots & \sum_{i=I}^{VIII} N_8(\xi_j,\eta_j,\mu_j)N_8(\xi_j,\eta_j,\mu_j) \end{bmatrix}_{8\times 8}^{-1}$$
$$\times \begin{bmatrix} N_1(\xi_I,\eta_I,\mu_I) & N_1(\xi_{II},\eta_{II},\mu_{II}) & \cdots & N_1(\xi_{VIII},\eta_{VIII},\mu_{VIII}) \\ N_2(\xi_I,\eta_I,\mu_I) & N_2(\xi_{II},\eta_{II},\mu_{II}) & \cdots & N_2(\xi_{VIII},\eta_{VIII},\mu_{VIII}) \\ : & : & : & : \\ N_8(\xi_I,\eta_I,\mu_I) & N_8(\xi_{II},\eta_{II},\mu_{II}) & \cdots & N_8(\xi_{VIII},\eta_{VIII},\mu_{VIII}) \end{bmatrix}_{8\times 8} \tag{3.114}$$

3.5. Impact induced damage in GLARE

GLARE FMLS are hybrid laminates comprising of alternating layers of glass/epoxy prepregs between thin aluminium layers which mostly find its application in aircraft structures. The damage of GLARE due to LVIs is inevitable and their accurate estimation in FMLs is complicated in nature. In most of the barely visible impacts where the impacting energy is much less and in the range of 1.5 J-2.5 J, internal damage in the form of delamination may initiate, especially at the metal/composite interfaces owing to their difference in material properties [121]. Such low-energy impacts cause subsurface damage without any visible deformation or penetration at the impact site but leaves an extensive area of failure in the form of delamination thereby making its assessment at the interfaces important, especially for the LVIs where visible damages are difficult to detect. The inner composite plies in FMLs is distinguished by their high sensitivity to impact loading. Due to the inferior strength properties of the matrix, intra-laminar damage in the form of matrix cracking and debonding between the fibres and matrix initiates when subjected to impact loading. Furthermore, inter-laminar damage in the form of delamination occurring between the adjacent plies and also at the metal/composite interfaces is a critical failure mode, significantly affecting the structural strength of the FML. The matrix cracks on account of LVI can occur as follows [35]:

- On account of LVI, the transverse cracks can initiate on the plies directly beneath the outer aluminium layer due to the high transverse shear stresses on the impacted surface near the impact location.
- Matrix (bending) cracks on plies at the non-impacted side due to higher local (flexural) deformation of the GLARE FML near the impact site inducing higher tensile bending stresses.
- An illustration of the impact induced damage in a GLARE plate is shown in **Figure 3.14**

The failure mode of the metal layers of the GLARE FML under LVI is comparatively straightforward compared to the complex failure modes of the composite layers. Elastic and plastic deformation are two parts of the metal's well-known two-phase deformation mechanism. The metal will deform plastically when the stress from the impact force exceeds the yield point. Due to strain hardening, the stress keeps rising until it reaches the failure stress, at which point cracks start to appear on the metal surface. In the present study of LVI on GLARE, the impact energy range considered is below the perforation limit and the main motive is to study the interfacial delamination and complex damage evolution of the inner composite plies subjected to LVI by a rigid impactor.

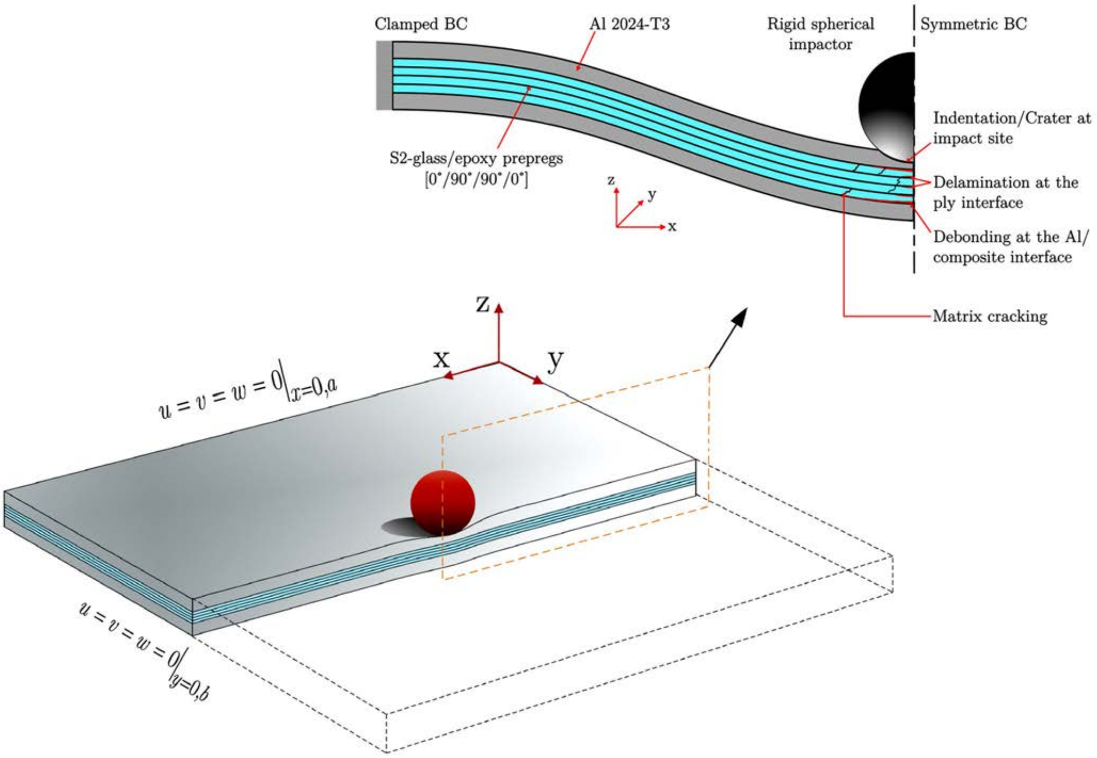

Figure 3.14: Low velocity impact induced damage in GLARE

3.5.1. Interfacial delamination

The delamination at the interfaces of the GLARE laminate due to LVI can occur when the combined stresses governing the growth of delamination exceeds the critical limit at the concerned interface. Considering ${}^{n}\overline{\tau}_{23}$, ${}^{n}\overline{\tau}_{13}$ and ${}^{n}\overline{\sigma}_{22}$ as the averaged inter-laminar stresses at the n^{th} interface, and ${}^{n}S_{i}$, ${}^{n}Y_{T}$, ${}^{n}Y_{C}$ as the shear strength, transverse tensile and transverse compressive strengths respectively, a semi-empirical criterion is used for assessing delamination at the interfaces as proposed by Choi et al. [189] such that delamination occurs when

$$\sqrt{D_{a}\left[\left(\frac{{}^{n}\overline{\tau}_{23}}{{}^{n}S_{i}}\right)^{2}+\left(\frac{{}^{n}\overline{\tau}_{13}}{{}^{n}S_{i}}\right)^{2}+\left(\frac{{}^{n}\overline{\sigma}_{22}}{{}^{n}Y}\right)^{2}\right]} \geq 1 \qquad (3.115)$$

$$\begin{aligned} {}^{n}Y &= {}^{n}Y \quad \text{if } \overline{\sigma}_{22} \geq 0 \\ {}^{n}Y &= {}^{n}Y_{C} \quad \text{if } \overline{\sigma}_{22} < 0 \\ D_{a} &= 1.8 \end{aligned}$$

3.5.2. Mode dependent failure criteria for composite plies

Composite plies undergo complex damage modes because of their different underlying micromechanical aspects. Usually within the individual plies, damage can be in the form of fibre breakage, matrix cracking or fibre-matrix interface damage. In the present damage evolution and progression analysis of the composite plies, 3D Hashin damage failure criterion [198] is used which is a mode dependent failure criteria accounting for the individual failure modes of the fibres and the matrix in addition to providing the critical strength parameters. The conditions for failure to occur according to Hashin failure criterion is as follows:

1. Fibre failure in tension $(\sigma_1 \geq 0)$

$$\left(\frac{\sigma_1}{X_T}\right)^2 + \frac{\tau_{12}^2}{S_{12}^2} + \frac{\tau_{13}^2}{S_{13}^2} \geq 1 \tag{3.116}$$

2. Fibre failure in compression $(\sigma_1 < 0)$

$$\left(\frac{\sigma_1}{X_C}\right)^2 \geq 1 \tag{3.117}$$

3. Matrix failure in tension $(\sigma_2 + \sigma_3 \geq 0)$

$$\frac{(\sigma_2 + \sigma_3)^2}{Y_T^2} + \frac{\tau_{23}^2 - \sigma_2\sigma_3}{S_{23}^2} + \frac{\tau_{12}^2}{S_{12}^2} + \frac{\tau_{13}^2}{S_{13}^2} \geq 1 \tag{3.118}$$

4. Matrix failure in compression $(\sigma_2 + \sigma_3 < 0)$

$$\left[\left(\frac{Y_C}{2S_{23}}\right)^2 - 1\right]\left(\frac{\sigma_2 + \sigma_3}{Y_C}\right) + \frac{\left(\sigma_2 + \sigma_3\right)^2}{4S_{23}^2} + \frac{\tau_{23}^2 - \sigma_2\sigma_3}{S_{23}^2} + \frac{\tau_{12}^2}{S_{12}^2} + \frac{\tau_{13}^2}{S_{13}^2} \geq 1 \tag{3.119}$$

where $\sigma_1, \sigma_2, \sigma_3, \tau_{12}, \tau_{13}$ and τ_{23} are the normal and shear stress components in the local (or material) coordinate system of the concerned ply. X_T, X_C and Y_T, Y_C are the tensile and compressive strengths of the ply in the longitudinal and transverse direction respectively and the shear strengths are S_{12}, S_{23} and S_{13}.

If the components of the undamaged material stiffness matrix $[C]$ are denoted by C_{ij}^o, and failure occurs for the inner composite plies based on Hashin damage criteria, then the in-situ material stiffness matrix can be progressively degraded to give the degraded stiffness matrix as follows:

The damage variables d_f and d_m are evaluated as

$$d_f = 1 - \left(1 - d_{ft}\right)\left(1 - d_{fc}\right) \text{ and } d_m = 1 - \left(1 - d_{mt}\right)\left(1 - d_{mc}\right) \tag{3.120}$$

where d_{ft}, d_{fc}, d_{mt} and d_{mc} are set to 1 when the respective failures occur according to the damage modes discussed in Eq. (3.116-3.119) viz. fibre failure in tension and compression and matrix failure in tension and compression respectively. The components of the degraded stiffness matrix is evaluated as

$$C_{11} = \left(1 - d_f\right) C_{11}^0 \tag{3.121.a}$$

$$C_{22} = \left(1 - d_f\right)\left(1 - d_m\right) C_{22}^0 \tag{3.121.b}$$

$$C_{33} = \left(1 - d_f\right)\left(1 - d_m\right) C_{33}^0 \tag{3.121.c}$$

$$C_{12} = \left(1 - d_f\right)\left(1 - d_m\right) C_{12}^0 \tag{3.121.d}$$

$$C_{23} = \left(1 - d_f\right)\left(1 - d_m\right) C_{23}^0 \tag{3.121.e}$$

$$C_{13} = \left(1 - d_f\right)\left(1 - d_m\right) C_{13}^0 \tag{3.121.f}$$

$$G_{12} = \left(1 - d_f\right)\left(1 - s_{mt} d_{mt}\right)\left(1 - s_{mc} d_{mc}\right) G_{12}^0 \tag{3.121.g}$$

$$G_{23} = \left(1 - d_f\right)\left(1 - s_{mt} d_{mt}\right)\left(1 - s_{mc} d_{mc}\right) G_{23}^0 \tag{3.121.h}$$

$$G_{31} = \left(1 - d_f\right)\left(1 - s_{mt} d_{mt}\right)\left(1 - s_{mc} d_{mc}\right) G_{31}^0 \tag{3.121.i}$$

The constants s_{mt} and s_{mc} are the loss control factors for shear stiffness due to matrix failure in tension and compression respectively. In the present study, the values of s_{mt} and s_{mc} are taken as 0.9 and 0.5 respectively [198]. From the degradation model of GLARE, the energy threshold of the target can be ascertained in addition to the resistance of the target to delamination at the metal/composite interfaces as well as the inner interfaces subjected to a LVI at a certain energy.

3.6. Repeated LVI by a rigid spherical impactor

The repetitive impact on a clamped GLARE plate is done by considering LVIs by a rigid spherical impactor striking at the same location. In order to analyse repetitive LVIs, the contact parameters associated with the projectile and the target needs to be updated so that in the event of another impact, the dynamic responses are correctly evaluated. This is necessary in the analysis of repetitive LVIs where the target may suffer damage due to the first impact leading to dents or indentation of the outer aluminium layer near the impact site as illustrated in **Figure 3.15**. In addition to delamination at the interfaces, by considering the damage for the inner composite plies (refer **Section 3.5**), the plate stiffness may decrease affecting the overall contact stiffness of the impactor-target system (refer Eq. (3.94-3.96)). But at the same time, the surficial dent will also affect the stiffness parameter because of the change in the approach geometries of the target relative to the impactor. This creates a complex relationship between global stiffness state of the target plate and the local stiffness at the contact site and thus require an inclusive approach in updating the parameters of the contact. The following sub-steps are augmented in the modelling of the LVI of GLARE by spherical impactors before the commencement of the second impact event:

- Note the maximum, $\alpha_{\max}$ corresponding to $f_N^{\max}$.
- Consider the impactor to be rigid and the indentation occurs only on the GLARE target due to the permanent plastic deformation of the top aluminium layer at the impact site.
- The radius of curvature of the indented surface is evaluated by [199]

$$R_2 = R^o \frac{k_l \alpha_{\max}^{3/2}}{f_N^{\max}} \tag{3.122}$$

- Evaluate the updated contact stiffness k_l (Eq. (3.88)) between the spherical impactor and the plate considering the effective radius of curvature at the indented site as

$$k_l = \frac{4}{3}\sqrt{R^o_{Effective}}\,E^* \tag{3.123}$$

  where the effective radius is given by [200]

$$R^o_{Effective} = \left[\frac{1}{R^o} + \frac{1}{R_2}\right]^{-1} \tag{3.124}$$

- It is to be noted that for the two contacting bodies, a convex curvature is considered to be positive while a concave curvature is taken as negative.
- Update the values of the variables in **Section 3.4.2**.

The above sub-steps are implemented for any arbitrary mass impactors having different velocities and accordingly the impact parameters pertaining to the geometrical aspects of the impact system are updated as discussed in **Section 3.5**.

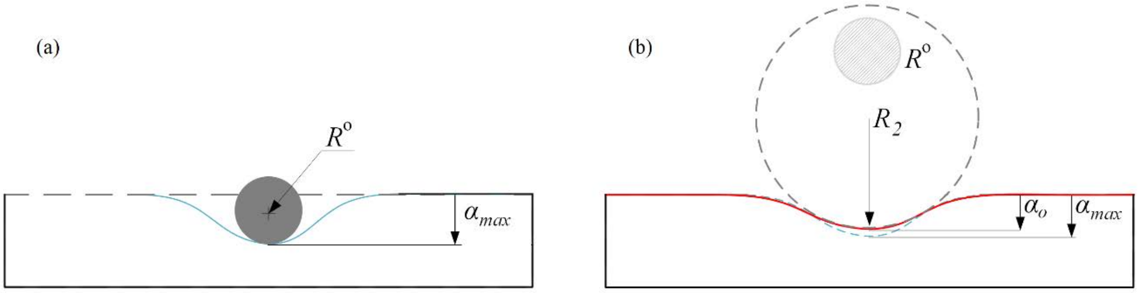

Figure 3.15: (a) First impact event by a spherical impactor on a flat target and (b) second impact event with initial dent at the impact location

3.7. Summary

The present chapter has discussed a complete method to investigate the LVI responses of a GLARE plate subjected to LVI by rigid projectiles.

The present analysis of LVI on GLARE focuses on the modelling of the impact by a rigid projectile, focused mainly for a spherical impactor at arbitrary obliquities for which the normal and tangential contact models are considered based on the Hertz theory and the theory of Mindlin and Deresiewicz respectively. Furthermore, the generic methodology for the dynamic response of the target on account of LVI enables to evaluate the contact impact response for different mass impactors and seamless integration for impact by impactors having different geometry (in the present case LVI by cylindrical impactors) incorporating the appropriate contact model. Furthermore, the multiple as well as repetitive impacts can be studied based on the current model. Considering solid elements in the present FE formulation, all six components of stress can be evaluated. The interface stresses can be accurately estimated by applying appropriate interpolation to assess the delamination at the interfaces.

Chapter 4

Normal spherical impact on GLARE

This chapter covers the LVI responses of GLARE due to impact by spherical impactors. A transient dynamic 3D FE code incorporating Newmark-β method and Hertzian contact law is used for simulating the contact impact of a rigid projectile on a clamped target. Both single and multiple normal impacts have been analysed and the effects of important parameters on the impact responses and associated delamination have been presented.

4.1. Introduction

Even though the influence of impact energy on the low velocity impact of laminated plate has been reported by many researchers, the influence of the mass of the impactor relative to the target has not been addressed extensively. In the present chapter, an effort is made to investigate the impact response of a clamped GLARE plate subjected to spherical impacts by varied masses exploring the other associated factors like the impactor velocity and the target plate size in concurrence with the impactor mass. Keeping note of the superior impact characteristics of GLARE laminates, the LVI responses of different GLARE configurations are explored including hybrid configurations to compare the impact responses.

4.2. Validation of the FE code

Based on the formulations described in **Chapter 3**, a 3D FE code has been developed in C for the analysis of LVI on GLARE. For the dynamic analysis, the clamped plate boundary conditions are as described in **Figure 4.1**. The appropriate selection and refinement of the mesh is essential for correctly evaluating the impact responses and contact forces. To ensure proper mesh selection for the LVI analysis, the mesh is refined in steps from 10×10×2 elements up to 32×32×2 elements. The different meshed GLARE plates are then subjected to a central LVI by a ϕ10 mm diameter steel spherical impactor at 10 m/s, and the time step increment is kept the same for all cases ($\Delta t = 1\mu s$). **Figure 4.2** shows the contact force variations and the impactor displacements for the different mesh sizes. The coarser mesh of 10×10×2 elements shows a stiffer response, and as the mesh becomes finer, the contact force peaks and the impactor displacement converge to a similar pattern. It is seen that increasing the mesh size from 24×24×2 to 32×32×2 does not show further variation in the LVI responses.

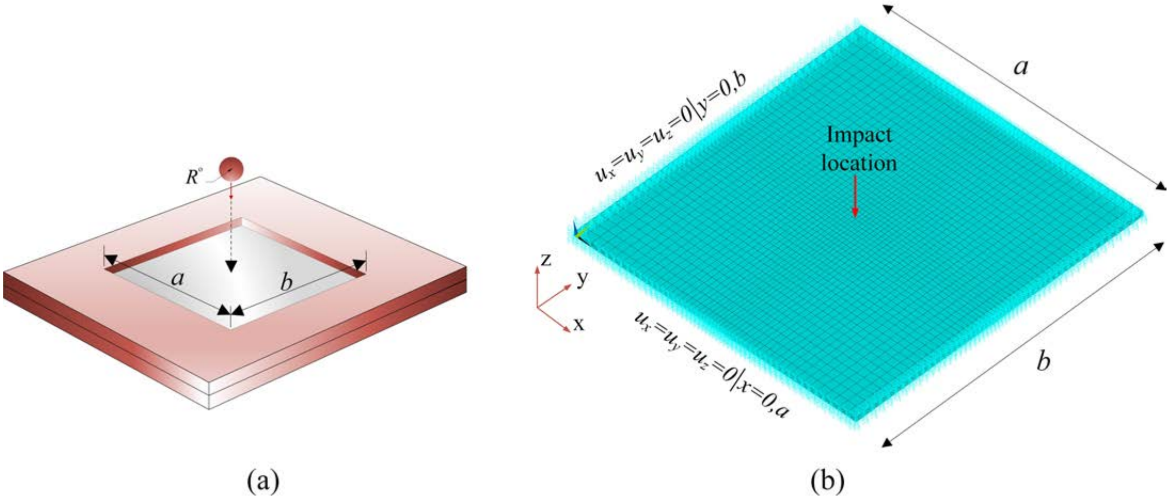

Figure 4.1: (a) Spherical impactor striking a clamped GLARE plate and (b) Typical meshed geometry and boundary conditions for a clamped plate

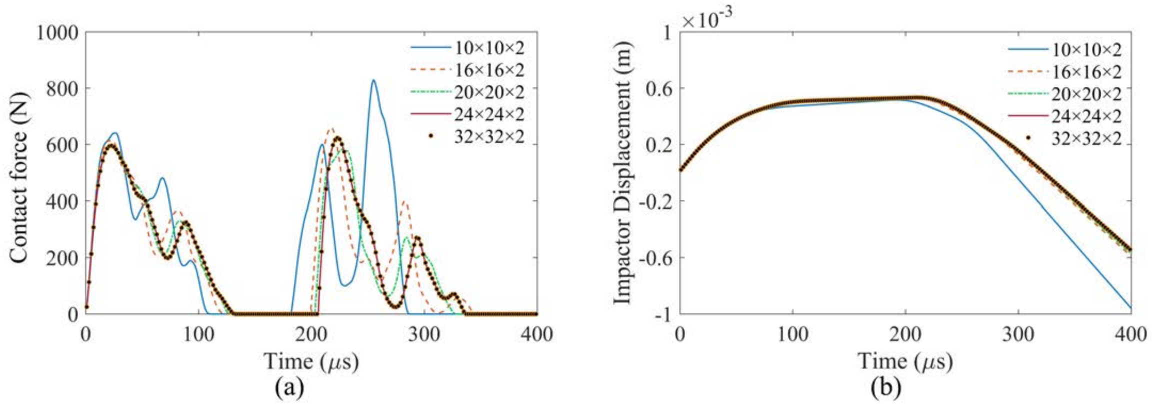

Figure 4.2: (a) Contact force and (b) impactor displacement for different mesh sizes

To validate the code for smaller mass impacts [201], the contact force history obtained by Wu and Chang [186] for a clamped $[0/\text{-}45/45/90]_{2S}$ graphite/epoxy plate having dimension 76.2 mm × 76.2 mm × 2.54 mm and impacted normally by a 12.7 mm diameter steel sphere (E=200 GPa and ρ=7800 kg/m^3) at 12.7 m/s is compared with that obtained using the present code. For comparison purposes, all the data in the imperial system of units were converted to the SI system of units to account for the uniformity of the scale used throughout the system. Following the work of [186], the material properties for the considered graphite/epoxy laminate are: $E_1 = 145.41$ GPa, $E_2 = 9.997$ GPa, $G_{12} = 5.689$ GPa, $\rho = 1535.681$ kg/m^3 and $\upsilon_{12} = \upsilon_{23} = 0.3$. For the dynamic analysis, a 32×32×2 mesh was found to be suitable with a time step of $\Delta t = 1\mu s$ and the plate boundary conditions are as described in **Figure 4.1**. **Figure 4.3(a)-(d)** compares the contact force history, impactor displacement and velocity and plate centre displacement in both FPS and SI units. From the comparisons, the obtained results are found to be in excellent agreement with the results of Wu and Chang [186].

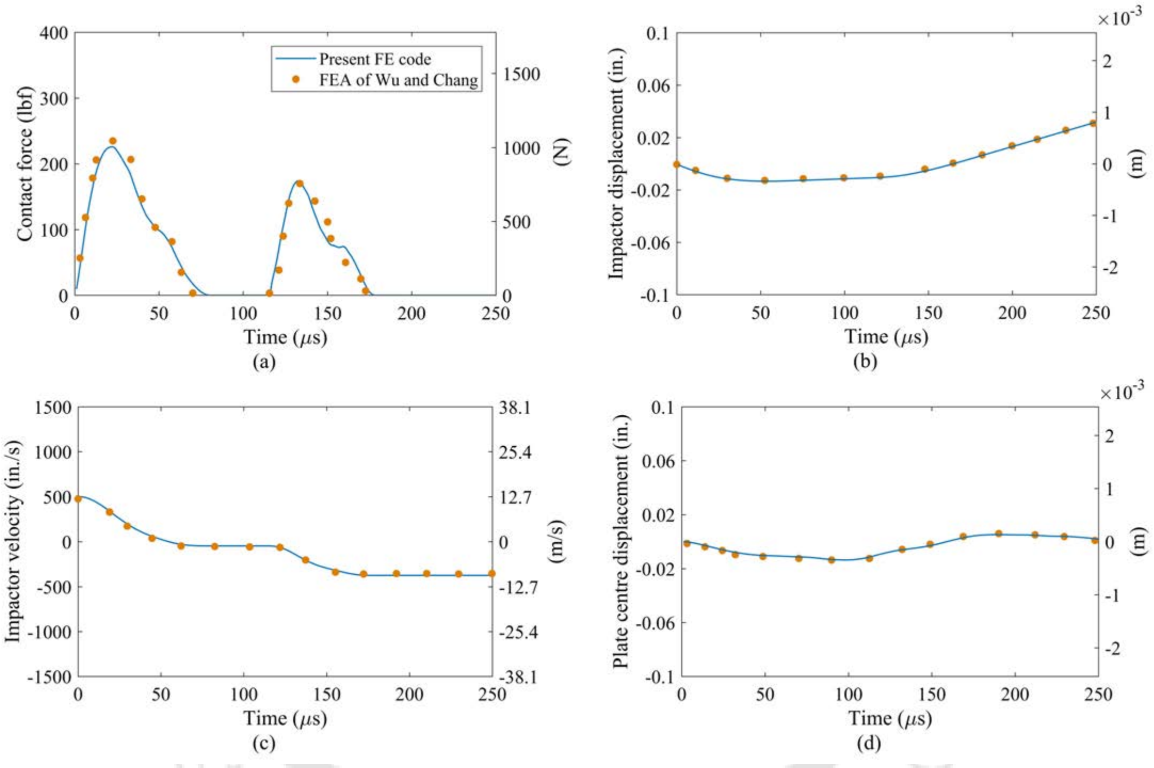

Figure 4.3: Contact force, displacement and velocity compared with results of Wu and Chang [186] for a $[0/{-45}/45/90]_{2S}$ graphite/epoxy laminate

In case of an impact by an impactor having larger mass than the mass of the plate, the present code is validated by comparing the contact force history obtained by Bienias et al. [202] as shown in **Figure 4.4(a)**. The impact test was done as per ASTM D7136 standard on a GLARE-2/1 plate having two composite layers with stacking sequence of [0/90] with each layer of thickness 0.25 mm and the 2024-T3 aluminium layers are 0.5 mm thick, taking the GLARE plate thickness to 1.5 mm. A drop weight impact tester with a 12.7 mm diameter hemispherical steel impactor and a mass of 2.01 kg strikes the 125 mm × 75 mm GLARE plate clamped at all edges with an impact energy of 10J. The plate mesh and the boundary conditions are as described in **Figure 4.1(b)** except for now $a = 75$ mm and $b = 125$ mm.

Following the work of [202], the material properties for the R-glass/epoxy plies of the laminate are: $E_1 = 46.43$ GPa, $E_2 = 14.92$ GPa, $G_{12} = 5.233$ GPa, $\rho = 2560$ kg/m^3, $\upsilon_{12} = 0.269$ and $\upsilon_{23} = 0.089$. It could be seen from **Figure 4.4(a)** that the present code evaluates the contact force in good agreement with the published result. Furthermore, in order to estimate the accuracy in evaluating the internal damage in proximity to the impact region, delamination at the interfaces is evaluated by the present code. As observed from **Figure 4.4(b)**, an elliptical delaminated region can be seen representative of the cumulative delamination at the interfaces and this is in close approximation to that obtained by Bienias et al. [202] with approximately 15% mismatch in their aerial spread.

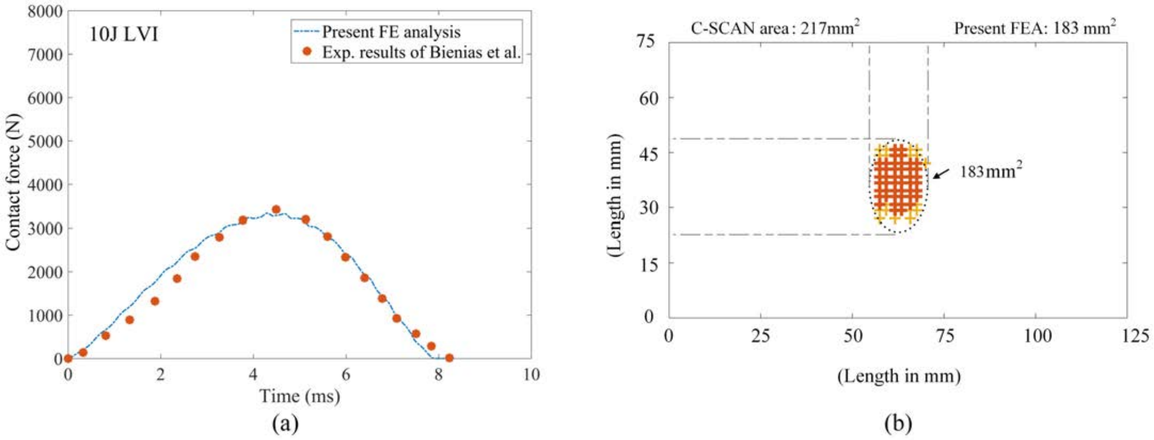

(a)

(b)

Figure 4.4: (a) Validation of contact force history for a 10 J impact on a GLARE 2/1 plate and (b) Delamination at the Al/glass fibre interface for impact by a 2.01kg spherical impactor [202]

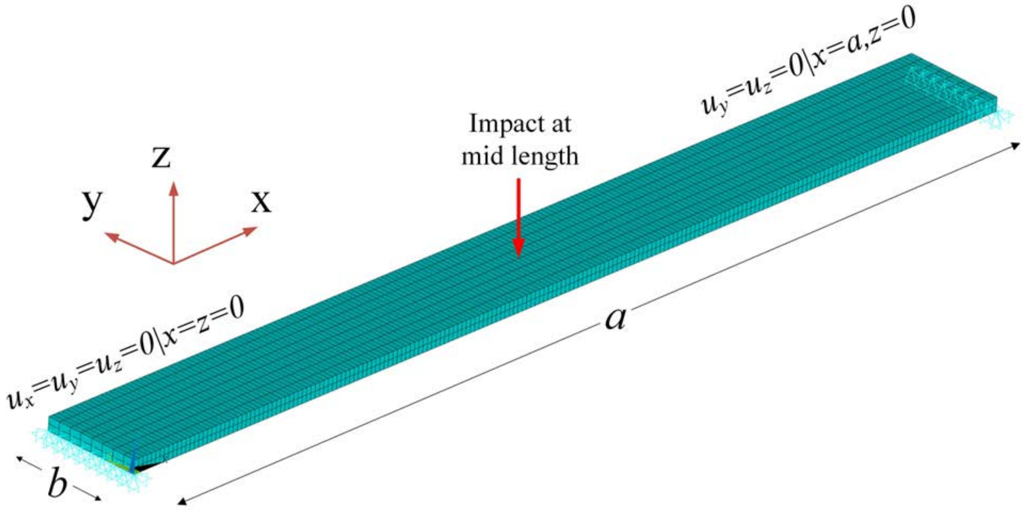

Figure 4.5: Impact by a steel sphere at 20m/s on a simply supported $[0/90/0/90/0]_S$ carbon/epoxy beam [203]

In order to confirm the correctness of the impact response for elastic-plastic impacts, the present code is validated with the works of Christoforou and Yigit [203] for the impact by a 12.7 mm diameter steel spherical impactor at 20 m/s on a $[0^{\circ}/90^{\circ}/0^{\circ}/90^{\circ}/0^{\circ}]_S$ T300/934 carbon/epoxy simply supported beam of span 200 mm and width 20 mm (refer **Figure 4.5**). The material properties of an individual lamina of the carbon/epoxy laminate are: $E_1 = 120$ GPa, $E_2 = 7.9$ GPa, $G_{12} = G_{23} = 5.5$ GPa, $\rho = 1580$ kg/m^3 and $\upsilon_{12} = \upsilon_{23} = 0.3$. The thickness of each individual lamina is 0.269 mm and the steel impactor is having a mass of 8.537 g. It can be seen from **Figure 4.6** that the obtained contact force history is in good agreement with the published results.

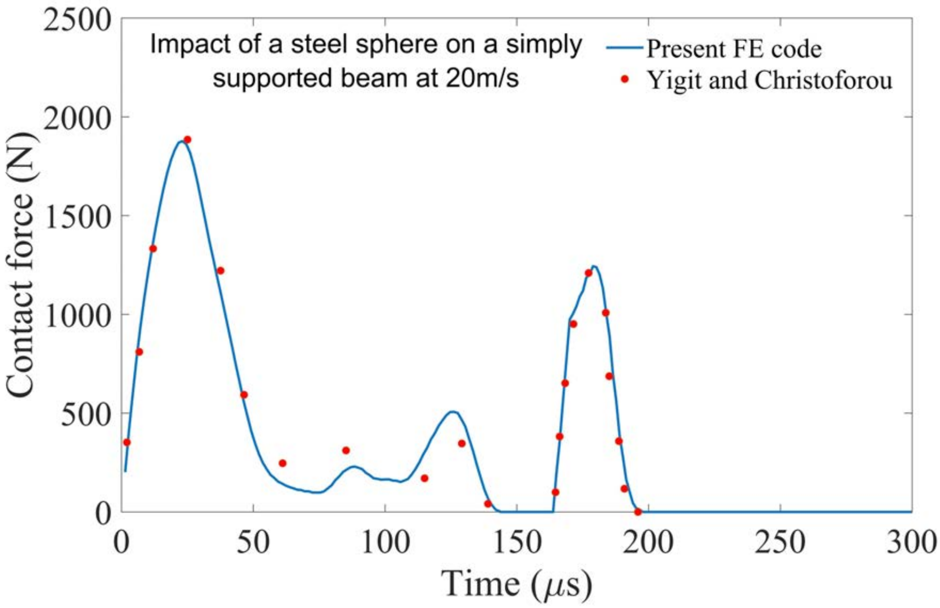

Figure 4.6: Contact force history for a simply supported carbon/epoxy beam for a central impact at 20m/s [203]

4.3. GLARE plate subjected to LVI by different mass impactors

The present section investigates the impact response of a clamped GLARE plate subjected to spherical impacts by varied masses exploring the other associated factors like the impactor velocity and the target plate size in concurrence with the impactor mass. The aim is to study the influence of impactor mass (relative to the plate) on the response of a clamped GLARE plate subjected to low-velocity normal impact at lower energies. In the present study, impact on the top surface of a clamped square GLARE 4-3/2 plate by rigid spherical impactors having different masses relative to the target plate mass has been considered. An illustration of the impact system is shown in **Figure 4.1 (a)**. In the present study, the plate is considered to be clamped on all sides between two rigid blocks with a cut out of dimension $a \times b$ and a spherical impactor strikes normally at the centre. **Figure 4.1 (b)** shows the meshed geometry along with the boundary conditions used in the LVI analysis for impact at the plate centre.

4.3.1. Problem definition

The present analysis is done on clamped square GLARE 4-3/2 plates with the spherical steel impactors having varied masses ranging from 0.016 kg to 2.05 kg striking the GLARE plates normally at the centre. **Table 4.1** lists all the material properties of GLARE [45,102,138] and

Table 4.2 shows the strength parameters where the subscripts n and i refer to the interfacial strengths in the normal and shear directions [204–206]. Using the present FE code developed, the effect of certain parameters namely the plate dimensions and impactor velocity in concurrence with changing impactor mass have been studied for the dynamic response of the clamped plates and the associated delamination at the interfaces is assessed for LVI at 1.2 J.

Table 4.1: Material properties [45,102,138]

Parameter	Notation	Al 2024-T3 alloy	UD S2-glass/FM94-epoxy prepregs	Steel
Density (kg/m^3)	ρ	2780	1980	7800
Poisson's ratio	υ	0.33	$\upsilon_{12} = 0.33, \upsilon_{23} = 0.33$	
Young's modulus (GPa)	E	72	$E_1 = 55, E_2 = 9.5$	200
Shear Modulus (GPa)	G	——	$G_{12} = 5.5, G_{23} = 3.5$	
Yield strength (MPa)	σ_{ys}	340	——	
Transverse tensile strength (MPa)	Y_T	——	50	
Transverse compressive strength (MPa)	Y_C	——	160	
In plane shear strength (MPa)	S_{lt}	——	70	

Table 4.2: Interface strengths [204–206]

Interfacial strengths	S2-glass/FM94-epoxy interfaces	S2-glass/FM94-epoxy and Aluminium 2024-T3
S_n (MPa)	43	40
S_i (MPa)	50	40

The layup detail of the GLARE 4-3/2 plate is as shown in **Figure 4.7** and two plate geometries are considered viz. a 0.125 m × 0.125 m (Plate A) and a 0.16 m × 0.16 m (Plate B). The steel impactors of different masses are having a tup diameter of 0.008 m and strike the plate at different velocities such that they impact with the same energy in all the cases.

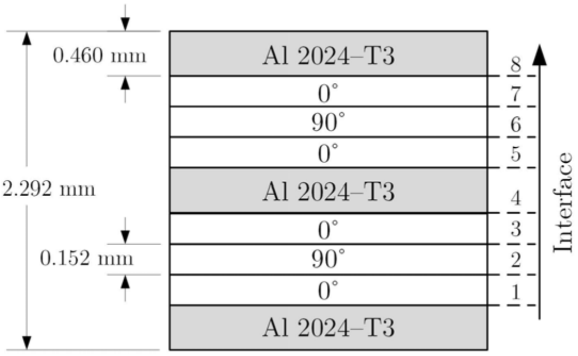

Figure 4.7: GLARE 4-3/2

4.3.2. Effect of impactor mass

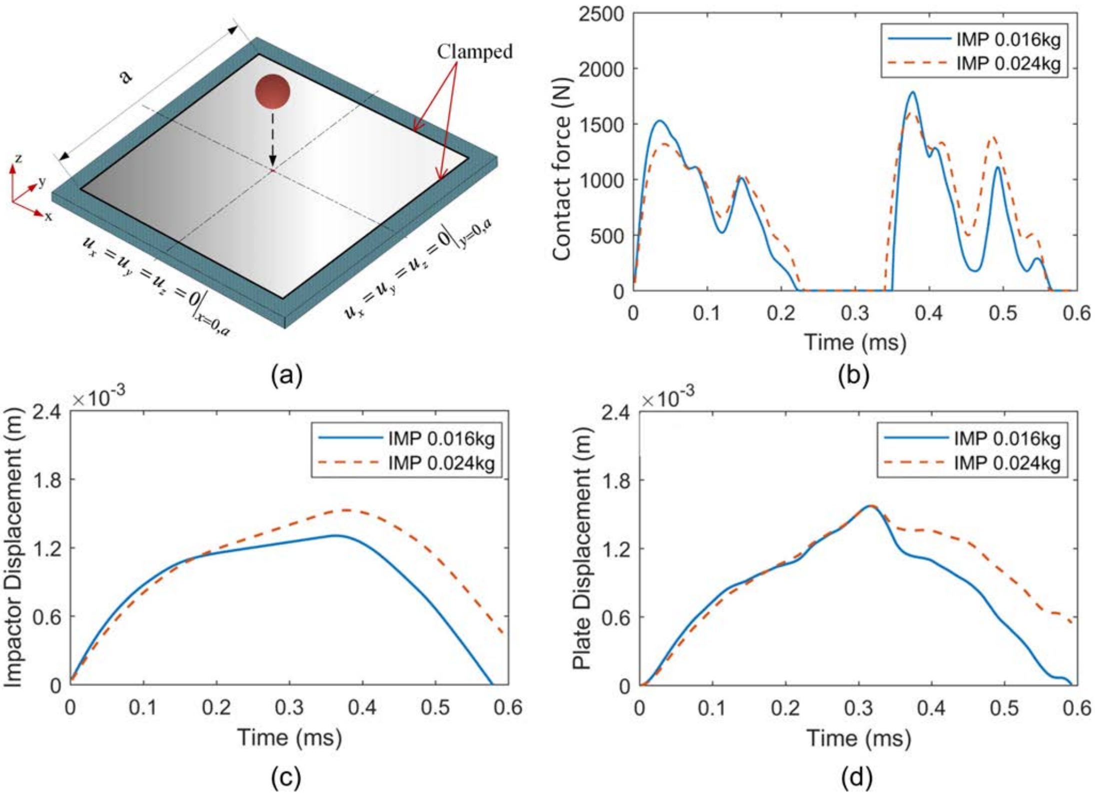

Figure 4.8: LVI on plate A by spherical impactors having mass much less than the plate mass

In order to investigate the effect of impactor mass relative to plate mass on the dynamic response due to LVI, plate A is struck normally at the centre by impactors with different masses such that they range from small mass impact regime to impacts by masses much higher than the target plates. It is seen from **Figure 4.8** and **Figure 4.9** that for the same impact energy, when the impactor mass is much lower than the mass of the target plates, the contact duration is very less. As the impactor mass increases the contact duration increases and the response transitions to a quasi-static case when the impactor mass is considerably higher than the target plate mass. As can be seen from **Figure 4.8(b)** and **Figure 4.9 (a)** and **(d)**, the peak contact force is relatively higher when the impactor masses fall within the small mass range. As the impactor/plate mass ratio increases, such that the impactor mass range transitions from small mass impacts to large mass impacts, there is a slight reduction in the peak contact force. However, within a certain impactor mass range, the contact force peaks are more or less similar.

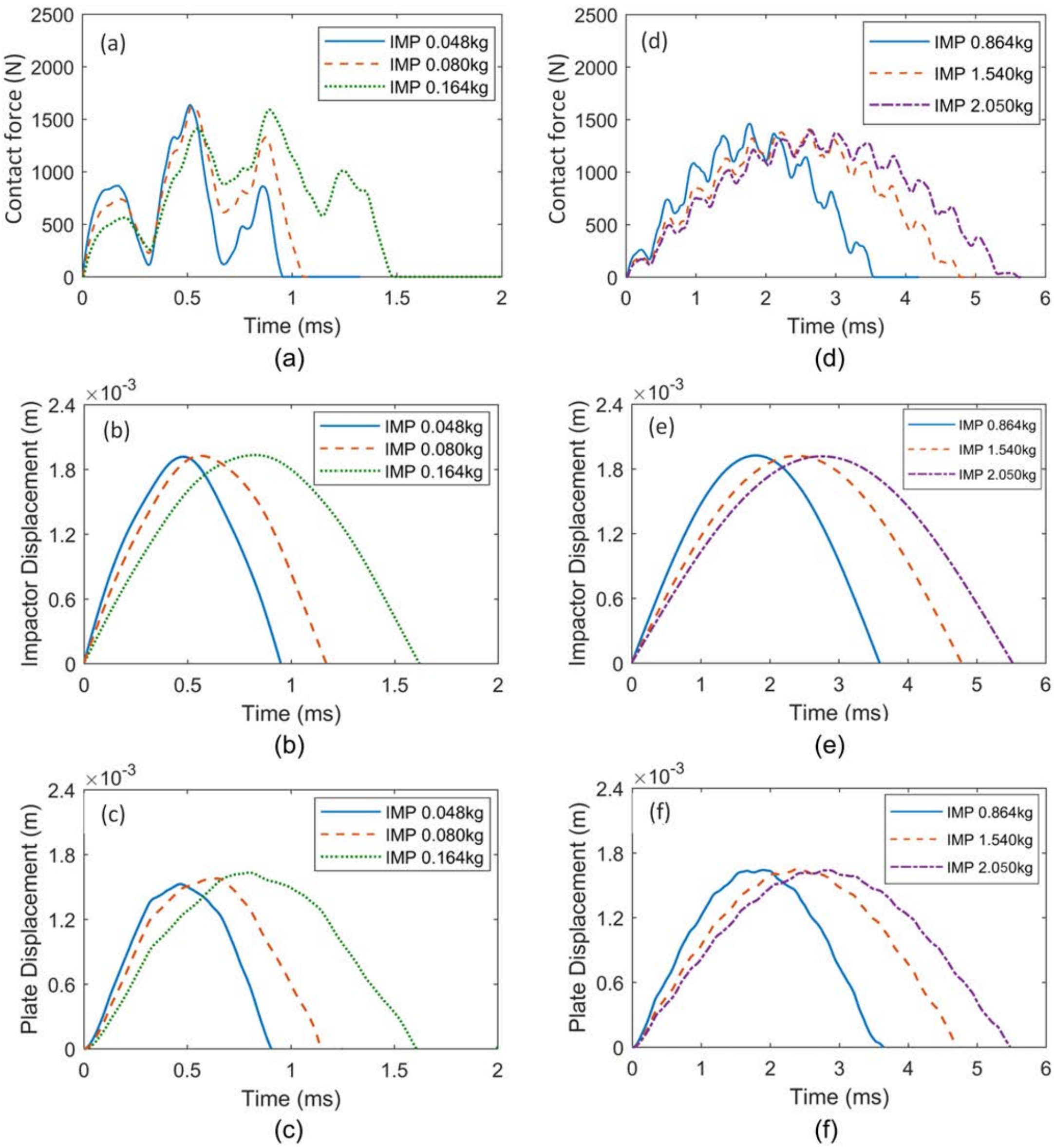

Figure 4.9: LVI by intermediate and larger mass impactors on plate A

For impactors having masses in close proximity to the plate mass, a transitional region of impactor mass exists relative to the plate mass where the contact response is complex in nature (**Figure 4.9(a)-(c)**) and as observed the peaks attained are comparable to the low mass impacts. From the contact response, it is observed that there are sharp drops followed by steep rise in the contact force response. This may be attributed to higher vibration modes that might occur in concurrence with the fundamental vibration mode leading to higher peaks in contact force than in the case for large mass impacts. For the impactors with mass much larger than the plate mass the contact responses are mostly governed by the plate structural response and is affected by the plate geometry and plate boundary conditions. Therefore, in case of the large mass LVIs, the global plate deflection of the target plate leads to a slight reduction in the indentation compared to the localised response in case for small mass LVIs. For the various impactor mass ranges, a second peak occurs in the contact response after a zero contact force period for the small mass impacts. This is due to the fact that on being struck by the small mass impactor, the plate motion increases as well as the deflection.

Moreover, as seen from the impactor and plate displacement histories as in **Figure 4.8(b)-(c)**, at a certain instant of time, the plate deflection becomes more than the displacement of the impactor thereby loosing contact and resulting in zero contact force in case of the small mass impacts. Subsequently due to the plate flexure, the plate return back from its maxima position and comes in contact with the impactor again leading to reversal of the motion and rise of the second contact force due to the rebound behaviour. This is not seen for the case of the intermediate and high mass impactors and the force and displacements are in phase (**Figure 4.9 (b)-(c)** and **(e)-(f)**) and the contact remains throughout the impact duration until the end.

4.3.3. Effect of plate geometry

Figure 4.10(a)-(e) show the impact responses corresponding to plates A and B respectively for a lighter mass impactor of mass 0.016 kg striking them normally at the centre with a velocity of 12.1 m/s. Although the lateral dimensions of the plates are different, not much difference is seen in the maximum contact force attained for the first impact (as seen from **Figure 4.10(a)**) when impacted by the smaller mass impactor, whose mass is less than $\frac{1}{5}th$ the mass of the target plates. It is observed from the impact histories pertaining to the small mass impacts that the first impact peak and impact duration are almost the same for plates A and B. But for the second impact that occurs on account of the plate rebound, the instant of their occurrences as well the peaks attained are different. Therefore, in the case of the LVIs by the small mass impactors, the influence of the plate geometry on the dynamic response can be seen during its rebound behaviour.

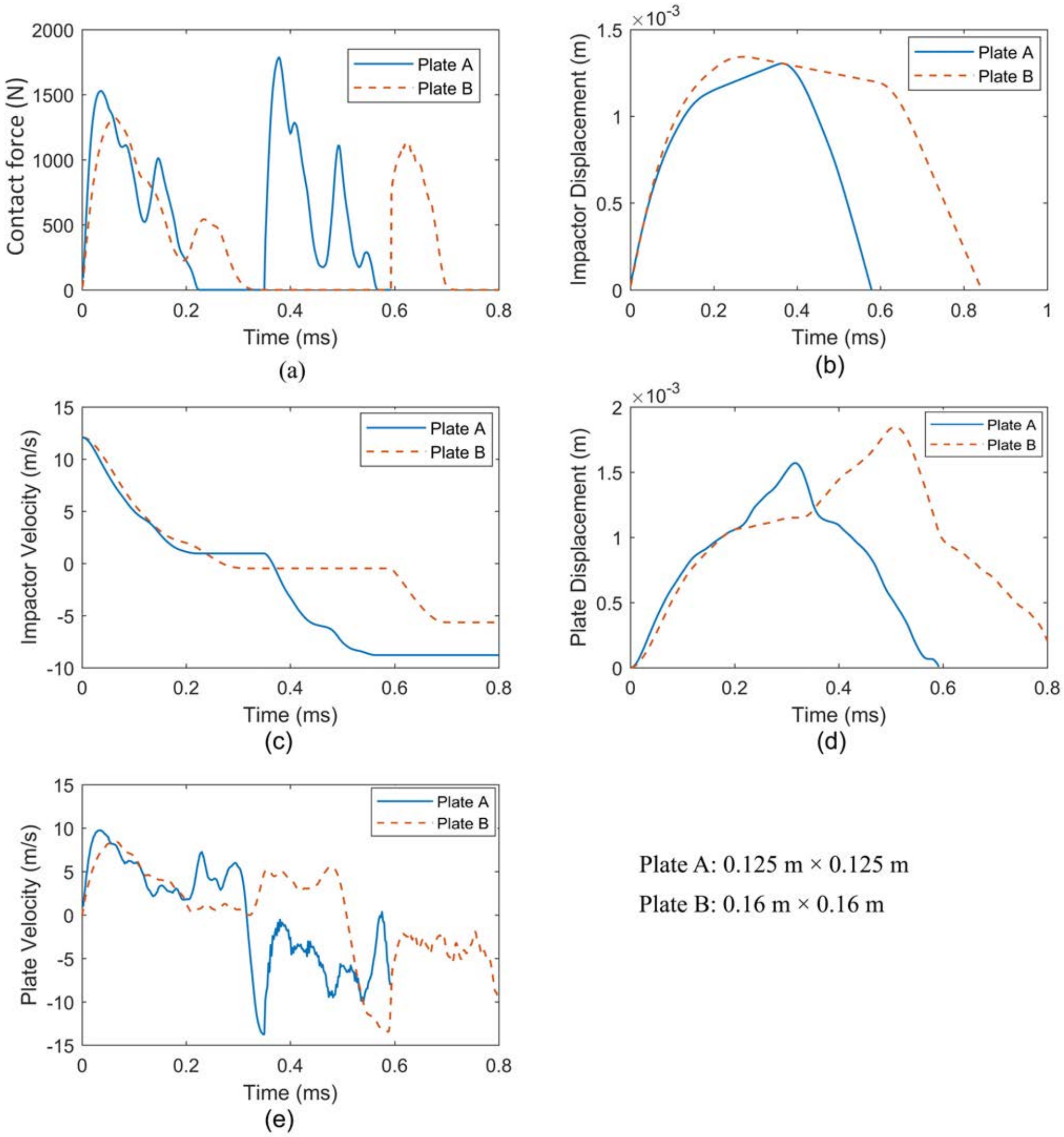

Figure 4.10: Impact response of the plates for LVI by an impactor of mass 0.016 kg at 1.2J

Figure 4.11(a)-(e) show the impact responses corresponding to plates A and B respectively when impacted by the larger mass impactors (0.864 kg and 2.05 kg), whose masses are much more than the mass of the plates. As discussed in the previous section, the impactor's contact duration is considerably longer when its mass is much more than the plate mass, and this type of impact can be termed as quasi-static in nature. The plate geometry influences the maximum contact force as plate B records the minimum contact force owing to its larger lateral dimension than plate A (refer **Figure 4.11(a)**). There is a continuous drop in impactor velocity as shown in **Figure 4.11(c)** unlike the case for the low mass impacts (**Figure 4.10(c)**). Moreover, the impactor and plate centre displacements are more or less of the same magnitude, and unlike in the case of the low mass impacts, the contact remains throughout the impact duration (**Figure 4.10(b)**, **(d)** and **Figure 4.11(b)**, **(d)**). The central deflection at the contact location is slightly more for the larger plate B due to its reduced flexural stiffness, which is clearly noticeable from **Figure 4.11(d)**. In addition, the difference in contact duration is comparable for both the plates along with the plate displacements in case of the impacts by larger mass impactors. For long-duration impacts of quasi-static in nature, the load and deflections are in phase, unlike the LVIs by smaller mass impactors and the dynamic responses are dependent on the plate geometry.

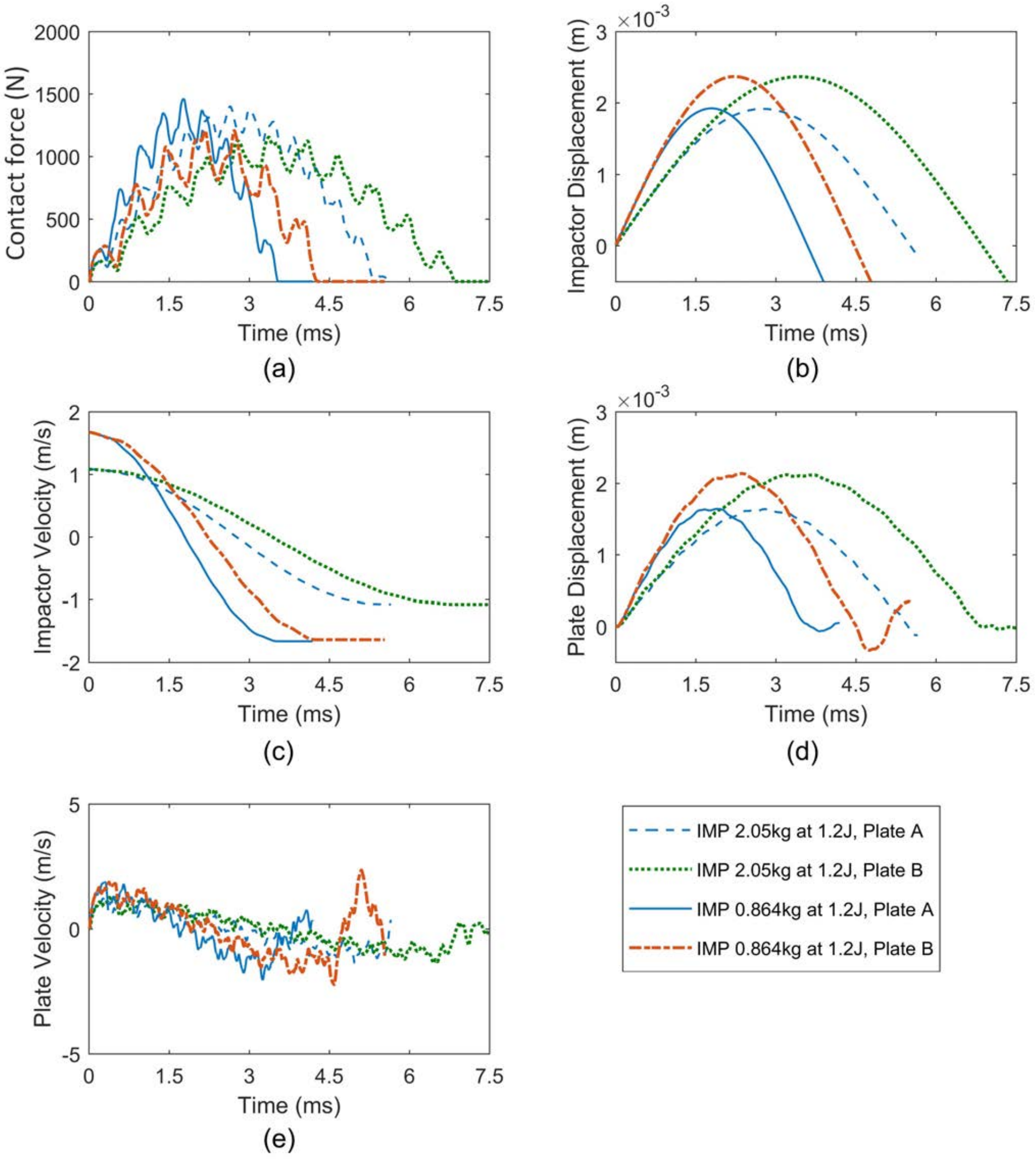

Figure 4.11: Impact response of the plates for LVI by impactors of much larger mass

4.3.4. Effect of change in impact energy

In the range of impactor mass considered, in order to study the effect of impactor energy (or impactor velocity), plate A is now impacted at a lower energy of 0.8 J by reducing the corresponding velocities of the different mass impactors and the peaks attained for the LVIs at different impactor masses are plotted in **Figure 4.12**. Also, in order to summarise the effect of plate dimension as discussed in **Section 4.3.3**, the plot shows the peaks attained by plates A and B for the impacts by the different impactors at 1.2 J. As already discussed, the peaks attained are lower for the impacts by the larger masses and there is a transitional range i.e. when the intermediate impactor masses are close to the target plate mass, there is an increase in the peak contact force compared to the peak loads attained in large mass impacts. Also, the plate B being larger in lateral dimensions, the contact force peaks attained are lower compared to those in plate A for the impacts occurring at same energies. This is because of the reduced flexural stiffness of the larger plate B leading to lower peaks in the contact force.

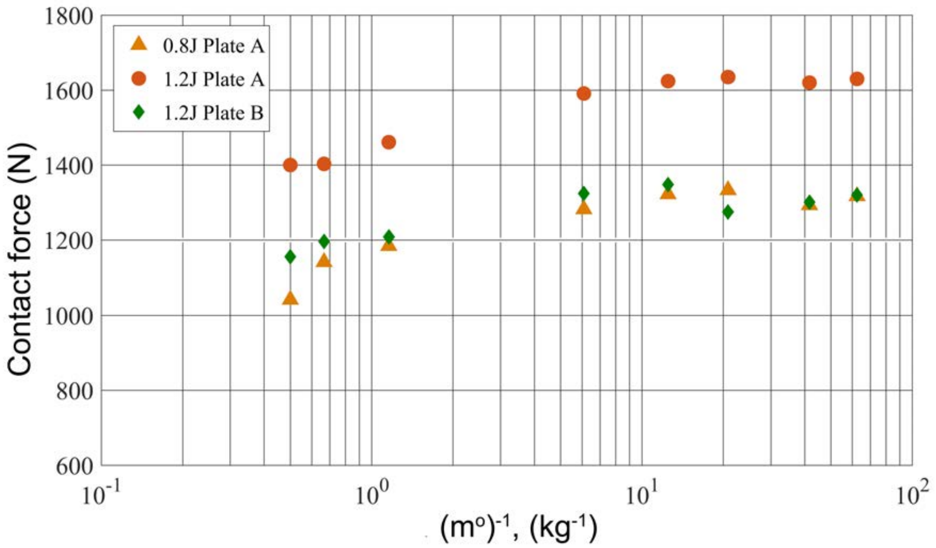

Figure 4.12: Variation of peak contact force with impactor mass for different impacting energy and plate size

Reducing the impactor velocities to change the impact energy from 1.2 J to 0.8 J do not alter the overall impact behaviour as can be seen from the contact response of plate A in **Figure 4.13**, although the magnitude of the contact forces would vary owing to the change in their corresponding impact velocities resulting in lower peaks at lower energies (refer **Figure 4.12**). This change in magnitude of the contact force can be attributed to the change in momentum of the impactor, thereby leading to a considerable change in the kinetic energy on account of reduced velocity. As shown in **Figure 4.13**, changing the impactor velocity does not affect the contact duration but the magnitude of the response as observed from the contact force histories for LVI by the lower (0.016 kg) and higher (0.864 kg) mass impactors striking plate A. Varying the impact energy from 1.2 J to 0.8 J by lowering their corresponding velocities do not change the trend of the contact response which is influenced by the impactor mass relative to the plate mass rather than the energy of the impact.

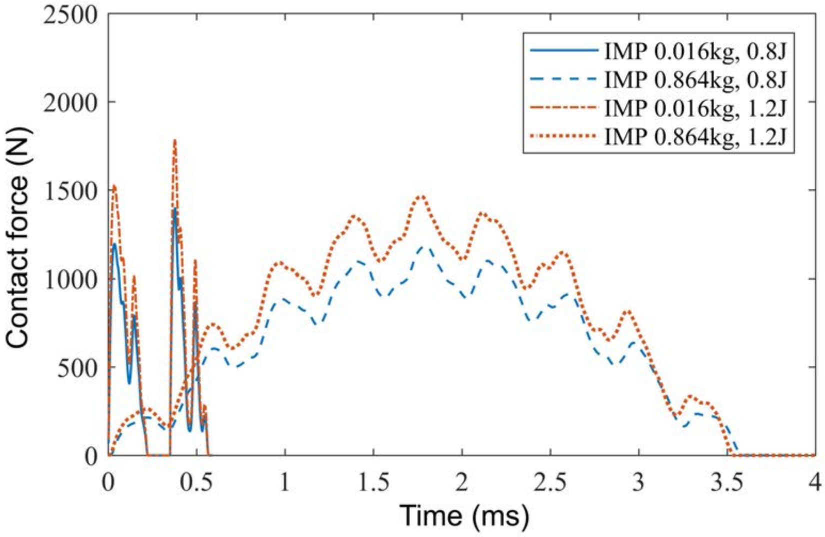

Figure 4.13: Effect of impact energy on the contact response of plate A

4.3.5. Interface stresses due to LVI by varied masses

In order to assess the delamination at the interfaces, it is necessary to determine the stresses that arise at the interfaces and how they vary with time. In case of short duration impacts by small mass, the stresses at the interfaces for such short impact times are generally wave controlled. **Figure 4.14** shows the stress wave for σ_y (due to LVI by 0.016 kg impactor) at the bottom aluminium/composite interface-1 for plate A, as it propagates from the impact location. It shows a more or less an elliptical wave pattern such that the stress is not of the same sign throughout the region and can be assumed to have a ripple as it propagates outward towards the boundary. On the contrary, in the case of large mass impacts (LVI by 0.864 kg impactor), a continuous variation of the stress at interface-1 can be seen as plotted for σ_y as shown in **Figure 4.15**. The stress distribution arising at the interface for this case can be attributed to the global plate deformation rather than the local response arising at the impact site.

Furthermore, to investigate the evolution of the interface stresses with time, the variation of σ_y, τ_{yz} and τ_{xz} at the bottom aluminium/composite interface-1 for plate A at arbitrary locations opposite to the impact site during the course of the impact is shown in **Figures 4.16- 4.17**. It can be seen that for the case of impact by the smaller mass impactor, the stresses attain maximum values just close to the time when the peak contact force occurs although the displacement at that instant is not maximum (refer **Figure 4.10** and **Figure 4.16**). This implies that the peak in the stress values is solely due to the local contact force and less likely being influenced by the global deflection of the target.

Moreover, it can be seen that, there is a change in the sign of stresses during the impact and the variation in the stress values at the different location follow different trend. This can be attributed to the fact that for impacts by smaller masses at relatively higher velocities causes a ripple wave to transmit through the target causing alternating stress states in the target site. Unlike the case for impacts by the smaller mass, in the case of impact by the heavier mass, it can be seen that the stress variation at the different arbitrary sites of interface-1 is in phase with the maximum plate deflection as well as the peak contact force and they attain the maximum values at the same time (refer **Figure 4.11** and **Figure 4.17**). Furthermore, there is negligible change in the stress states during the course of the impact and it can be noted that the stress evolution is mainly due to the global plate deflection. Similar trends were also observed in the case of plate B.

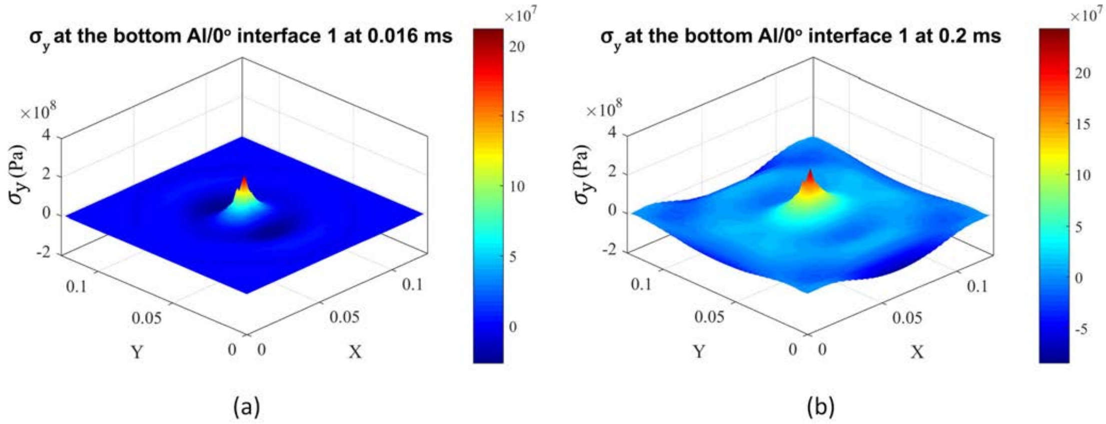

(a) (b)

Figure 4.14: Typical stress profile for LVI by a 0.016 kg impactor on plate A at 1.2J

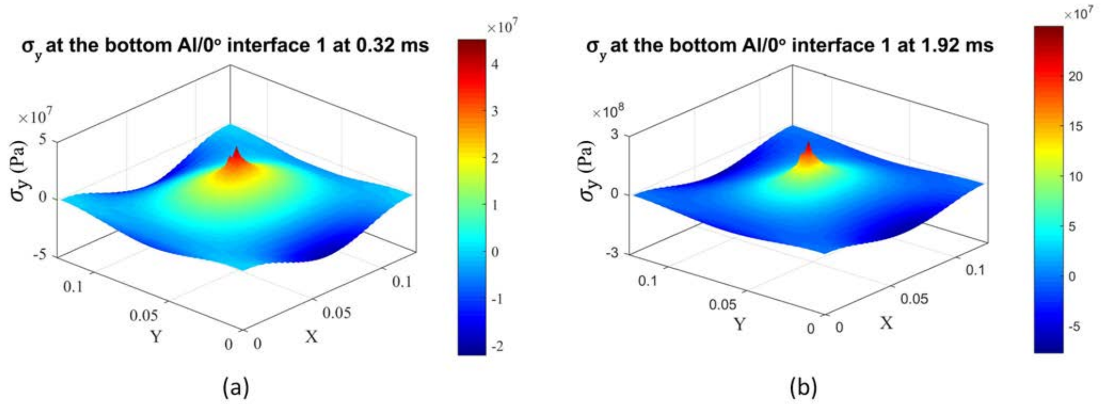

(a) (b)

Figure 4.15: Typical stress profile for LVI by a 0.864 kg impactor on plate A at 1.2J

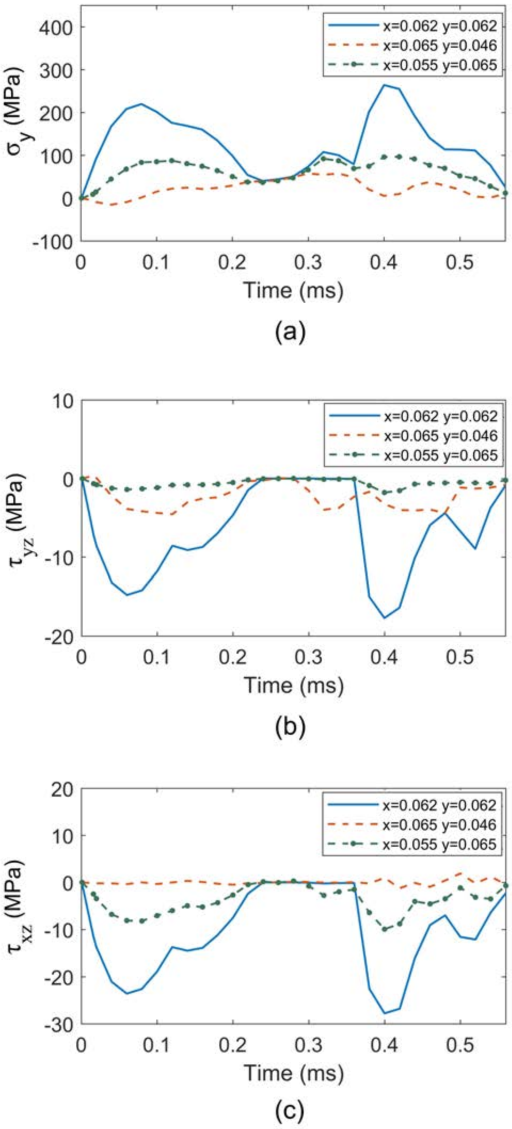

Figure 4.16: Variation of stresses at interface 1 due to impact by the smaller mass impactor of 0.016 kg on plate A at 1.2 J

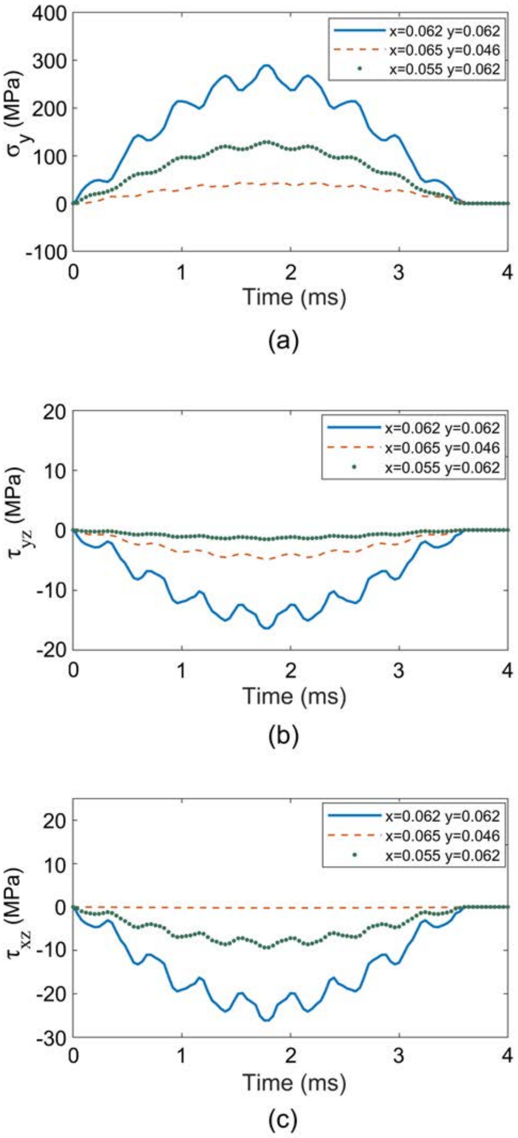

Figure 4.17: Variation of stresses at interface 1 due to impact by the larger mass impactor of 0.864 kg on plate A at 1.2 J

4.3.6. Delamination at the interfaces

The difference in variation of the stresses with time at the interfaces of the plates A and B due to the impacts by both the impactors, makes the assessment of delamination at the interfaces an important area to look into to estimate the extent of the damage incurred due to LVI.

Figures 4.18-4.19 show the delamination at the interfaces resulting from the impacts by the smaller mass impactor of 0.024 kg at 1.2 J and **Figures 4.20-4.21** show the delamination as a result of the quasi-static impact by the heavier mass impactor of 0.864 kg at 1.2 J for the plates A and B. It is seen that the extent of delamination at the interfaces is more for impact by the smaller mass impactor at a higher velocity than the quasi-static impact by the larger mass impactor for the same impact energy. In addition, the extent of delamination is maximum at the bottom aluminium/composite interface, followed by the top aluminium/composite interface. The extent of delamination at the inner glass/epoxy composite interfaces and the inner aluminium/composite interfaces is less and centred around the impacted region compared to the top and bottom metal/composite interfaces for all the cases, asserting the advantage of the outer aluminium layer in restricting the delamination growth at the inner interfaces, thereby protecting them.

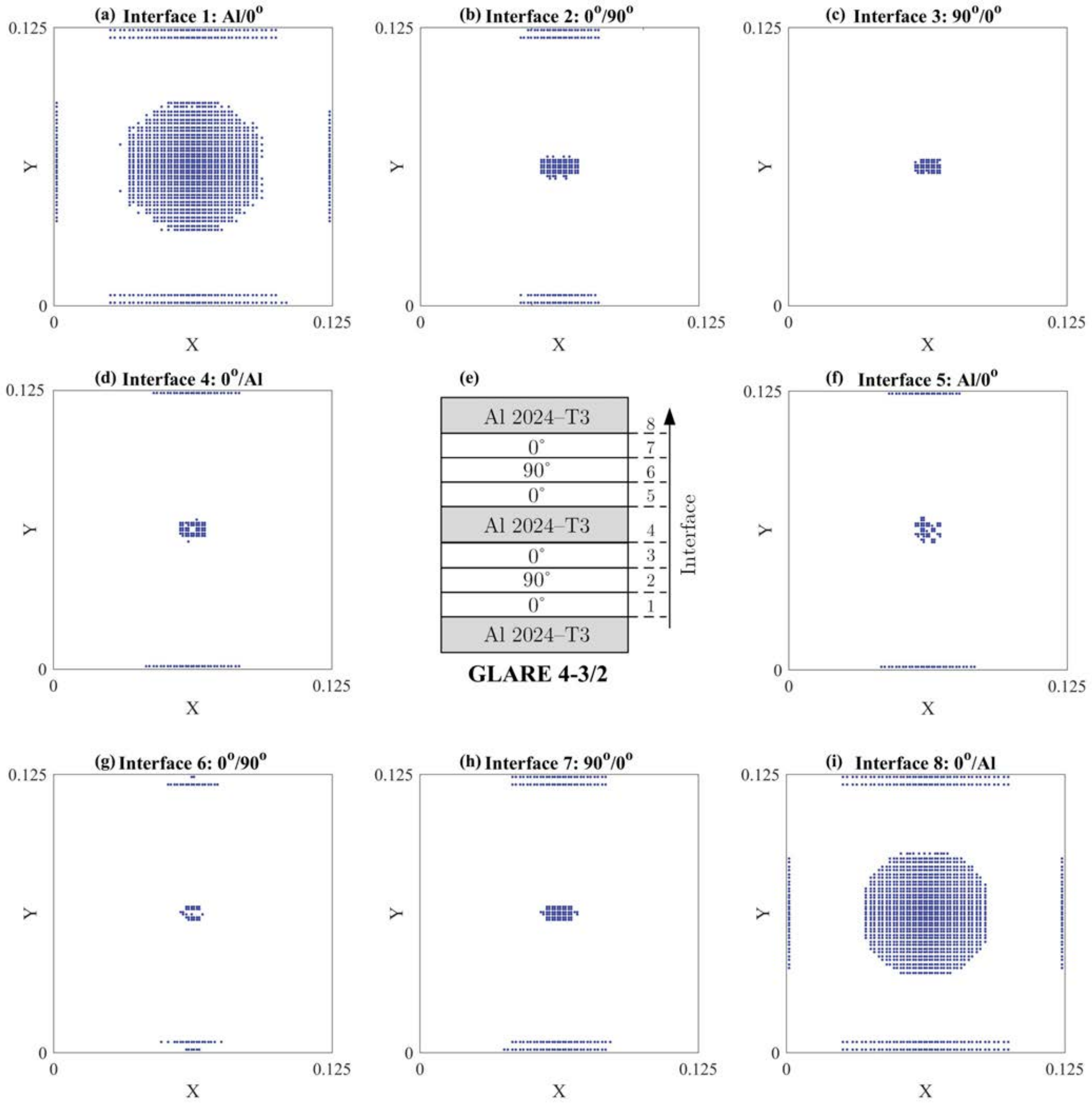

Figure 4.18: Interfacial delamination in plate A due to LVI by 0.024 kg impactor at 1.2 J

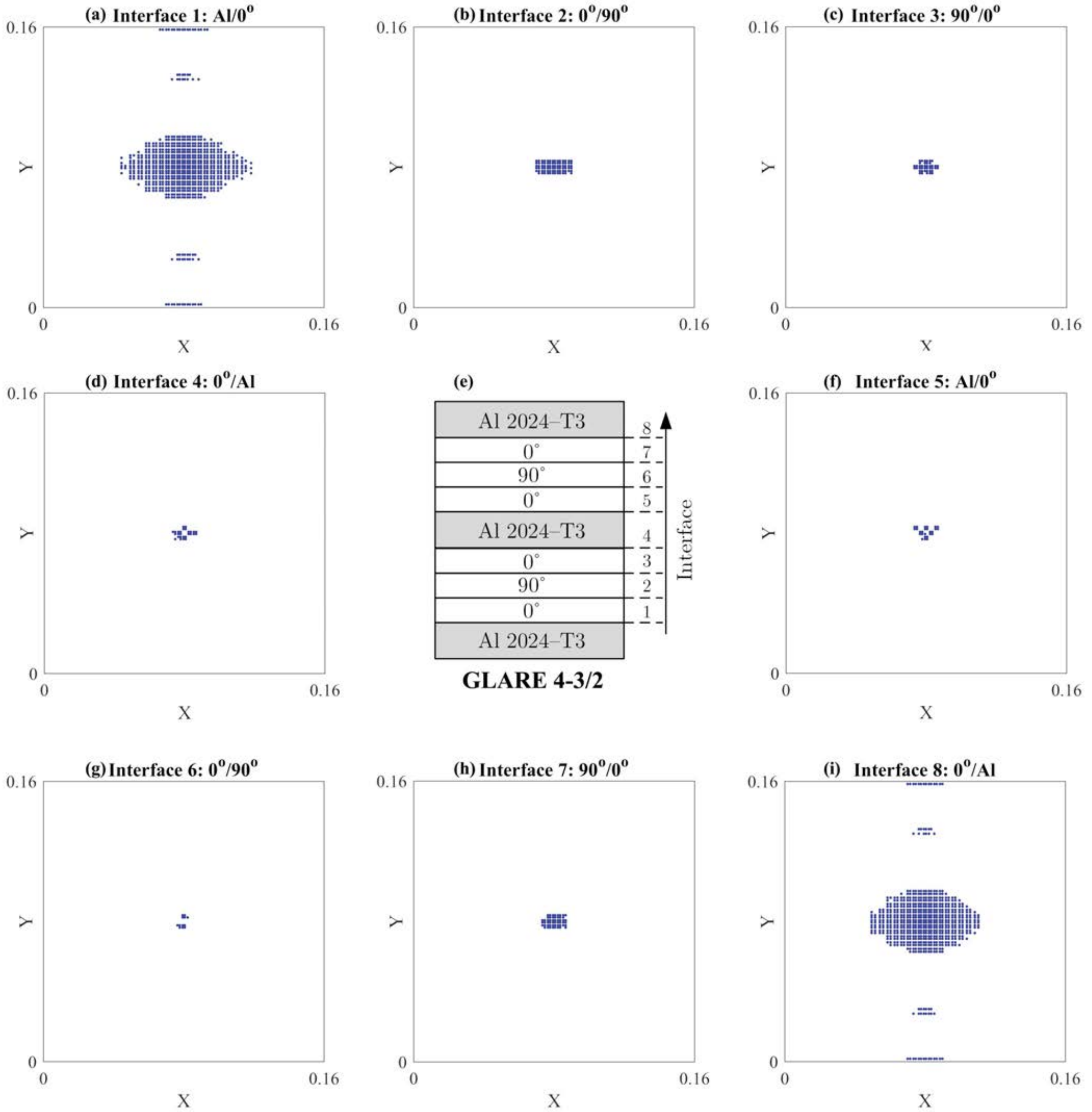

Figure 4.19: Interfacial delamination in plate B due to LVI by 0.024 kg impactor at 1.2 J

In case of the LVI by the smaller mass impactors on plate A, the delaminated region at the aluminium/composite interfaces are nearly circular in nature compared to the elliptical delaminated region for LVI by the larger mass impactor. For both the plates A and B, the major axis of the delaminated region at the aluminium/composite interfaces is aligned along the fibre direction of the underlying lamina in case of the LVI by the heavier impactor. Also, it is seen that for the larger plate B, due to its reduced flexural stiffness, the extent of delamination is less compared to that of plate A and the pattern of the delamination changes at the aluminium/composite interfaces for the case of LVI by the 0.024 kg impactor impacting at 1.2 J (refer **Figure 4.19**). This highlights the influence of the plate geometry in addition to the impactor to plate mass ratio in the evolution of interfacial delamination.

In the case of smaller mass impacts, although the delamination tends to propagate along the fibre direction of the underlying layer, it is more profound in case of the quasi-static impacts by the larger mass impactors occurring at lower velocities (refer **Figures 4.20-4.21**). In case of the LVI by the 0.864 kg impactor, the pattern of the delamination is similar for both the plates, although the extent of delamination is less for the larger plate B. This is because plate B is more compliant in undergoing the out-of-plane deflection on account of impact due to its reduced flexural stiffness owing to its larger dimensions (0.16 m × 0.016 m) compared to plate A (0.125 m × 0.125 m).

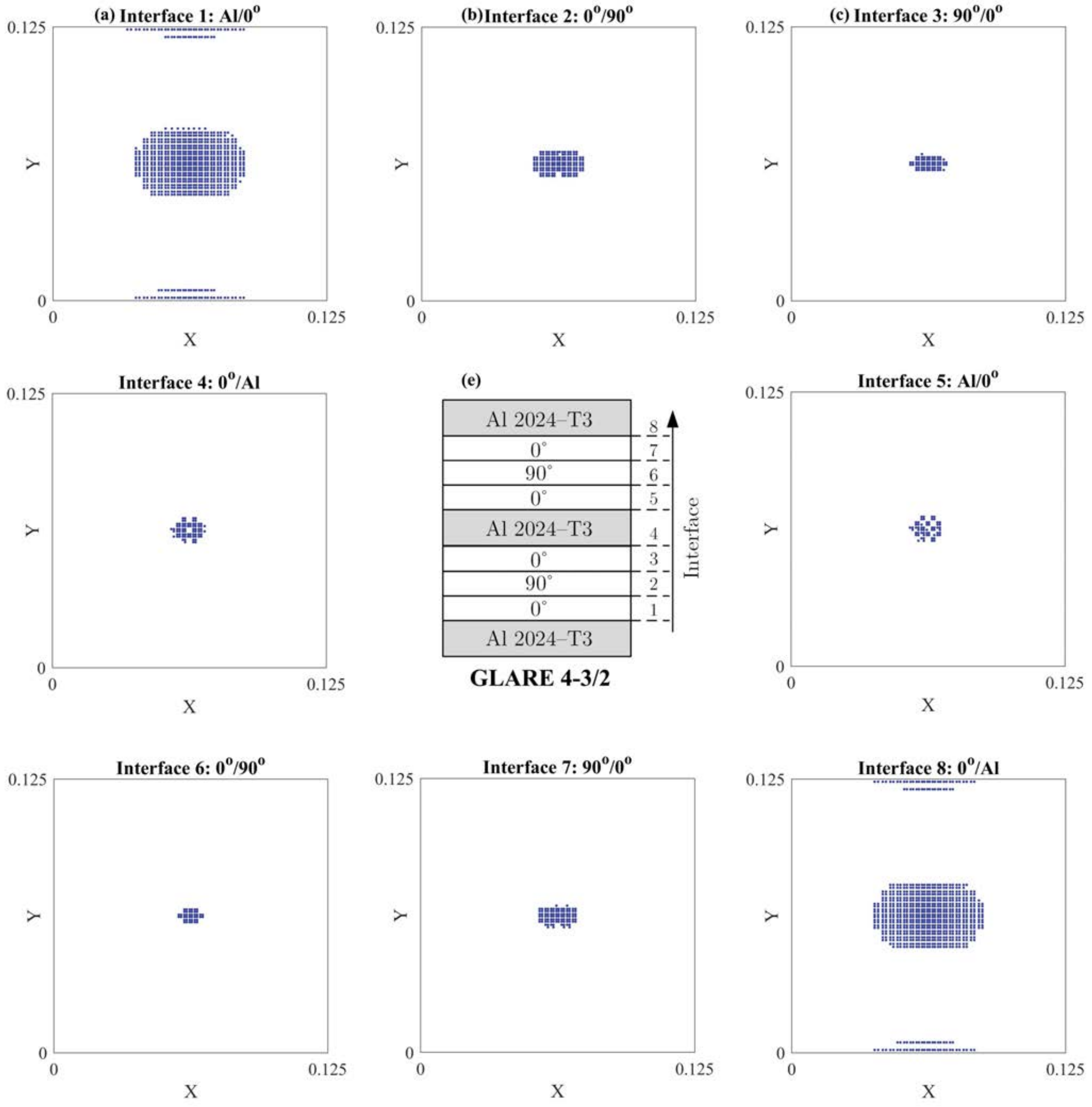

Figure 4.20: Interfacial delamination in plate A due to LVI by 0.864 kg impactor at 1.2J

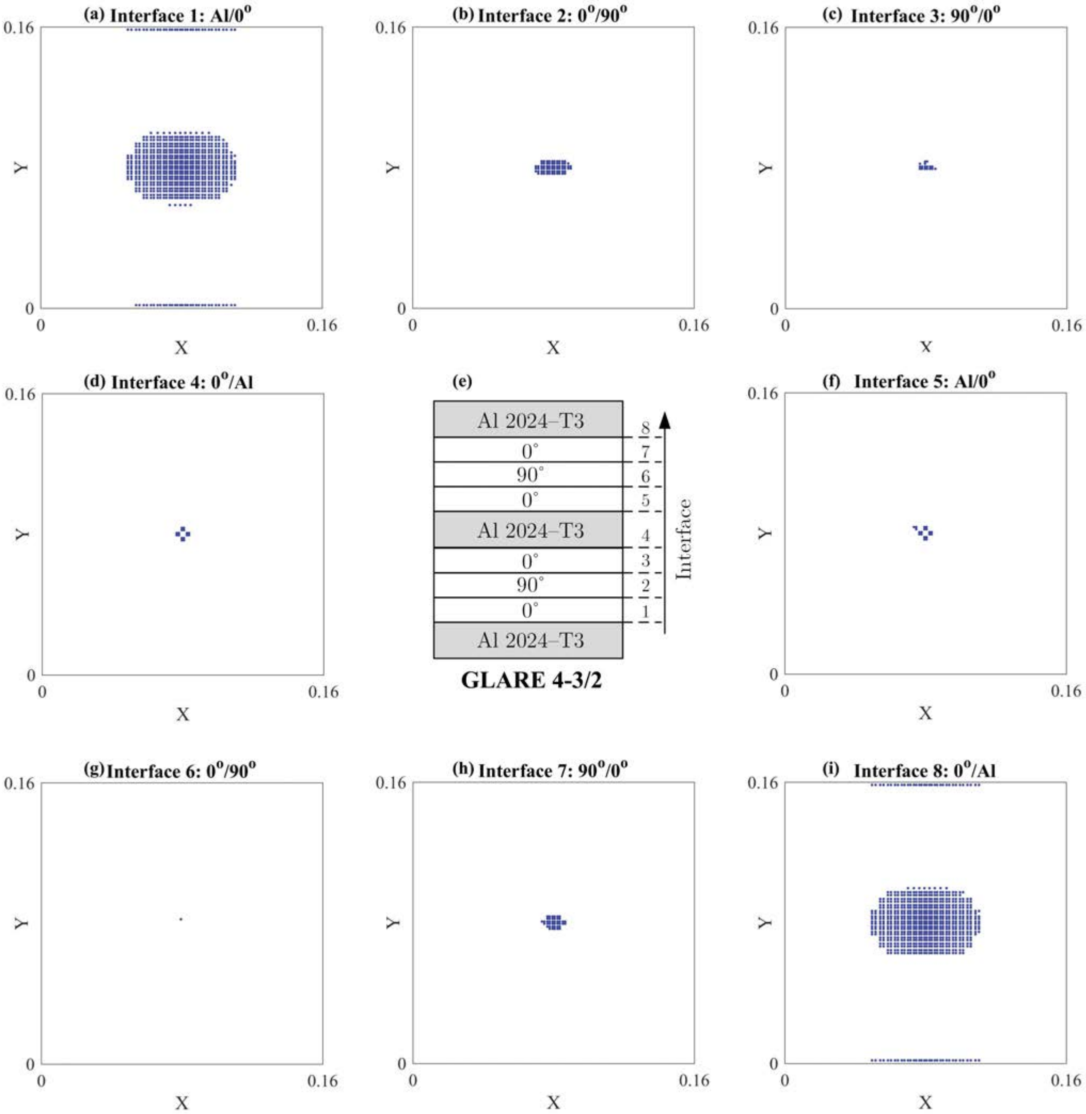

Figure 4.21: Interfacial delamination in plate B due to LVI by 0.864 kg impactor at 1.2J

4.4. LVI response of different GLARE configurations

In order to see the effect of the different GLARE configurations, two types of configurations are considered as shown in **Figure 4.22**. The interfaces are numbered in a bottom to top order with interface-1 being the bottom most and the considered target is having a square geometry with all sides clamped.

4.4.1. Problem definition

For investigating the LVI responses, 0.08 m × 0.08 m clamped GLARE plates are impacted normally at the centre by a 10 mm diameter spherical steel impactor at different velocities. The material properties of aluminium and unidirectional S2-glass/FM94-epoxy composites are listed in **Table 4.1** [45,102,138].

Table 4.2 [204–206] shows the strength parameters, where the subscripts n and i refer to the interfacial strengths in the normal and shear directions. The out of plane shear value is taken to be same as the in-plane shear. The different types of GLARE plates considered (A1, A2, A3, B, C1, C2) are listed in **Table 4.3** and they are studied to understand the effect of important parameters like thickness of aluminium layers and laminate configurations on the impact response. In addition, three different impactor velocities viz. 8 m/s, 10 m/s and 12 m/s are considered to study the effect of impactor velocities on the impact response and delamination of GLARE.

Table 4.3: GLARE plates with different configurations

GLARE Type	**Stacking sequence**	**Plate Code**	**Aluminium thickness (mm)**	**S2-glass/ FM94-epoxy ply thickness (mm)**	**Total thickness (mm)**
GLARE 5-2/1	$[\mathrm{Al}/0^{\circ}/90^{\circ}]_S$	A1	0.489	0.146	1.562
		A2	0.584	0.146	1.752
		A3	0.620	0.146	1.824
GLARE 4-3/2	$[\mathrm{Al}/0^{\circ}/90^{\circ}/0^{\circ}/\overline{\mathrm{Al}}]_S$	B	0.304	0.152	1.824
GLARE 5-2/2	$[\mathrm{Al}/0^{\circ}/(90^{\circ})_2/0^{\circ}]_S$	C1	0.328	0.146	1.824
GLARE 2/1	$[\mathrm{Al}/0^{\circ}/\pm45^{\circ}/90^{\circ}]_S$	C2	0.328	0.146	1.824

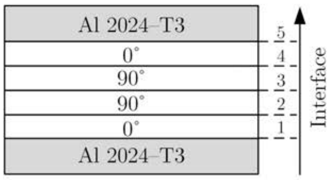

(a) GLARE 5-2/1

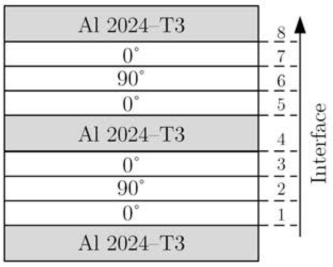

(b) GLARE 4-3/2

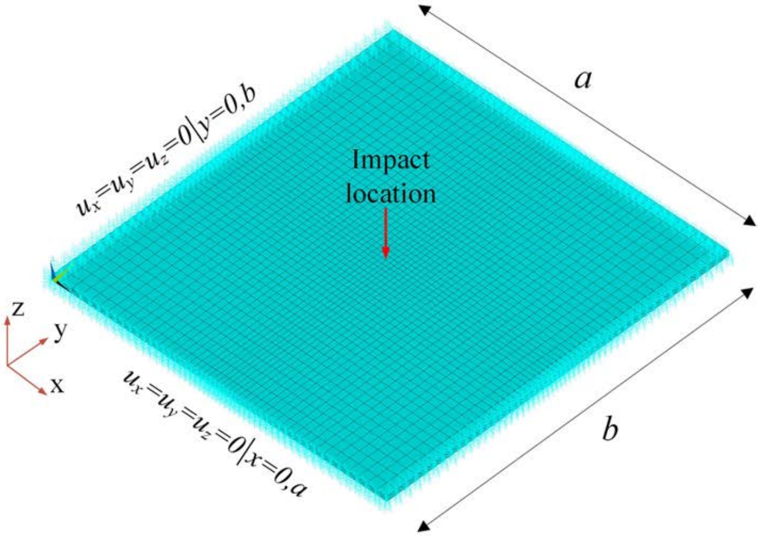

(c) Clamped plate meshed geometry

Figure 4.22: (a) GLARE 5-2/1 (b) GLARE 4-3/2 and (c) meshed geometry of a clamped plate

4.4.2. Impact responses of GLARE 5-21 and GLARE 4-3/2

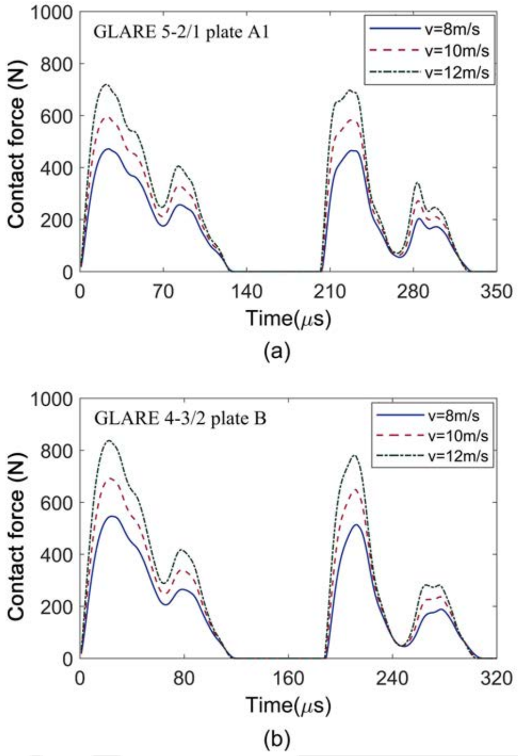

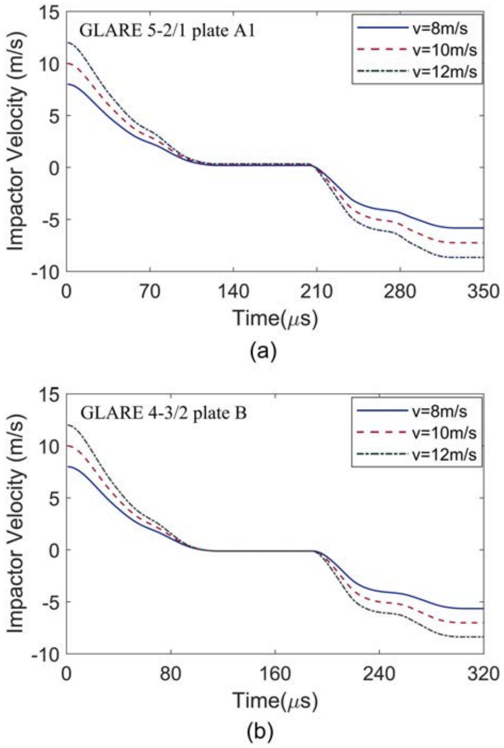

Figure 4.23: Comparison of contact forces between GLARE plates A1 and B

Figure 4.24: Comparison of impactor velocities between GLARE plates (a) A1 and (b) B

The impact responses are evaluated for the clamped GLARE plates viz. A1 and B to understand their relative behaviour when subjected to normal impact of a steel spherical impactor at the centre. **Figure 4.23 (a)** and **(b)** show the contact force histories of the GLARE plates A1 and B respectively subjected to LVIs at three different velocities. It is seen that with increasing impactor velocities the contact force increases. As can be seen, the overall contact force duration is slightly more for GLARE 5-2/1 plate A1 as compared to GLARE 4-3/2 plate B.

The maximum value of contact force is more for GLARE 4-3/2 (plate B) as compared to GLARE 5-2/1 (plate A1) for a given impactor velocity implying that GLARE 4-3/2 is relatively stiffer than GLARE 5-2/1. Even though this is expected due to more number of layers in GLARE plate B but it will be interesting to see how the delamination at the interfaces compare for these two GLAREs. **Figure 4.24 (a)** and **(b)** show the impactor velocities as functions of time for the GLARE plates A1 and B respectively. After the first impact has occurred there is period for which the velocity of the impactor remains zero as observed from **Figure 4.24** which corresponds to the zero contact force period (refer **Figure 4.23**). The rise in contact force is seen for the second time after the plate reverses its direction of motion and makes contact again with the spherical impactor. The negative velocity of the impactor, as seen in the latter part of **Figure 4.24** implies that the motion is in the opposite direction.

The displacements of the impactor and the plate centre during impact are shown in **Figure 4.25** and **Figure 4.26** for both GLARE 5-2/1 and GLARE 4-3/2 plates A1 and B respectively. Similar to the contact force history, it is seen that the displacements show an increasing trend with increasing impactor velocities. From **Figures 4.25-4.26**, it is observed that the impactor displacement remains greater than the plate centre displacement during the contact period and vice versa for the case of zero contact force. GLARE 4-3/2 being stiffer than GLARE 5-2/1, their plate centre displacements are lesser for the same impactor velocity as can be observed from **Figure 4.26 (a)** and **(b)**.

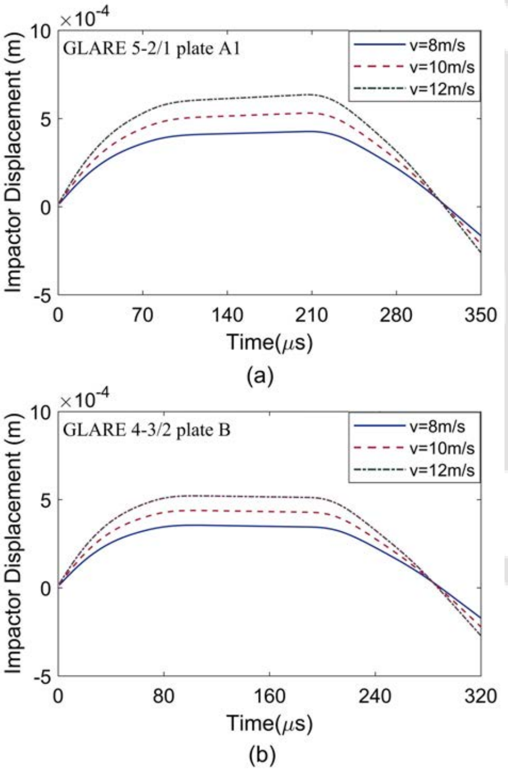

Figure 4.25: Impactor displacements of GLARE plates (a) A1 and (b) B

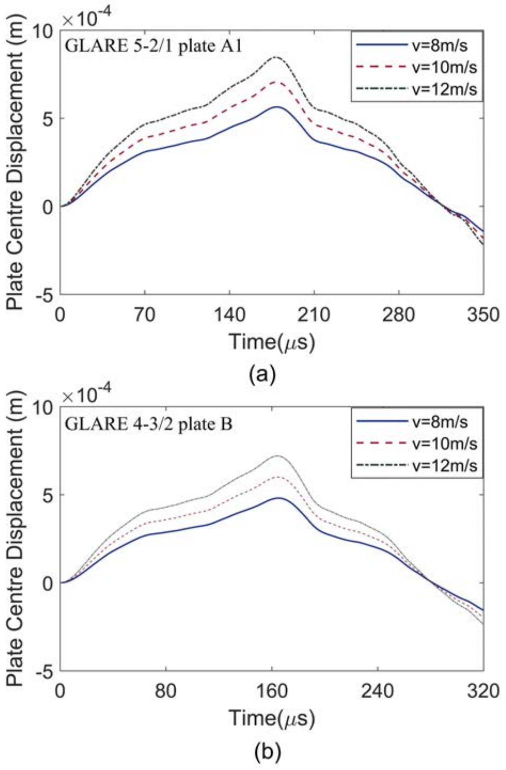

Figure 4.26: Plate centre displacements of GLARE plates (a) A1 and (b) B

4.4.3. Effect of outer aluminium thickness

Figure 4.27 (a)-(d) shows the impact responses of GLARE 5-2/1 plates A1, A2, A3 at an impactor velocity of 12 m/s. It could be seen from **Figure 4.27(a)** that with increasing thickness of the outer aluminium layers of GLARE 5-2/1 plates, the contact duration decreases owing to increased stiffness and there is a rise in contact force. There is a lateral shift towards the left for the contact forces as well as the drops in impactor velocities with increasing overall thickness of the plates as can be observed from **Figure 4.27 (a)** and **(b)** respectively. As expected, the impactor and plate displacements decrease with increasing outer aluminium thickness as seen from **Figure 4.27 (c)** and **(d)**.

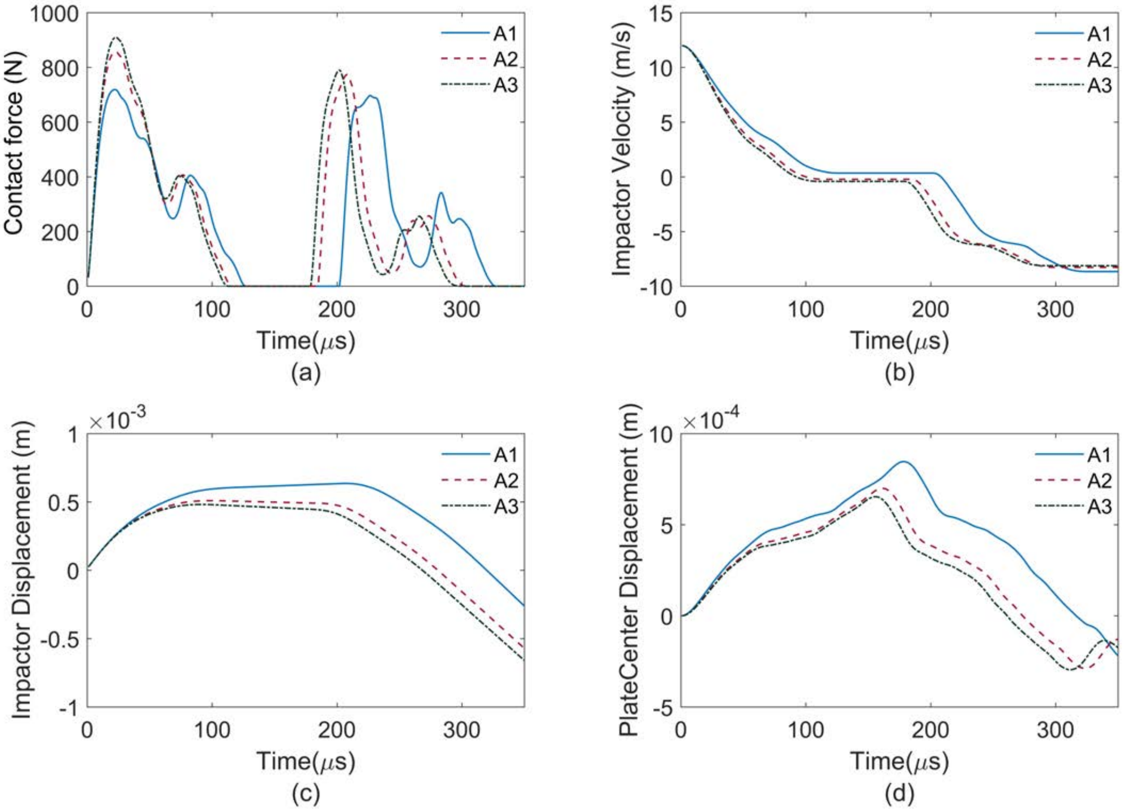

(a) (b) (c) (d)

Figure 4.27: Impact responses of GLARE plates A1, A2, A3 for an impactor velocity of 12 m/s

4.4.4. Effect of total thickness

In order to observe the effect of total thickness on the LVI response of the GLARE plates, the contact forces and impactor displacements are plotted in **Figure 4.28** for the plates A1, A3, B, C1 and C2 subjected to an LVI of 12 m/s. It is seen that with increasing overall plate thickness the contact force peak increases while the impactor displacement decreases. The thickness effect on the plate stiffness can be clearly seen from peaks in the contact forces and impactor displacements as plate A1 has the least peak contact force and the maximum impactor displacement compared to the rest.

For the plates A3, B, C1 and C2, although the total plate thicknesses are the same but there is a observable difference in the peaks attained by the respective contact forces and the impactor displacements. As seen, the plate A3 has the highest contact force followed by plate

B and then plates C1 and C2 which are having identical contact responses. This can be attributed to the higher stiffness of the plate A3 compared to the rest due to higher metal volume fraction (MVF) in plate A3 (refer **Table 4.4**). It can be inferred that although the total thickness affect the contact responses in terms of the peak values attained, but the influence of MVF on the peak values attained is much more significant.

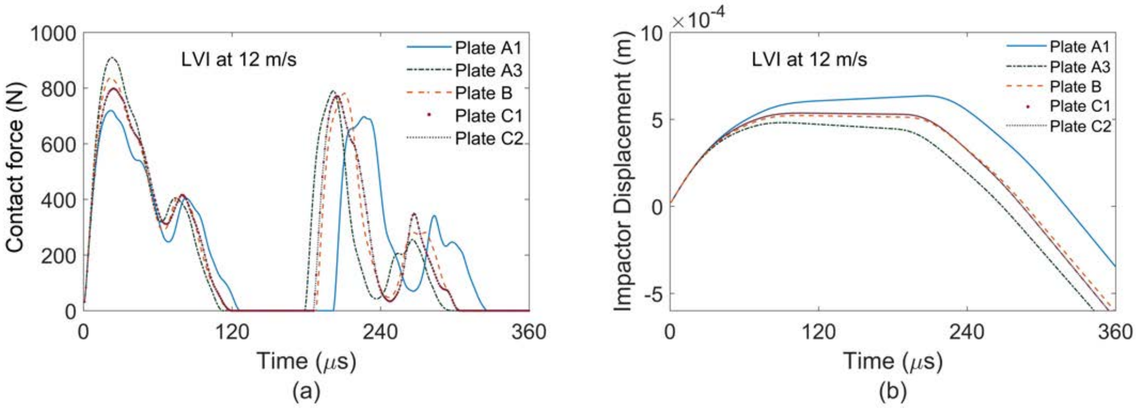

Figure 4.28: Effect of total thickness on the (a) contact force and (b) impactor displacement

Table 4.4: MVF of the different plates

GLARE Type	Stacking sequence	Plate Code	Aluminium thickness (mm)	Total thickness (mm)	Metal volume fraction (MVF)
GLARE 5-2/1	$[Al/0^{\circ}/90^{\circ}]_S$	A1	0.489	1.562	0.63
		A2	0.584	1.752	0.67
		A3	0.620	1.824	0.68
GLARE 4-3/2	$[Al/0^{\circ}/90^{\circ}/0^{\circ}/\overline{Al}]_S$	B	0.304	1.824	0.50
GLARE 5-2/2	$[Al/0^{\circ}/(90^{\circ})_2/0^{\circ}]_S$	C1	0.328	1.824	0.36
GLARE 2/1	$[Al/0^{\circ}/\pm 45^{\circ}/90^{\circ}]_S$	C2	0.328	1.824	0.36

4.4.5. Delamination at the interfaces

Figure 4.29 and **Figure 4.30** show the variation of the six components of stresses with respect to time at location (0.04 m,0.04 m) of the first interface (i.e. between bottom aluminium layer and 0° ply) for GLARE 5-2/1 and GLARE 4-3/2 plates A1 and B respectively. There is a noticeable variation of the stresses with time at higher velocities of 10 m/s and 12 m/s of the impactor, and peak stresses reached for GLARE 4-3/2 are higher than those for GLARE 5-2/1 at that particular location. Similar trends could also be observed for the other interfaces though with different magnitudes. It could be seen that all these stresses show highest magnitudes corresponding to the period when contact force is maximum. The peaks are attained earlier in GLARE 4-3/2 as compared to GLARE 5-2/1 for the same initial velocity of the impactor which may signify that the failure by delamination at that particular interface may get initiated earlier for GLARE 4-3/2 as compared to the latter. As expected it was observed that the magnitudes of stresses increased with increasing impactor velocities. Based on these stresses and delamination criterion, delamination at the interfaces are assessed.

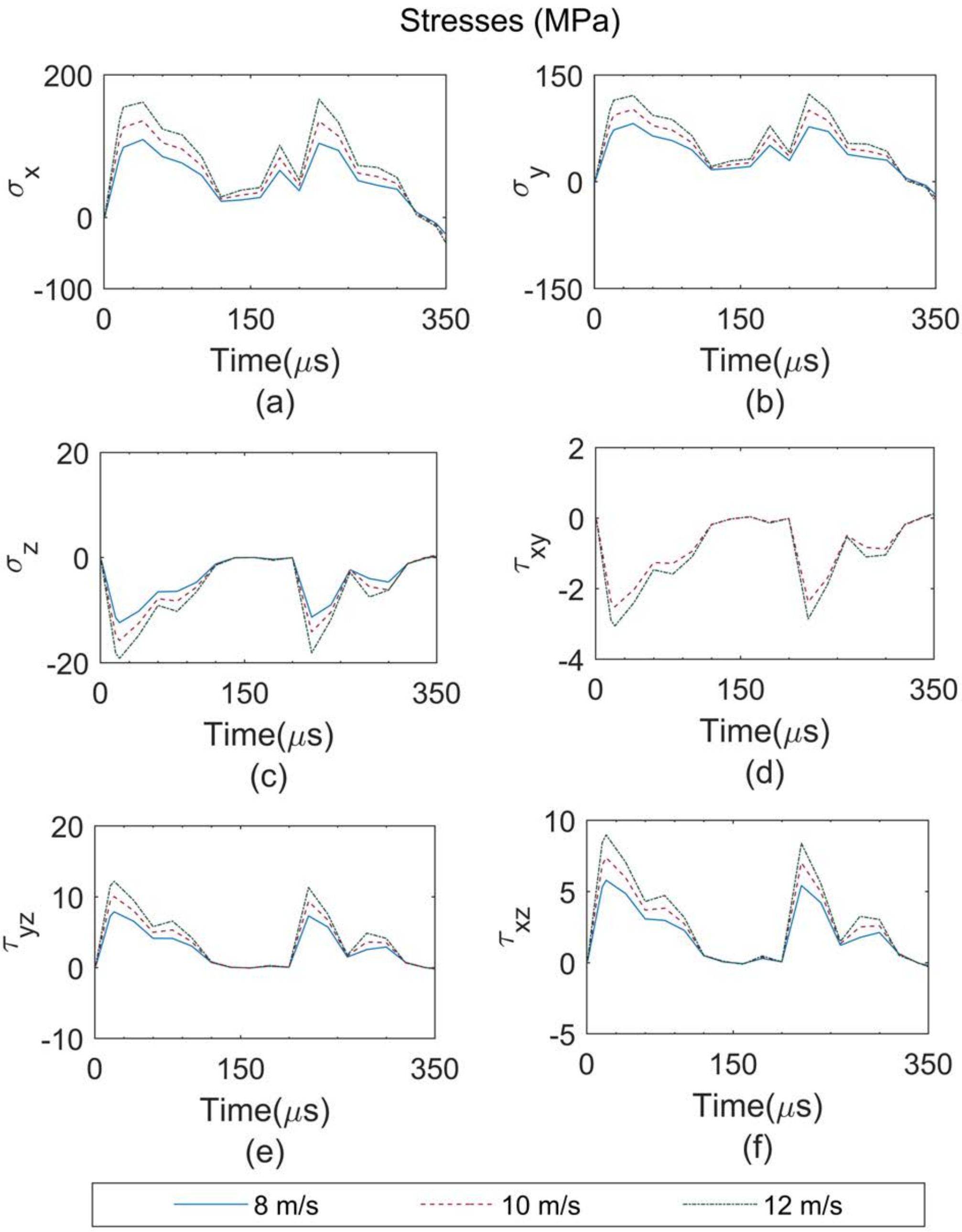

Figure 4.29: Variation of stresses with time at location (0.04 m, 0.04 m) of the first interface of GLARE 5-2/1 plate A1

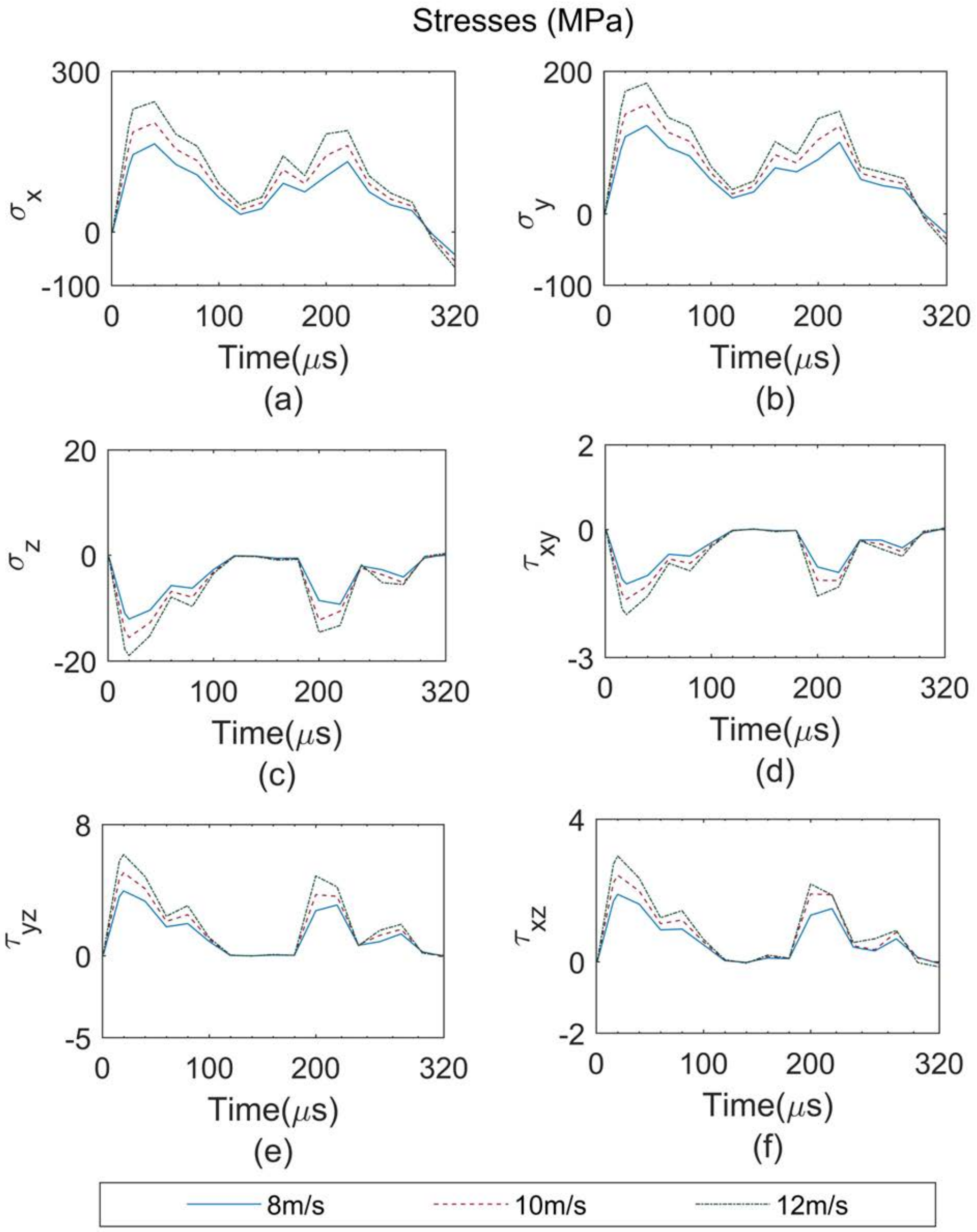

Figure 4.30: Variation of stresses with time at location (0.04 m, 0.04 m) of the first interface of GLARE 4-3/2 plate B

4.4.5.1. Effect of impactor velocity on delamination

Figures 4.31-4.33 show the delamination at the different interfaces of GLARE 5-2/1 plate A1 at $t = 25\mu s$ for the different impactor velocities. It is observed that delamination region for A1 is located centrally around the impact location and occurs mostly at the interfaces between the Al and 0° ply. Delamination is observed to occur along the 0° fibre direction in both the lower and upper Al and 0° ply interfaces, even though the extent of delamination are different in the lower and upper interfaces. The rest of the interfaces show no delamination due to LVIs at 8 m/s and 10 m/s. However, at 12 m/s, delamination is seen to just initiate at interface-2 (**Figure 4.33**).

For all the three impactor velocities viz. 8, 10 and 12 m/s it is seen that the bottom aluminium and 0° ply interface (interface-1) experiences more delamination compared to the top (interface-5) in GLARE 5-2/1 plate A1. Also, as expected, the extent of delamination increases with increasing impactor velocities. Similar trends were observed for GLARE plates A2 and A3.

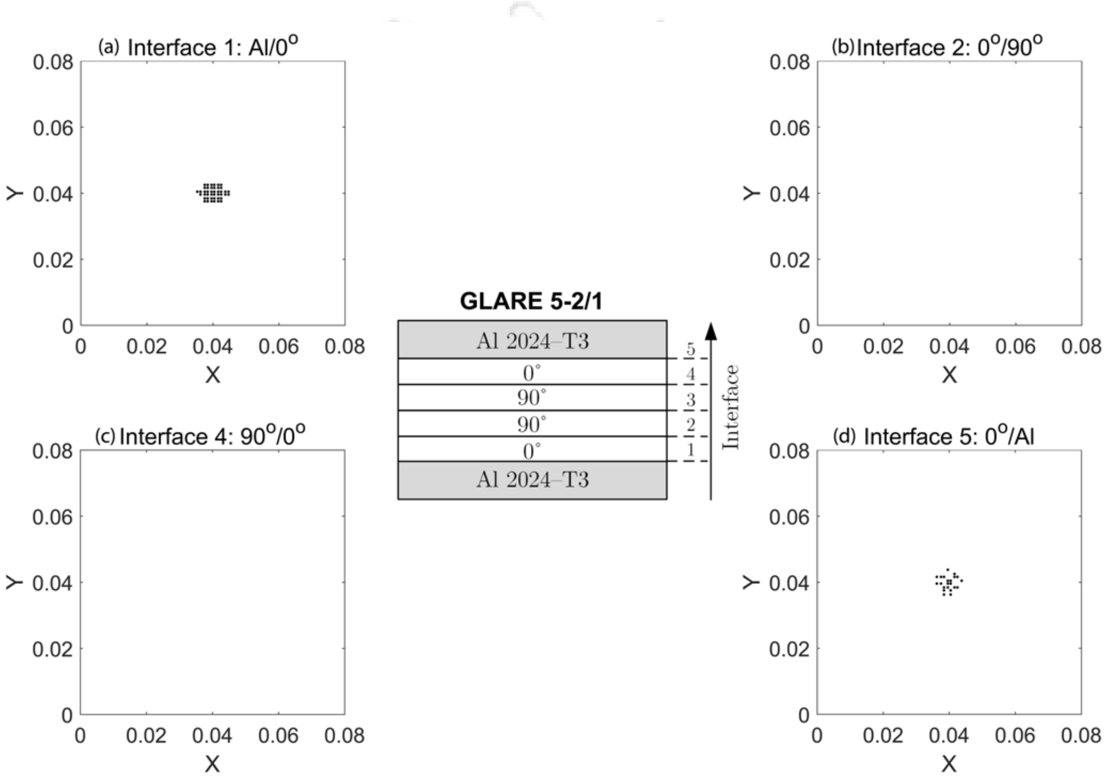

Figure 4.31: Delamination at the interfaces of plate A1 for an impactor velocity of 8 m/s

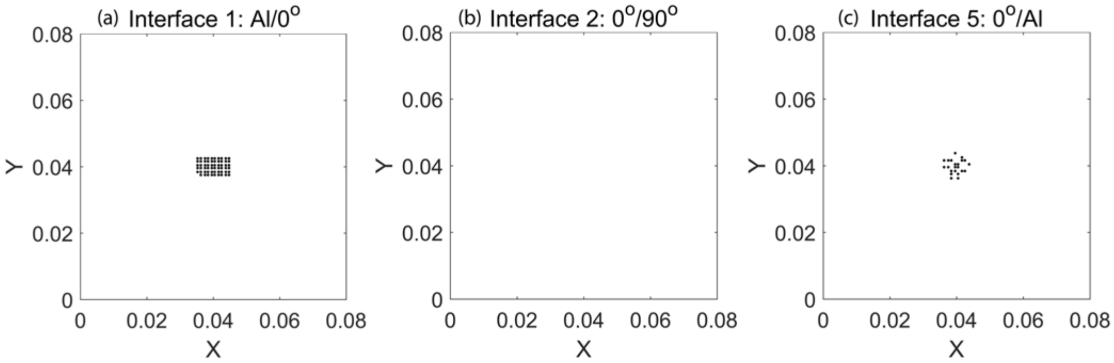

Figure 4.32: Delamination at the interfaces of plate A1 for an impactor velocity of 10 m/s

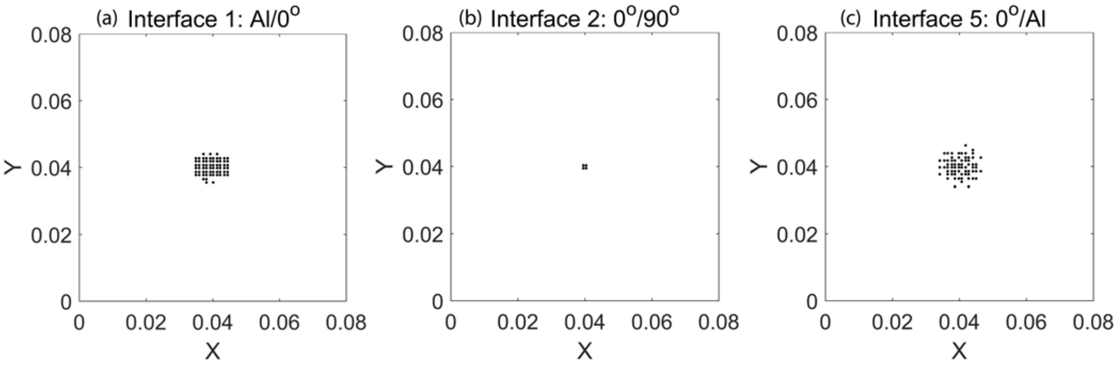

Figure 4.33: Delamination at the interfaces of plate A1 for an impactor velocity of 12 m/s

4.4.5.2. Effect of outer aluminium thickness on delamination

The delamination at the interfaces of GLARE 5-2/1 plates A2 and A3 are plotted in **Figure 4.34** and **Figure 4.35** for an impactor velocity of 12 m/s. Comparing **Figures 4.33-4.35** it is seen that with increasing thickness of the outer aluminium layer there is a slight decrease in the extent of delamination at the interfaces. This can be attributed to more energy being absorbed by the outer aluminium layer during the LVIs.

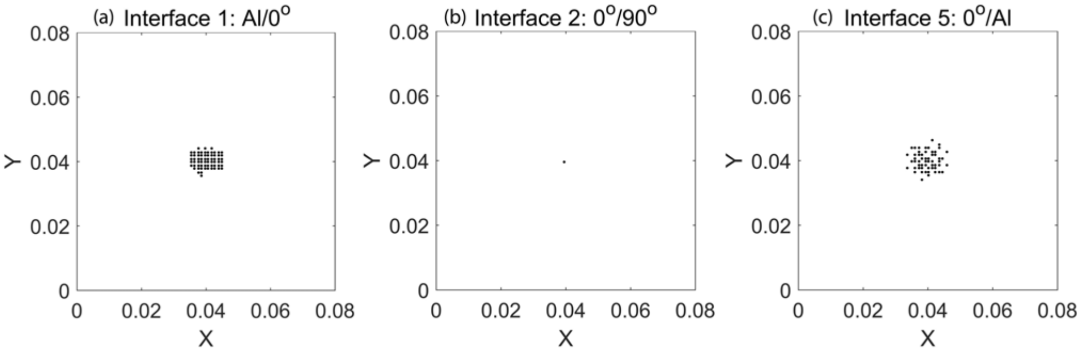

Figure 4.34: Delamination at the interfaces of plate A2 for an impactor velocity of 12 m/s

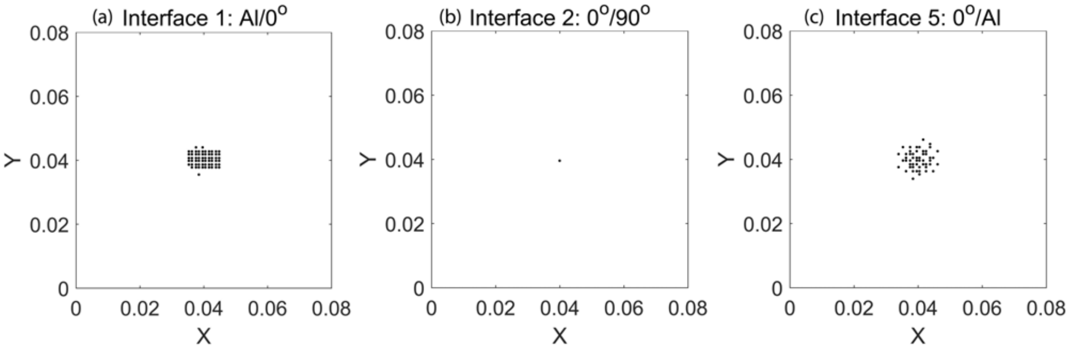

Figure 4.35: Delamination at the interfaces of plate A3 for an impactor velocity of 12 m/s

4.4.5.3. Effect of GLARE configurations on delamination

Figures 4.36-4.38 show the delamination at the interfaces for GLARE 4-3/2 FML plate B at $t = 25\mu s$ for the impactor velocities of 8 m/s, 10 m/s and 12 m/s respectively. It is seen from **Figure 4.31** and **Figure 4.36** that at an impactor velocity of 8 m/s the extent of delamination in GLARE 4-3/2 plate B is more compared to that in GLARE 5-2/1 plate A1. The delamination region for GLARE 4-3/2 is more at interface-1 and along the fibre direction of the 0° ply. The interface-4 between the lower face of the middle aluminium and upper face of the 0° ply shows very less delamination compared to the other two metal ply interfaces.

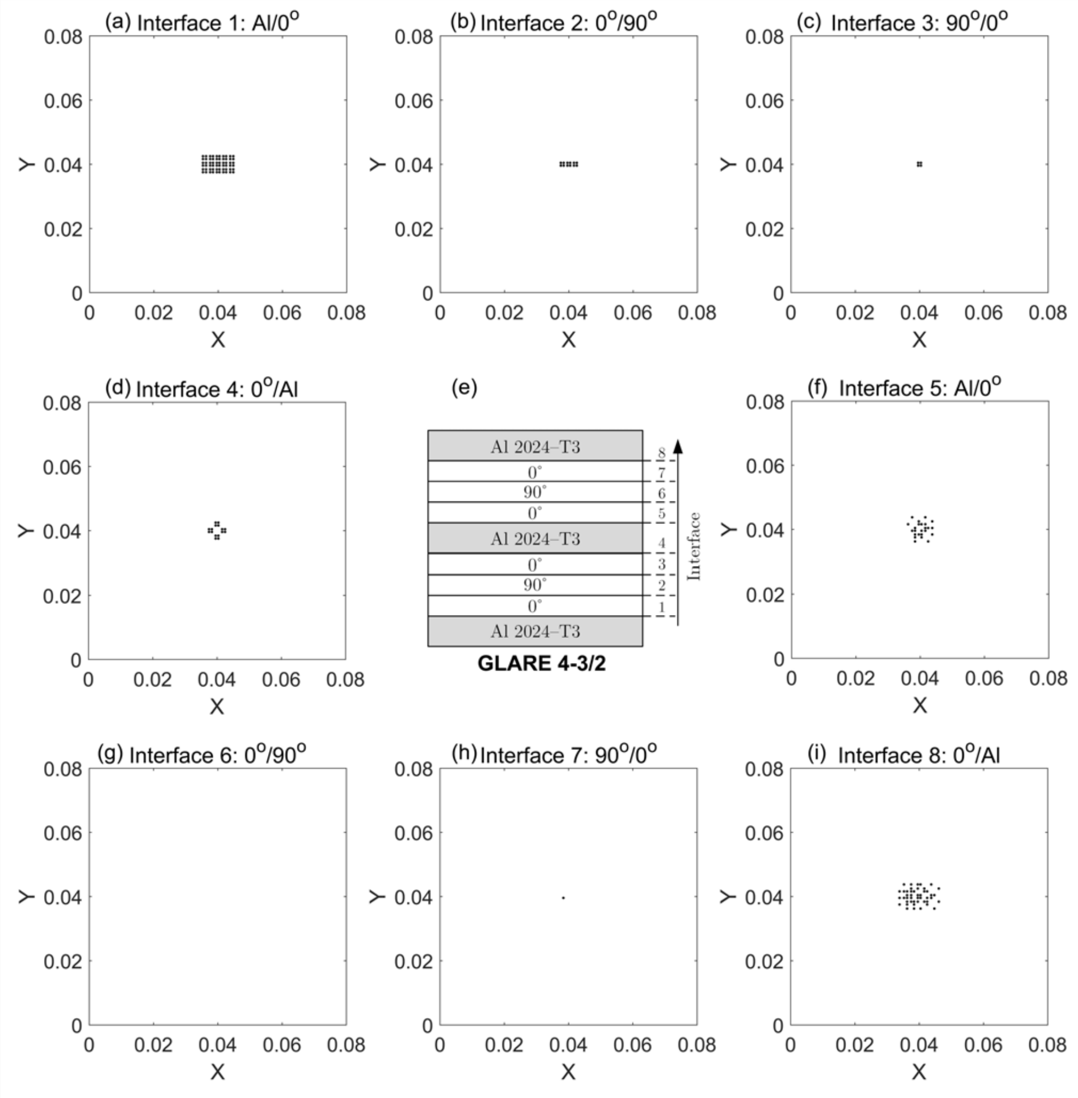

Figure 4.36: Delamination at the interfaces of GLARE 4-3/2 plate B for LVI at 8 m/s

The bottom interface-2 between the 0° and 90° plies shows delamination along the fibre direction of the bottom ply and its size increases with increasing impactor velocities as observed from **Figures 4.36-4.38**. At higher velocities of 10 m/s and 12 m/s it can be seen from **Figures 4.37-4.38** that the extent of delamination increases at the interfaces 1 and 8. The delamination size for the interface-4 almost remains same with increasing impactor velocities. Moreover, the delamination initiates at interface-7 for when the impactor velocity is 10 m/s and expands in size as the impacting velocity increases to 12 m/s. The delamination at top interface-8 is more like an elliptical region which is similar to the case of GLARE 5-2/1 plates A1, A2 and A3.

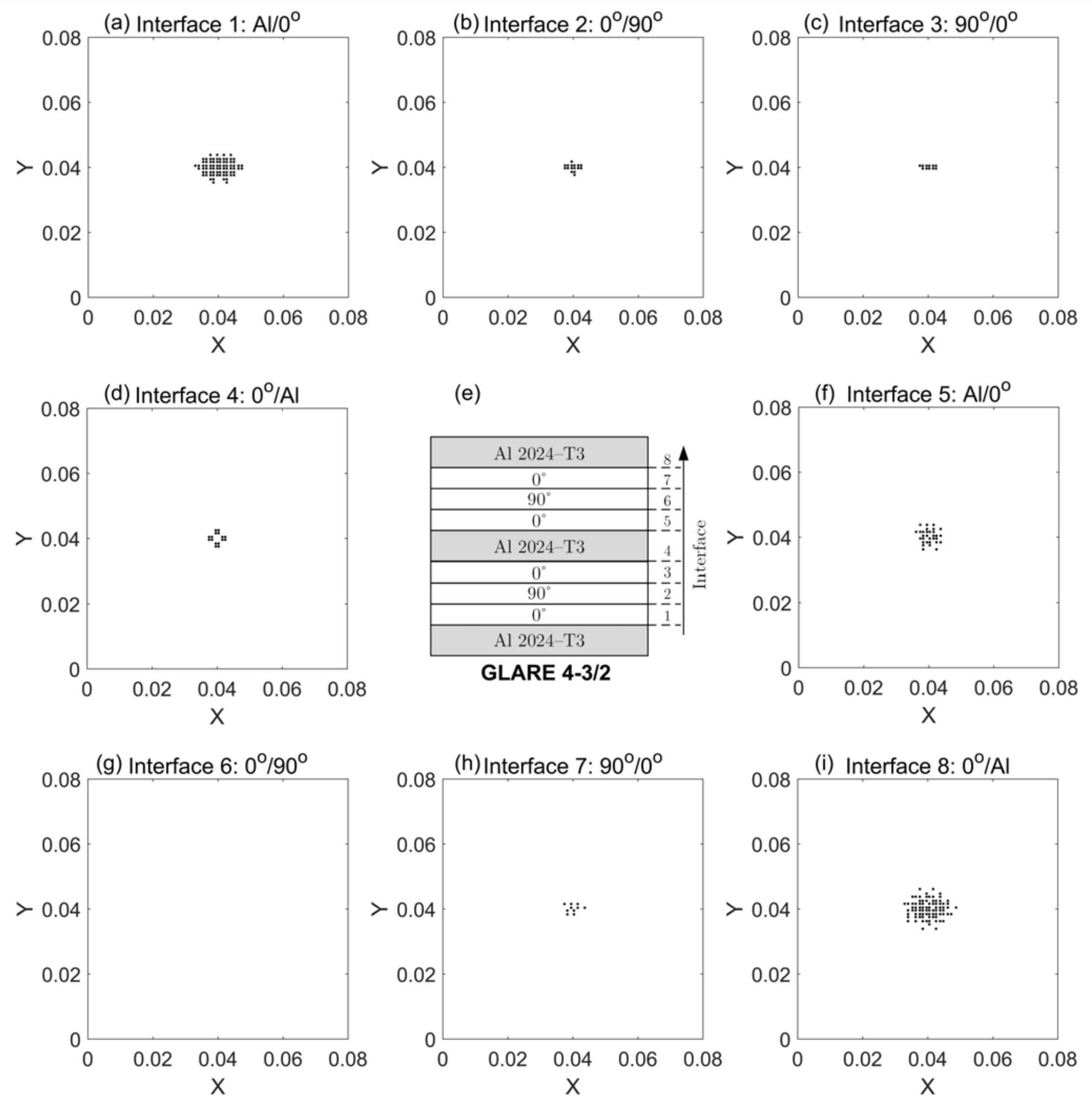

Figure 4.37: Delamination at the interfaces of GLARE 4-3/2 plate B for LVI at 10 m/s

The extent of delamination is more in case of GLARE 4-3/2 plate B as compared to GLARE 5-2/1 plate A3 which are having the same overall thicknesses. This can be clearly seen from **Figure 4.35** and **Figure 4.38** for an impactor velocity of 12 m/s, even though the contact force is higher in case of GLARE plate A3 (refer **Figure 4.28**). Therefore, the GLARE configuration also influences the extent of delamination at the interfaces subjected to LVIs.

Clearly, the GLARE 5-2/1 configuration is better with the least delamination at the interfaces when subjected to LVIs.

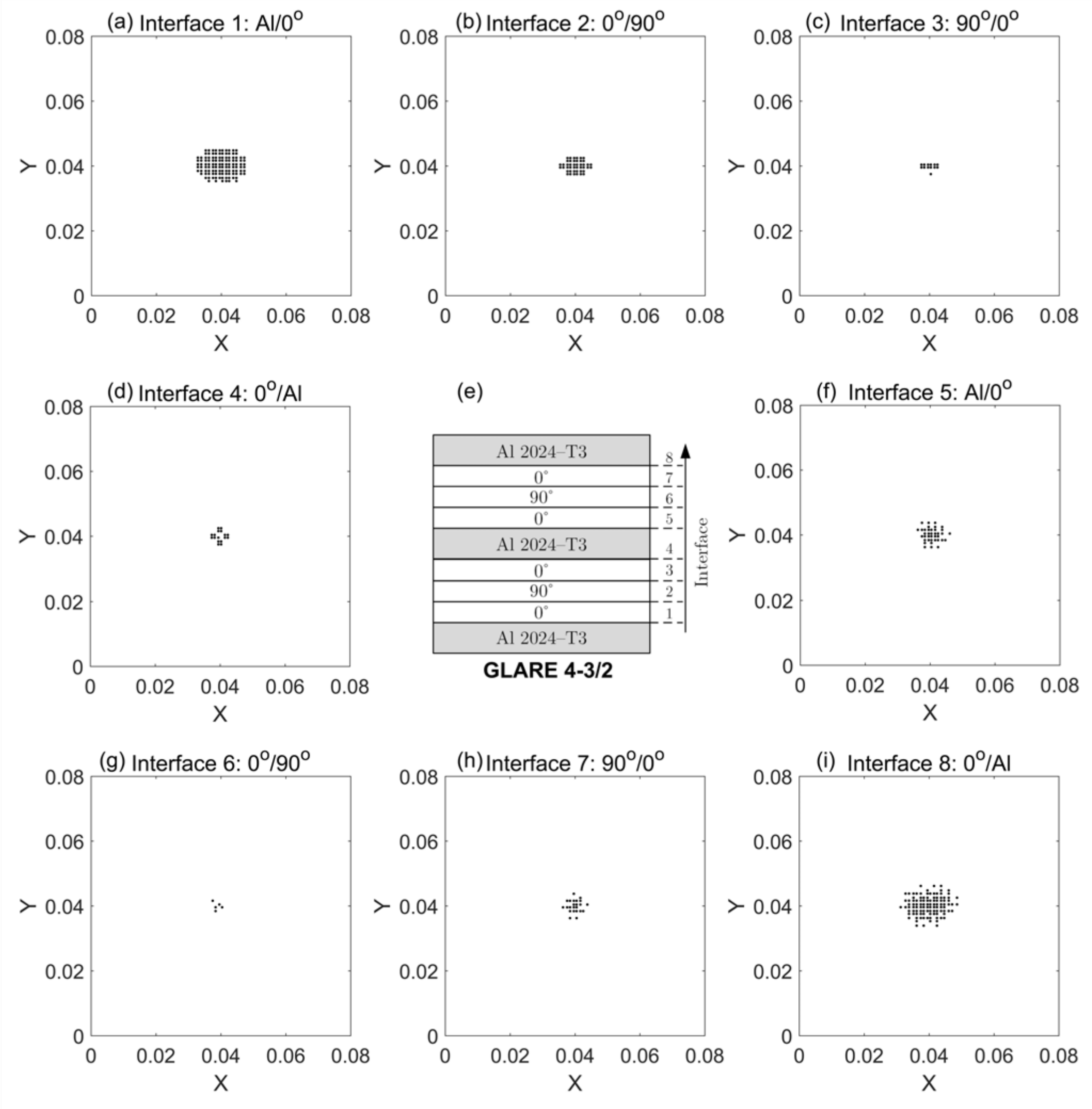

Figure 4.38: Delamination at the interfaces of GLARE 4-3/2 plate B for LVI at 12 m/s

Figures 4.39-4.40 show the delamination at the interfaces of GLARE 5-2/2 plate C1 and GLARE 2/1 plate C2 at time $t = 25\mu s$ for an impactor velocity of 12 m/s which highlight the effect of stacking sequence on the delamination extent at the interfaces. It is seen that the extent of delamination is greater at the interfaces 2 and 8 for GLARE plate C1 as compared to C2. Delamination is seen to occur at more number of interfaces of plate C2 and located around the centre of the plate. Although, it was observed that both the plates C1 and C2 had similar contact force histories (refer **Figure 4.28**) but the delamination extent is observed to be dependent on the stacking sequence of the laminates.

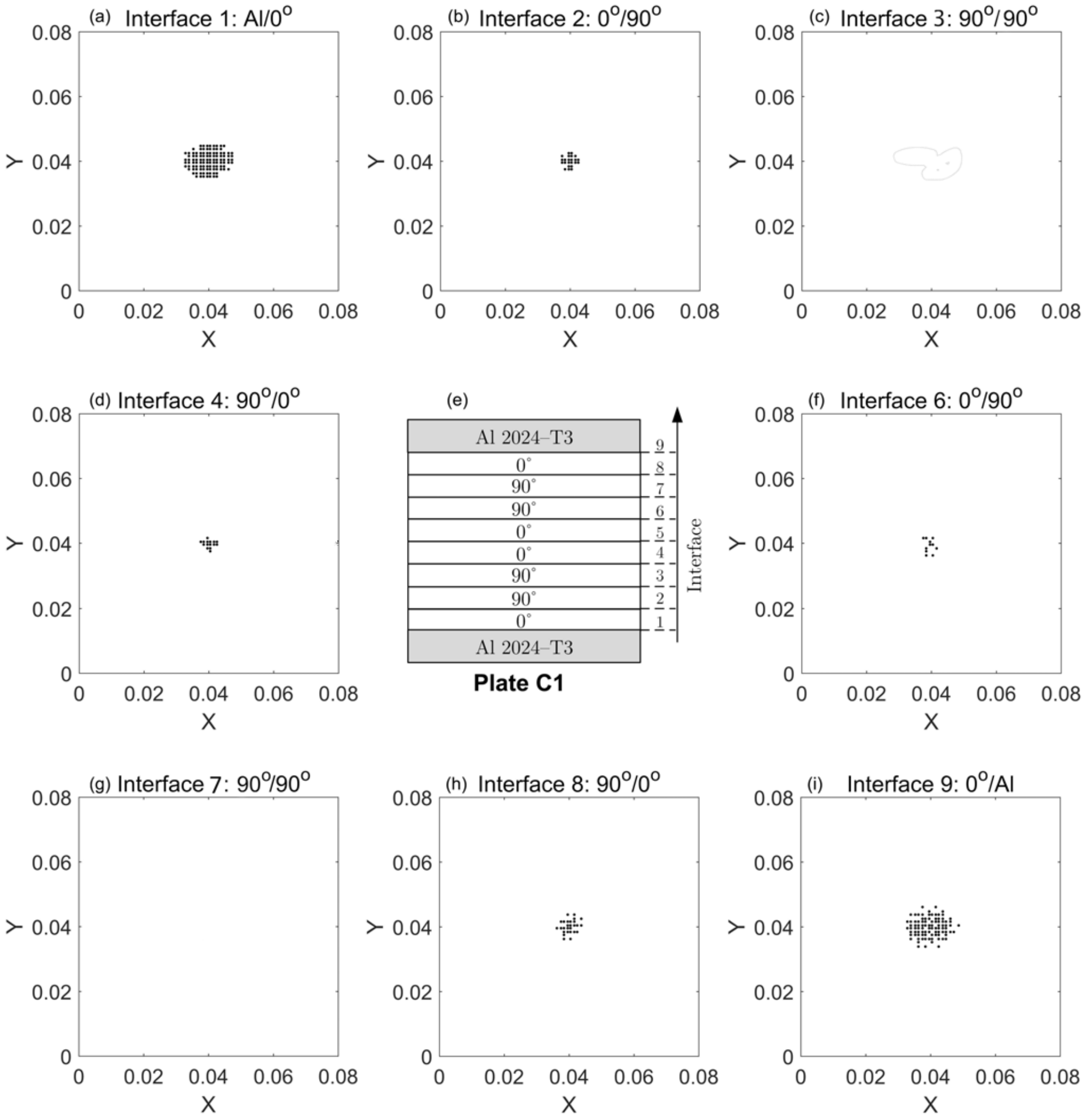

Figure 4.39: Delamination at the interfaces of GLARE 5-2/2 plate C1 for LVI at 12 m/s

It is observed that the extent of delamination in GLARE 4-3/2 is more compared to GLARE 5-2/1 for the same impacting energy. The stresses developed at the interfaces of the thicker GLARE 4-3/2 are higher as compared to GLARE 5-2/1 because of higher stiffness of the thicker plate which restricts it deflection during impact thereby increasing the contact stresses. Therefore the GLARE 5-2/1 laminate having thinner high strength glass/epoxy layers can sustain larger deformations as observed from **Figure 4.28(b)**. This implies that the specific energy absorbed by the thinner GLARE 5-2/1 is higher making it a better material for situations where low velocity impacts might occur. In both GLARE 5-2/1 and GLARE 4-3/2, the delamination is more prevalent for the aluminium composite interfaces at the top and bottom. In case of GLARE 4-3/2, delamination at the middle aluminium composite interface-4 is concentrated centrally and does not progress with increasing impact energy compared to the top and bottom aluminum composite interfaces. Similar is the case for other composite interfaces where the delamination region is mostly concentrated around the impacted region.

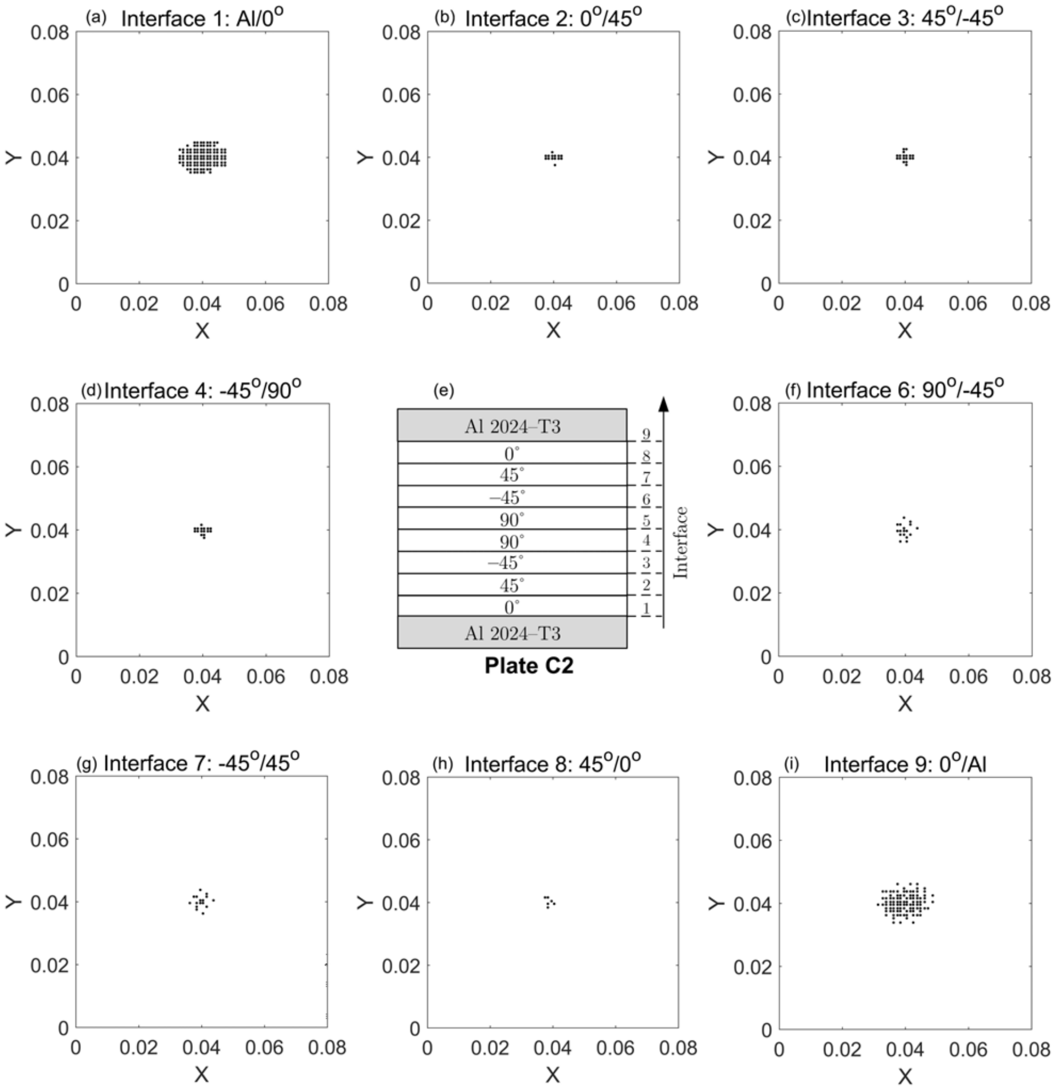

Figure 4.40: Delamination at the interfaces of GLARE 5-2/2 plate C2 for LVI at 12 m/s

4.5. Effect of hybridisation on LVI response

Exploring the weight saving aspects, hybrid laminates can result in further reduction in the overall weight of the structure and enable to tailor the structural performances. In order to investigate the effect of hybridisation, the impact responses are compared between GLARE 4-3/2 plate (AGA) and a hybrid laminate having Kevlar-49/epoxy layers replacing the middle aluminium layer (AGK) and a third hybrid configuration containing Kevlar-49/epoxy layers in place of the 90° glass/epoxy plies (AGKGA). The material properties are given in Table 4.5 [45,138,205–208] and the plate configurations are shown in Figure 4.41 with the details in **Table 4.6**. For investigating the LVI responses, 0.08 m × 0.08 m clamped plates are impacted normally at the centre by a 10 mm diameter rigid spherical steel impactor at 10 m/s and the impact responses are compared.

Table 4.5: Material parameters of S2-glass/epoxy and Kevlar-49/epoxy [45,138,205–208]

Parameter	Notation	UD S2-glass/FM94-epoxy prepregs (G)	UD Kevlar-49/epoxy (K)
Density (kg/m³)	ρ	1980	1390
Poisson's ratio	υ	$\upsilon_{12} = 0.33$, $\upsilon_{23} = 0.33$	$\upsilon_{12} = 0.34$, $\upsilon_{23} = 0.34$
Young's modulus (GPa)	E	$E_1 = 55$, $E_2 = 9.5$	$E_1 = 75$, $E_2 = 5.5$
Shear Modulus (GPa)	G	$G_{12} = 5.5$, $G_{23} = 3.5$	$G_{12} = 2.2$, $G_{23} = 1.8$
Yield strength (MPa)	σ_{ys}	—	—
Transverse tensile strength (MPa)	Y_T	50	21
Transverse compressive strength (MPa)	Y_C	160	130
In plane shear strength (MPa)	S_{lt}	70	66
Interlaminar shear strength (MPa)	*ILSS*	50	48

Table 4.6: GLARE plate hybridisation details

	GLARE plate configurations		
Stacking sequence	$[A/0_G/90_G/0_G/\bar{A}]$	$[A/0_G/90_K/0_G/\bar{A}]_S$	$[A/0_G/90_G/0_G/0_K]$
Plate Code	**AGA**	**AGKGA**	**AGK**
Aluminium thickness (mm)	0.304	0.304	0.304
S2-glass/epoxy ply thickness (mm)	0.152	0.152	0.152
Kevlar-49/epoxy ply thickness (mm)	0.152	0.152	0.152
Total thickness (mm)	1.824	1.824	1.824

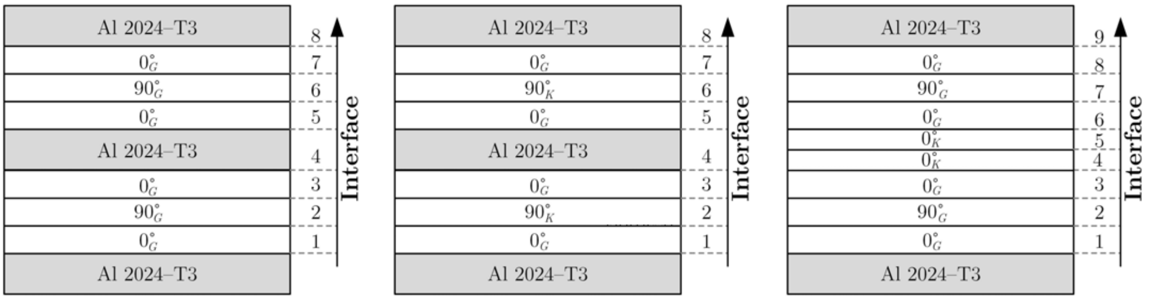

(a) AGA (b) AGKGA (c) AGK

Figure 4.41: Hybrid configurations with Kevlar layers

4.5.1. LVI responses of GLARE 4-3/2 and hybrid GLAREs

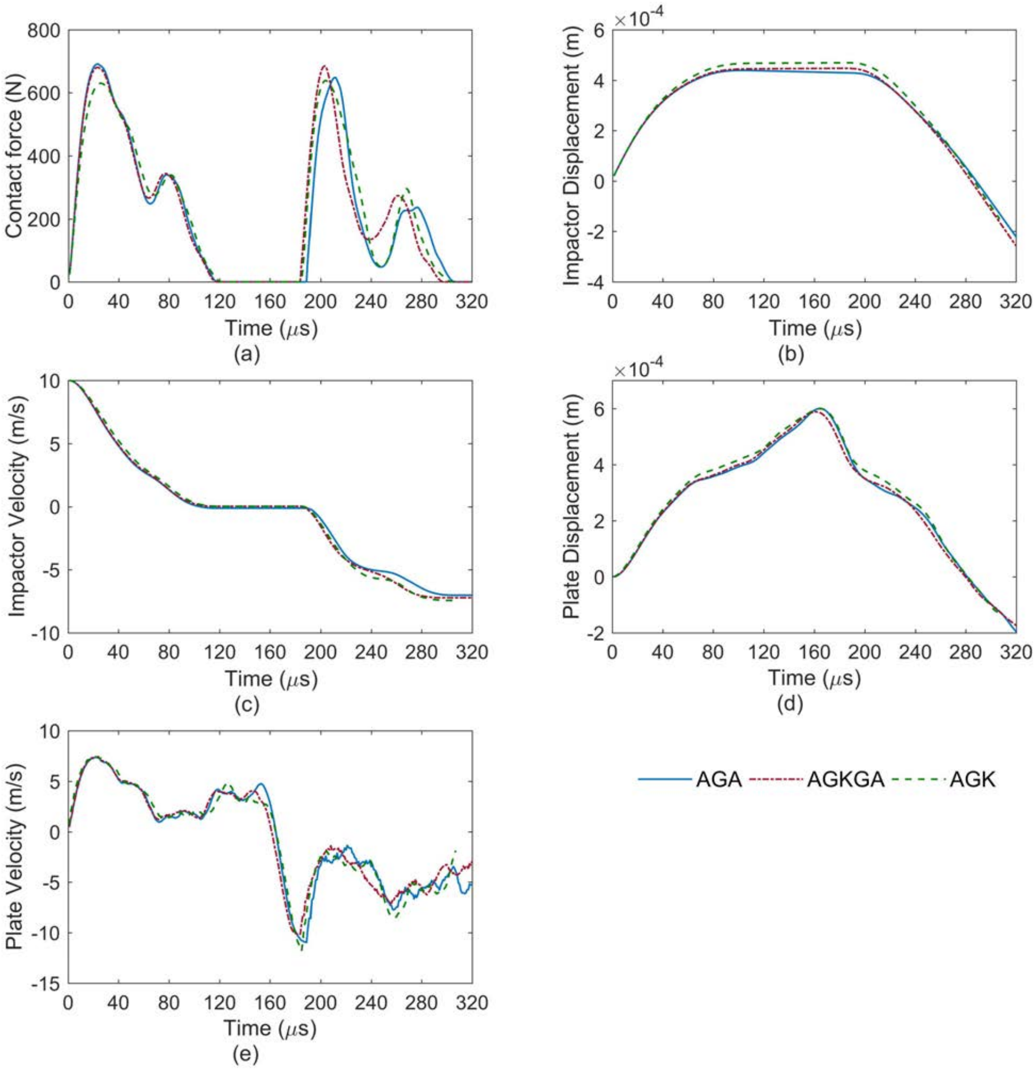

Figure 4.42: LVI responses of the plates due to a spherical steel impactor striking at 10 m/s

The dynamic responses of the plates are shown in **Figure 4.42**. **Figure 4.42(a)** shows the contact force histories of the three plates considered. It is seen that the peak contact forces are same for the plates AGA and AGKGA while there is a slight decrease in the peak contact force for the plate AGK. This slight decrease in the peak contact force may be attributed to the reduction in overall mass of the plate AGK because of replacing the middle aluminium layer with lower density Kevlar/epoxy. This in turn slightly decreases the inertia of the plate globally, thereby enabling the plate to respond comparatively quicker to the striking impactor, thus resulting in lesser indentation of the plate at the contact location. This can also be correlated to the slightly higher deflection of the plate AGK compared to AGA and AGKGA as seen from **Figure 4.42(d)** due to its reduced stiffness in the transverse direction. It is seen that the impactor displacement and velocities (**Figure 4.42 (b)** and **(c)**) for all the three plates are similar and the contact duration is also same which implies that the time of contact is influenced by the impactor mass. After the first contact between the impactor and the target plate there is a short gap when the contact is lost between them as the plate displacement is more compared to the impactor during that period resulting in zero contact force. The second contact occurs on reversal of the plate motion after reaching its peak displaced position and makes contact with the impactor on its way in the opposite direction which can be inferred from the negative velocities of plate and impactor during the course of duration of the second impact.

4.5.2. Effect of hybridisation on delamination at the interfaces

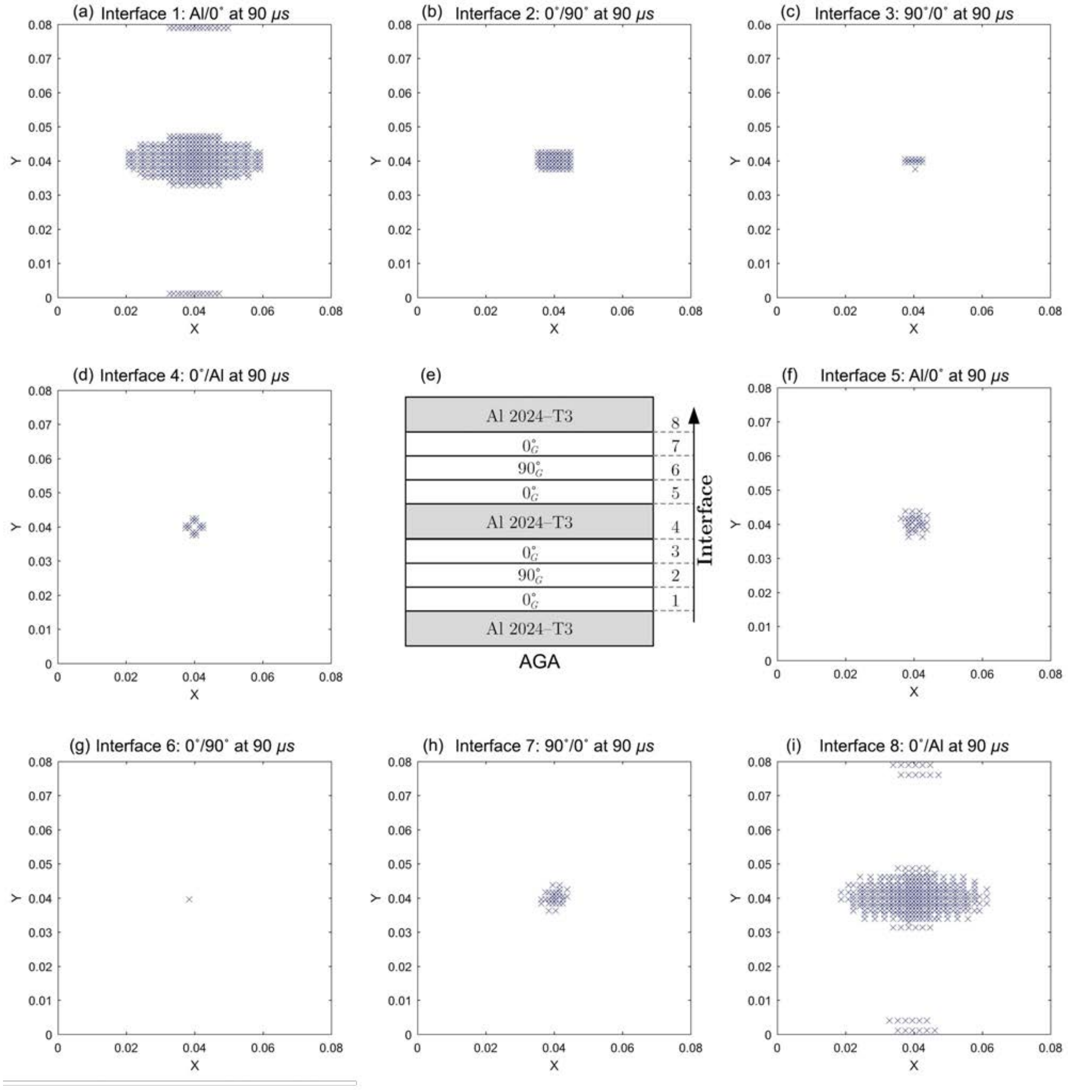

Figure 4.43: Delamination at the interfaces for plate AGA due to LVI at 10m/s

Upon obtaining the impact responses of the GLARE plates, it is important to know the extent of interfacial delamination they incur. Delamination at the fibre-metal interfaces is of major concern in GLARE similar to other FMLs and in order to ensure their operational safety as well as easier physical inspection, it is necessary to accurately estimate the extent of delamination at the interfaces. **Figures 4.43-4.45** show the delamination at the interfaces of the plates AGA, AGKGA and AGK respectively at 90 μs .

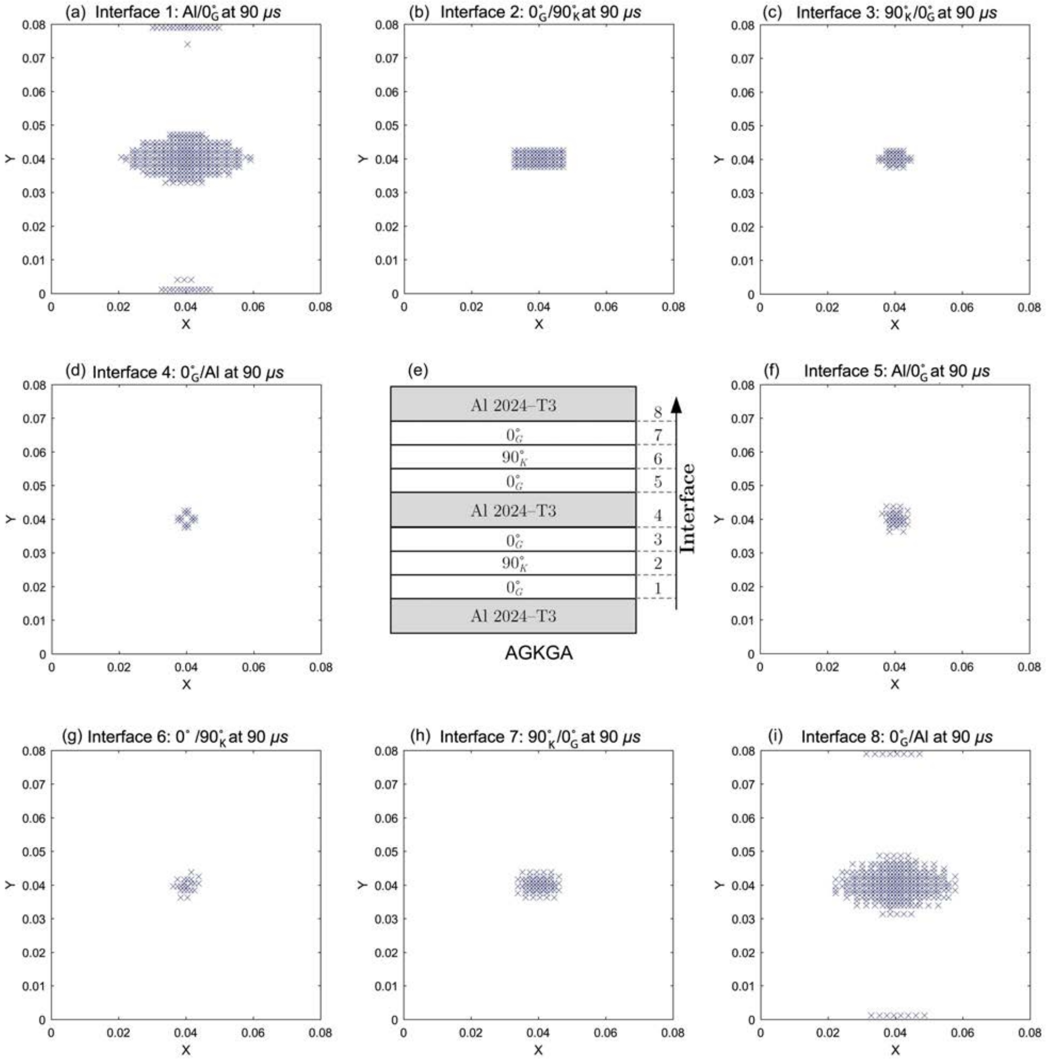

Figure 4.44: Delamination at the interfaces for plate AGKGA due to LVI at 10m/s

It is seen that in all the cases, the outer fibre-metal interfaces suffer the maximum extent of delamination as compared to the rest of the interfaces. The delamination at the top and bottom fibre-metal interfaces of the laminates is observed to be located within the impact area and its progression is influenced by the fibre orientation of the ply below it which is evident from **Figures 4.43-4.45** where the delamination progression is along the 0° fibre direction and delamination at any interface is initiated within the impact location. The extent of delamination is comparatively more at the bottom interfaces compared to the top.

Replacing the mid aluminium layer with Kevlar-49/epoxy laminates as in case for plate AGK, it is seen that there is a reduction in the extent of delamination at the interfaces with no visible delamination at interfaces 4 and 6 (the S2-glass/epoxy-Kevlar-49 ply interfaces).

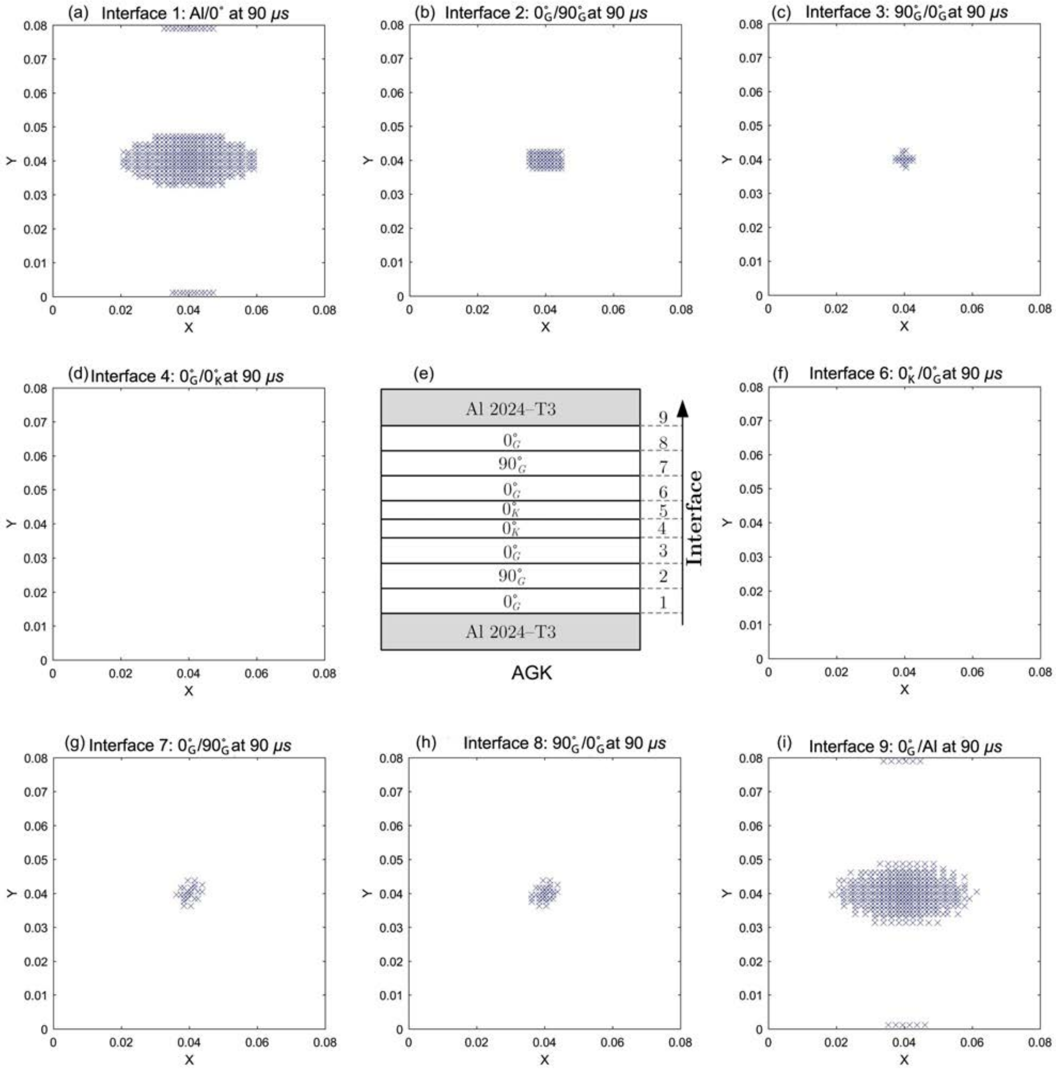

Figure 4.45: Delamination at the interfaces for plate AGK due to LVI at 10m/s

Furthermore, it is observed that replacing 90° glass/epoxy plies with Kevlar-49/epoxy plies as in case of plate AGKGA, does not improve the impact characteristics as can be seen from **Figure 4.44**. The delamination is seen to have slightly increased which may be due to a greater mismatch in the engineering properties between the differently oriented plies. In case of the plate AGK, as seen from **Figure 4.42** and **Figure 4.45**, along with a slight decrease in the peak contact force, there is considerable reduction in the delamination at the interior interfaces making it a suitable configuration for structures prone to impacts.

4.6. Multiple normal LVIs on GLARE

From the existing literatures, it is seen that in studying the LVI responses of GLARE and FMLs in general, the studies are done considering a single impactor hitting the target either once or in succession at the same impact site. Numerous works have been reported on single LVI considering GLARE targets [45,209,210] but in practical scenario, occurrences of multiple LVIs are common due to runaway debris, hailstorms and impacts by small particles that can cause severe internal damage in the form of delamination which are difficult to assess during routine visual inspections. Accordingly, the study of the impact response resulting from such scenarios can be of significant importance to intricately understand the way the target responds to arbitrary impacts at different time intervals and resulting delamination in GLARE FMLs in case of multiple LVIs occurring arbitrarily.

4.6.1. Problem definition

In the analysis of multiple LVI, 0.08 m × 0.08 m GLARE plates clamped on all sides are impacted normally by two spherical steel impactors each of diameter 10 mm at different locations at arbitrary times and with arbitrary velocities as shown in **Figure 4.46**. **Table 4.1** lists all the material properties of GLARE [45,102,138] and

Table 4.2 shows the strength parameters where the subscripts n and i refer to the interfacial strengths in the normal and shear directions [204–206].

Table 4.7: GLARE plate configurations

GLARE		GLARE 5-2/1		GLARE 4-3/2
Plate	A1	A2	A3	B1
Al thickness (mm)	0.424	0.489	0.554	0.304
Ply thickness (mm)	0.146	0.146	0.146	0.152
Total thickness (mm)	1.432	1.562	1.692	1.824

To study the effects of MVF, three different GLARE 5-2/1 plates are considered as listed in **Table 4.7** namely A1, A2 and A3 and to study the effect of GLARE configuration, a GLARE 4-3/2 plate B1 is also considered. The impact responses are obtained considering the impactors to hit each of these clamped plates symmetrically at the respective locations viz. IMP1 (impactor-1: x=0.04 m, y=0.02 m) and IMP2 (impactor-2: x=0.04 m, y=0.06 m).

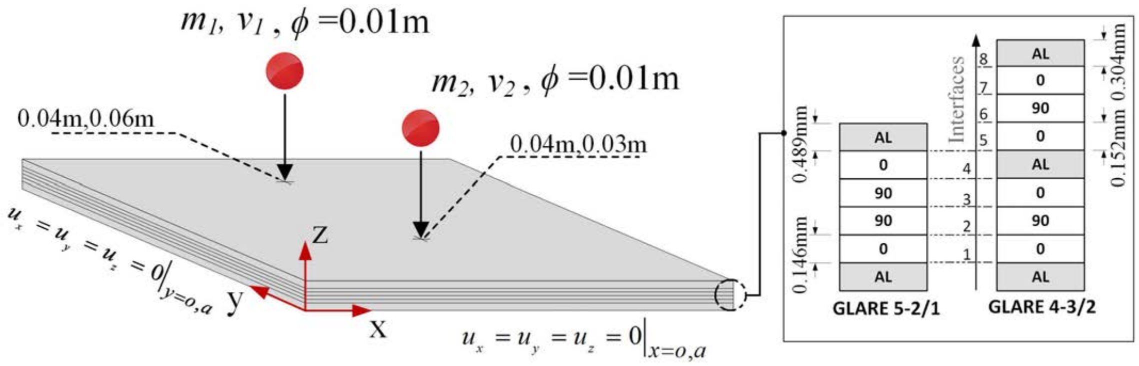

Figure 4.46: Spherical impactors normally striking a clamped GLARE plate

4.6.2. Validation of multiple LVI

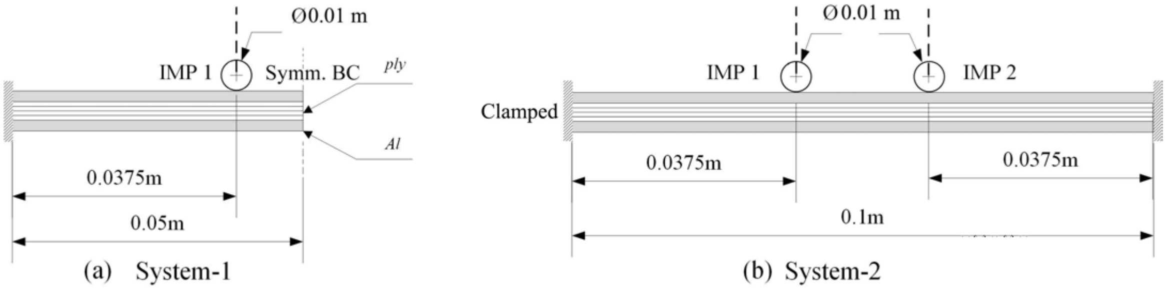

Figure 4.47: GLARE beam (a) clamped at one end and subjected to a single impact: System-1. (b) clamped at both the ends and subjected to equally offset impacts: System-2

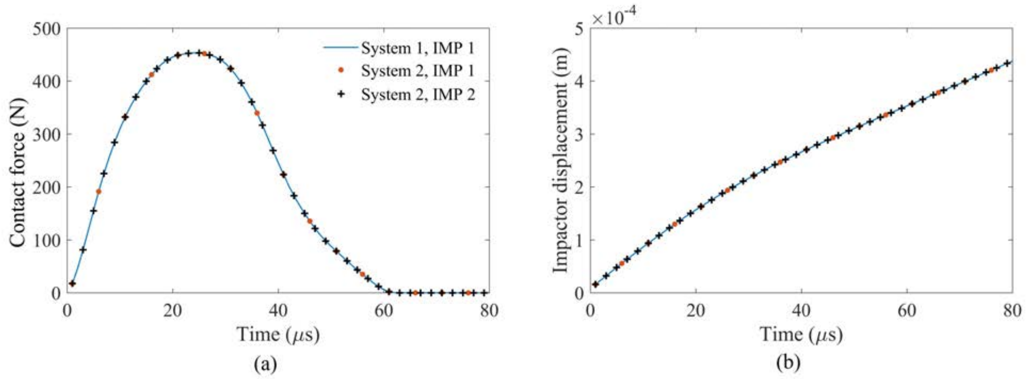

Figure 4.48: (a) Contact force history of system-1 and 2 (b) Impactor displacement at the free end of system-1 and midpoint of system-2

In case of multiple impacts with arbitrary masses and velocities, very few literatures studying impacts occurring at different locations and arbitrary time delays are available. In order to establish the robustness of the developed FE code, an alternate method is adopted as described by Lam and Sathiyamoorthy [211]. Two separate systems are considered as shown in **Figure 4.47**, where both the GLARE 5-2/1 beams are having uniform cross sections of width 0.01562 m and thickness 0.001562 m with beam in system-1 being half the length of system-2. The layup details of the GLARE beams are as per configuration A2 as mentioned in **Table 4.7**. System-1 represents the symmetric portion of system-2 about its middle and has a single 0.01 m diameter steel impactor striking the 0.05 m long beam at 0.0375 m from the left clamped end at 8 m/s and the other end is defined with symmetric boundary conditions. The 0.1 m long beam in system-2 has both its ends clamped and two similar 0.01 m diameter steel impactors strike it at 0.0375 m from the clamped ends with velocities 8 m/s each. **Figure 4.48 (a)-(b)** shows the dynamic responses of both the systems and it is seen to be the same thereby validating the code for multiple impacts.

4.6.3. Effect of MVF for two simultaneous spherical LVIs

To observe the thickness effect of the outer aluminium layer, the impact responses of three clamped GLARE plates viz. A1, A2 and A3 are evaluated. The two spherical steel impactors simultaneously strike the plates with a velocity of 10 m/s symmetrically at locations as illustrated in **Figure 4.46** and the impact responses are shown in **Figure 4.49**.

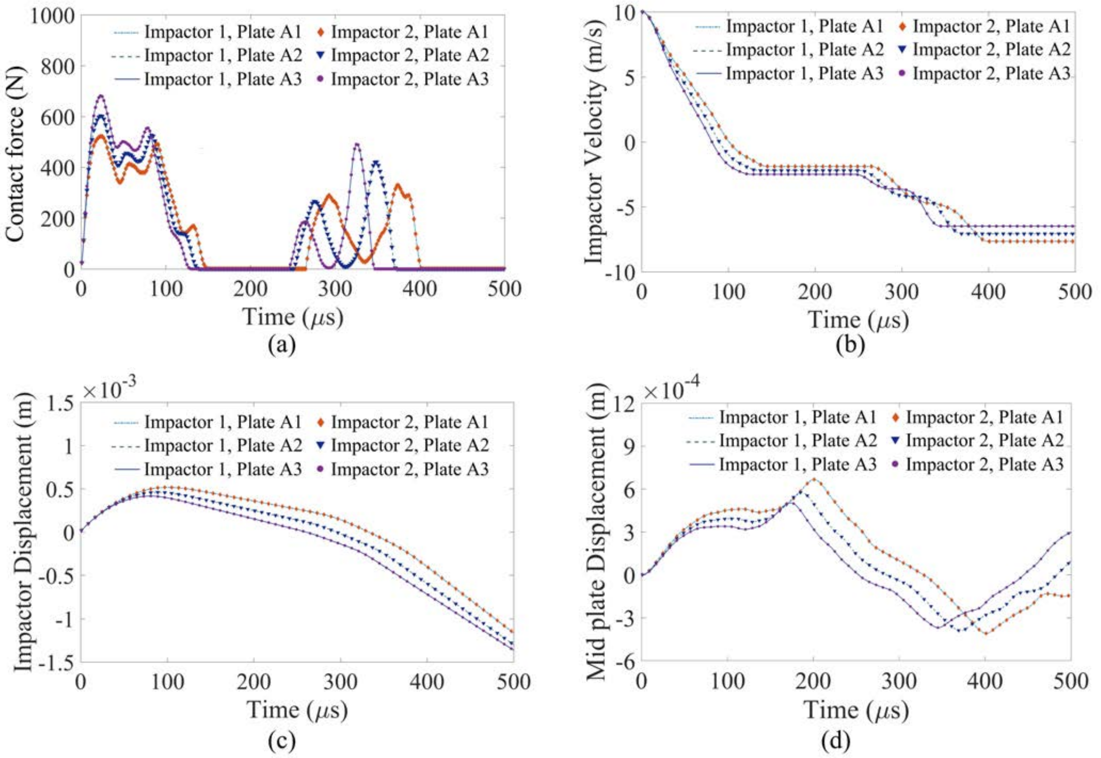

Figure 4.49: Effect of outer aluminium layer thickness on simultaneous multiple impact by two spherical impactors at 10 m/s

As observed, the contact force responses, impactor displacements and velocities and plate displacements at the two contact points are identical in case of simultaneous impacts for each case. It is seen from **Figure 4.49(a)** that the contact duration decreases with increasing thickness of the outer aluminium layers of the GLARE 5-2/1 plates as a result of increased stiffness, leading to a rise in contact force. Also, from **Figure 4.49 (a)** and **(b)** it is observed that with increasing overall thickness of the plates there is a lateral shift towards the left for the contact forces and velocity drops of the impactors respectively. It can be seen from **Figure 4.49 (c)** and **(d)** that the impactor and plate displacements vary inversely with the outer aluminium thickness.

4.6.4. Effect of delay between the two spherical LVIs

The plate A2 is taken for studying the impacts by the two impactors striking with a velocity of 10 m/s at symmetric locations and time delays $\Delta T = 20\mu s, 40\mu s$ and $80\mu s$ between them. The contact force histories and the dynamic responses for the plate and impactors are shown in **Figure 4.50** for $\Delta T = 40\mu s$ between the two successive impacts and **Figure 4.51** lists the same for $\Delta T = 20\mu s$ and $80\mu s$.

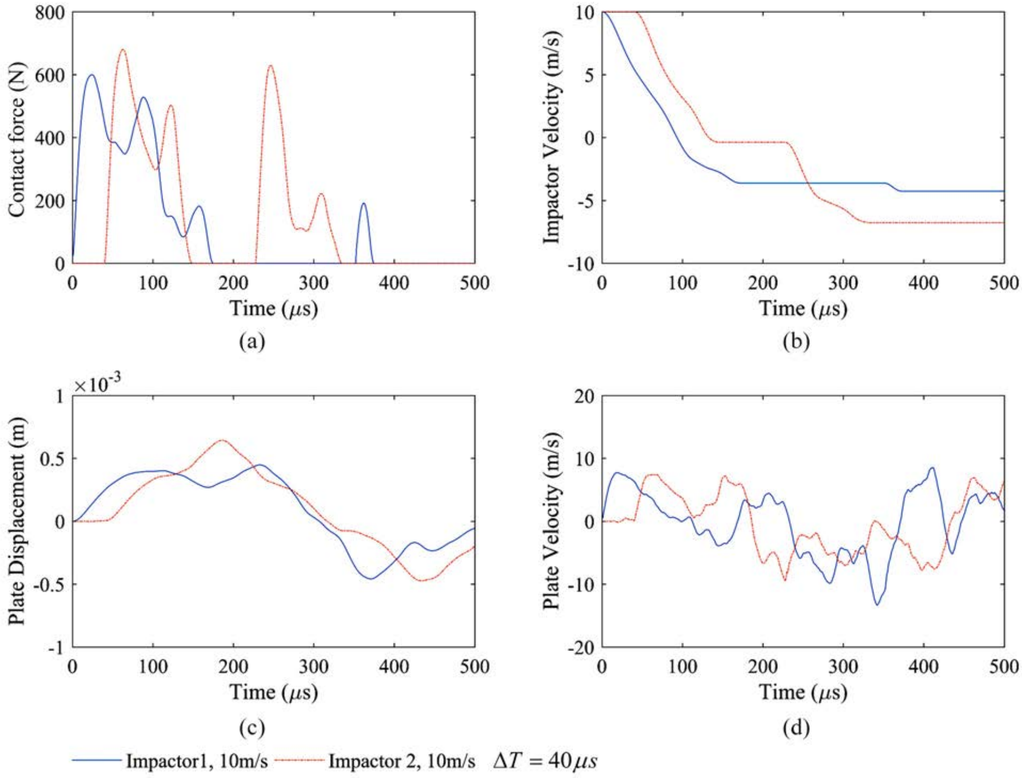

Figure 4.50: Impact responses of plate A2 for time delay of ΔT= 40 μs between the two impacts occurring at 10 m/s

It is observed from the contact force histories that as the time gap between the two successive impacts increases, the magnitude of the second impactor's maximum contact force increases and in case of $\Delta T = 80\mu s$ it is the maximum as can be inferred by comparing **Figure 4.49 (a)** and **Figure 4.50 (a)** and **Figure 4.51 (a)** and **(e)** for plate A2. The second impactor comes in contact twice and the intensity of the contact force for the second time for

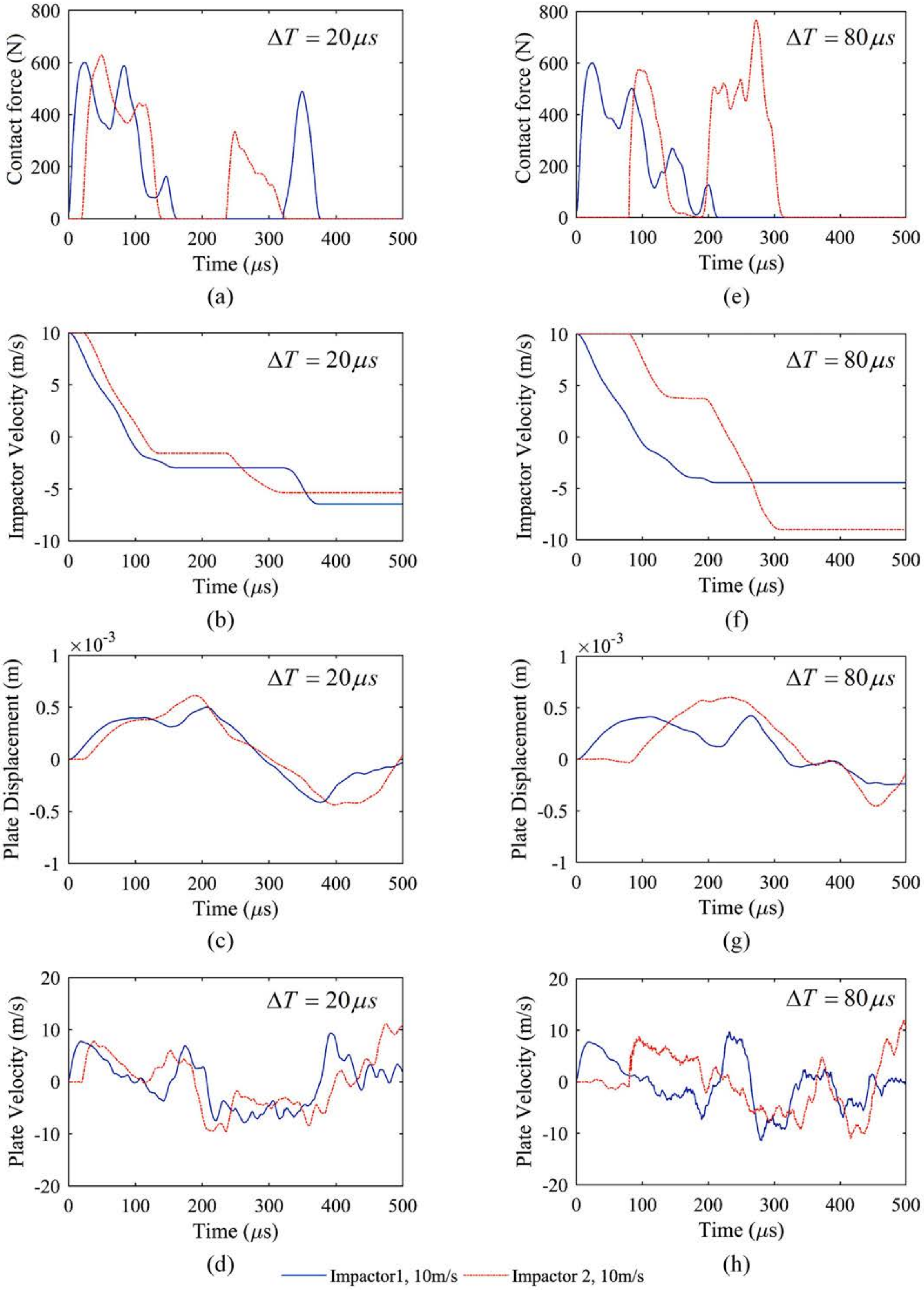

Figure 4.51: Impact responses of plate A2 for time delays of ΔT= 20 μs and ΔT= 80 μs between the two impacts occurring at 10 m/s

the first impactor decreases as the time between the two successive contacts increase. It is seen that the first impactor's contact is negligible for the second time as compared to the first time for $\Delta T = 40\mu s$ between the successive impacts (**Figure 4.50(a)**). The first impactor comes in contact only once for the case when the second impactor hits the plate $80\mu s$ after the first impact (**Figure 4.51(e)**). This is also evident from the velocity responses of the first impactor as seen from **Figure 4.50(b)** and **Figure 4.51(f)** considering plate A2 showing negligible to nil velocity drop after the first impact implying the first impactor does not come in contact for the second time as the time between the successive impacts increase. The reason for the increase in contact force of the second impactor with increasing time gap between the two impacts is because the plate velocity gradually increases (**Figure 4.50(d)** and **Figure 4.51 (d)** and **(h)**) with the first impact and more the delay in the second impactor's impact, greater is the plate velocity when meeting the second impactor. Thus, in case of multiple impacts, the maximum magnitude of the contact force is seen to be influenced by the time interval between the successive impacts.

4.6.5. Two Impactors striking with different velocities

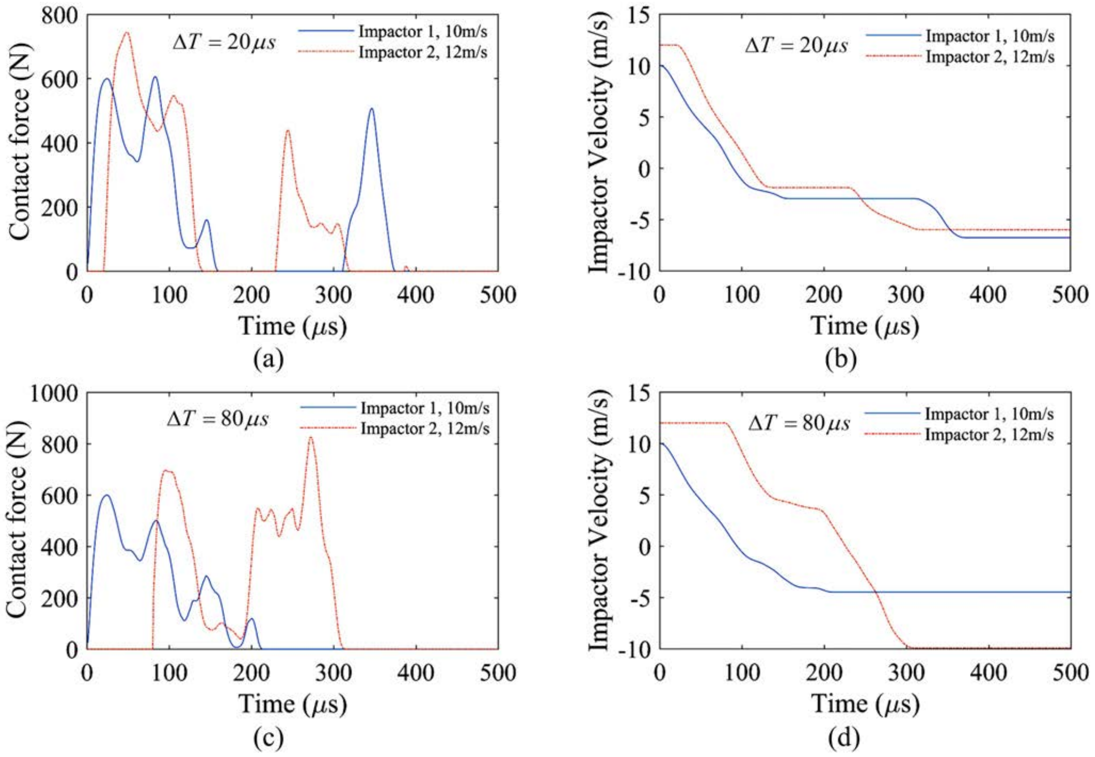

Figure 4.52: Contact force, impactor and plate velocities for impactors striking plate A2 at different velocities

The first and the second impactor hit the plate A2 at their respective locations with velocities 10 m/s and 12 m/s respectively and the contact force responses and impactor velocities are plotted in **Figure 4.52 (a)-(b)** and **Figure 4.52 (c)-(d)** for the impacts occurring at time intervals of $\Delta T = 20\mu s$ and $80\mu s$ respectively. A similar trend is observed for the two impacts as seen previously for the impactors striking at same velocities except for the fact that the contact force for the second impactor is higher owing to its higher velocity.

Comparing **Figure 4.52 (b)** and **(d)** clearly show that the impacts that occur at $20\mu s$ delay between them have two velocity drops with a constant velocity duration in between implying no contact with the plate during that period which can be seen by the zero contact force (**Figure 4.52(a)**) for that duration. Moreover, the impactors contact the plate only once when the time delay between the impacts is $80\mu s$ unlike the case when the second impact occurs at $20\mu s$ delay as evident from **Figure 4.52 (a)** and **(c)**.

4.6.6. Delamination at the interfaces

Going through the impact responses of the GLARE plates considering the various cases it is necessary to know the extent of interfacial delamination they undergo in such situations.

4.6.6.1. Influence of outer aluminium thickness

Figure 4.53 shows the extent of delamination at the bottom and top Al/composite interface 1 and 5 of the plates A1, A2 and A3 for the multiple impacts occurring simultaneously at 10 m/s. No delamination is seen at the inner composite interfaces for the impacts occurring at the symmetric impact sites at the considered impactor velocities. For the two multiple LVIs occurring simultaneously, the delaminations form a symmetric pattern in case of all the plates. The metal-composite interfaces of plate A1 undergo maximum extent of delamination and plate A3 the least. This is due to the presence of a thicker aluminium layer in plate A3 enabling the impact energies associated with the LVIs to be absorbed to a greater extent. This highlights the influence of the MVF of the aluminium layers along with the outer aluminium layer thickness in a given GLARE FML. It is seen that the delaminations coalesce to single larger delamination in case of plate A1 and in case of plate A2 although they coalesce, the extent is smaller and the least for plate A3 where the delaminations are separately formed around the impact locations. The bottom interface undergoes more delamination in comparison to the top interface and the out-of-plane bending causes the developed interfacial shear stresses to initiate debonding at the aluminium composite interface.

4.6.6.2. Influence of delay between the impacts

For the same impact locations as previous and the identical impactors striking at 10 m/s, the effect of the time delay between the two successive LVIs on the progression of interfacial

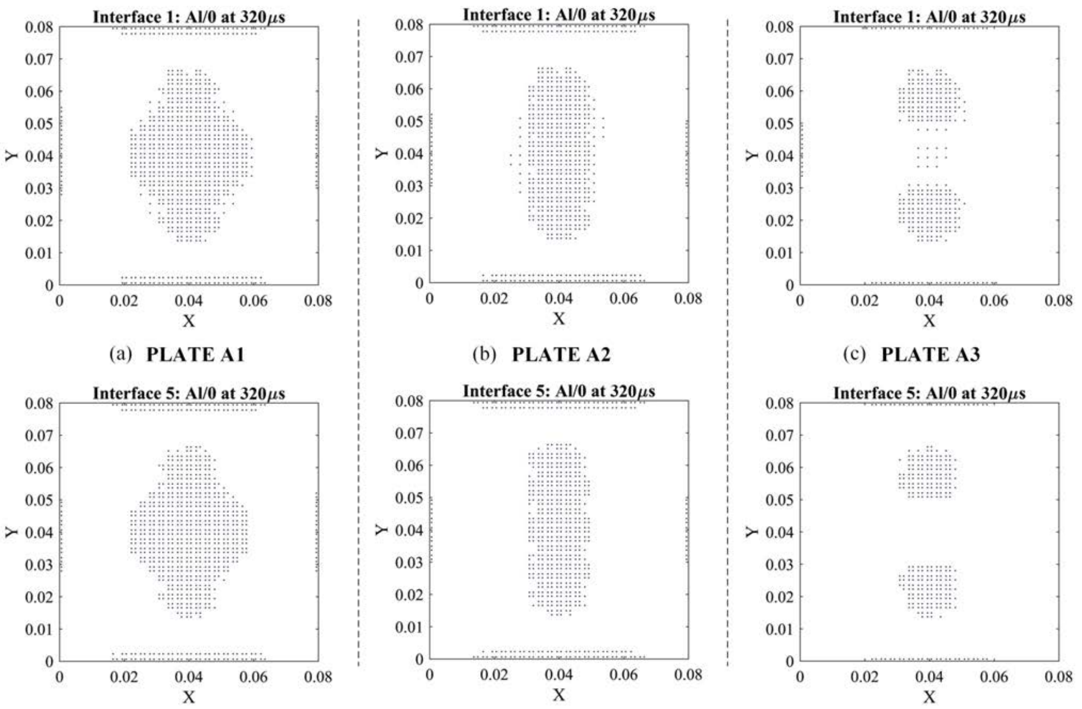

(a) **PLATE A1** (b) **PLATE A2** (c) **PLATE A3**

Figure 4.53: Delamination at the bottom and top interfaces of plates A1, A2 and A3 for LVIs at 10 m/s

delamination is studied for the time intervals $\Delta T = 20\mu s, 40\mu s$ and $80\mu s$ as shown in **Figures 4.54-4.56**. Comparing **Figure 4.53-4.56** show that the extent of delamination varies with the time gap between the two successive impacts. For simultaneously occurring LVIs (**Figure 4.53(b)**), the delaminations coalesce to form a single continuous debonded area, and as the time gap increases, the delaminations gradually remain unmerged. Furthermore, as seen from the contact force responses for the impacts occurring at different time intervals (refer to **Figure 4.50** and **Figure 4.51**), where the second impact attributes to a higher contact force, the delamination around the second impact location (x=0.04 m, y=0.06 m) tends to be more significant as evident from **Figures 4.54-4.56** and the delaminations are not symmetric, unlike the case for multiple simultaneous impacts occurring at symmetric locations. It is seen that the extent of delamination is marginally more for the bottom interface (interface-1). It is observed that the spread of the delamination around the impact location tends to be along the fibre direction of the 0° S2-glass/epoxy ply (x-direction) adjacent to the aluminium layer for the GLARE laminate and more pronounced for the thinner GLARE plate A1 (**Figure 4.53(a)**) forming an elliptical delaminated area at the top and bottom interfaces. It is also evident for the GLARE plate A2 (**Figures 4.54-4.56**) where a higher contact force of the second impactor's impact, results the delaminated area to form an elliptical shape around the impacted location.

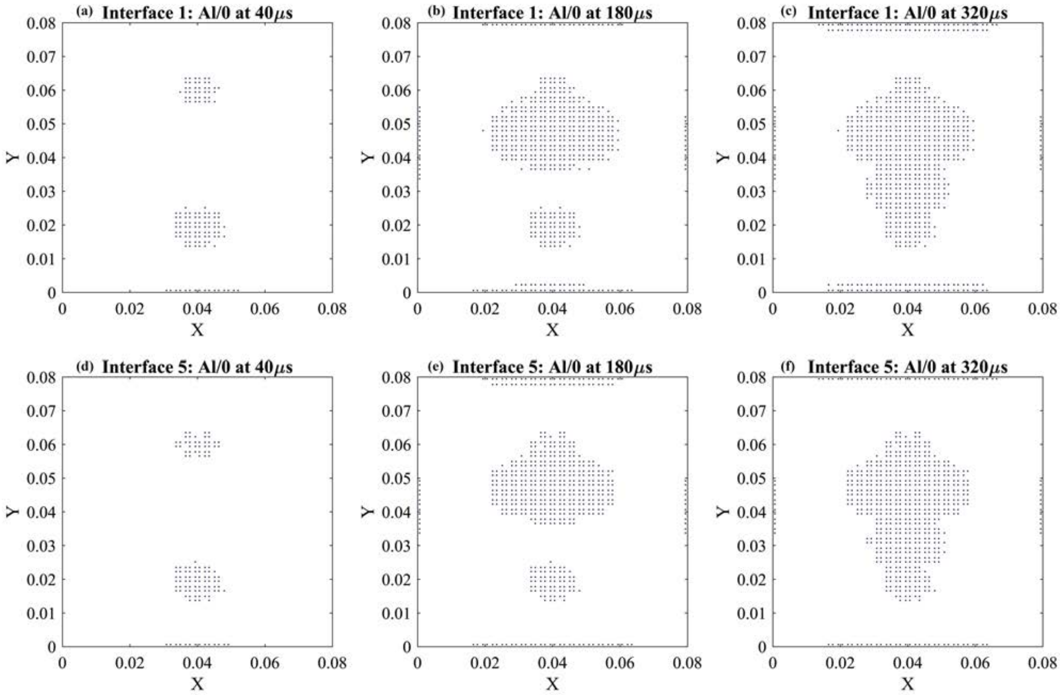

Figure 4.54: Delamination at the bottom (interface 1) and top (interface 5) interfaces of plate A2 for impacts at 10 m/s and time delay of 20 μs between the two impacts

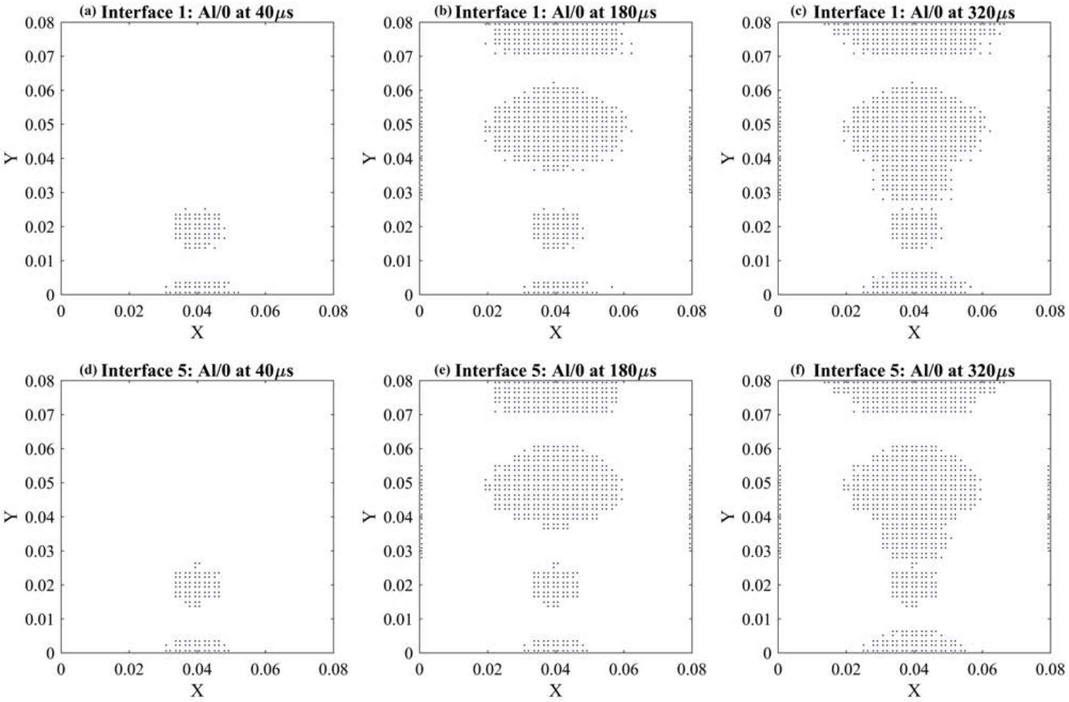

Figure 4.55: Delamination at the bottom (interface 1) and top (interface 5) interfaces of plate A2 for impacts at 10 m/s and time delay of 40 μs between the two impacts

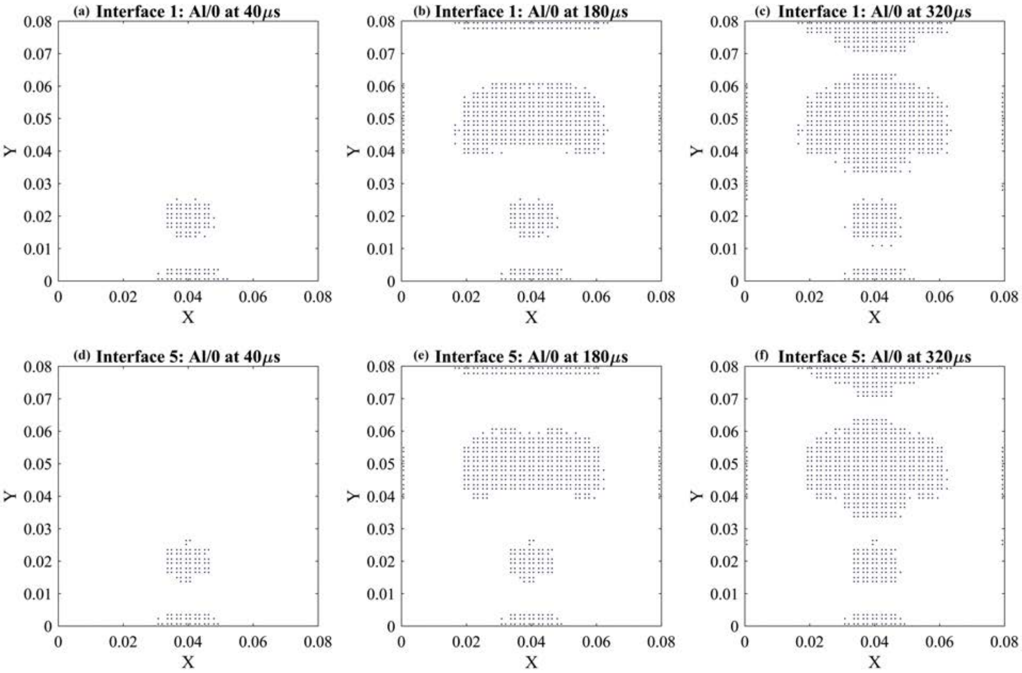

Figure 4.56: Delamination at the bottom (interface 1) and top (interface 5) interfaces of plate A2 for impacts at 10 m/s and time delay of 80 μs between the two impacts

4.6.6.3. Influence of different impactor velocities

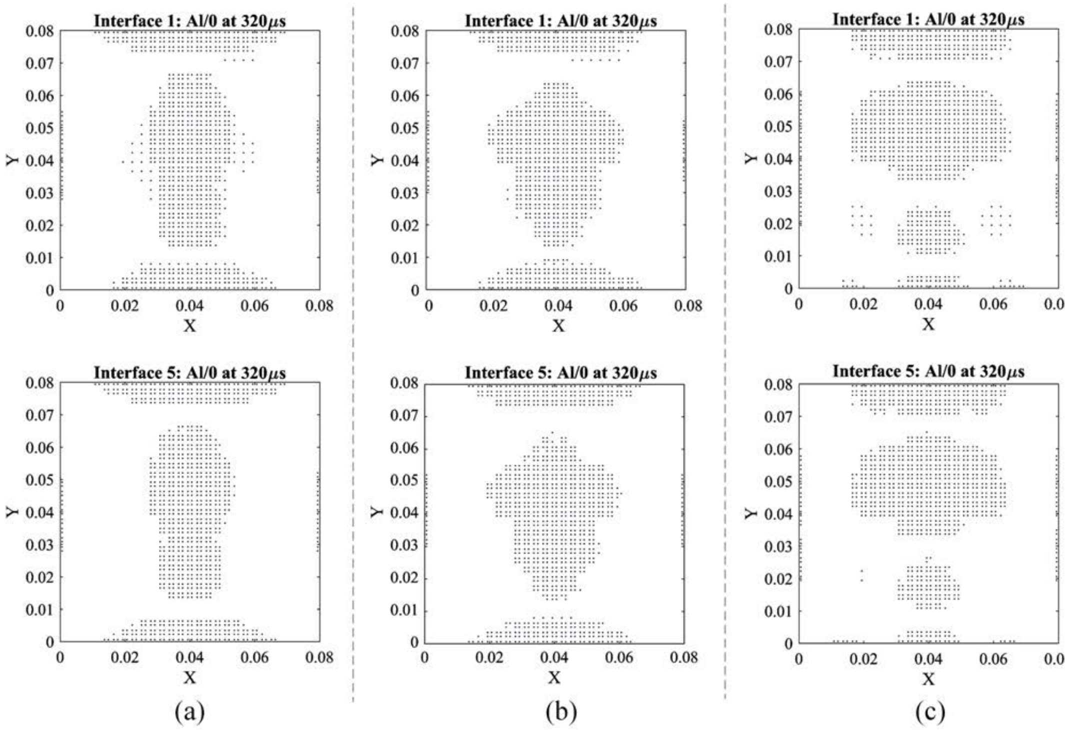

Figure 4.57: Delamination at the Al/0° interfaces of plate A2 for LVIs occurring at 10 m/s (x=0.04 m and y=0.02 m) and 12 m/s (x=0.04 m and y=0.06 m) and time delay of (a) 0 μs (b) 20 μs and (c) 80 μs

The delaminations are unsymmetrical for the impacts occurring at different impactor velocities of 10 m/s and 12 m/s. As expected, the extent of delamination is more for the impact location with a higher impact velocity of 12 m/s (x=0.04 m, y=0.06 m), as shown in **Figure 4.57**. The delaminations do not merge for the increased time delay of $80\mu s$ between the two impacts, and the delamination at interface-1 is comparatively more than at interface-5, as seen in earlier cases.

4.6.7. Effect of stacking configuration

To understand the effect of stacking configuration on the contact response as well as the associated delamination, the LVIs at 10 m/s were studied for simultaneous impacts and for a delay of $80\mu s$ on a clamped GLARE 4-3/2 plate B1 at the mentioned locations. **Figure 4.58** shows a similar trend for the contact force history, although the contact force peaks attained are comparatively higher and comparable to that of the GLARE 5 plate A3 (refer to **Figure 4.49**). This shows that even though the total thickness of the plate directly influences the contact force, the effect of outer aluminium layer thickness is much more significant.

Moreover, the delamination at the inner metal/composite interfaces occur near the impact sites. When the LVIs occur simultaneously, the delaminations at the impact sites grow and coalesce at the bottommost and topmost composite/aluminium interfaces, as seen in **Figure 4.59**. At the top interface-8, it is in the form of a peanut shape, and compared to the other interfaces, the extent of delamination is maximum at the bottom interface-1. When the LVIs occur with a delay of $80\mu s$ between them, the delaminations occurring near the impact sites do not coalesce, and the extent of delamination is more within the area of the LVI by the second impactor, as seen from **Figure 4.60**. Further, it is seen that the delamination at the $0^\circ/90^\circ$ composite ply interfaces is confined within the impact locations and tends to grow along the underlying fibre direction.

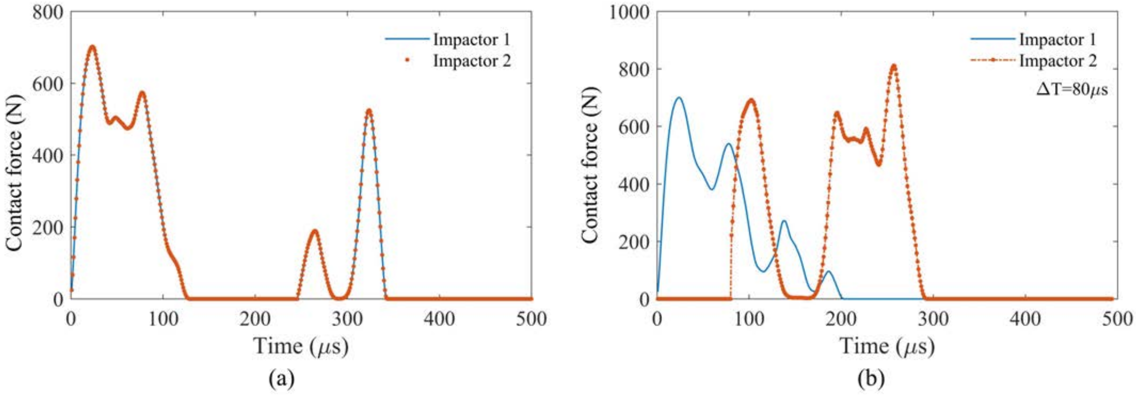

Figure 4.58: Multiple spherical LVI on plate B1 at different time intervals

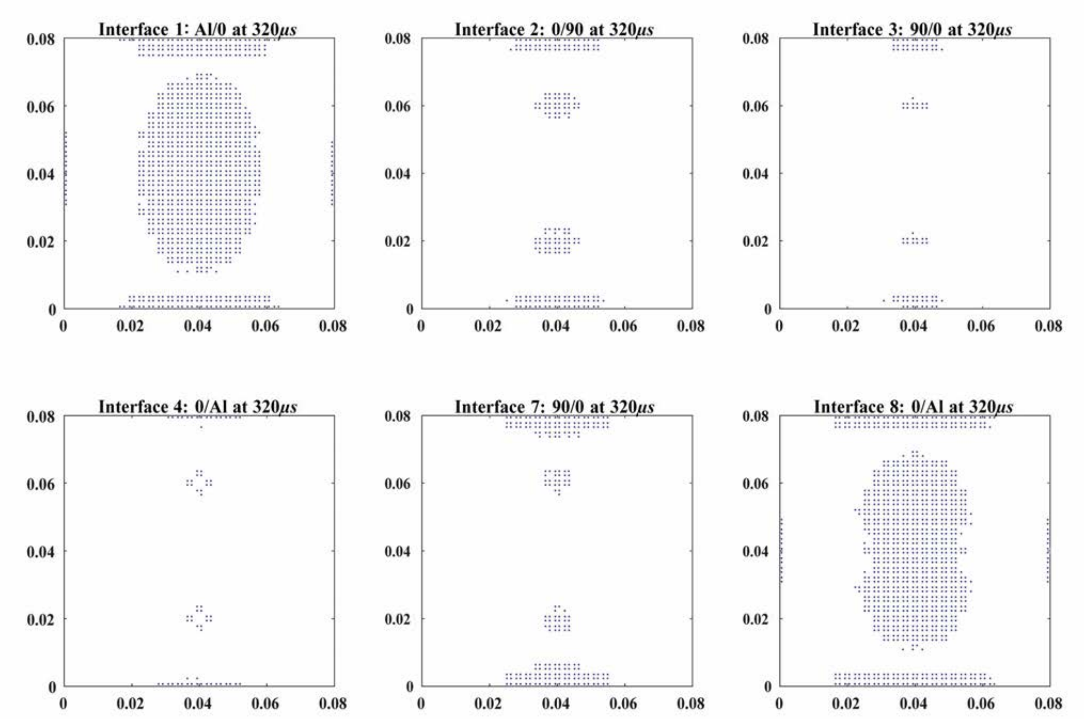

Figure 4.59: Delamination at the Al/0 ° interfaces of plate B1 for LVIs occurring at 10 m/s (x=0.04 m and y=0.02 m) and 10 m/s (x=0.04 m and y=0.06 m)

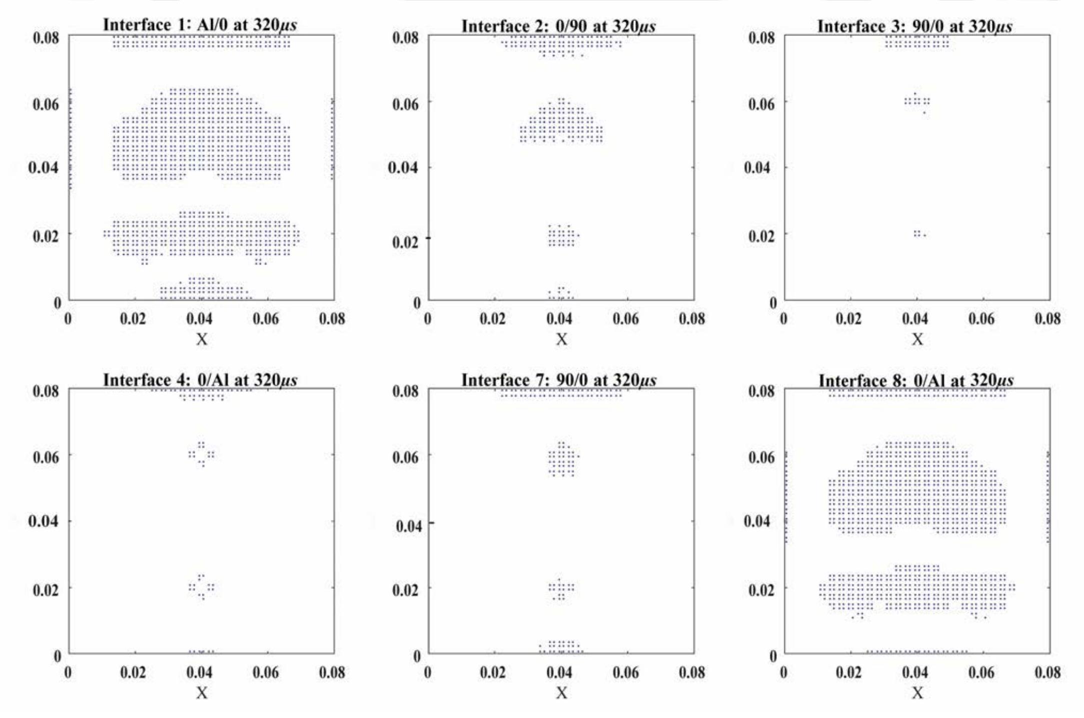

Figure 4.60: Delamination at the Al/0 ° interfaces of plate B1 for LVIs occurring at 10 m/s (x=0.04 m and y=0.02 m) and 10 m/s (x=0.04 m and y=0.06 m) and time delay of 80 μs

4.7. Summary

The LVI responses of GLAREs are evaluated using the developed FE code, and the influence of the impactor mass and plate parameters like the plate geometries and stacking configurations on the impact response and the extent of delamination has been investigated. In addition, the multiple LVIs on a GLARE plate have been investigated to observe the effect of time intervals between the impacts and other associated important parameters. In view of the weight-saving goal, the LVI responses by incorporating Kevlar-49/epoxy layers to form hybrid GLARE laminates have been explored. Important conclusions drawn are as follows:

- Ratio of the impactor mass to the plate mass plays a significant role in the contact impact response of GLARE, both in terms of magnitude and duration of the contact force and the consequential delamination at the interface.

- A higher magnitude of contact force is associated with the smaller mass impacts for the same impact energy. As a result, the extent of delamination damage is more for the impacts by the smaller mass impactors than for the impacts by a larger mass impactor. Therefore, the small-mass impacts are more critical.

- Mass of the impactor decides the nature of evolution of the interfacial stresses and hence influences the extent of delamination at the interfaces.

- The effect of plate geometry can be seen on the magnitude of the contact force in case of the LVIs which influences the delamination at the interfaces in both high and low mass LVIs. The plate geometry affects the rebound response in case of small mass impacts.

- For the impacts by the larger mass impactor, the delamination region at the aluminium/composite interfaces is confined within the impact location, unlike the small mass impacts.

- Although the impactor velocity is an important parameter in classifying the impact event, the response type is significantly influenced by the impactor/plate mass ratio rather than the impactor velocity alone. The use of impactor velocity for the classification of the impact events is highly relative, and its effect is visible on the amplitude of the response. In contrast, the mass of the impactor influences the duration of the impact.

- LVI can cause internal damage to laminated structures by initiating delamination at the interfaces, and the fibre-metal interfaces are the sites prone to delamination, which tends to progress along the fibre direction of the underlying ply.
- The effect of increasing the thickness of outer aluminium layer is clearly seen by the noticeable rise in contact forces which is greater than for the case of increasing the number of glass/epoxy layers for a plate with same overall thickness. This highlights the influence of MVF.
- Increasing the outer aluminium thickness shows a decrease in the extent of delamination which may be due to more amount of energy absorbed by the outer aluminium layer.
- Stacking sequence affects the extent of delamination at the interfaces. GLARE 5-2/1 plate with $[Al/0^{\circ}/90^{\circ}]_S$ configuration was found to have the least extent of delamination at the interfaces.
- Replacing the middle aluminium layer with Kevlar-49/epoxy laminates improves the overall impact characteristics of the hybrid laminate. Introducing lower density Kevlar-49/epoxy laminates makes plate AGK the lightest compared to the plates AGA and AGKGA, enabling it to respond quickly to an impact. This clearly reveals that the relative inertias of both the impactor and the plate are important aspects in the response of a laminate subjected to LVI and it cannot be solely described by the impactor or the target.
- In case of multiple LVIs, interfacial delamination at the aluminium/composite interfaces initiates close to and around the impact sites, and the delaminated region tends to merge to form a continuous region.
- In estimating the extent of delamination, particularly at the fibre/metal interfaces, the delay between the LVIs has a significant influence. When there is more time between two subsequent impacts, the delaminations around the affected sites tend to remain discrete. However, when there is less time between the impacts of the two impactors, they combine to create a single delaminated area.
- Time elapsed between the two impacts affects the second impact's contact force's amplitude.

Chapter 5

Impact response of GLARE plates having open holes

From the review of literature in **Chapter 2**, it was seen that the discontinuities in the form of cut-outs or open holes could significantly affect the impact performances. Stressing the importance of studying such aspects in GLARE, the present chapter investigates the impact performances of such GLARE plates having cut-outs and their positions relative to the impact site.

5.1. Introduction

Many structural components involving composite materials require existence of open holes to allow passage for access to inner components like wires, pipes and assemblies or for maintenance activities. The laminated structures being susceptible to delamination when subjected to low-velocity impact, it is important that investigation of the impact response for such components having open hole be done to assess their safety and integrity. The presence of such discontinuities in the form of cut-outs or open holes can have significant influence on the way delamination grows around these locations due to increased stress concentrations under transverse loads [125] on account of LVIs. The central cut-out reduces the effective stiffness of the plate. As a result, the presence of a cut-out generally leads to an increase in plate deflection for a given load and the extent of the stiffness reduction depends on the size and shape of the cut-out. Therefore, it is important to study the LVI response of such panels having open holes and accurately estimate the underlying delamination at the interfaces such that it enables prompt repair/replacement of components, preventing catastrophic accidents. FE analysis have been performed using the developed FE code and the LVI response of GLARE laminates with cut-outs have been studied.

5.2. GLARE plate with central cut-out subjected to offset LVI

In the present section, the LVI responses of a GLARE plate with a central circular hole subjected to impact by a steel spherical impactor are investigated. The effect of offsetting the impact relative to the hole position on the contact response and delamination at the interfaces are assessed. Further, the effect of hybridisation with Kevlar-49 layers are evaluated for the impact responses and the delamination at the interfaces are assessed. Influence of important geometrical parameters like effect of hole size and their positions relative to the impact point are explored.

5.2.1. Problem definition

The impact responses of a clamped GLARE 5-2/1 laminate having a central circular cut-out and subjected to offset LVIs as shown in **Figure 5.1** is studied. The 100 mm × 100 mm clamped GLARE plates having a 8 mm diameter central cut-out is subjected to a normal impact at different offset locations along x-direction (x1=8 mm, x2=16 mm and x3=25 mm; y1= y2=y3=0) from the centre by a 10 mm diameter spherical steel impactor (ρ=7800 kg/m^3 and E=200 GPa) at 10 m/s and the dynamic responses are evaluated. Furthermore, the effect of change in the cut-out shape from circular to a square cut-out of sides 8 mm is studied on the dynamic responses and associated delamination has been studied. **Table 5.1** [45,138,205–208] lists the material properties used in the FE model along with the strength parameters and the details of the plate configurations are given in **Table 5.2**.

Table 5.1: Material parameters of S2-glass/epoxy and Kevlar-49/epoxy [45,138,205–208]

Parameter	Notation	UD S2-glass/FM94-epoxy prepregs (G)	UD Kevlar-49/epoxy (K)
Density (kg/m^3)	ρ	1980	1390
Poisson's ratio	υ	$\upsilon_{12} = 0.33$, $\upsilon_{23} = 0.33$	$\upsilon_{12} = 0.34$, $\upsilon_{23} = 0.34$
Young's modulus (GPa)	E	$E_1 = 55, E_2 = 9.5$	$E_1 = 75, E_2 = 5.5$
Shear Modulus (GPa)	G	$G_{12} = 5.5, G_{23} = 3.5$	$G_{12} = 2.2$, $G_{23} = 1.8$
Yield strength (MPa)	σ_{ys}	———	———
Transverse tensile strength (MPa)	Y_T	50	21
Transverse compressive strength (MPa)	Y_C	160	130
In plane shear strength (MPa)	S_{lt}	70	66
Interlaminar shear strength (MPa)	*ILSS*	50	48

Table 5.2: Plate details

	Plate configurations			
Plate Code	A1	A2	A3	A4
Layup details	$[\mathrm{Al}/0_G/90_G]_S$	$[\mathrm{Al}/0_K/90_K]_S$	$[\mathrm{Al}/0_G/90_K]_S$	$[\mathrm{Al}/0_G/0_K/90_K]_S$
Central cut-out type	Circular and Square	Circular	Circular	Circular
Al thickness (mm)	0.452	0.452	0.452	0.342
S2-glass/epoxy ply (mm)	0.158	-------	0.158	0.142
Kevlar-49/epoxy ply (mm)	-------	0.158	0.158	0.142
Total thickness (mm)	1.536	1.536	1.536	1.536

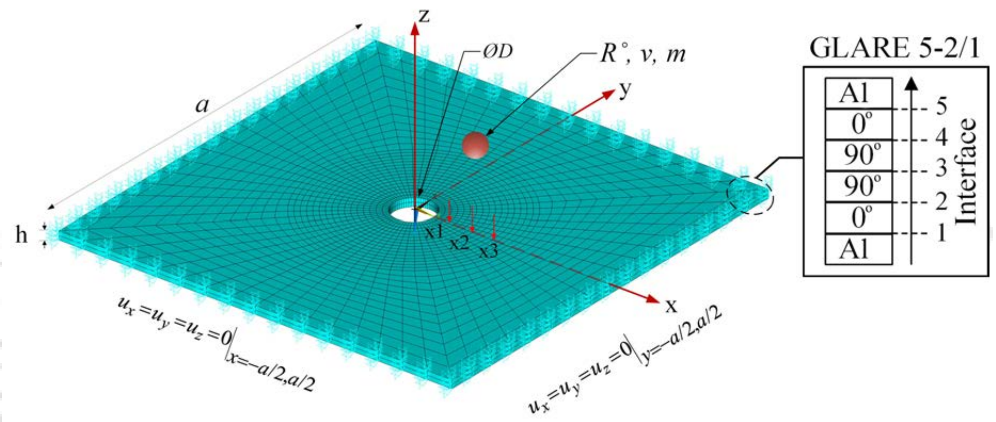

Figure 5.1: Clamped GLARE plate with central cut-out subjected to offset LVI

5.2.2. Effect of impact offset from centre

To observe the influence of the impact offset distance from the centre, plate A1 is subjected to LVI at locations x1=8 mm, x2=16 mm and x3=25 mm from the centre along x-direction and their impact responses are shown in **Figure 5.2(a)-(d)**, comparing the same to that of a plate without hole. It is seen that with decreasing offset distance from the hole centre, the contact force peak reduces and the plate deflection increases. This is evident due to the presence of the circular cut-out, which further reduces the flexural stiffness near to the centre resulting in higher deflections. As the distance of offset increases and the impact location shifts closer to the plate boundary, the increasing bending stiffness results in higher peaks of the contact forces and also the overall contact time decreases. When the impact is at location x1, the rebound behaviour of the impactor is delayed compared to the impacts at locations x2 and x3. There is a continuous velocity drop for the impacts occurring at locations x2 and x3 with a very short region of constant velocity for impact at location x2 and negligible at x3 (**Figure 5.2(c)**). At location x1, the impactor has a longer constant velocity region during which the plate displacement is greater (**Figure 5.2(d)**) than the impactor displacement (**Figure 5.2(b)**). This is because as the impact location is closer to the plate centre, the lower bending stiffness of the plate near the plate centre make it more compliant. This results in a quicker response of the plate to the incoming impact and a higher plate deflection compared to the other two locations (x2 and x3). The rebound response occurs when the plate from its peak position reverses its motion and recontact occurs at around 300 μs. Moreover, for a plate without hole, the impact responses were similar to those of a plate with hole for the impact offsets of 16 mm and 25 mm in terms of peak contact force and displacements. But, for the impact offset of 8 mm, the plate without hole shows higher contact force peak and lower impactor and plate displacement. This shows that the presence of a cutout can significantly lower the stiffness near its vicinity.

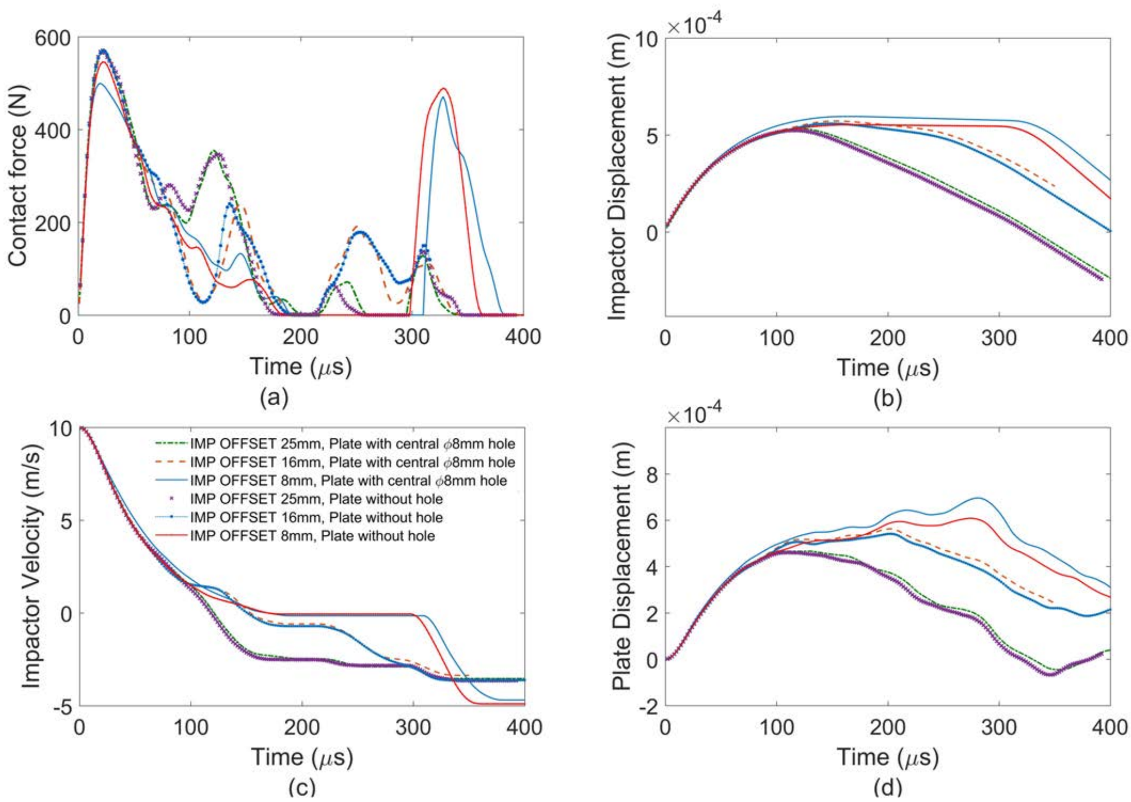

Figure 5.2: LVI on a GLARE 5 plate A1 at different offset distances from the centre

5.2.3. Effect of hybrid plate configurations

The contact force histories and impactor displacements are compared for the LVI on plates A1, A2, A3 and A4 for impact at an offset distance of 8 mm from the centre, as shown in **Figure 5.3**. The overall plate thicknesses are kept same to have a uniformity in comparing their dynamic responses. It is seen that replacing all the S2-glass/epoxy plies with Kevlar-49 layers as in plate A2 and replacing only the inner 90 ° S2-glass/epoxy plies as in plate A3 such that the metal volume fraction is kept constant (MVF=0.588) do not cause a significant change in the peak contact forces attained when the outer aluminium thickness is the same. But for the case of plate A4, where the outer aluminium thickness is reduced from 0.452 mm to 0.342 mm such that the MVF=0.445, there is a drop in the peak contact force as seen in **Figure 5.3(a)**, and the impactor displacement is maximum (**Figure 5.3(b)**). There is a slight shift towards the left for the contact forces during the rebound phase when inner Kevlar49 layers are present. This shift is due to the change in the overall flexural stiffness of the plate and the net plate mass, which affect their response behaviour because of the difference in their inertia. As seen from **Figure 5.3(b)**, the peak impactor displacements tend to increase when more Kevalr-49 layers are present for the same MVF.

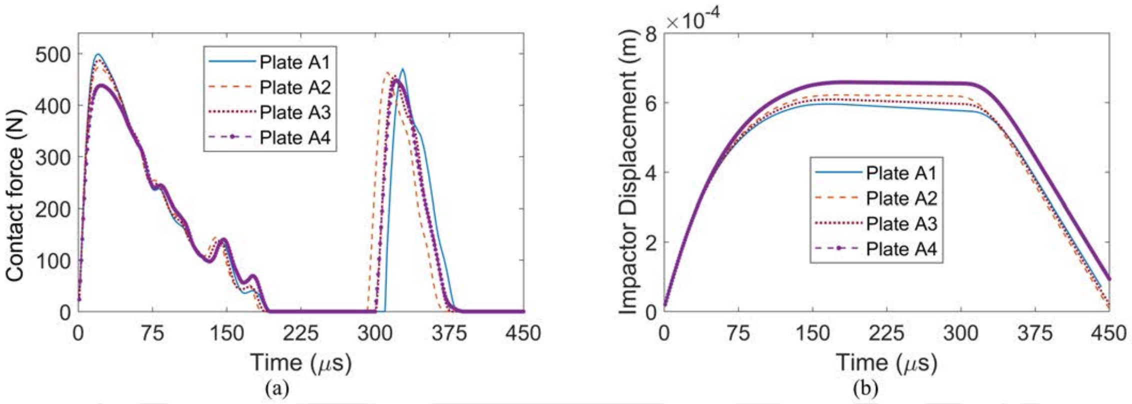

(a) (b)

Figure 5.3: (a) Contact force and (b) Impactor displacements for LVI at 10m/s on plates A1, A2, A3 and A4

5.2.4. Delamination at the interfaces

In the case of LVIs, interfacial delamination can cause significant damage to a structure, compromising its safety. The delamination at the interfaces is assessed and compared for the plates A1, A2, A3 and A4 considered in the present study.

5.2.4.1. Effect of Impact Offset Distance

Figure 5.4(a)-(d) show the delamination at the interfaces for plate A1 for the different impact offsets on a plate with central hole and at interface-1 for the GLARE plate without hole. It is seen that the extent of delamination is greater for the plate having central hole for all the three impact locations. Moreover, the delamination at the metal/composite interfaces are localised within the impact region in case of the plate without any hole. For the plate with hole, increasing offset distance from the centre reduces the delamination near the hole periphery, and in all cases, the delamination at the bottom aluminium/composite interface-1 is maximum. The delamination at the inner composite interfaces is centered around the impact site and becomes negligible when the impact offset distance increases. The delamination propagates along the underlying fibre direction and towards the hole edges.

When the impact offset distance is 25 mm from the hole centre, the delamination at the top interface-5 does not form a continuous patch up to the hole boundary, although local delamination at the hole periphery occurs in all cases.

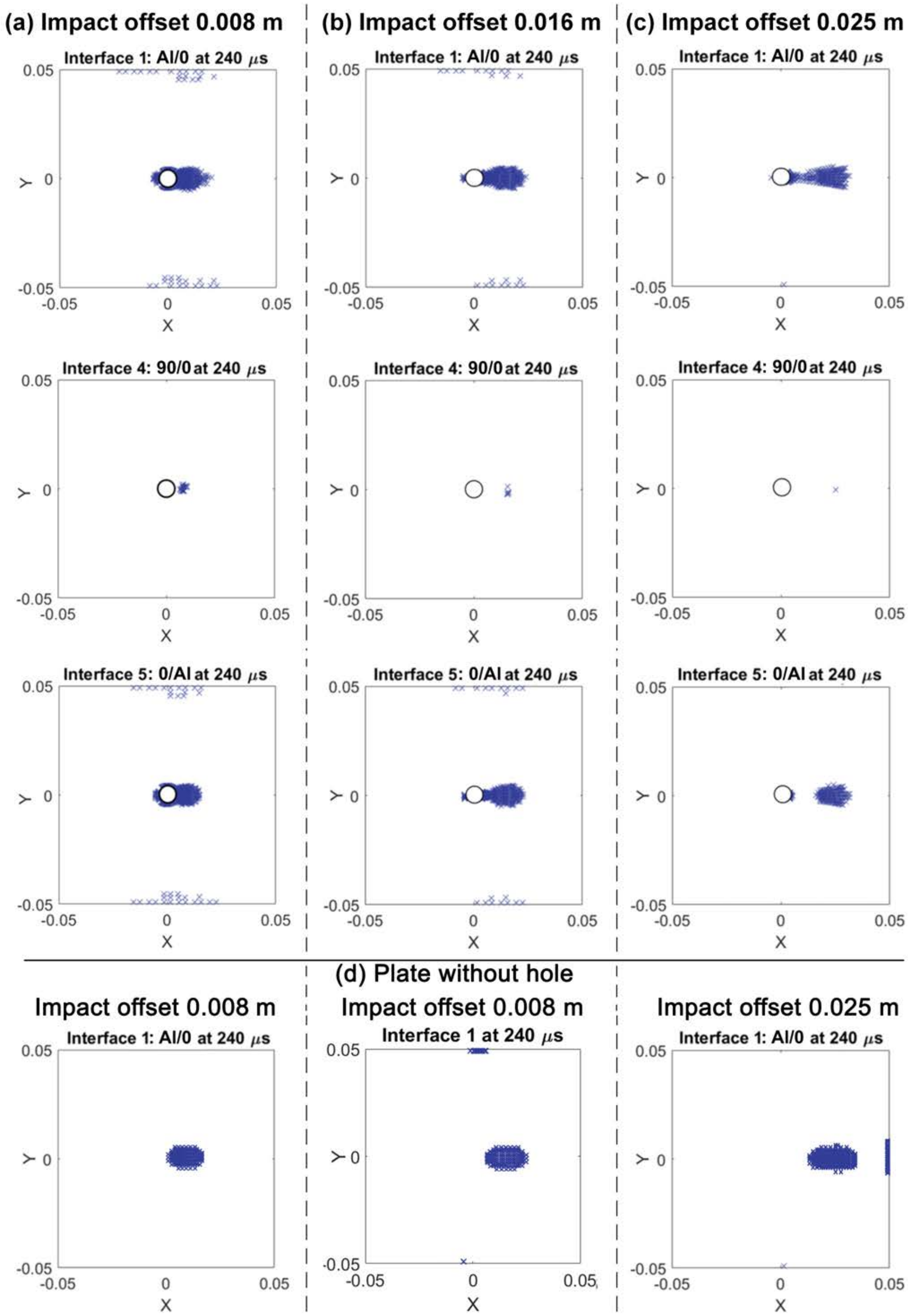

Figure 5.4: Delamination at the interfaces of plate A1 for different impact offset distances

5.2.4.2. Effect of cut-out shape

To see the effect of the cut-out shape, a square cut-out of sides 8 mm is made in plate A1 (standard GLARE 5-2/1) and the contact responses are recorded. From **Figure 5.5(a)** it is observed that the peak contact forces corresponding to the different offset locations are almost same as for the case of plate A1 having a circular cut-out and the impactor displacements also follow a similar trend in their variation with the impact offset distance (**Figure 5.5(b)**).

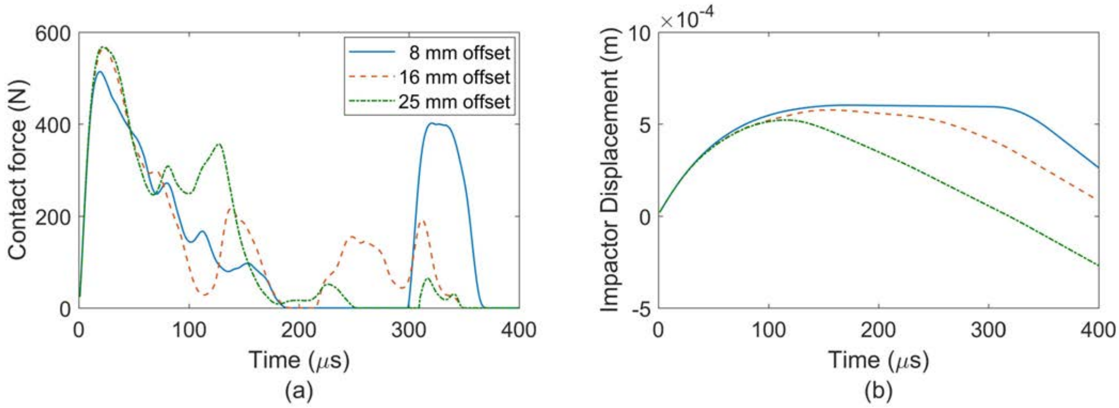

Figure 5.5: Effect of square cut-out on the (a) contact force and (b) impactor displacement

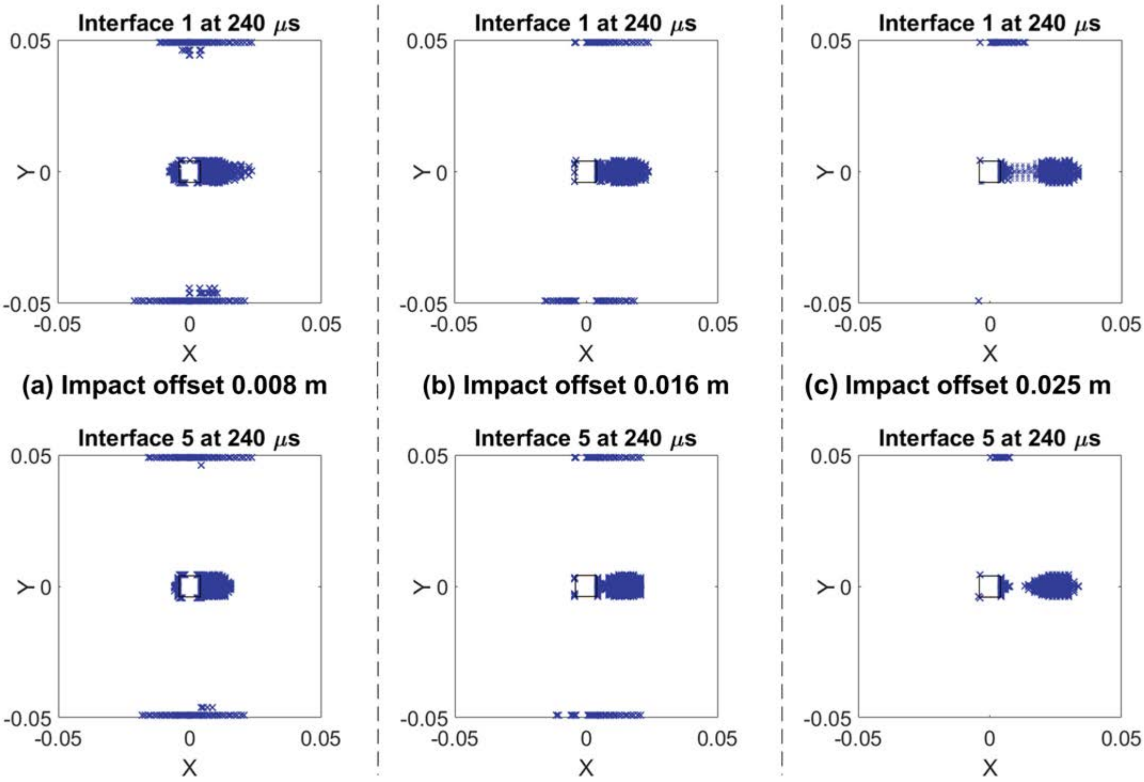

Figure 5.6: Delamination for different impact offsets for plate A1 having square cut-out

Although, the contact responses are seen to be similar, the delamination at the metal/composite interfaces of the GLARE plate A1 is comparatively more in case of a central square cut-out compared to that having a circular cut-out as can be inferred by comparing **Figure 5.4** and **Figure 5.6** for the different imapact offset distances. From **Figure 5.6(a)-(c)** it is seen that the delamination around the cut-out edges is more, and for the case when impact offset is 25 mm, the delamination around the edges of the square cut-out is visibly greater compared to that of a cicular cut-out (refer to **Figure 5.4**). Also, at the edge corners, some delamination initiates which may be attributed to higher stress concentration zones near the corners compared to a circular hole.

5.2.4.3. Effect of hybrid configurations

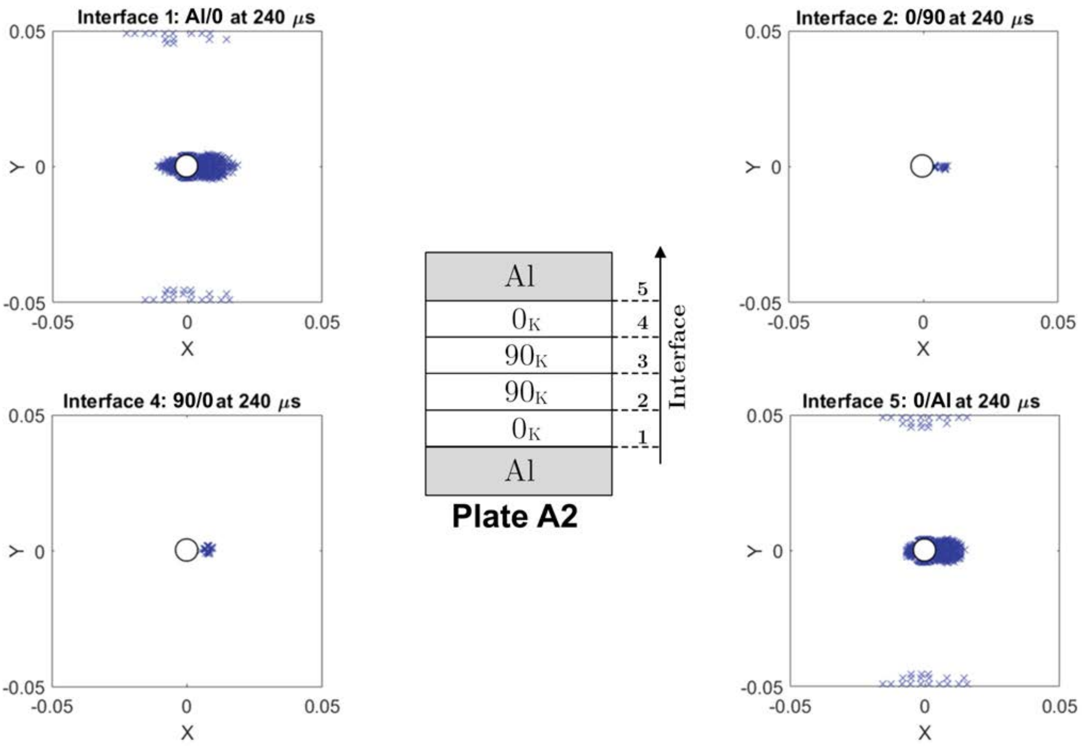

Figure 5.7: Delamination at the interfaces of plate A2 for offset 0.008 m

Although the contact responses for plates A1, A2 and A3 are similar in terms of the peak forces attained, the differences in the material properties of the inner composite plies in plates A2 and A3 can significantly influence the contour of delamination at the interfaces. **Figure 5.7Figure 5.9** show the delamination at the interfaces for plates A2, A3 and A4 for LVI at 10 m/s at an offset distance of 8 mm (location x1) from the centre. Comparing the delamination for the plates A1, A2 and A3, the delamination at the inner interfaces for the plates are more or less the same but at the aluminium/composite interfaces, the plates A1 and A3 shows lesser (similar delaminated area in A1 and A3) extent of delamination compared to that in the case of plate A2. It is seen that for the configuration A4, although the peak contact force was found to be less (refer **Figure 5.3(a)**), the extent of delamination at the metal/composite interfaces is maximum, highlighting the effect of outer aluminium layer thickness in arresting delamination on account of LVI.

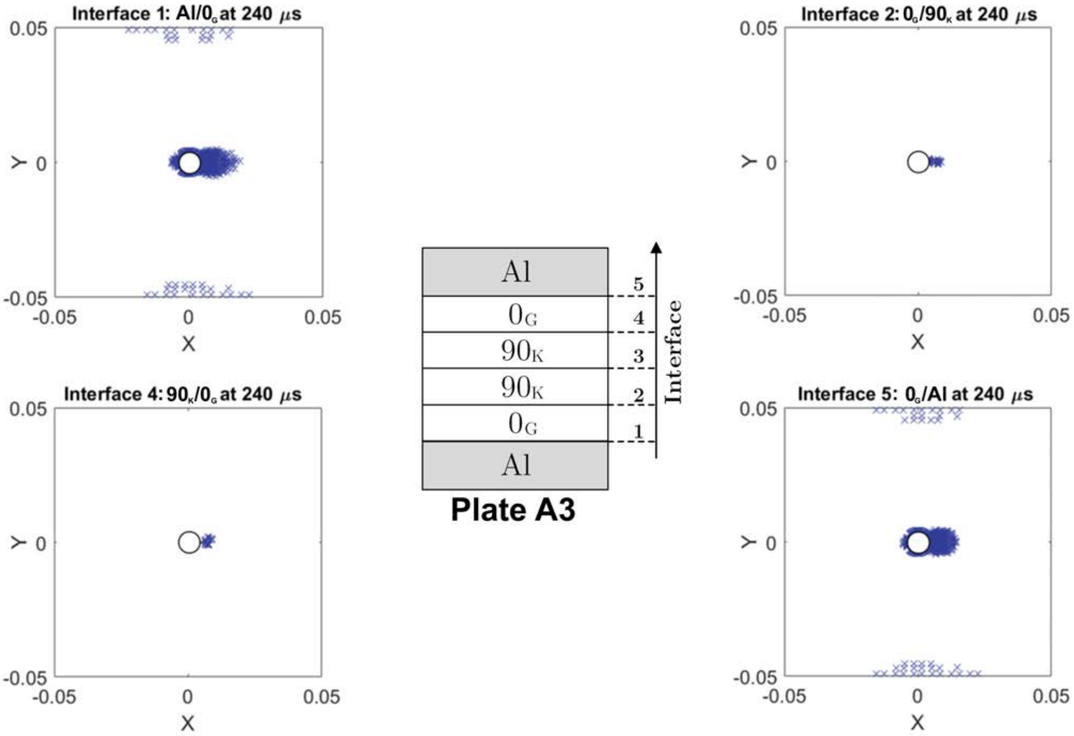

Figure 5.8: Delamination at the interfaces of plate A3 for offset 0.008 m

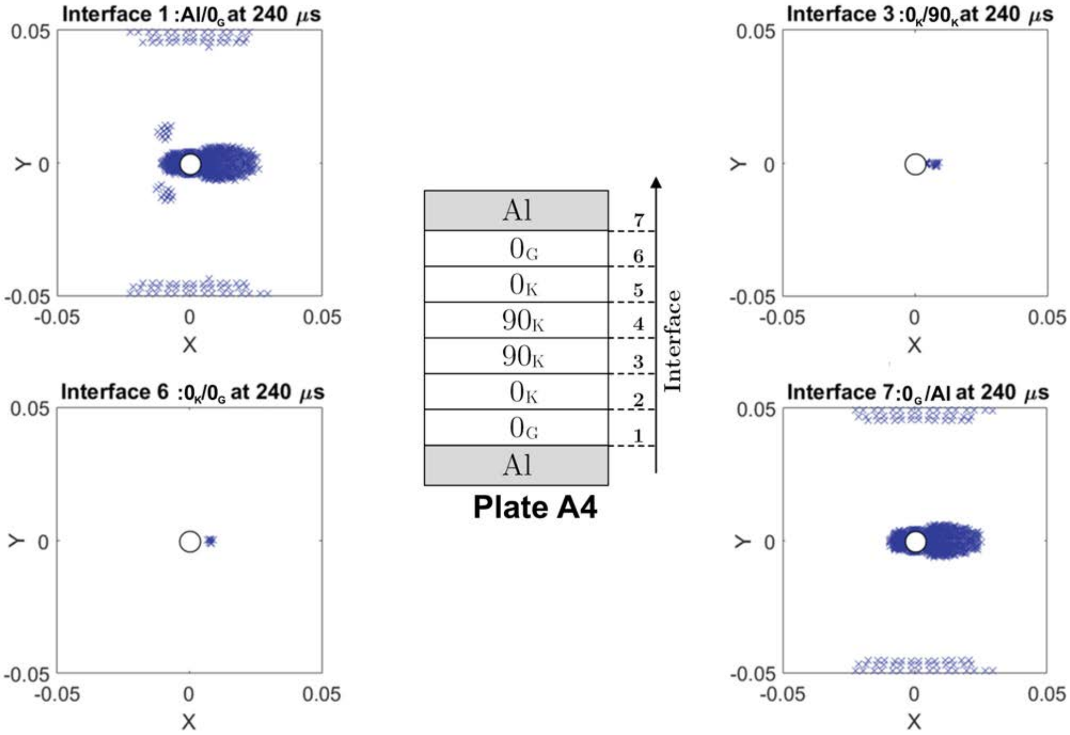

Figure 5.9: Delamination at the interfaces of plate A4 for offset 0.008 m

5.3. GLARE plate having equally offset holes subjected to spherical LVI

To further explore the influence of important geometrical parameters like effect of holes of different sizes and their positions at different distances from the central impact point, the LVI responses of GLARE 5-2/1 plates with symmetrically placed holes are studied. The S2-glass/epoxy laminate comprises of four prepreg layers of [0 ° /90 ° /90 ° /0 °] configuration with 0.152 mm thick plies and the aluminium layers are 0.502 mm thick thereby taking the total thickness to 1.612 mm.

5.3.1. Problem definition

A clamped square GLARE plate having sides 100 mm with the circular holes symmetrically placed along x-axis is considered as shown in **Figure 5.10** and **Figure 5.11** shows the meshed geometry of the target GLARE plate. The target GLARE plate having equally offset holes is

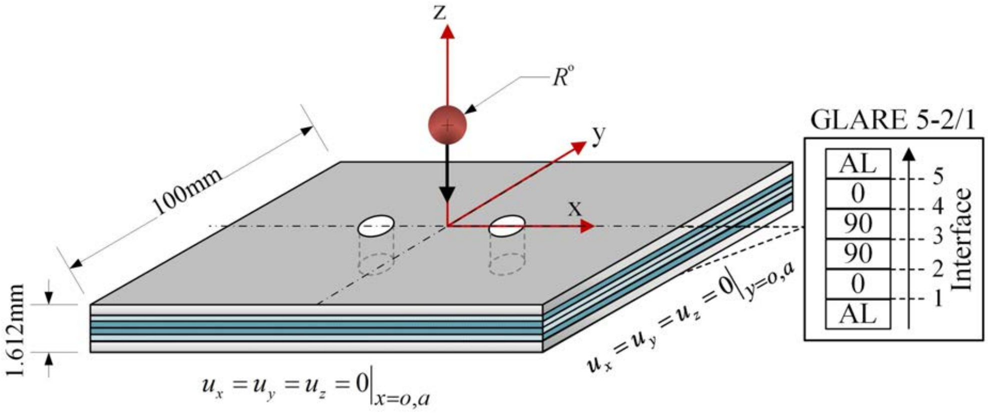

Figure 5.10: GLARE 5-2/1 plate with two holes subjected to central normal LVI

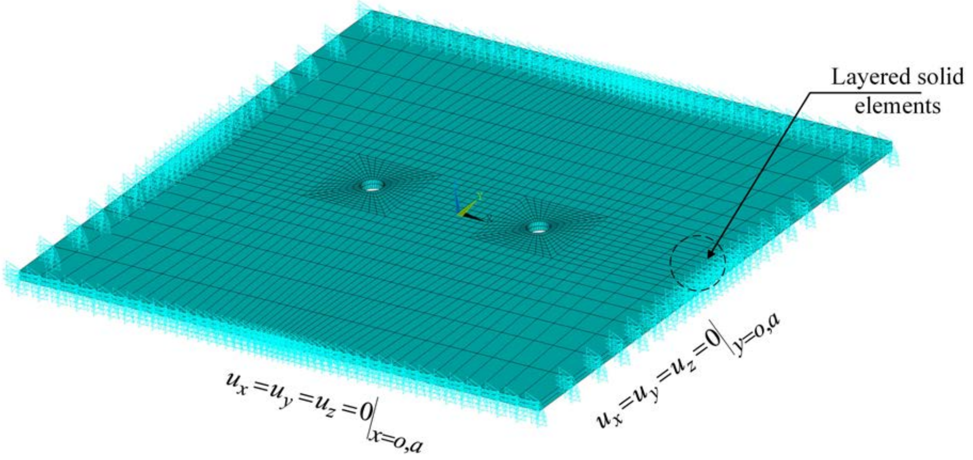

Figure 5.11: Meshed geometry of the GLARE clamped plate

impacted at the centre by a rigid steel spherical impactor at 10 m/s and the impact responses and delamination at the interfaces are assessed. Varying the hole diameters as well as their relative distances, the LVI responses are investigated and compared to that of a GLARE plate without any holes. Furthermore, the shape and orientation of the holes on the LVI response are explored and their influence on the interfacial delamination are investigated.

5.3.2. Effect of hole size on the dynamic response

In order to investigate the effect of the hole size, the dynamic response of a conventional GLARE plate is compared to that of a GLARE plate having two symmetrically placed holes 32 mm apart from each other considering two hole diameters viz. 4 mm and 8 mm.

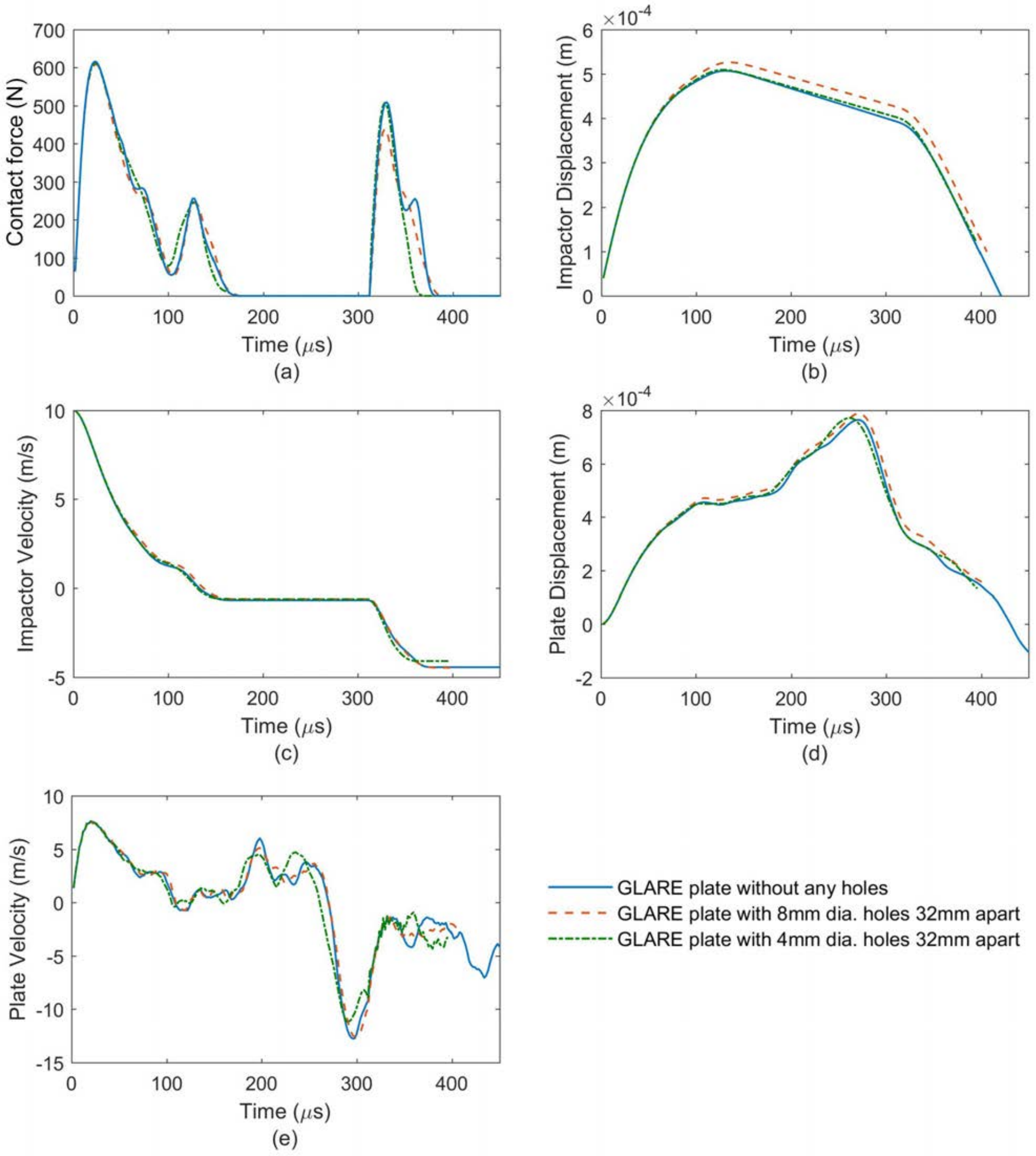

Figure 5.12: Dynamic response of the GLARE plates due to LVI by a spherical steel impactor at 10 m/s

Plotting the dynamic responses as shown in **Figure 5.12 (a)-(e)** it can be seen that the peak contact force and the impactor velocity for all the three GLARE plates are almost same when impacted by the spherical steel impactor at 10 m/s but the central deflection is seen to be the most for the plate having 8 mm diameter holes and the least for the plate without any holes. Secondly, the peaks attained during its rebound response is slightly different and as seen it is the least for the plates having 8 mm diameter holes and no significant difference is seen in the contact force response for the plate having 4 mm diameter holes implying that there is a threshold hole size relative to the plate size below which there is no significant variation in the contact response of the target. The plate velocity at the contact location more or less follows the same trend as can be seen from **Figure 5.12(e)**. Therefore it can be ascertained that the size of the holes affect the dynamic response of the GLARE plates on account of reduction in the plate flexural stiffness.

5.3.3. Effect of hole position

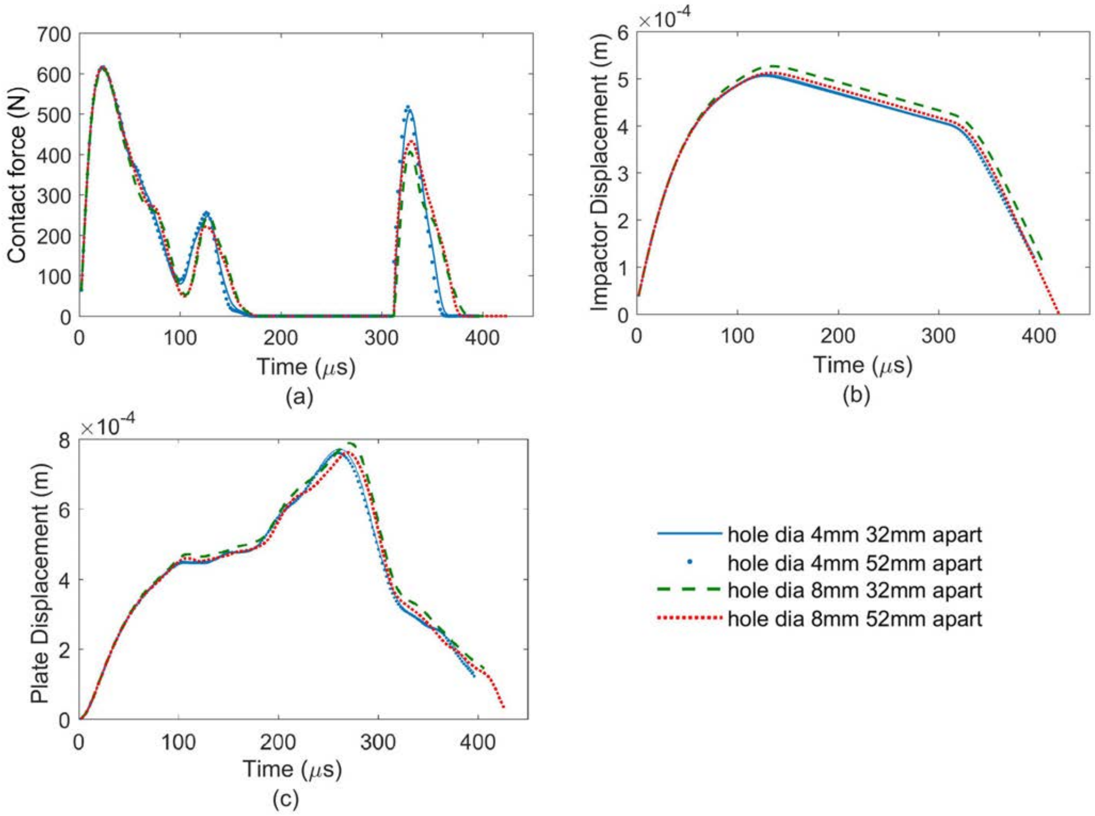

Figure 5.13: Effect of hole position on (a) contact force; (b) impactor displacement and (c) plate displacement

In order to see the effect of relative hole positions, the holes having diameters 4 mm and 8 mm are placed further apart at 52 mm from each other along x-axis. The dynamic responses are compared for the contact force and impactor and plate centre displacements to that for the case where the holes are 32 mm apart as shown in **Figure 5.13 (a)-(c)** for the same impactor velocity of 10 m/s. It can be seen that although the peak contact force is almost same, there is a slight difference in the second peak force during the rebound behaviour when the position of the 8 mm diameter holes are varied relative to each other. But no significant difference is seen in the contact response for the GLARE plate having 4 mm diameter holes in both the cases. Also, as the distance between the holes increases, the plate central deflection decreases in case of the plates having 8 mm diameter holes. Based on the observation it can be inferred that although the size and position of the holes can affect the dynamic responses, there is a critical size for the holes relative to the plate dimensions below which the position of the holes do not have any significant influence on the global dynamic response.

5.3.4. Effect of outer aluminium thickness

In order to study the influence of the outer aluminium thickness, the GLARE plate having 4 mm diameter holes placed 52 mm apart is subjected to LVI at 10 m/s. To investigate the influence of MVF on the dynamic response, the outer aluminium thickness is reduced from 0.502 mm to 0.405 mm keeping all the other parameters same and in another case, the number of S2-glass/epoxy layers are increased and the thickness of the outer aluminium layers are reduced such that the overall plate thickness remains the same at 1.612 mm (**Figure 5.14(a)**) and the contact responses are shown in **Figure 5.14(b)-(d)**.

It is observed that the peak contact force decreases and the impactor and plate displacement increases with the decrease in the outer aluminium thickness because of the reduced flexural stiffness of the plate. On reducing the aluminium thickness further to 0.35 mm and increasing the number of 0° glass/epoxy layers by two times such that the overall plate thickness remains same at 1.612 mm, it is seen that although there is a rise in the contact force compared to the plate having 0.405 mm thick aluminium layers, but increasing the glass/epoxy layers do not lead to greater rise in the peak values of the contact force compared to increasing the outer aluminium thickness.

A similar analogy but in the opposite sense can be observed for the impactor and plate displacements and the GLARE plate having 0.502 mm thick aluminium layers undergoes the minimum deflection. It is seen that with the decrease in the outer aluminium thickness from 0.502 mm to 0.405 mm the duration of the contact gets slightly prolonged but for the plate having 0.35 mm thick aluminium layers, the contact duration is almost same as the plate having 0.502 mm aluminium layers. From the contact force and displacement response of the target plates it is seen that the outer aluminium layers have greater influence on the overall flexural stiffness of the target plate thereby dominating the dynamic behaviour of the plates compared to the increase in the glass/epoxy layers. In order to further assess the effect of these parameters on the structural integrity of the laminate, the interfacial delamination undergone by the GLARE plate is investigated in the next section.

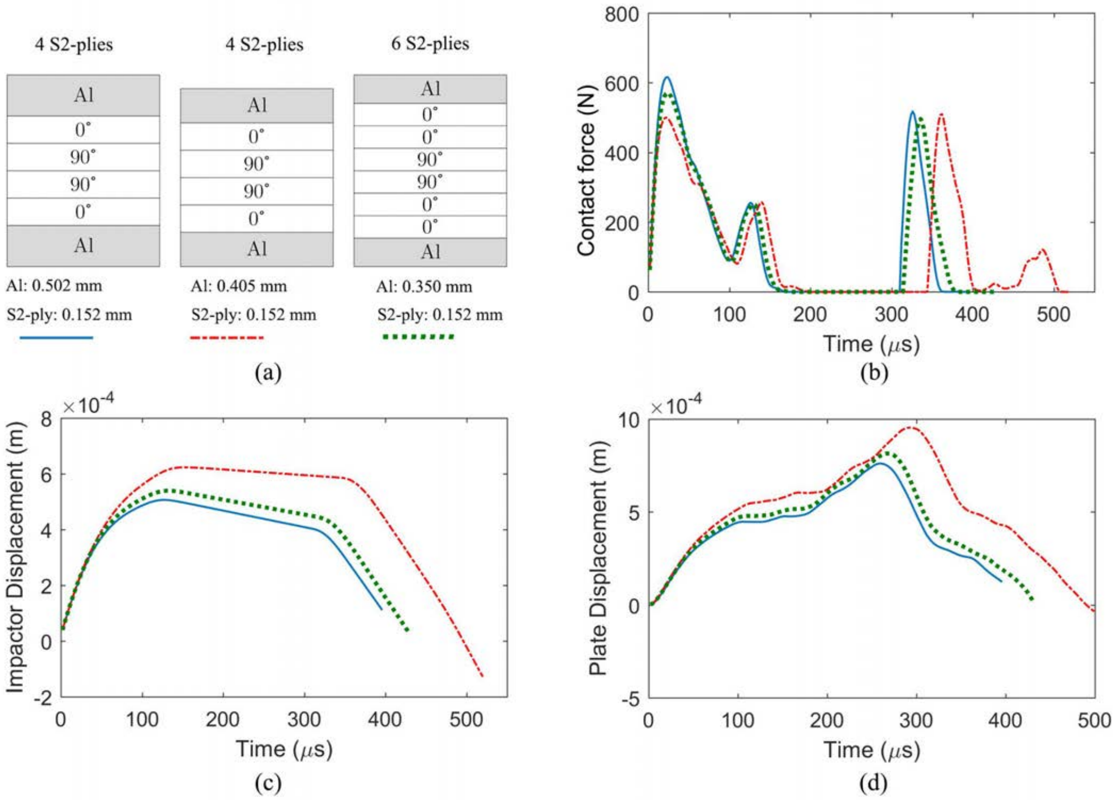

Figure 5.14: Effect of outer aluminium thickness on the LVI response

5.3.5. Interfacial delamination

Delamination at the fibre/metal interfaces are critical to the structural stability of a GLARE laminate and on being subjected to LVI considerable damage may initiate at the interfaces although visual inspection for damages on the target might be barely visible.

5.3.5.1. Effect of position and size of holes

Figure 5.15 and **Figure 5.16** show the interfacial delamination at the bottom and top fibre/metal interfaces 1 and 5 respectively for the GLARE plates having 0.502 mm thick aluminium layers and subjected to LVI by a steel sphere at 10 m/s. **Figure 5.15** shows the delamination for the case of a GLARE plate without any holes followed by the GLARE plates having 4 mm diameter holes placed 32 mm and 52 mm apart from each other. **Figure 5.16** plots the delamination for the GLARE plates having 8 mm diameter holes. As can be seen, the extent of delamination is the least for the plate without any holes (**Figure 5.15 (a)-(b)**) and is highest for the GLARE plate with 4 mm diameter holes placed 52 mm apart (**Figure 5.15 (e)-(f)**).

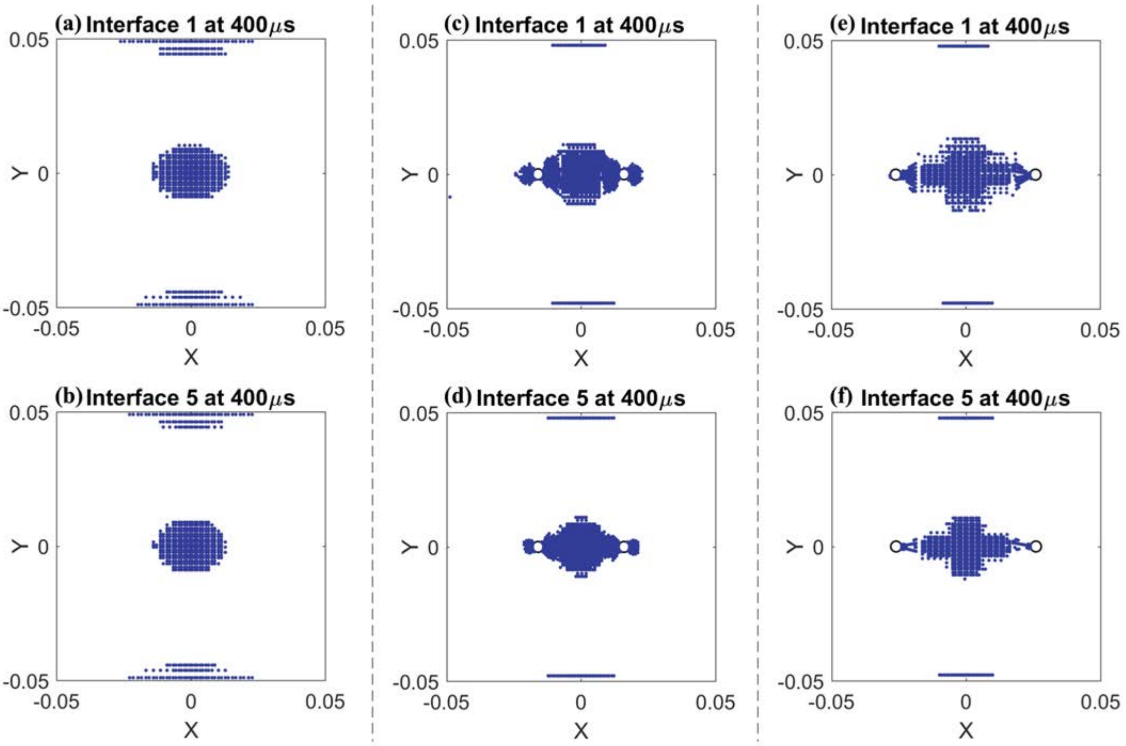

Figure 5.15: Delamination at the fibre/metal interfaces of the GLARE plate (a)-(b) without holes; (c)-(d) ϕ4 mm holes 32 mm apart; (e)-(f) ϕ4 mm holes 52 mm apart

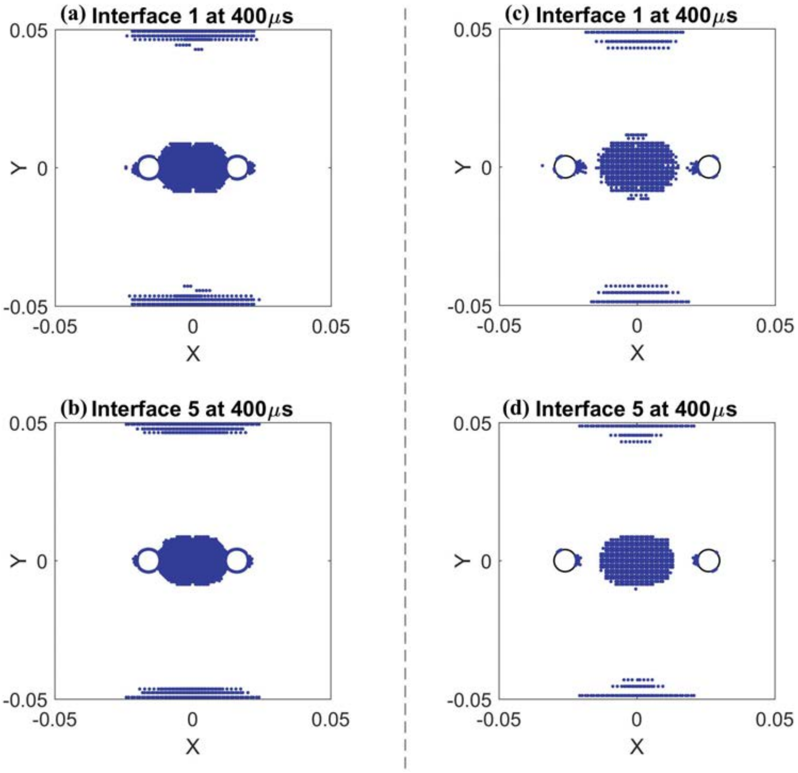

Figure 5.16: Delamination of the GLARE plate having ϕ8 mm holes (a)-(b) 32 mm apart; (c)-(d) 52mm apart

Comparing **Figure 5.15(a)-(f)** and **Figure 5.16(a)-(d)**, it is observed that delamination is more likely to propagate faster towards and across the holes along the fibre direction of the lamina immediately adjacent to the aluminium layer. Compared to the GLARE plate having 8 mm diameter holes, the extent of delamination is more for the GLARE plates having 4 mm diameter holes. As seen, the delamination occurs around the periphery of the holes in all the cases indicating them to be critical sites where delamination tends to initiate on account of LVI. For the case of the GLARE plate having 8 mm diameter holes (**Figure 5.16**), when they are farther apart, the delamination do not form a continuous stretch as in case of the GLARE plate having 4 mm diameter holes although local delamination initiates around the hole peripheries. For all the cases, the inner composite interfaces showed negligible to nil delamination and the bottom aluminium/composite interface undergoes more delamination compared to the top interface.

5.3.5.2. Effect of hole shape

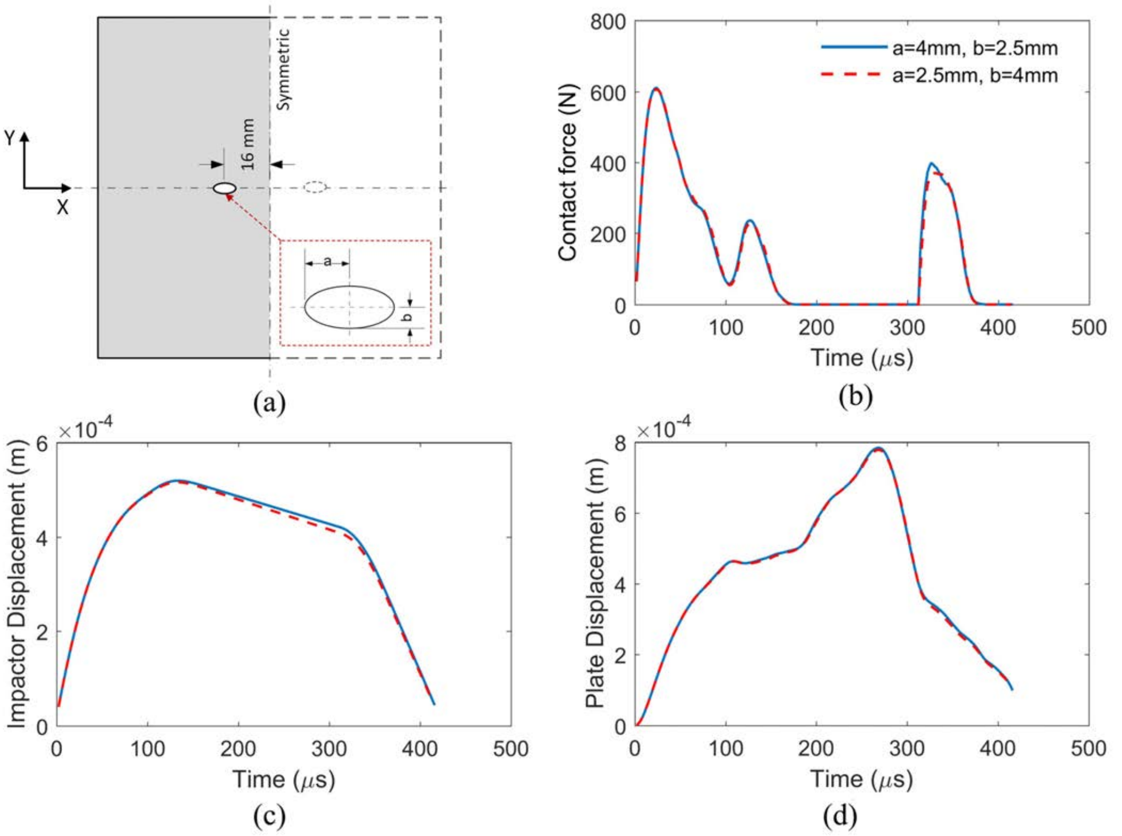

(a) (b) (c) (d)

Figure 5.17: Effect of hole shape on the LVI response

To investigate the effect hole shape on the delamination at the interfaces two cases are considered viz. elliptical holes with semi-major axis as 4 mm and semi-minor axis as 2.5 mm with the major axis aligned along x-direction once and along y-direction in the latter case.

The elliptical holes are set 32 mm apart from each other and the GLARE plate is impacted at 10 m/s at the centre keeping the impactor parameters same. Although, not much difference is observed in the contact response for the two cases as can be seen from **Figure 5.17(b)-(d)**, it is observed that when the semi major axis of the elliptical holes are aligned along the fibre direction of the 0° ply, the extent of delamination is comparatively greater at the fibre/metal interfaces and this is evident from **Figure 5.18(a)-(d)**. It is also observed that the delamination around the periphery of the elliptical hole at the fibre/metal interface tends to propagate more across and along the region having narrower curvature when the semi-major axis is aligned along the fibre direction as can be inferred by comparing **Figure 5.18 (a)** and **(c)**.

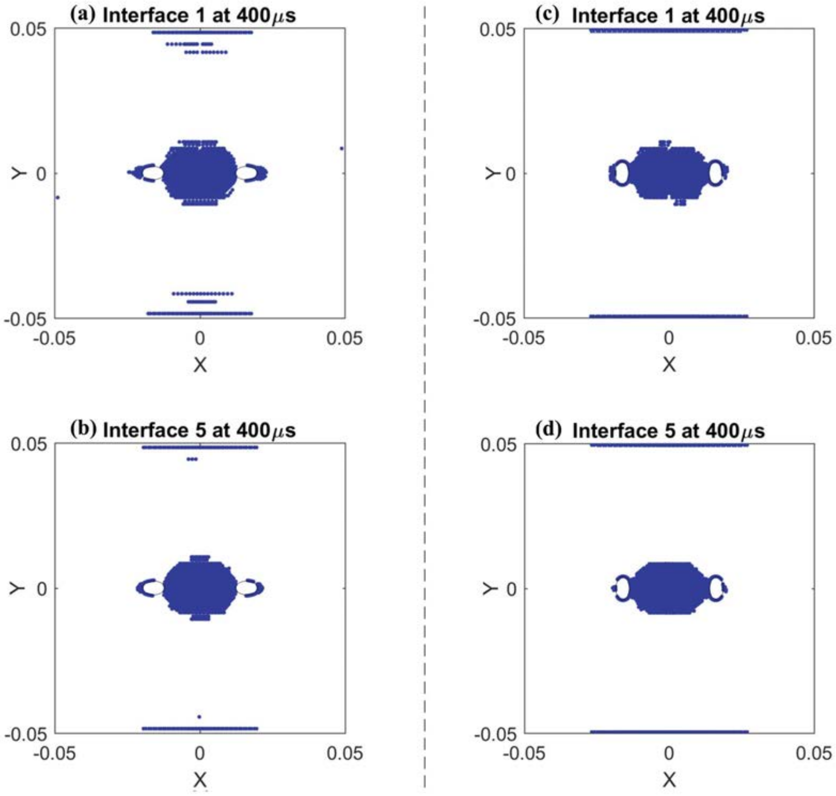

Figure 5.18: Delamination at the aluminium/composite interfaces of the GLARE plates having elliptical holes 32 mm apart with major axes aligned along (a)-(b) x-direction and (c)-(d) y-direction

5.3.5.3. Effect of metal volume fraction

To see the effect of MVF on the associated delamination at the fibre/metal interfaces and around the hole periphery, a comparison of the delamination at the bottom and top aluminium/glass-epoxy interfaces is shown in **Figure 5.19 (a)** and **(b)** for the plates having 4 mm diameter holes positioned 52 mm apart. **Figure 5.19(a)** shows the delamination for the case when the outer aluminium layer thickness is reduced to 0.405 mm keeping the glass/epoxy layers the same and **Figure 5.19(b)** shows the same when the overall thickness of the GLARE plate is kept fixed at 1.612 mm by increasing the number of 0° layers by two and reducing the outer aluminium thickness further to 0.35 mm. It is seen that for the plates having the same overall thickness, with decrease in the MVF, the extent of delamination increases and the delamination near the hole edges tend to increase (refer **Figure 5.15 (e)-(f)** and **Figure 5.19(b)**) although the peak contact force is lower in the latter case (refer **Figure 5.14(a)**). In both the cases, a continuous delaminated region forms between the two holes. But for the thinner GLARE plate having 0.405 mm aluminium layers, the extent of delamination is seen to be lesser as seen in **Figure 5.19 (a)** and the delaminated region at the top aluminium/composite interface do not reach the hole edges. It can be inferred that although the outer aluminium layer provides considerable strength against impacts, the thinner plate on account of reduced inertia reacts more quickly to the impact thereby reducing the peak contact force and hence the delamination.

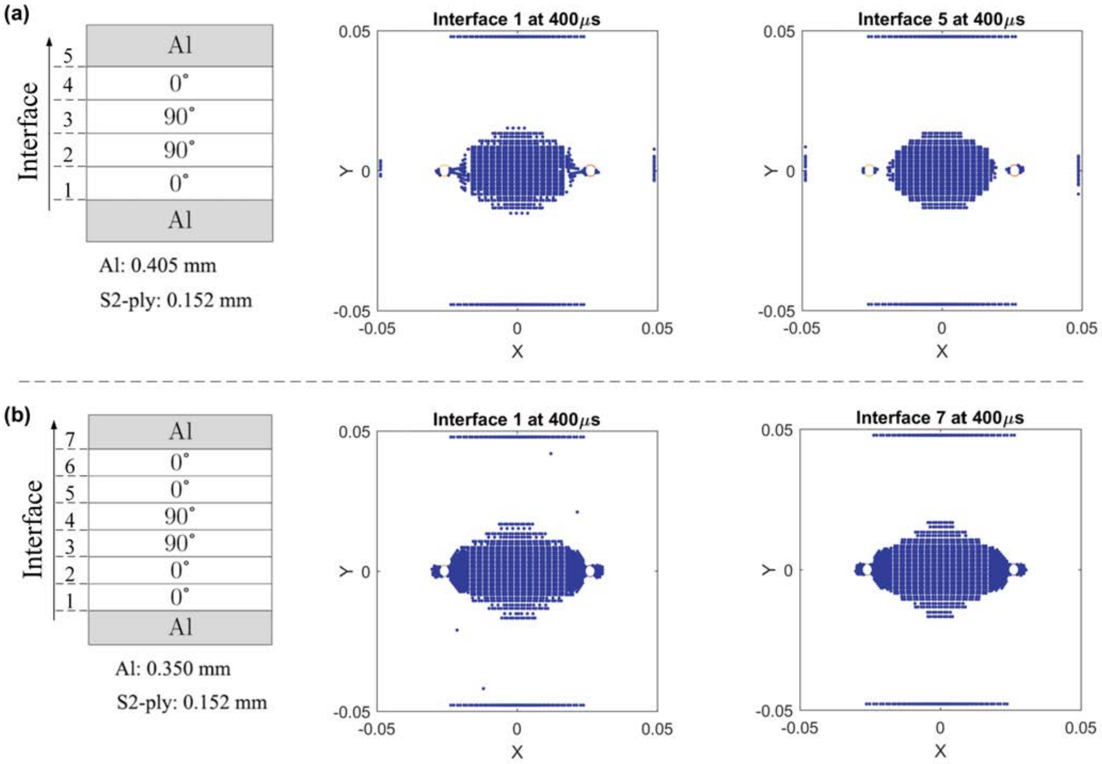

Figure 5.19: Delamination at the aluminium/composite interfaces for MVF (a) 0.571 (b) 0.434

5.4. GLARE plate having equally offset holes subjected to LVI by a cylindrical impactor

Most of the published literatures investigated the LVI on a FML laminate considering a spherical impactor and not much literature is present investigating the LVI responses due to impact by a cylindrical impactor on GLARE considering the effect of hole position, size and their shape and the interfacial delamination the target undergoes on account of impact [36,123,212,213]. In order to see the effect of impactor geometry on the dynamic response of the GLARE plates with holes, the same GLARE plates are subjected to a cylindrical impact as shown in **Figure 5.20**.

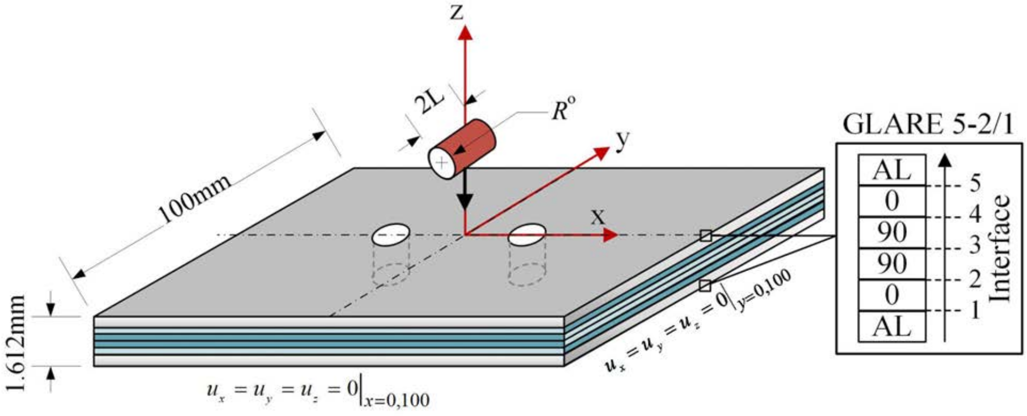

Figure 5.20: GLARE 5-2/1 plate with open holes subjected to central cylindrical impact

5.4.1. Problem definition

The clamped square GLARE plate is having sides 100 mm and the steel cylindrical impactor of length $2L$ and radius R° strikes the top plate surface as shown in **Figure 5.20**. The GLARE plate is having two 0.502 mm thick outer aluminium layers and the thickness of each S2-glass/epoxy ply is 0.152 mm. The circular holes are offset symmetrically from the plate along x-direction at distances of 32 mm and 52 mm from each other and their diameters are varied from 4 mm to 8 mm for the analysis of LVI.

5.4.2. Effect of hole size and shape on the LVI response

To investigate the effect of the hole shape and size, the impact response of a conventional GLARE plate is first evaluated and then compared to that of a GLARE plate having two symmetrically placed open holes. The hole centres are placed 16 mm apart from the centreline and their diameters are varied from 4 mm to 8 mm. Furthermore, the shape of the holes are made elliptical having a semi-major axis of length 4 mm and semi-minor axis of length 2.5 mm and they are positioned such that once the major axes are aligned along x-axis and then along y-axis. Comparing the dynamic responses as shown in **Figure 5.21 (a)-(e)** due to LVI by a steel cylinder of length 10 mm and radius 4 mm striking the plate at 10 m/s, the peak contact force values and the impactor velocities for all the cases are almost same except for the case of the plate having 8 mm diameter holes for which it is slightly lower. The central deflection is seen to be the maximum for the plate having 8 mm diameter holes and the least for the plate without any holes. This can be attributed to a reduction in the plate flexural stiffness on account of the open holes near to the impact site. It is also seen that the contact duration for the plate without any holes and for the plate having 4 mm holes is slightly less compared to the rest. The plate velocity at the contact location more or less follows the same trend as can be seen from **Figure 5.21(e)**.

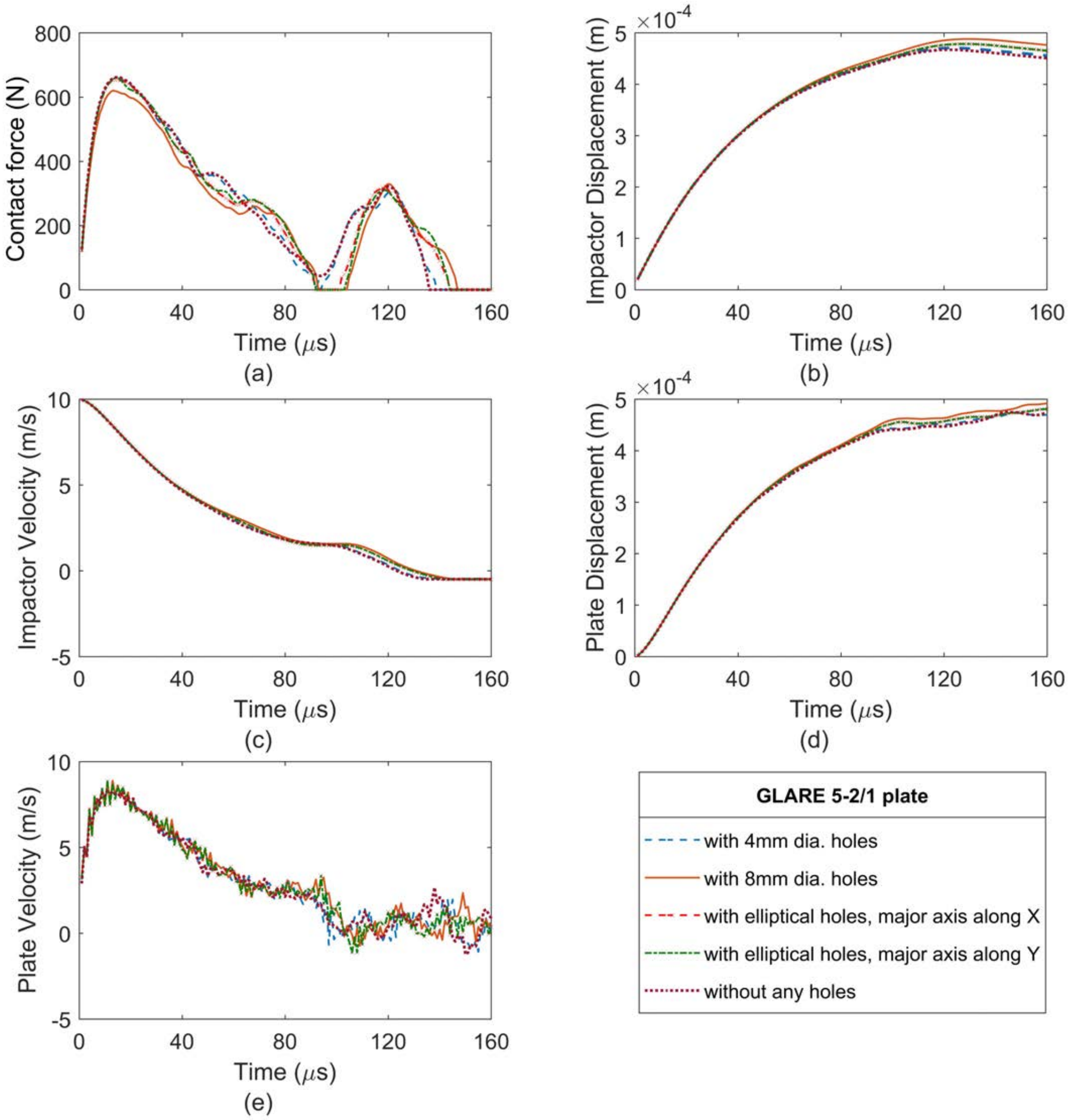

Figure 5.21: Effect of hole shape and size on the response due to cylindrical LVI

5.4.3. Influence of relative position of the holes

To observe the effect of the relative pitch between the holes of diameters 4 mm and 8 mm, they are placed further apart at 52 mm from each other along x-axis. Considering the same impactor parameters, the contact force, impactor and plate displacements are plotted in **Figure 5.22 (a)-(c)**. It can be seen that although the peak contact forces are almost same, there is a slight change in the peak force when the position of the 8 mm diameter holes are varied relative to each other. Moving the holes further apart from each other leads to the peak forces to be same as for the case of the plate having 4 mm holes and also the impactor and plate displacements decrease. From the contact responses it can be emphasised that for a particular plate dimension, along with the pitch between the holes there is a critical size for the holes below which they do not have significant influence on the magnitude of the contact responses.

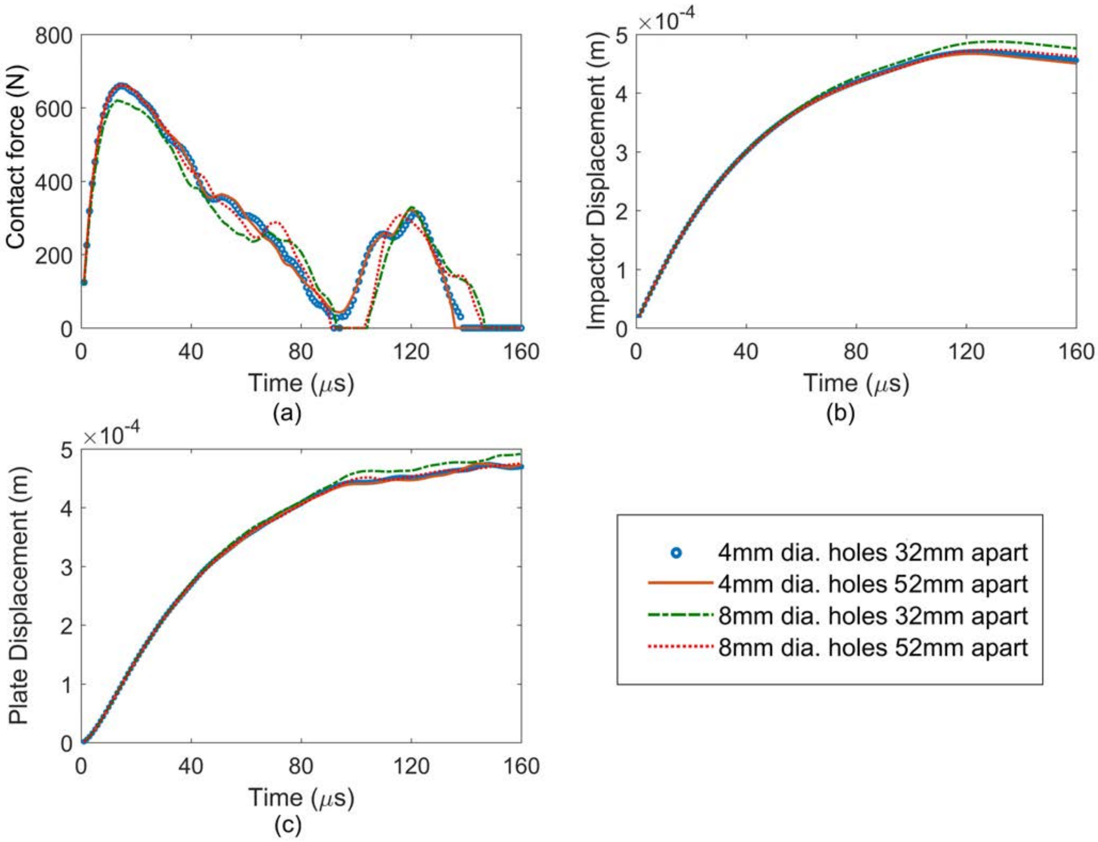

Figure 5.22: Cylindrical LVI on GLARE plates having symmetrically placed holes

5.4.4. Influence of impactor dimension

In order to study the effect of impactor dimension on the contact response, the length of the cylindrical impactor is made 20 mm and the diameter is reduced to 5.64 mm such that the overall mass of the impactor remains the same. The contact response for the GLARE plates having holes 32 mm apart is shown in **Figure 5.23 (a)-(c)** for the contact force and impactor and plate displacements respectively considering an impact velocity of 10 m/s. Comparing the contact force histories in **Figure 5.23(a)**, it is seen that the peak contact force is slightly higher when the impactor length is doubled. The increase in the contact length leads to a higher peak contact force although the change in the displacement of the impactor and plate is negligibly small.

Secondly, keeping the diameter same at 5.64 mm, the cylinder length is made 10 mm so that the impactor mass is reduced by half. It is seen that the contact duration more or less remains the same for the impacts by similar mass impactors and the duration reduces when the impactor mass decreases signifying that the duration of the contact is governed by impactor mass. It is also seen that there is a decrease in the peak values attained when the impactor mass decreases due to a reduction in the inertia of the impactor and hence the impacting energy.

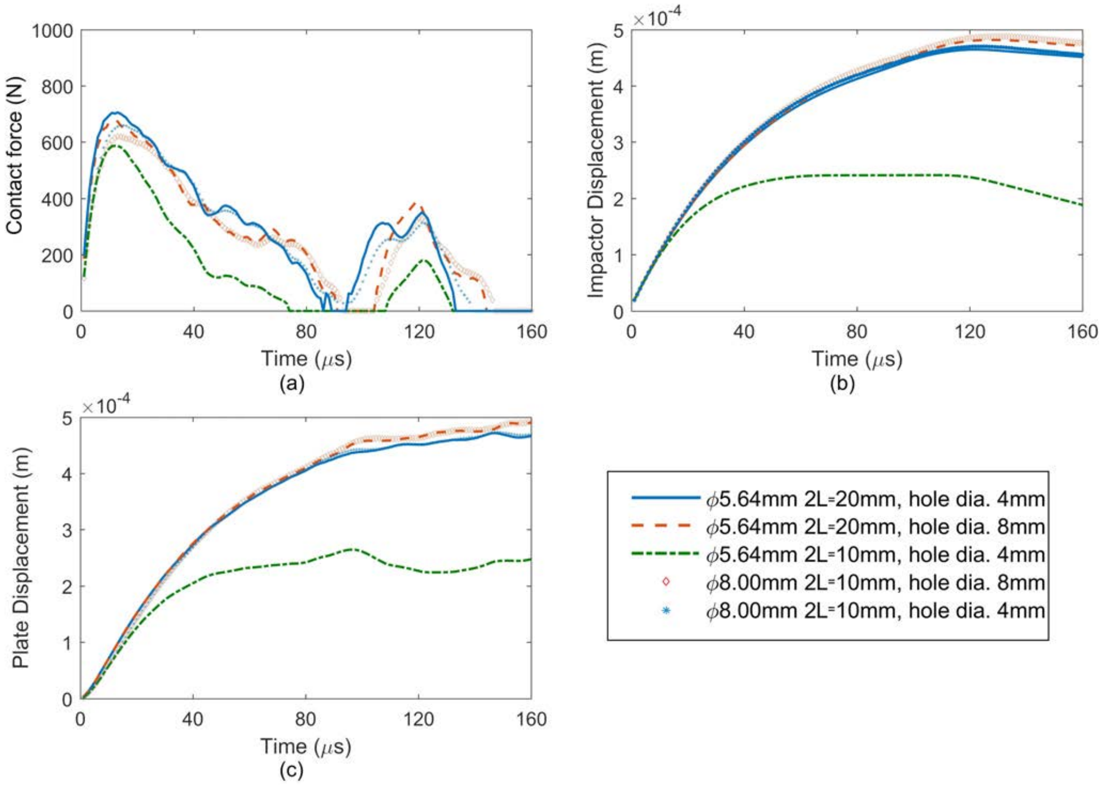

Figure 5.23: Effect of cylinder dimension on the impact response for the GLARE plates with hole pitch of 32 mm

5.4.5. Delamination at the interfaces

The extent of delamination at the interfaces is estimated for LVI by cylindrical impactor and the effect of open holes on the progression of delamination is assessed.

5.4.5.1. Effect of hole size and hole pitch

Figures 5.24-5.26 show the delamination at the aluminium/composite as well as inner composite interfaces for the GLARE plate without any holes and those having 4 mm and 8 mm holes respectively when subjected to LVI by a steel cylinder at 10 m/s.

It is seen that the plate without any holes (**Figure 5.24**) experienced the least delamination compared to the plates with holes. The delamination at the fibre metal interfaces was noticeably the maximum for the GLARE plate with 4 mm diameter holes (refer **Figure 5.25**). It is seen that the fibre/metal interface opposite to the impact side experienced the maximum delamination in all the cases. From **Figures 5.25-5.26**, it is seen that the delamination tends to move faster towards the holes and along the fibre direction at the fibre/metal interfaces and the extent of delamination in the plate having 4 mm diameter holes is more compared to the plate having 8 mm diameter holes. This is due to higher stress concentration around the holes of 4 mm diameter leading to a sharp increase in the stress along periphery of the holes and as seen from **Figure 5.25** the delaminated region grows outward along x-axis beyond the hole edges.

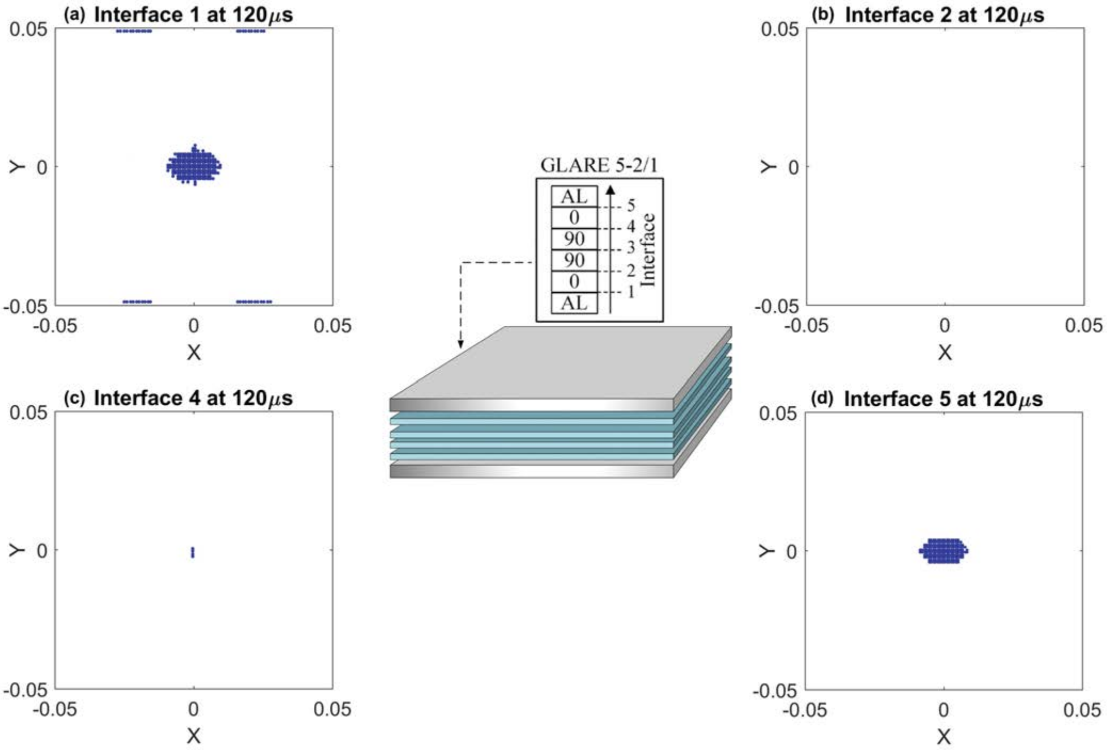

Figure 5.24: Interfacial delamination for a general GLARE 5-2/1 plate

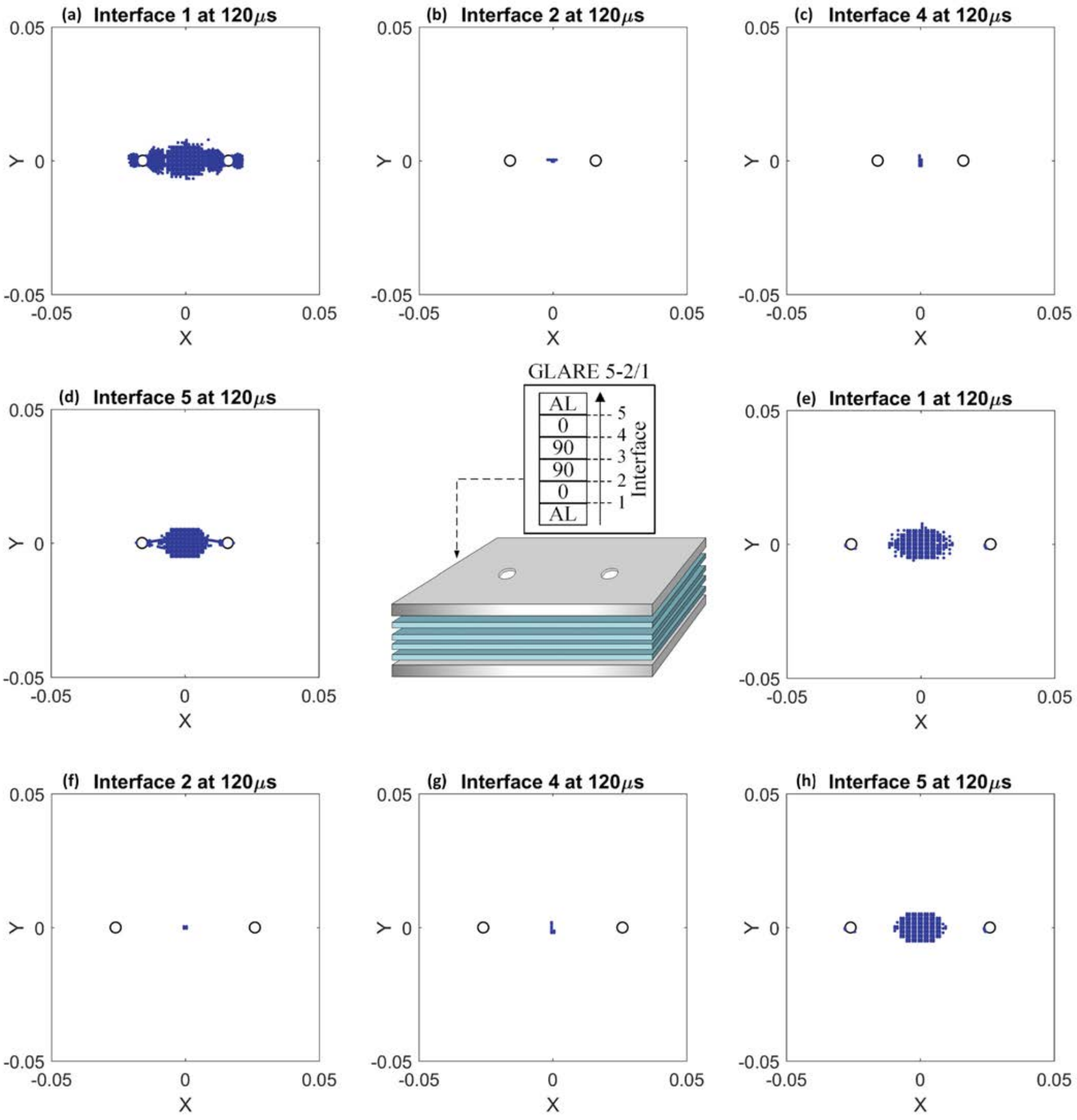

Figure 5.25: Interfacial delamination for a GLARE plate having ϕ4 mm holes (a)-(d) 32 mm apart, (e)-(h) 52 mm apart

Furthermore, the delamination tends to initiate around the periphery of the holes in all the cases making them critical sites when subjected to impact loadings. When the holes are farther apart, the delamination do not form a single stretch although for the GLARE plate having 4 mm diameter holes, the local delamination around the impact site is more and delamination initiates around the hole peripheries. The inner interfaces concerning the glass/epoxy plies experience negligible delamination in all the cases. It is seen that with the increase in the pitch between the holes, the delamination between the fibre/metal interfaces decreases although for the inner interfaces, it more or less remains the same.

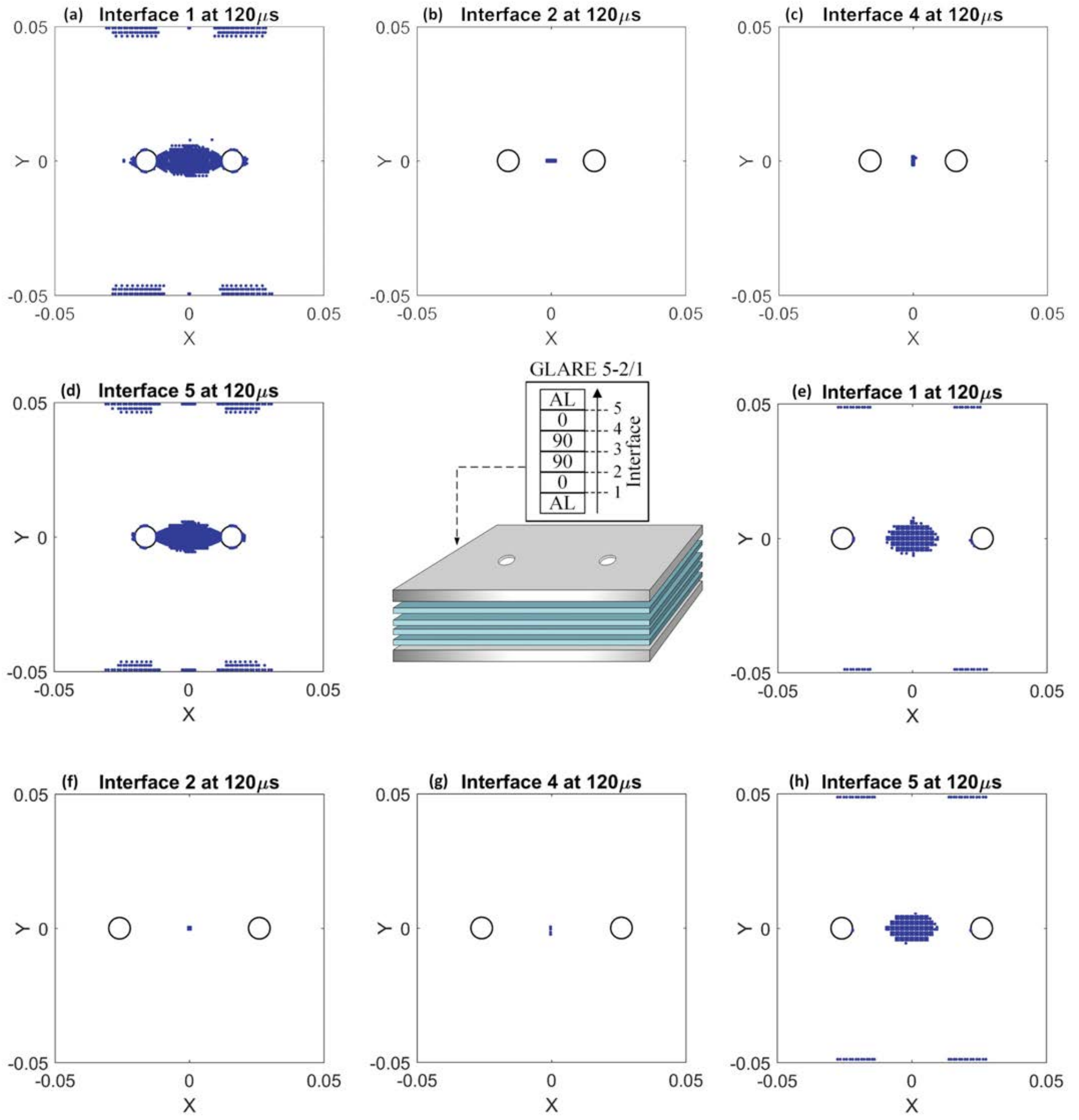

Figure 5.26: Interfacial delamination for a GLARE plate having ϕ8 mm holes (a)-(d) 32 mm apart, (e)-(h) 52 mm apart

5.4.5.2. Effect of hole shape

The shape and orientation of the holes can also influence the delamination at the interfaces although the contact force may be similar (refer **Figure 5.21**) for the cut-outs of similar area. Elliptical holes having dimensions as mentioned previously are placed 16mm apart from the centre, initially aligning the semi major axis along x-direction and then along y-direction.

It is seen that when the semi major axis of the elliptical holes are parallel to the fibre direction of the underlying 0° lamina, delamination is comparatively greater at the fibre/metal interfaces and grows towards the outer edges in case of the elliptical holes whose major axes are along the x-direction as shown in **Figure 5.27**. This shows that for a GLARE plate having elliptical cut-outs, the delamination may easily propagate across and along the narrower edge of the holes when the semi-major axis for the elliptical holes are along the fibre direction. For all the inner interfaces, the extent of delamination remains more or less the same and around the periphery of the contact site.

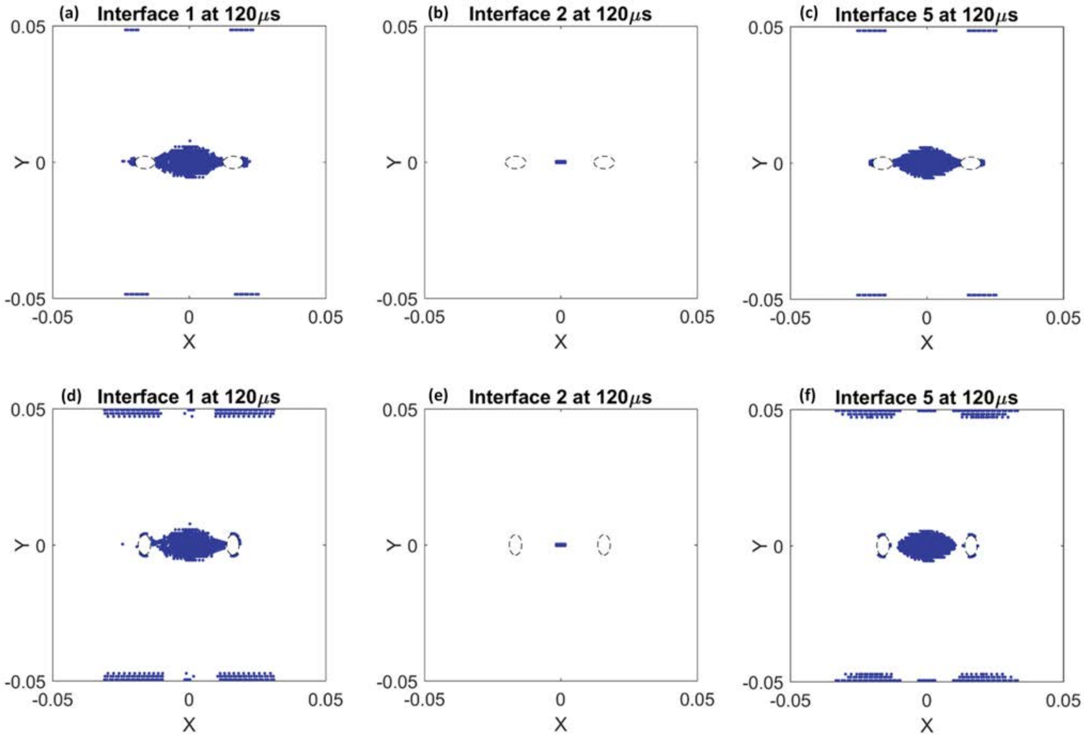

Figure 5.27: Interfacial delamination for a GLARE plate with the major axes of the elliptical holes aligned along (a)-(c) x-direction (d)-(f) y-direction with the hole centres 32 mm apart

5.4.5.3. Effect of impactor dimension

As discussed previously in **Section 5.4.4**, in addition to influencing the magnitude of the contact response due to a change in the impactor dimension, the delamination at the interfaces might also change. The increase in the cylindrical impactor's contact length lead to the peak values of the contact force to be comparatively higher compared to that due to the increase in the impactor radius (refer to **Figure 5.23**). Considering the cylindrical impactor's length to be twice its initial length and other impact parameters same, the delamination at the interfaces for the plates having 4 mm and 8 mm diameter holes placed 32 mm apart from each other is assessed as shown in **Figure 5.28**. The delamination at the aluminium/composite interfaces are more when the contact length is increased as can be observed by comparing **Figure 5.25**, **Figure 5.26** and **Figure 5.28**, although for the inner interfaces the extent of delamination remains more or less the same. It is also observed that for the case of the plate having 4 mm diameter holes, the delamination around the holes is more and extends further outwards along the fibre direction compared to the plate having 8 mm diameter holes.

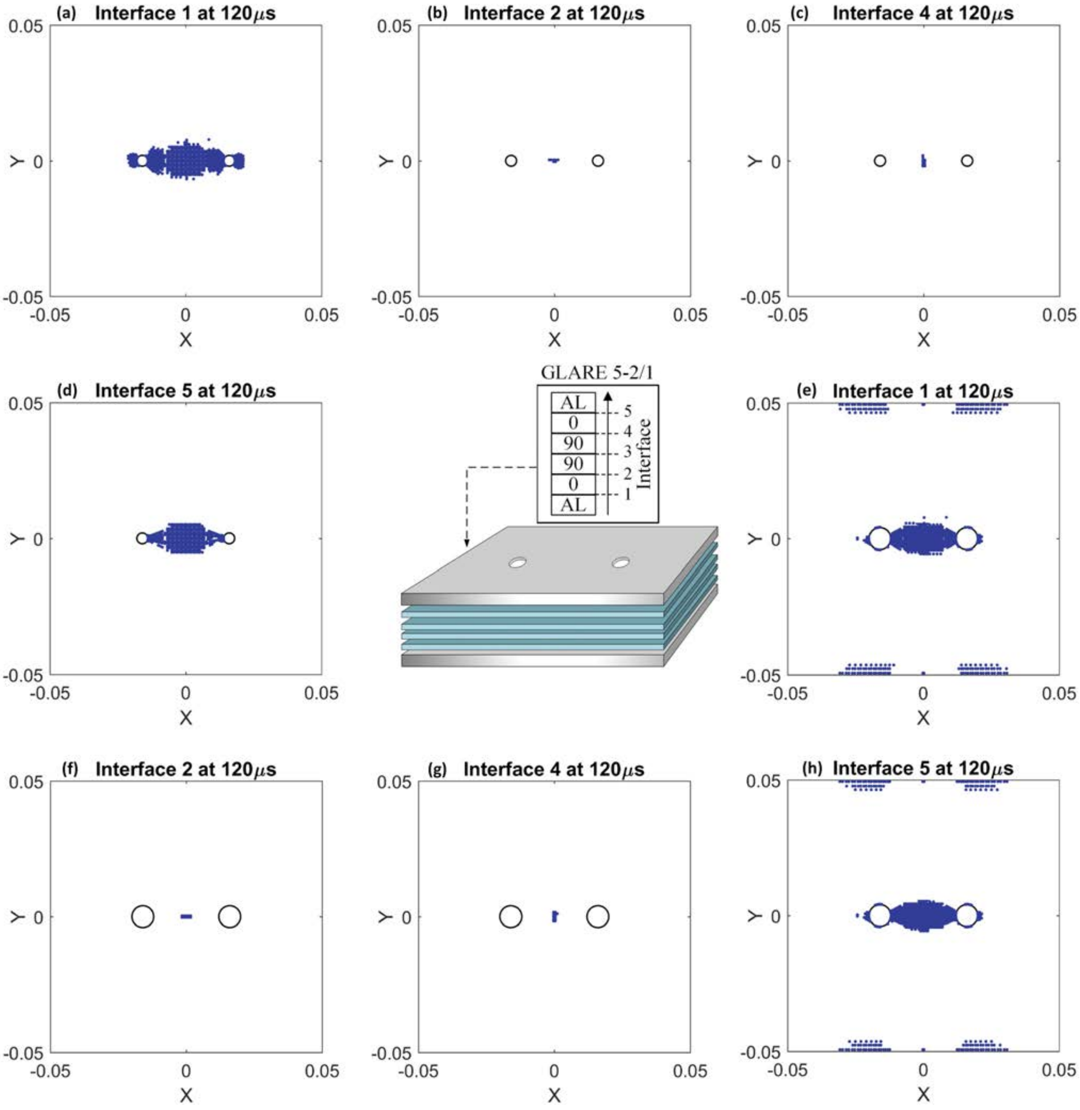

Figure 5.28: Delamination due to LVI by cylindrical impactor (2L=20mm, ϕ=5.64mm) in a GLARE plate having (a)-(d) ϕ4 mm holes 32 mm apart (e)-(h) ϕ8 mm holes 32 mm apart

5.4.5.4. Effect of MVF

The overall thickness of the plate can influence the contact response as observed from **Figure 5.29** for the case of a LVI at 10 m/s on a GLARE plate having 4 mm diameter holes with a pitch of 32 mm. When the thickness of the aluminium layers are reduced from 0.502 mm to 0.402 mm, thereby reducing the MVF from 0.623 to 0.569, it is seen that the peak contact force decreases and the impactor displacement increases due to the reduction in the flexural stiffness of the plate. Another inference that can be drawn is that the outer aluminium layer has a significant role in influencing the magnitude of the overall impact behaviour of the GLARE plate due to LVI by the cylindrical impactor and the duration of the contact slightly increases with reduction in the MVF. This change in the peak values influences the delamination at the interfaces as shown in **Figure 5.30** and **Figure 5.31** for the GLARE plates having 4 mm and 8 mm diameter holes placed 32 mm apart from each other.

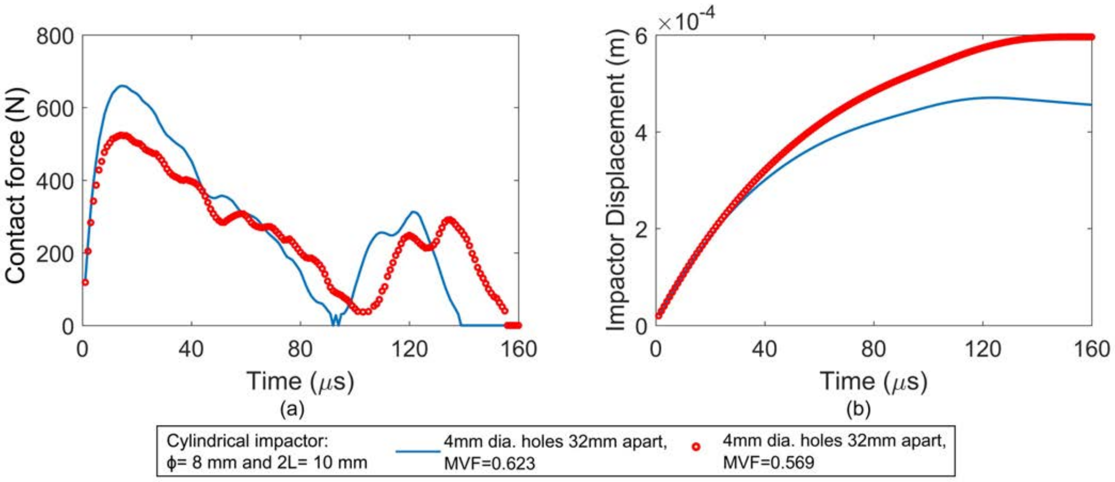

Figure 5.29: Effect of plate thickness on the cylindrical LVI response (a) contact force and (b) impactor displacement for impact at 10 m/s

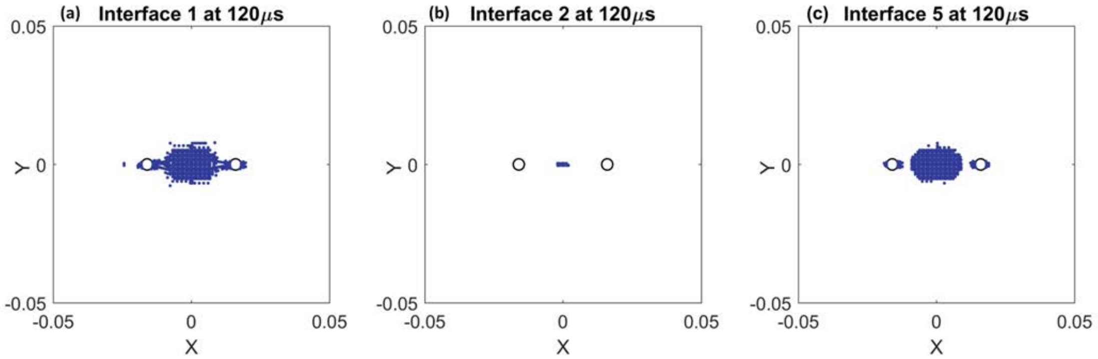

Figure 5.30: Interfacial delamination for a GLARE plate (MVF=0.569) having 4 mm dia. holes 32 mm apart subjected to cylindrical LVI at 10 m/s

It is seen that for the case of the plate having 4 mm diameter holes, the decrease in the plate thickness on account of thinner aluminium layers leads to a slight decrease in the delamination at the top aluminium/composite interface as can be observed by comparing **Figure 5.25** and **Figure 5.30**. Also, the delaminated region do not form a continuous area at the top aluminium/composite interface-5 as in case of the plate having 0.502 mm thick aluminium layer but the lateral spread of the delamination at the bottom and top interfaces

1 and 5 is slightly greater. Although the outer aluminium layer provides considerable strength against impacts, the lighter plate on account of thinner aluminium layer responds promptly to the impact because of its reduced inertia, lowering the peak contact force and hence the delamination. For the case of the GLARE plate having 8 mm diameter holes (refer **Figure 5.31**), the extent of delamination was more or less the same and for all cases delamination initiated around the hole periphery signifying the criticality of failure due to delamination in presence of open holes in a laminated component. As seen, the plate thickness, the size of holes and hole pitch together influence the contact response as well as the associated delamination, especially at the aluminium/composite interfaces.

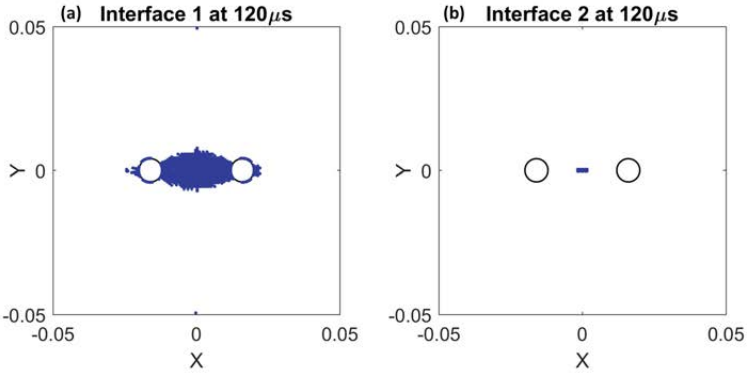

Figure 5.31: Interfacial delamination for a GLARE plate (MVF=0.569) having 8 mm dia. holes 32 mm apart subjected to cylindrical LVI at 10 m/s

5.5. GLARE plate with central hole subjected to multiple cylindrical LVIs

The present section investigates interfacial delamination in a GLARE fibre metal laminate having a central circular hole under multiple low-velocity impacts (LVIs) by cylindrical impactors. Influence of important parameters like length and radius of impactor, order of occurrence and location of impact on the extent of delamination have been studied.

5.5.1. Problem definition

A GLARE 5-2/1 plate having dimensions of 0.08 m × 0.08 m with a central circular hole of diameter 8 mm, clamped at all sides is considered to be impacted by two cylindrical steel impactors at different locations, at arbitrary times and with different velocities. The impactors hit the clamped GLARE plate symmetrically at locations (x=0, y=0.012 m) and (x=0, y=–0.012 m) respectively as shown in **Figure 5.32** and the impact responses are obtained. The plate configuration and cylindrical impactor details are given in **Table 5.3**. The effect of various parameters like the impact location, effect of impactor length and radius as well as the time between the impact occurrences and the influence of outer aluminium thickness on the impact response are investigated. The extent of delamination at the interfaces and near the free edge of the hole due to multiple LVIs by cylindrical impactors are assessed. **Figure 5.32 (a)** shows a typical cylindrical impactor and **Figure 5.32(b)** illustrates a clamped GLARE plate having a central circular hole being normally impacted upon by multiple cylindrical impactors of arbitrary masses and initial velocities at different locations.

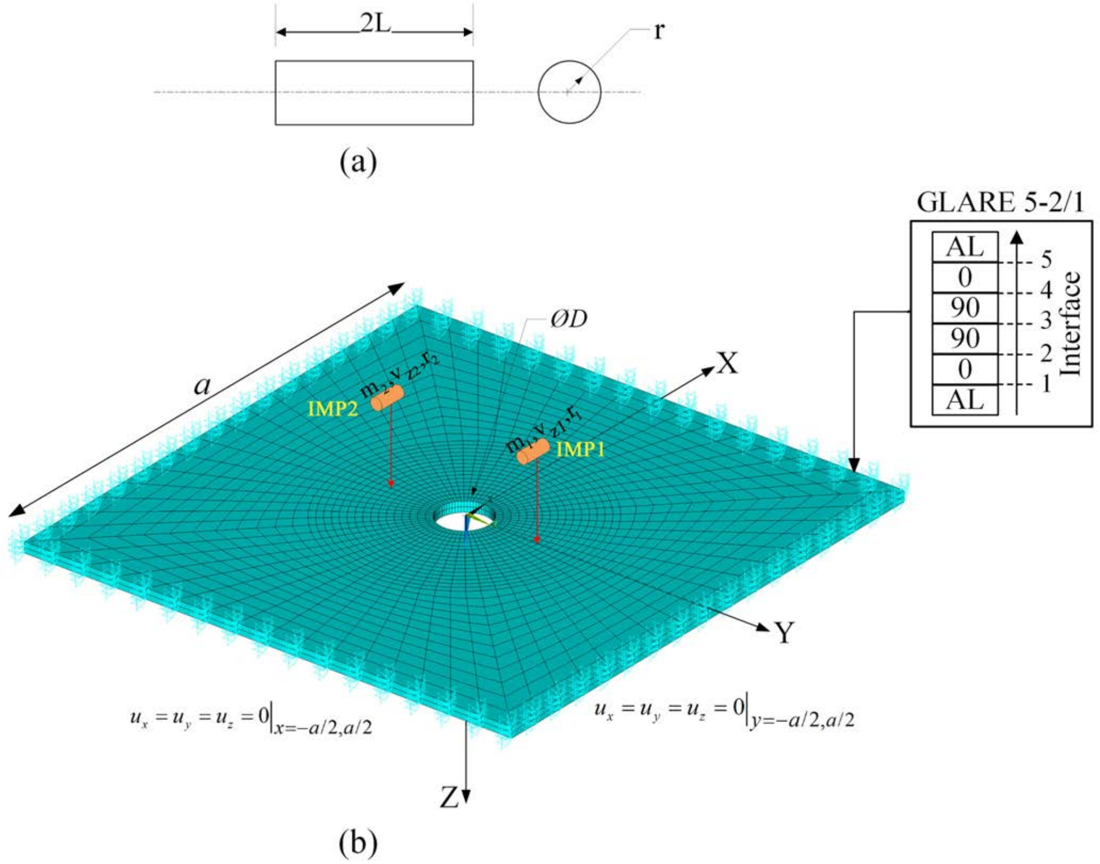

Figure 5.32: (a) Cylindrical impactor (b) Cylindrical impactors striking a clamped GLARE plate with central hole

Table 5.3: Plate and impactor details

Ply thickness	0.152 mm
Aluminium thickness	0.518 mm (Plate A) 0.580 mm (Plate B)
Total plate thickness	1.644 mm (Plate A) 1.768 mm (Plate B)
Steel cylinder radius	2.8 mm
Steel cylinder length	10 mm

5.5.2. Effect of outer aluminium thickness for two simultaneous impacts

The two steel cylindrical impactors strike the plate at symmetric locations simultaneously as mentioned earlier with velocities 10 m/s each and the dynamic responses are shown in **Figure 5.33 (a)-(d)**. It could be seen that the contact force responses, impactor displacements and velocities and plate displacements at the two contact points are identical in case of simultaneous impacts for each case. It is seen from **Figure 5.33 (a)** that the contact duration decreases marginally with increasing thickness of the outer aluminium layers of GLARE 5-2/1 (plate B) due to increased stiffness and there is a rise in contact force. **Figure 5.33 (a)** and **(d)** also show that with increasing overall thickness of the plates, the contact force and the impactor velocity experiences a slight shift towards the left. In addition, the decrease in impactor velocity is more with the increase in overall thickness of the plates. It could also be seen that the magnitudes of the contact forces in the second impact is much less compared to those in the first contact although the contact force in plate A is comparatively higher than that in plate B during the second impact. It can be seen from **Figure 5.33 (b)** and **(c)** that the impactor and plate displacements vary inversely with the outer aluminium thickness.

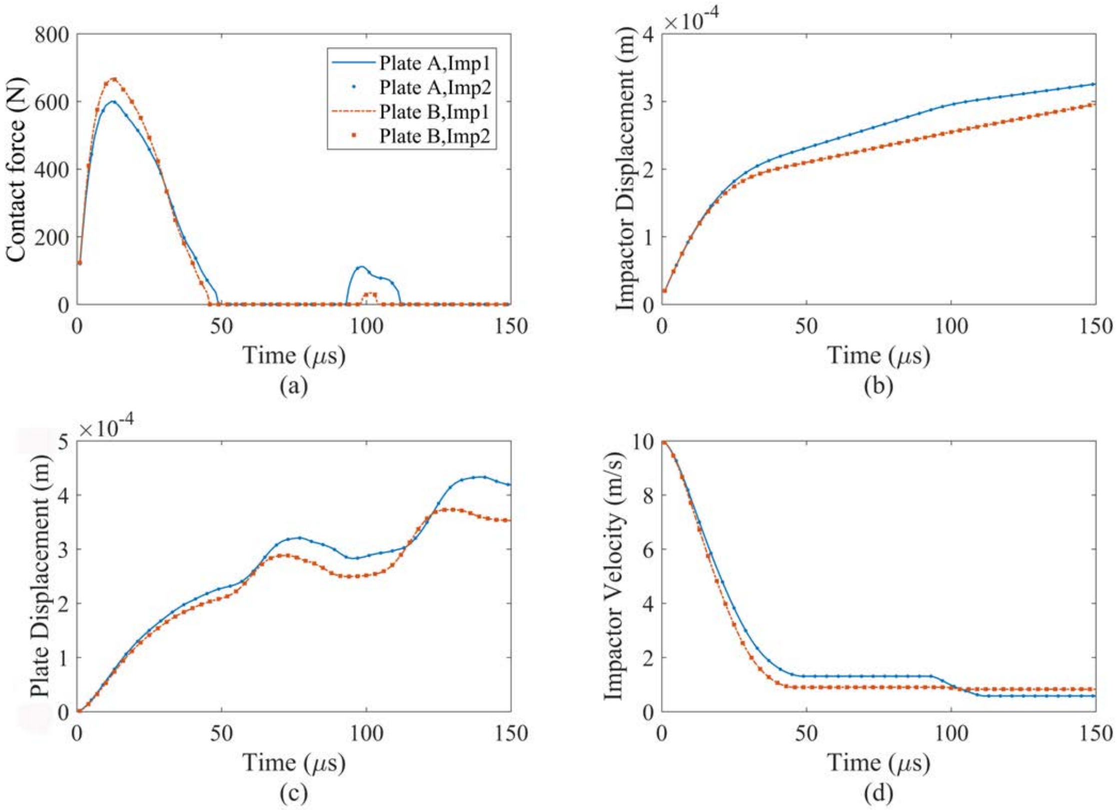

Figure 5.33: Effect of outer aluminium thickness on simultaneous multiple impact by two similar cylindrical impactors at 10 m/s

5.5.3. Two cylindrical impactors striking at different times

The plate A is taken for studying the impacts by the two cylindrical impactors striking with a velocity of 10 m/s at symmetric locations and time delays $\Delta T = 20\mu s$ and $40\mu s$ between them. The contact force histories and the dynamic responses for the plate and impactors are shown in **Figure 5.34** and **Figure 5.35**.

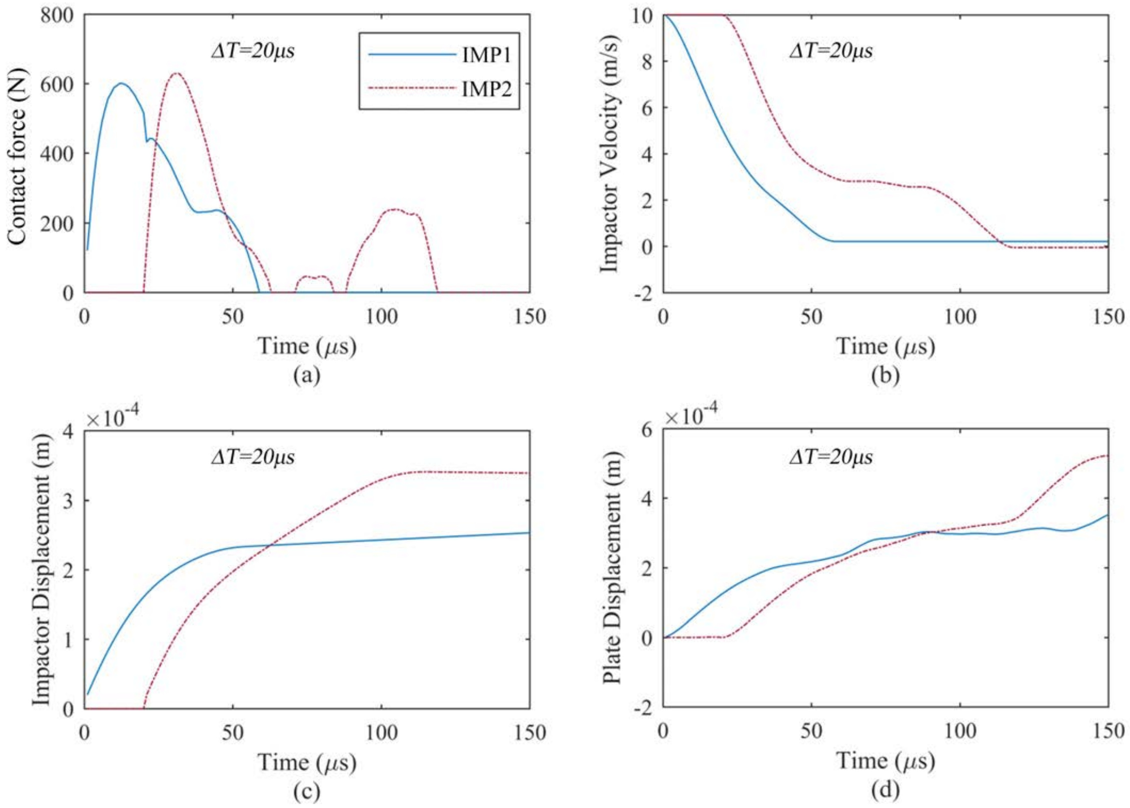

Figure 5.34: Impact responses of plate A for time delay of ΔT=20μs between the two impacts occurring at 10 m/s

It is observed from the contact force histories (**Figure 5.34(a)** and **Figure 5.35(a)**) that as the time gap between the two successive impacts increases, the magnitude of the second impactor's maximum contact force first increases as in case of $\Delta T = 20\mu s$. On increasing the delay between the successive impacts to $\Delta T = 40\mu s$, the second impactor's contact force decreases since the plate motion is in the same direction as the impactor (refer **Figure 5.34(b)**, **Figure 5.35(b)** and **Figure 5.36(a)-(b)**) and the second contact point location readily attains a higher velocity. It is also seen from **Figure 5.33(a)** that further delay in the impact interval would render the analysis as two separate impact events as the duration of the first impact is about $50\mu s$ for the simultaneous impacts at symmetric locations although there would be some plate motion. It is seen that the first impactor's contact force is negligible for the second time as compared to the first time for all the time delays between the successive impacts. In case of $\Delta T = 20\mu s$, only the second impactor comes in contact twice with a comparable reloading peak force. Therefore, it can be said that the delay in impact between the two impactors causes a change in the contact force for the second impactor.

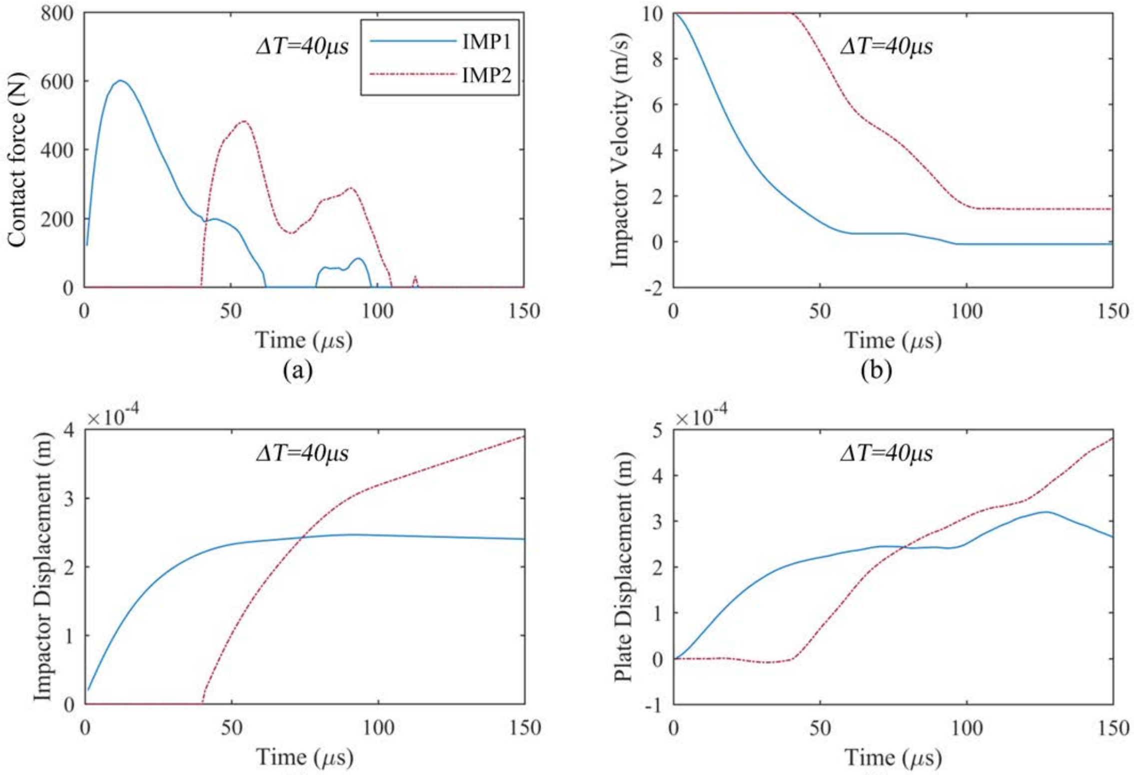

(a) (b)

(c) (d)

Figure 5.35: Impact responses of plate A for time delay of ΔT=40μs between the two impacts occurring at 10 m/s

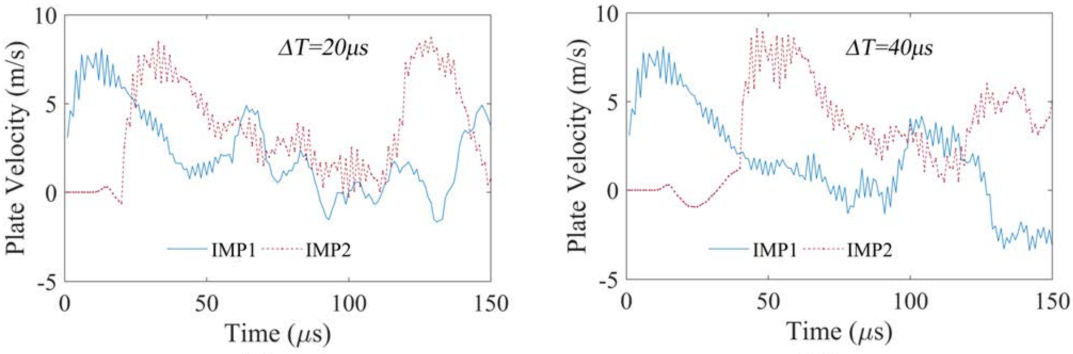

(a) (b)

Figure 5.36: Plate velocities for time delay of (a) ΔT=20μs and (b) ΔT=40μs between the two impacts occurring at 10 m/s

5.5.4. Effect of impactor radius and contact length

In order to observe the effect of geometric parameters of the impactor on the dynamic response, first the cylinder radius is increased from 2.8 mm to 4 mm keeping the cylinder length same as original dimension and secondly the length of the cylinder is doubled keeping the radius unchanged such that the net mass of the cylinders in both the cases are same and almost twice that of the original cylinder considered.

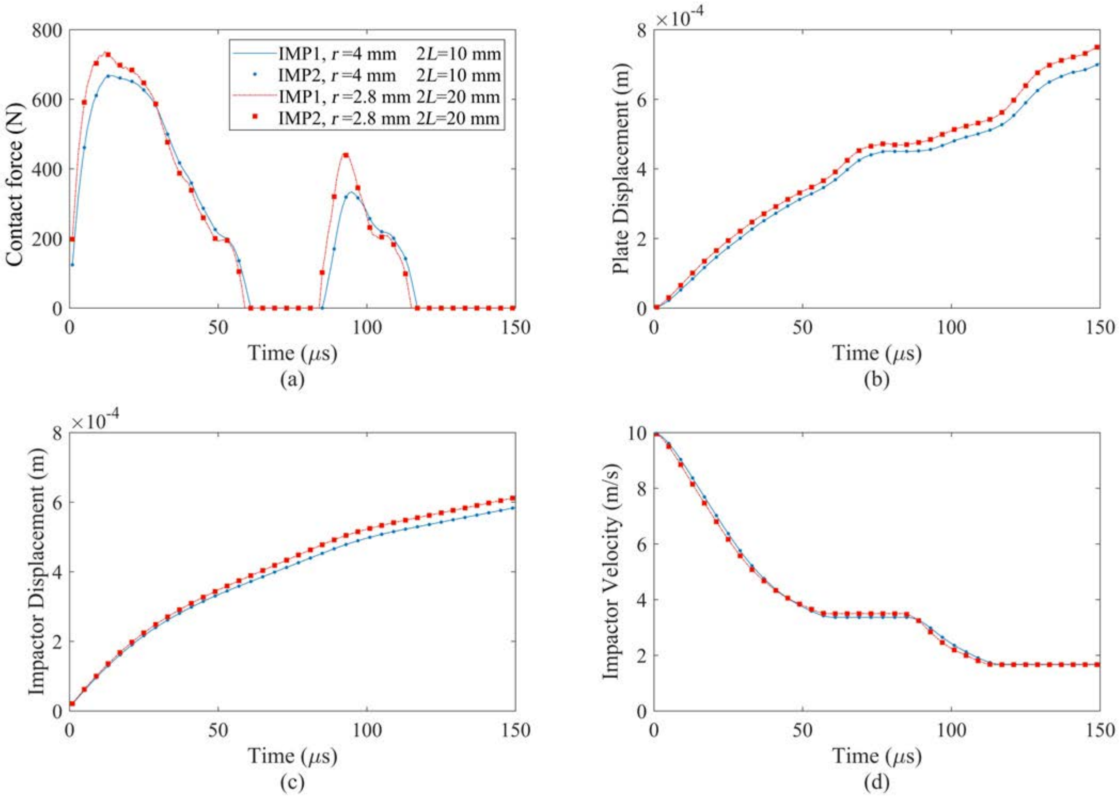

Figure 5.37: (a) Contact force, (b)plate and (c) impactor displacement and (d) impactor velocity for impacts by cylindrical impactors of different dimensions at 10m/s on plate A

The cylindrical impactor geometry can also influence the magnitude of the contact force at impact location although the duration of the impact is governed by the impactor mass as can be seen from **Figure 5.37(a)**. Also, the magnitude of the contact forces for second impact of the impactors are comparable. Increased inertia of the impactors with higher mass tends to stretch the impact duration and as can be seen from **Figure 5.37(a)-(c)**, the increase in the cylinder length which in turn increases the contact length leads to slightly higher values in peak contact force, plate and impactor displacements compared to that due to the increase in the impactor radius. However, the impactor velocity shows negligible difference (**Figure 5.37(d)**) owing to similar inertias of the impactors.

5.5.5. Interfacial delamination under multiple cylindrical LVIs

Delamination at the interfaces being one of the critical causes of failure in FMLs, it is important to assess the extent of delamination at the free edge of the hole under impact loading of GLARE by multiple cylindrical impactors. In the present case, delamination at different interfaces have been estimated for GLARE subjected to different cases of multiple cylindrical impacts.

5.5.5.1. Influence of outer aluminium thickness

Figure 5.38 and **Figure 5.39** show the delamination progression after $120\mu s$ at the interfaces of the GLARE plates A and B for simultaneous impacts by the steel cylindrical impactors of length 10 mm and radius 2.8 mm at 10 m/s. The inner glass/epoxy ply interfaces show minute delaminations for the impacts occurring at the said velocities. The delamination at the interfaces are located about the impact location and it is observed that the path of delamination is along the fibre direction of the lamina below the surface. The first impactor strikes the GLARE plates at location x = 0 and y = 0.012 m and the second identical impactor at x = 0 and y = −0.012 m. It is observed that the delamination occurs symmetrically at the

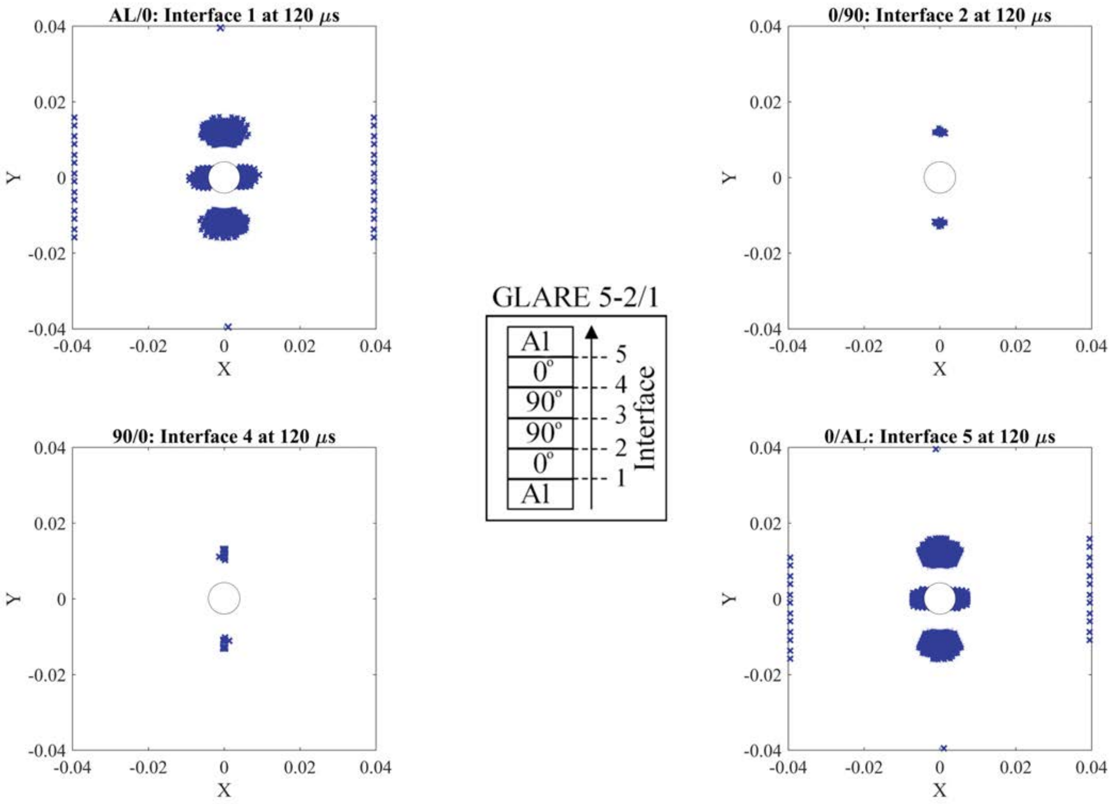

Figure 5.38: Delamination due to multiple cylindrical impacts at 10 m/s on plate A

contact locations of the two impactors and the extent of delamination is influenced by the outer aluminium layer thickness. Around the open hole, the delaminations tend to initiate only at the metal composite interfaces along the fibre direction of the underlying lamina and the progression is along the midline from the diametrically opposite tips of the hole in X-direction. As can be seen from **Figure 5.38** and **Figure 5.39**, the extent of delamination is more in plate A than that in plate B which is having a thicker aluminium layer enabling a greater absorption of the impact energies associated with the LVIs. But in both the cases the metal composite interfaces experience the maximum extent of delamination. It is also observed that the extent of delamination at the bottom interface is slightly more than that at the top interface and the delaminations indicate that the interfacial shear stresses that arise as a result of bending initiate the debonding at the aluminium composite interfaces which in turn enables efficient energy absorption during impacts.

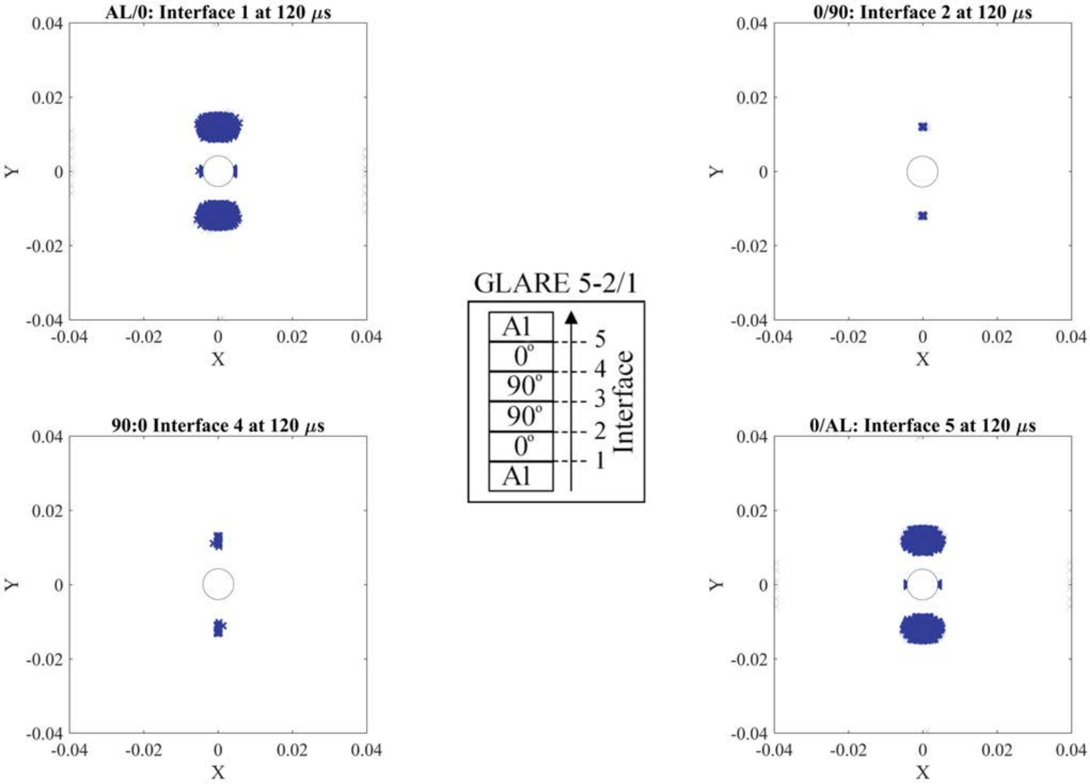

Figure 5.39: Delamination due to multiple cylindrical impacts at 10 m/s on plate B

5.5.5.2. Influence of time delay between the cylindrical impacts

Now, for the same symmetrical impact locations and the identical impactors striking plate A at 10 m/s, the effect of the time delay between the two successive impacts on delamination progression are studied for the time intervals $\Delta T = 20\mu s$ and $40\mu s$ as shown in **Figure 5.40** and **Figure 5.41** respectively. Comparing **Figure 5.38**, **Figure 5.41** and **Figure 5.42**, it is seen that the extent of delamination varies with the time gap between the two successive impacts. When occurring simultaneously (**Figure 5.38**) the delaminations are symmetric and equal and as the time gap increases the delaminations become asymmetric, gradually increasing first and then decrease when $\Delta T = 40\mu s$. Also, as seen from the force responses for the impacts occurring at different time intervals (**Figure 5.33(a)**, **Figure 5.34(a)** and **Figure 5.35(a)**) where the second impact attributes to higher contact force when $\Delta T = 20\mu s$, the delamination around the vicinity of the second impact location (x=0, y=–0.012 m) tends to be larger as evident from **Figures 5.40-5.41**. It is seen that the extent of delamination is marginally more for the bottom aluminium/composite interface (interface 1) as discussed and it is observed that the spread of the delamination around the impact location tends to be along the fibre direction of the 0° glass/epoxy ply (x-direction) adjacent to the aluminium layer of the GLARE laminate. In all the cases, delamination initiates only at the top and bottom interfaces around the periphery of the hole and along the fibre direction of the underlying layer of the aluminium/composite interfaces.

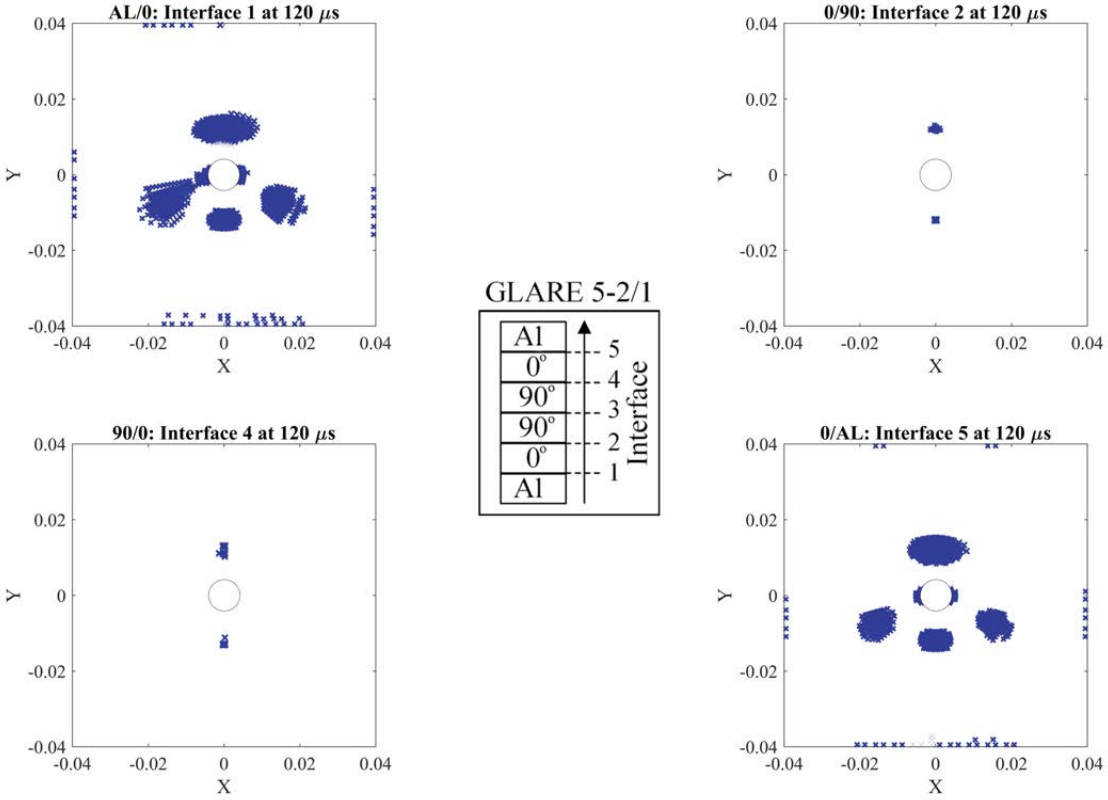

Figure 5.40: Delamination due to multiple cylindrical impacts at 10 m/s on plate A with ΔT=20μs between the two impacts

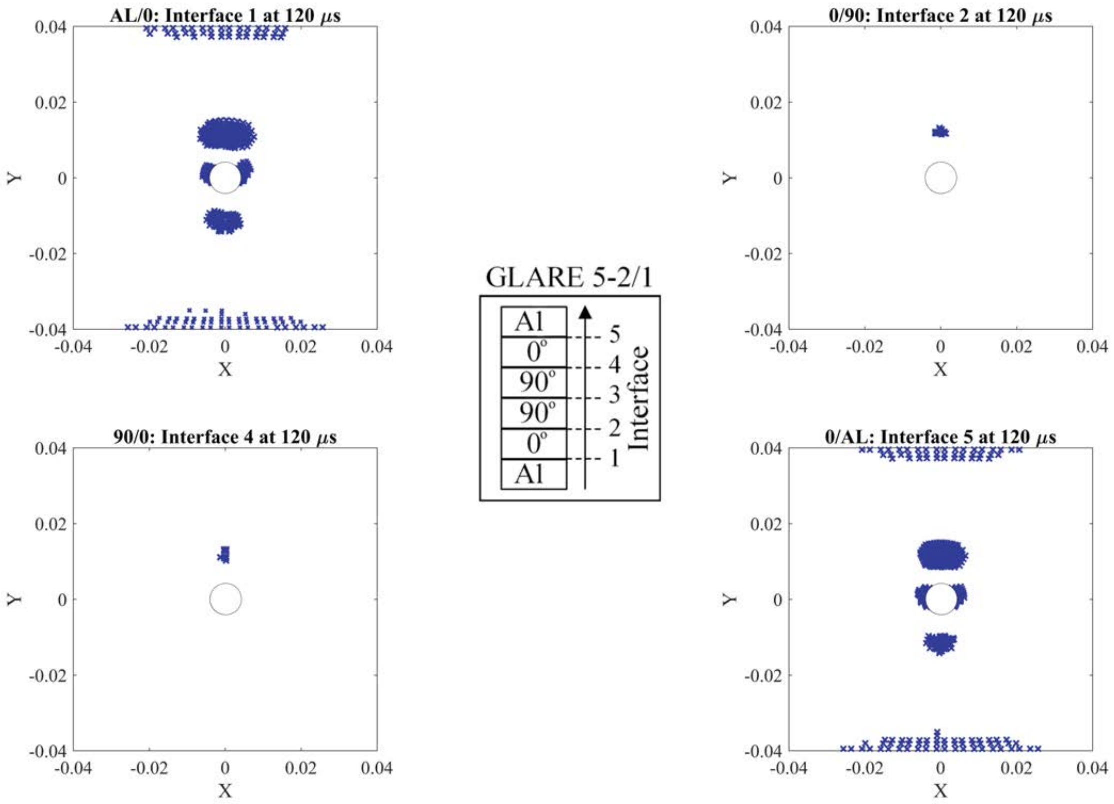

Figure 5.41: Delamination due to multiple cylindrical impacts at 10 m/s on plate A with ΔT=40μs between the two impacts

5.5.5.3. Influence of impactor dimensions

Figure 5.42 shows the delamination at the interfaces of GLARE plate A due to impacts by the 10 mm long cylindrical impactors with larger radius of 4 mm and **Figure 5.43** shows the same for impactors of twice the original length and radius unchanged. It is seen that due to increased mass of the impactors, along with the rise in contact forces (refer **Figure 5.37(a)**), the extent of delamination also increases at the fibre/metal interfaces. As before, along with the localised delamination at the contact locations, the delamination along the periphery of the hole at the metal/fibre interfaces increase along x-direction and the tendency to coalesce into a single delaminated region encompassing the hole and contact locations is easily predictable with increasing contact force. Also, with overall increase in the delamination area, the extent of delamination is seen to be comparatively more for the case of increase in length of the cylinder compared to increase in cylinder radius. Also, at the inner composite interfaces, the delamination more or less remains the same.

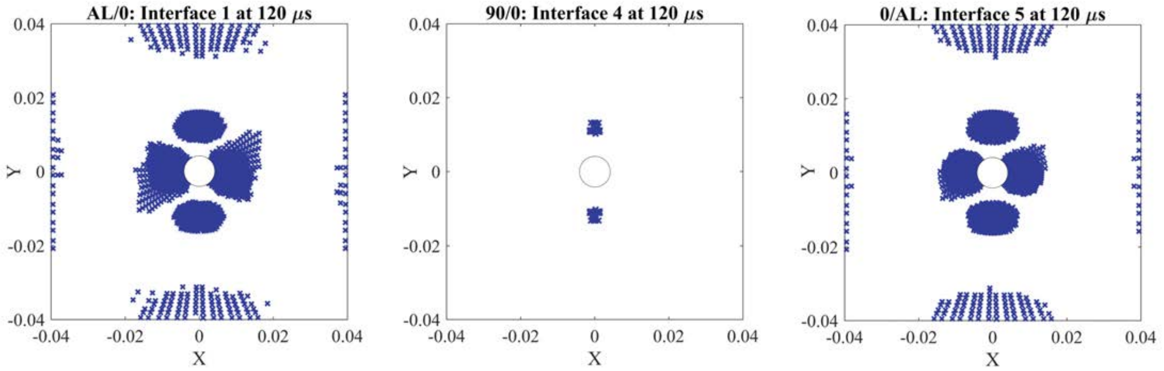

Figure 5.42: Delamination due to multiple cylindrical impacts at 10 m/s on plate A by cylindrical impactors of length 10 mm and radius 4 mm

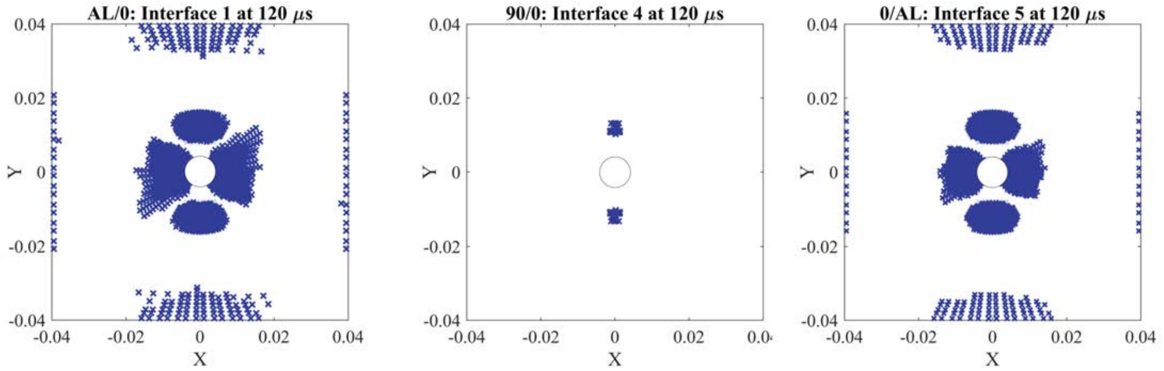

Figure 5.43: Delamination due to multiple cylindrical impacts at 10 m/s on plate A by cylindrical impactors of length 20 mm and radius 2.8 mm

5.5.5.4. Effect of impact location about the hole periphery

In order to observe the effect of impact location on the delamination at the interfaces, the cylinders strike at locations (0, 0.02 m) and (0, –0.02 m) at 10 m/s on plate A. Comparing the contact force responses from **Figure 5.33(a)**, **Figure 5.34(a)**, **Figure 5.35(a)** and **Figure 5.44**, it can be inferred that peaks in the contact forces of the first impact are almost same and unaffected by the impact location although the duration of the impact varies based on the location of the impacts and the peak forces of the second impact is seen to be affected by the time delay as well as location of the impacts as a result of the variation of the global deformation of the plate. So, keeping in view of the criticality of the fibre/metal interfaces, the delamination at these interfaces are assessed for different time delays between the impacts as shown in **Figure 5.45**. It is seen that although the nature of the extent of local delamination about the contact area remains nearly the same, the extent of delamination around the periphery of the hole reduces. In the current case also, it is seen that when the peaks of the impacts occur close to one another for $\Delta T = 20\mu s$ the extent of delamination is more and when the delay increases there is no delamination around the hole for $\Delta T = 40\mu s$.

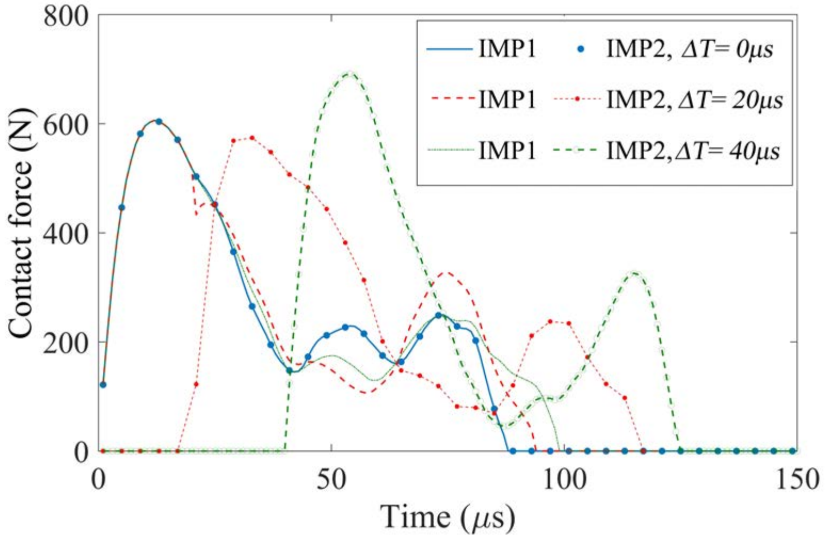

Figure 5.44: Contact force for impacts at 0.02m symmetrically from centre along y-axis on plate A

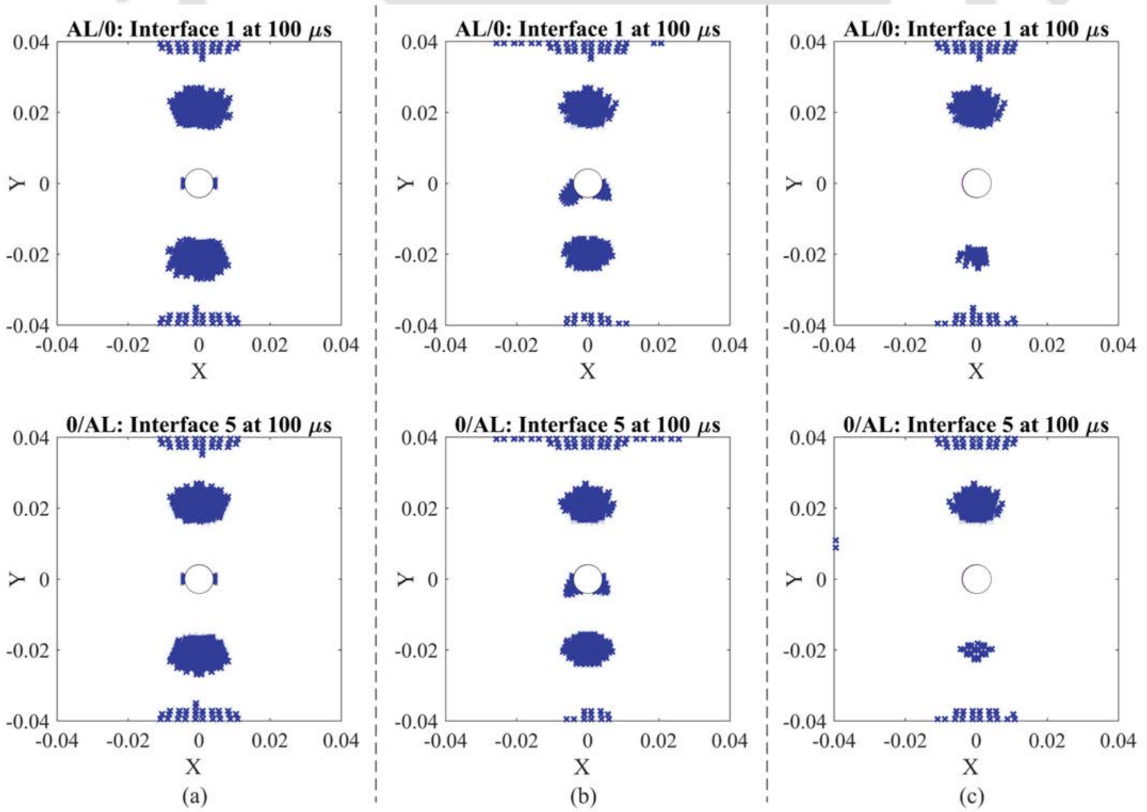

Figure 5.45: Delamination at the bottom and top fibre/metal interfaces of plate A for cylindrical impacts at locations 0.02m from centre along y-axis for (a) ΔT=0 (b) ΔT=20μs (c) ΔT=40μs

5.6. Summary

The LVI responses of a standard GLARE 5-2/1 plate is compared to those having discontinuities in the form of holes/cut-outs. The effect of important parameters like the relative offset between the hole and the impact site, impactor geometry and relative pitch between the holes are investigated. Furthermore, the effect of hybridisation with Kevlar-49 layers and different MVF on the impact response are explored. In addition, the multiple LVIs on a plate having a central circular cut-out subjected to cylindrical impacts is studied to see the effect of relative impactor positions, delay between their impacts and other associated important parameters. Based on the present analysis, the following important conclusions can be drawn as follows:

- The impact location can significantly affect the contour of the delamination at the fibre/metal interfaces. Closer is the impact to the open hole, more is the damage caused due to delamination. Thus, area around the hole is more prone to delamination.
- The shape of the central cut-out can be a critical factor in initiation of delamination near the periphery of the cut-out and care should be taken in deciding the geometry of these cut-outs.
- The presence of discontinuities in the form of cut-outs can reduce the plate flexure, resulting in higher transverse deflections and lower peaks in the contact force when the impacts occur close to the cut-out.
- The geometry/size of the impactor influence the contact response in terms of the peak values attained and the impactor mass affects the contact duration. For cylindrical impactors with identical masses, the increase in cylinder length leads to a greater raise in the peak contact force values compared to increase in diameter.
- The MVF along with the plate thickness influence the plate flexural stiffness. This can affect the delamination at the interfaces based on the size and pitch of the holes.
- In case of the inner interfaces, the delamination is generally located around the contact region and for all the cases, the direction of the delamination is influenced by the fibre direction of the underlying layer.
- Relative to the GLARE plate dimension, for holes having diameters below a critical minimum, the position of the holes have minor effect on the dynamic response. But the same is not true for the interfacial delamination and its extent at the fibre/metal interfaces. Therefore, the pitch between two holes is an important aspect that needs to be considered while making holes required for certain applications on a GLARE laminate.

- The hole shape and their orientation relative to the fibre direction of the underlying ply influences the delamination at the aluminium/glass-epoxy interfaces and also around the hole periphery.
- In case of multiple cylindrical impacts, the delamination at the fibre-metal interfaces initiate at the contact locations and around the periphery of the open circular hole, and depending on the magnitude of the contact force there is a tendency to coalesce into a single delaminated area around the hole.
- The magnitude of the contact force for the second impact is influenced by the time interval between the two impacts and also by the location of the impacts.
- Geometric parameters of the cylindrical impactor also influence the extent of delamination and the effect of contact length is more pronounced compared to that of cylinder radius.
- The hybrid configurations having inner Kevlar-49 plies can be a viable option which can reduce the overall weight compared to standard GLARE configurations.

Chapter 6

Oblique LVI on GLARE considering friction

The present chapter numerically investigates the oblique low velocity impact (OLVI) behaviour of clamped GLARE plates by a spherical impactor to study the influence of obliquity and coefficient of friction on the impact mechanism and on the extent of interfacial delamination. In addition, the multiple OLVIs on GLARE is investigated studying the effect of the time interval between the impacts, their relative trajectories and geometrical parameters like the impactor size on the impact response.

6.1. Introduction

In practical applications, the impactor's trajectory of incidence can be arbitrary relative to the target and not much work is reported investigating the OLVI on GLARE considering the normal and tangential contact responses simultaneously and assessing the interfacial delamination that emanates on account of it. Delamination being a critical mode of failure in laminated structures, the interest of the present analysis is to investigate the dynamic responses of GLARE 4-3/2 FMLs due to OLVI by a spherical steel impactor at different incident angles and velocities and understand their influence on interfacial delamination. As depicted in **Figure 6.1**, the GLARE 4-3/2 configuration has two outer aluminium layers and one middle aluminium layer stacked alternately between the $[0^\circ/90^\circ/0^\circ]$ S2-glass/epoxy laminates and the interfaces are numbered from bottom to top.

6.2. Oblique LVI on a clamped GLARE plate

In the case of OLVI, the normal component (f_N) and the tangential component (f_T) of the contact force need to be evaluated simultaneously. In the present work, Hertzian force-displacement relation is used to evaluate the normal contact force and the tangential contact force is computed by using the theory of Mindlin and Deresiewicz [176,177,214]. A three dimensional finite element formulation employing Newmark-β method has been developed for analyzing the oblique contact impact response of GLARE plate where Hertzian contact model is used for the normal component of contact and Mindlin and Deresiewicz theory [176,177,214] is used for the tangential component as described in **Chapter 3**.

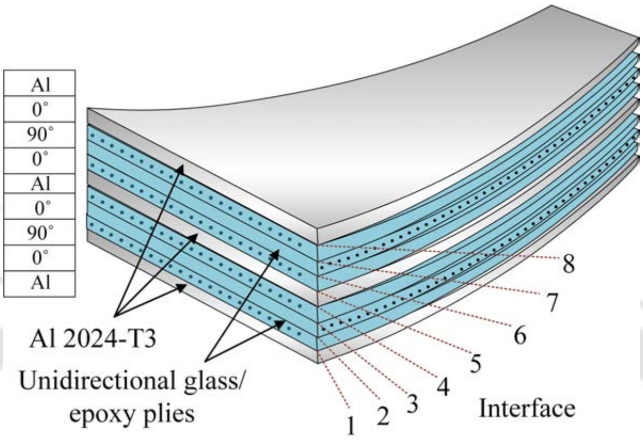

Figure 6.1: GLARE 4-3/2

6.2.1. Problem definition

As shown in **Figure 6.2**, a square clamped GLARE 4-3/2 plate of 0.08 m × 0.08 m is impacted by a 5 mm diameter spherical steel impactor at different angles of incidence θ at the centre with x-z being the plane of impactor motion such that the components of velocity along the normal and tangential direction are v_n and v_t respectively. The thickness of each aluminium layer is 0.304×10^{-3} m and that of S2-glass/FM94-epoxy lamina is 0.156×10^{-3} m, taking the total thickness of the GLARE plate to 1.848×10^{-3} m.

In order to observe the change in contact response due to obliquity, first, the spherical impactor is considered to strike the target at different angles with a fixed initial speed. Next, the obliquity is varied keeping the initial normal component of the velocity fixed at 10 m/s such that it results in a change in the tangential component of the initial velocity only and a direct comparison can be drawn between the tangential response and the normal contact force. A simple illustration is presented to show the variation of the normal and tangential component of velocity with obliquity: (a) for a fixed initial speed and (b) for a fixed initial normal component of velocity as shown in **Figure 6.3**. Effect of the coefficient of friction on the tangential contact force has also been investigated for different angles of incidence. Finally, the extent of delamination at the interfaces due to OLVI is assessed for different plane of the impact.

Table 6.1 [204–206] lists the interface strengths and the material parameters for aluminium alloy and S2-glass/FM94-epoxy laminates and steel are listed in **Table 6.2** [45,102,138].

Table 6.1: Interface strengths [204–206]

Interfacial strengths	S2-glass/FM94-epoxy interfaces	S2-glass/FM94-epoxy and Aluminium 2024-T3
S_n (MPa)	43	40
S_i (MPa)	50	40

Table 6.2: Material properties [45,102,138]

Parameter	Notation	Al 2024-T3 alloy	UD S2-glass/FM94-epoxy prepregs	Steel
Density (kg/m^3)	ρ	2780	1980	7800
Poisson's ratio	υ	0.33	$\upsilon_{12} = 0.33, \upsilon_{23} = 0.33$	
Young's modulus (GPa)	E	72	$E_1 = 55, E_2 = 9.5$	200
Shear Modulus (GPa)	G	—	$G_{12} = 5.5, G_{23} = 3.5$	
Yield strength (MPa)	σ_{ys}	340	—	
Transverse tensile strength (MPa)	Y_T	—	50	
Transverse compressive strength (MPa)	Y_C	—	160	
In plane shear strength (MPa)	S_{lt}	—	70	

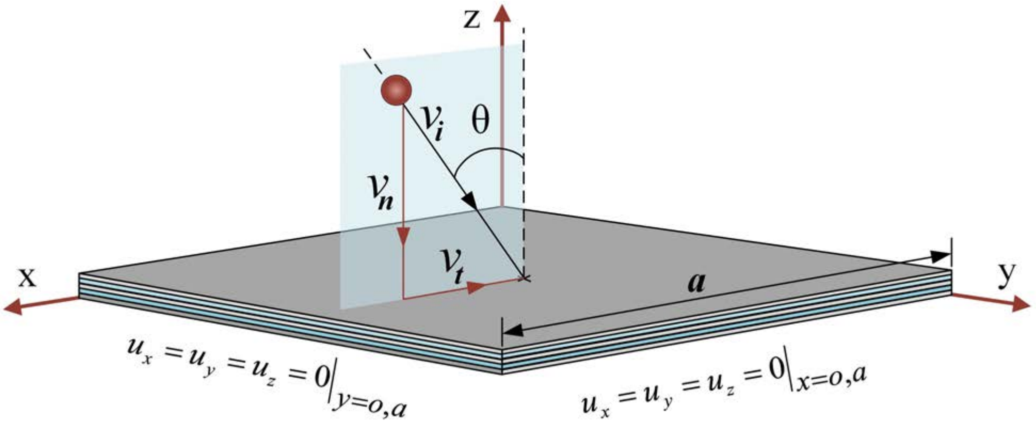

Figure 6.2: Oblique impact by a steel sphere on a clamped GLARE 4-3/2 plate

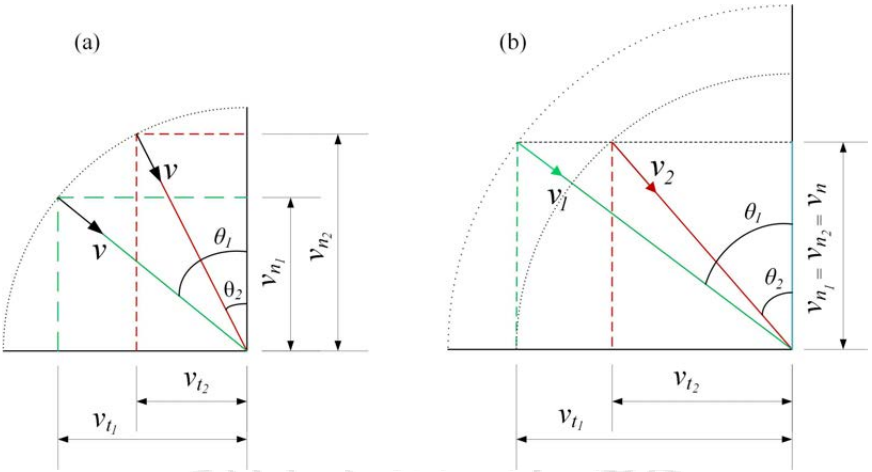

Figure 6.3: Variation of the normal and tangential component of velocity with obliquity

6.2.2. Validation of the FE code

To reinforce the accuracy of the present code, it is validated with the results of Christoforou and Yigit [203] for the contact force when a 12.7 mm diameter steel spherical impactor normally strikes a simply supported carbon/epoxy beam of span 0.2 m and width 0.02 m and having a stacking sequence [0 ° /90 ° /0 ° /90 ° /0 °]$_s$ at the centre with a velocity of 3 m/s (refer **Figure 6.4(a)**). The carbon/epoxy plies have the following material parameters: E_1 =120 GPa, E_2 =7.9 GPa, G_{12}=5.5 GPa, ρ =1580 kg/m^3, $\upsilon_{12} = \upsilon_{23}$ =0.3 and the plies are 0.269 mm thick. Refining the mesh from coarser to a finer mesh in steps, a mesh size of 64×16×2 elements and a time step of $\Delta t = 1\,\mu s$ is taken for the dynamic analysis of the simply supported composite beam and the contact force obtained as shown in **Figure 6.4(b)** shows an excellent match with the published works of Christoforou and Yigit [203].

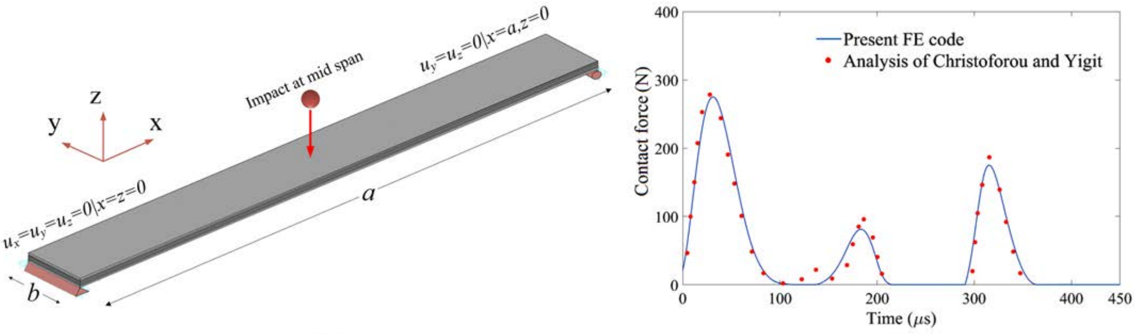

(a) (b)

Figure 6.4: Simply supported [0/90/0/90/0]$_S$ carbon/epoxy beam and (b) contact force history for impact by a steel sphere [203]

Furthermore, the present code is also validated with the experimental results of Seo et al. [138] where a clamped circular GLARE 5-2/1 plate is impacted by a hemispherical steel impactor with 12.7 J as shown in **Figure 6.5(a)**. Contact force history computed by the present code shows a good agreement with the experimental results of Seo et al. [138] as shown in **Figure 6.5(b)**.

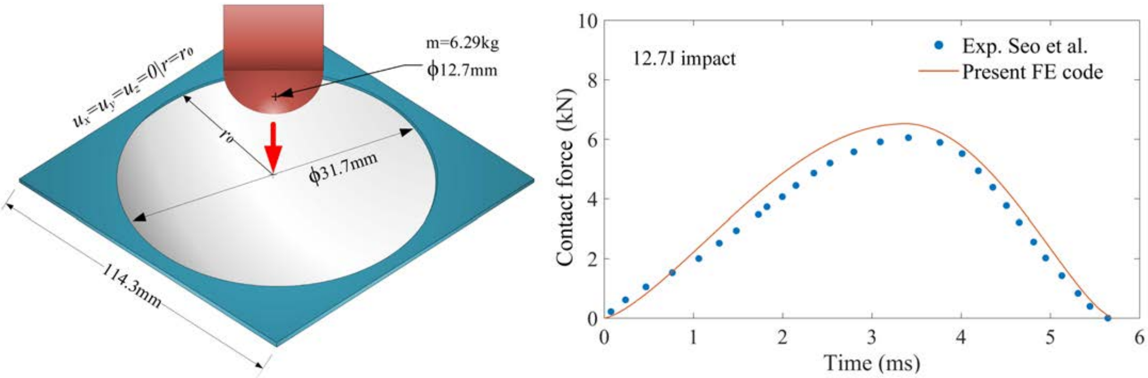

(a) (b)

Figure 6.5: (a) Impact on a clamped circular GLARE 2/1 plate by a spherical impactor (b) Validation of contact force history [138]

From the review of literature in **Chapter 2**, there are not many literatures where simultaneous normal and tangential contact responses are investigated for OLVI on GLARE. To determine the computational effectiveness of the present FE code for investigating the OLVI, a system having geometrical dimensions of similar order as reported in the works of Wu et al. [215] considering the material parameters as: E =208 GPa, ρ = 7850 kg/m^3, ν =0.3 and μ_f =0.3 are considered. A steel sphere of radius 10 μm strikes an elastic half space of dimension 60 μm × 60 μm × 10 μm at different angles of incidence with a fixed initial normal velocity of v_{ni} =5 m/s. The nodes on the boundaries i.e. at planes x = ±30 μm, y = ±30 μm and z = −10 μm are fixed. Normal force-displacement relationship obtained from the present analysis shows a good agreement with the results of Wu et al. [215] as shown in **Figure 6.6**. Furthermore, to verify the manner of evolution of the tangential contact force at a constant initial normal component of velocity, the impact angles are varied and the tangential contact force evolution is plotted in **Figure 6.7**. It could be observed from **Figure 6.7** that the maximum tangential contact force is limited to the value of $f_T = \mu_f f_N$ which is of general notion and it can be seen that as the impact angle increases, the region of negative tangential force decreases and finally at high impact angles there is sliding throughout the contact period. These observations are in good agreement with the results of Maw et al. [216] thereby establishing the validity of the present FE code.

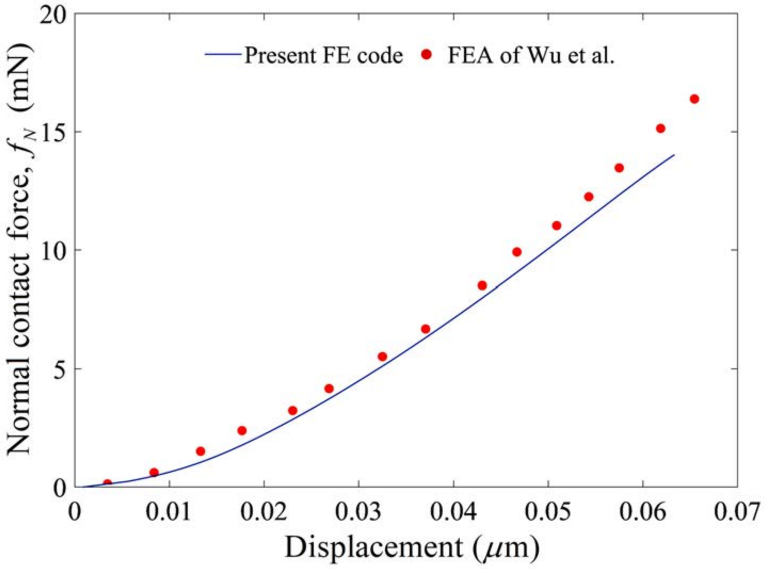

Figure 6.6: Normal contact force-displacement for LVI by a rigid steel sphere with v_{ni} =5 m/s [215]

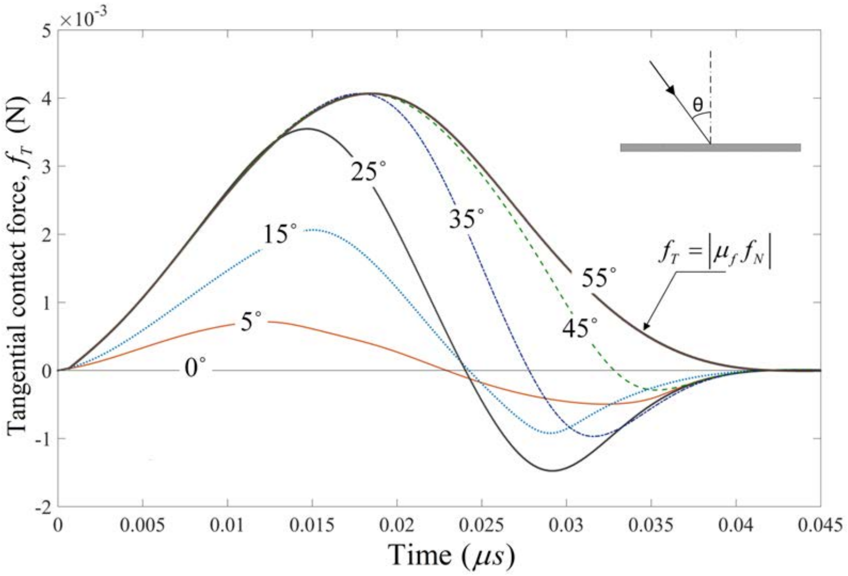

Figure 6.7: Tangential contact force histories for LVIs at different θ with fixed v_{ni}=5 m/s

6.2.3. Effect of obliquity on contact response at an initial fixed speed

The magnitude of peak contact forces attained is of significant importance as this decides the nature and extent of interfacial delamination damage induced in the target during an impact. **Figure 6.8(a)** shows the time history of the normal component of the contact force and **Figure 6.9(a)** shows the same for tangential component of the contact force for oblique impact of spherical impactor on the GLARE plate with an initial speed of 10 m/s for different obliquities corresponding to a coefficient of friction μ_f = 0.47 between the impactor and the plate.

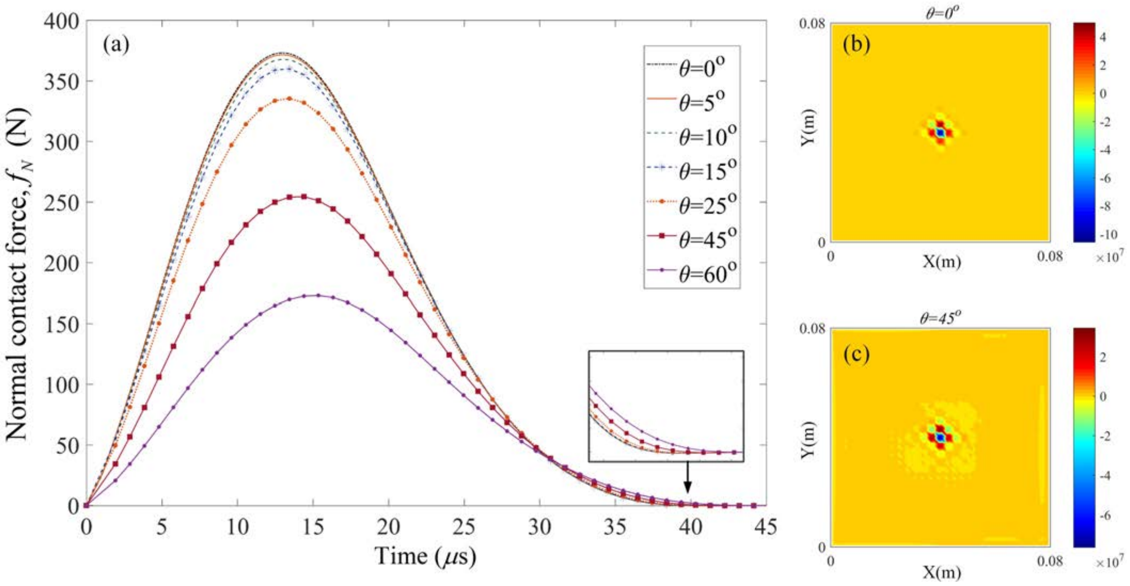

Figure 6.8: (a) Normal contact force at different angles of impact for a fixed initial impact speed of 10 m/s; σ_z (N/m^2) at interface-8 (Al/composite) for (b) θ =5° (c) θ =45° at 15 μs

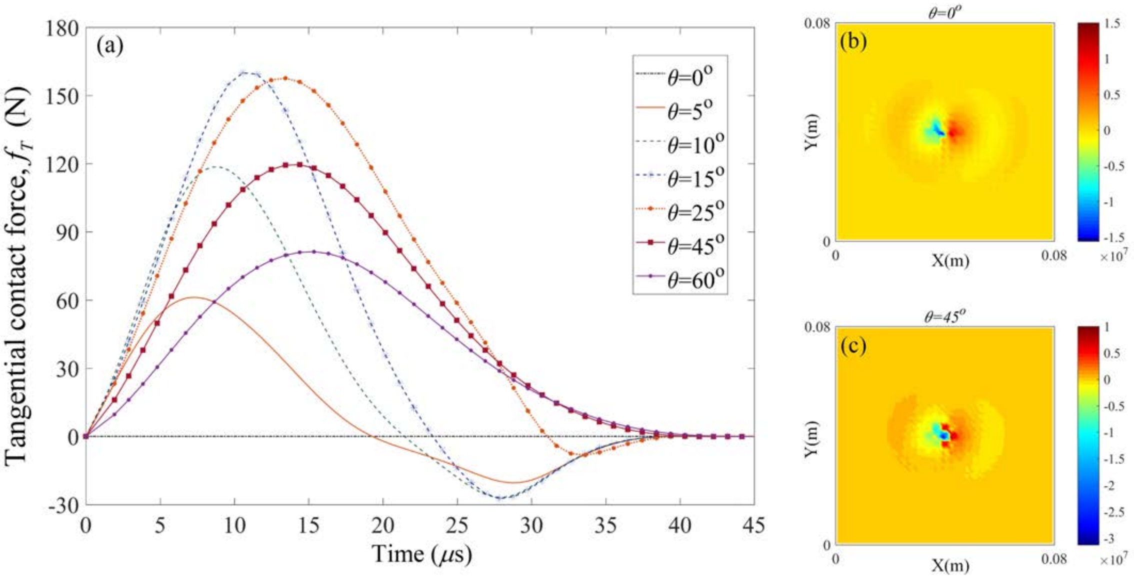

Figure 6.9: (a) Tangential contact force at different angles of impact for a fixed initial impact speed of 10 m/s; τ_{xz} (N/m^2) at interface-8 (Al/composite) for (b) θ=5° (c) θ=45° at 15 μs

It could be observed from **Figure 6.8(a)** that whereas the magnitude of peak normal contact force decreases with the increase in oblique angle, the duration of normal contact increases. However, the tangential contact force history shown in **Figure 6.9(a)** reveals that the magnitude of the peak tangential contact force increase with the increase in oblique angle θ while $\theta < 15^\circ$ and beyond that the magnitude of tangential contact force reduces. This is because initially with increasing obliquity the normal component of the velocity increases leading to a rise in the tangential contact force while $f_T \leq \mu_f f_N$. In addition, the tangential contact force reverses its direction during contact due to stick slip and the instant of reversal is delayed with increasing oblique angle. Also the duration of negative tangential contact force decreases with increasing oblique angle. With higher oblique angle, $\theta > 45^\circ$, the reversal is negligible and there is almost no stick and a complete slip occurs. This is due to the fact that when the tangential contact force reaches values $f_T > \mu_f f_N$, sliding occurs and the tangential contact force value becomes $f_T = \mu_f f_N$. The typical stress profiles at the top aluminium/composite interface-8 is shown in **Figure 6.8(b)-(c)** and **Figure 6.9(b)-(c)** for the out-of-plane stresses and corresponding to $\theta = 5^\circ$ and $\theta = 45^\circ$ respectively at t = 15 μs. It can be observed that the stress magnitude changes and a change in the stress contour is seen when the incident obliquity is varied for the impacts occurring at a fixed initial speed.

Figure 6.10 shows the impactor displacement history for different oblique angle of impact. It could be observed from **Figure 6.10** that an increase in the obliquity of impact leads to a decrease in the impactor displacement in the normal direction leading to a lesser indentation at the point of contact and hence lower peaks of the normal contact forces, as shown in **Figure 6.8**. **Figure 6.11** shows the impactor energy during the impact duration and it is seen that at larger obliquities the final energy of the impactor is higher, showing that at large impact angles the energy absorbed by the target reduces.

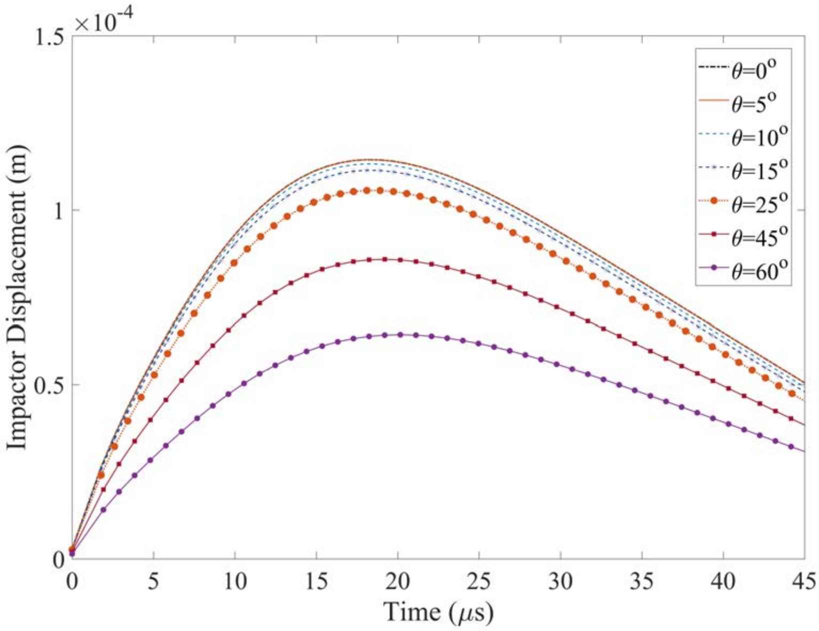

Figure 6.10: Normal impactor displacement at different angles of impact for a fixed initial impact speed of 10 m/s

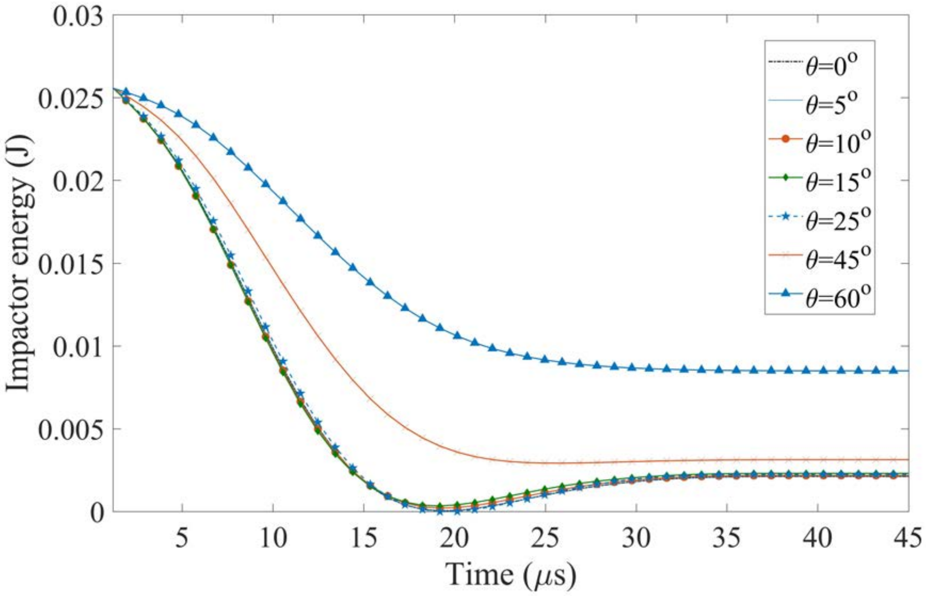

Figure 6.11: Impactor energy at different angles of impact for a fixed initial impact speed of 10 m/s

6.2.4. Effect of obliquity on contact response at an initial fixed normal velocity

In the previous section, the analysis showed the effect of obliquity on the OLVI by an impactor with a fixed initial speed. The obliquity of impact results in varying normal and tangential components of initial velocities, thereby causing changes in both the normal as well as tangential responses. As a result, exploring their coupled interaction on the target may not be clearly possible, although it is to be noted that the normal and tangential contact forces do not interfere with each other. Therefore, in the second case, the normal component of initial velocity is fixed at 10 m/s throughout the range of obliquities during OLVI on the clamped GLARE plate and the coefficient of friction is $\mu_f = 0.47$. **Figure 6.12** shows the variation of the tangential contact force with oblique impact angle and the normal force profile in terms of $f_T = \mu_f f_N$ when the impactor strikes with the initial normal component of velocity fixed at 10 m/s. It is seen from **Figure 6.12** that for the same normal force profile on account of the fixed initial normal component of velocity, the increase in obliquity results in an increase in the peak tangential contact force. Compared to **Figure 6.9(a)**, where the impactor strikes at a fixed initial speed of 10 m/s, the tangential contact force attains the maximum value when the oblique angle of incidence reaches 25°.

Further increase in the obliquity results in the peak value of tangential contact force to remain essentially unchanged when $\theta \geq 25^\circ$ and slip occurs throughout the impact regime with $f_T = \mu_f f_N$ when $\theta \geq 45^\circ$. It is clearly evident from the relative tangential displacement of the impactor as shown in **Figure 6.13**, where at small impact angles the relative tangential displacement of the impactor remains unchanged close to zero until just before the impact concludes. At intermediate angles, there is an initial increase in the relative tangential displacement followed by a steady unaltered region when there is no sliding and finally the relative tangential displacement decreases towards the end, indicating the displacement direction is opposite, and at higher angles beyond $\theta = 45^\circ$, there is sliding throughout the whole impact duration.

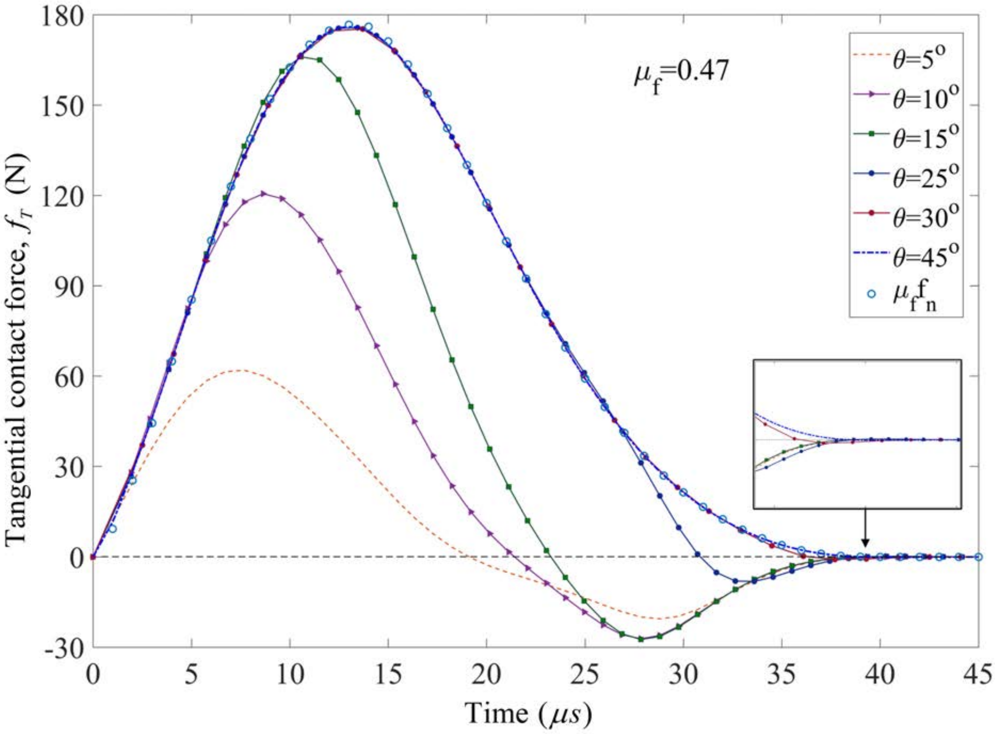

Figure 6.12: Contact force variation with the obliquity of impact for a fixed v_n=10 m/s

These can be visualised by considering the target surface to act as a non-linear spring along the tangential contact such that initially there is gross slip in the direction of the initial tangential velocity and as the friction force compresses the spring, the contact surfaces stick and once the maximum compression is attained, the annulus of microslip grows inward. Subsequently, this causes regions of counter- slip to be generated near to the boundary of contact. These become more dominant as the impact proceeds until there are no stuck regions left and slip occurs throughout. This oscillation of stick and slip follows until towards the end of the cycle and is reflected in the tangential loading history. When the angle of incidence is larger, the occurrence of gross slip is seen initially which delays the start of the cycle of stick and slip but the same behaviour is seen in general. As the incident angle becomes larger than the critical limit, gross slip occurs throughout the impact duration. Therefore, the normal component of velocity, which influences the peak value attained by the normal contact force, together with the obliquity of the impact, affects the contact force response in the tangential direction during impact.

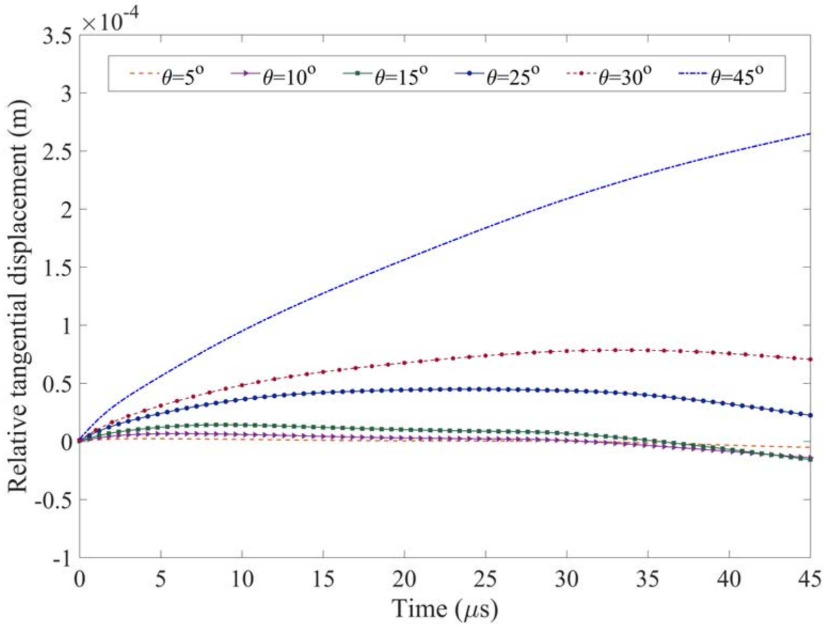

Figure 6.13: Relative tangential displacement of the impactor at different impact angles

6.2.5. Effect of coefficient of friction on the tangential contact response

In order to understand the correlation between the coefficient of friction and obliquity of impact on the evolution of tangential component of the contact force, the contact force responses are evaluated varying the value of μ_f between 0.28 and 0.67 for a fixed normal component of initial impact velocity of 10 m/s at a lower impact angle of $\theta = 5^\circ$ and an intermediate angle of $\theta = 30^\circ$. It is seen from **Figure 6.14** that the variation of the tangential contact response with the coefficient of friction is negligible at lower values of oblique impact angle. As the obliquity of the impact increases, the influence of the coefficient of friction is evident in determining the evolution of the tangential response and the peak contact force. For a certain angle of impact, as the coefficient of friction decreases, the tendency to slip throughout the impact increases at intermediate values of incident angle and no reversal in tangential force is observed at lower values of μ_f. However, as μ_f increases, the reversal point of the tangential force shifts towards left and the duration of negative tangential contact force increases at intermediate angles of impact.

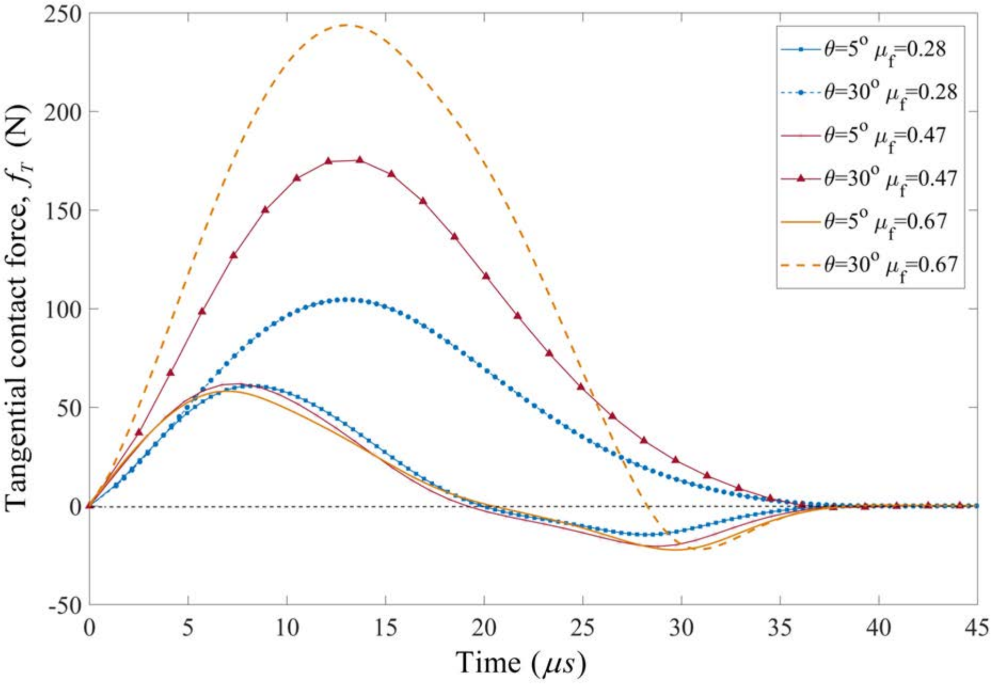

Figure 6.14: Influence of μ_f on tangential contact force at different obliquities

6.2.6. Delamination at the interfaces

It is necessary to investigate the delamination damages at the interfaces of the GLARE due to oblique impact and the influence of different factors on the extent of such interfacial damage. **Figure 6.15(a)** and **Figure 6.16** show the typical interfacial stress profile of σ_y at the top aluminium/0° ply (interface-8) for different impact scenarios with v_{ni}=10 m/s and at an instant $t = 15\,\mu s$ and the difference in their variations around the impact location can be seen clearly. For clarity of the interface considered, the layup of GLARE 4-3/2 is shown in **Figure 6.15(b)**. It could be seen from **Figure 6.15(a)** that for a normal impact (θ = 0 °), it is symmetric but **Figure 6.16** shows different stress profiles at the interface as the impactor strikes obliquely at θ = 30° from the positive x-direction (**Figure 6.16(a)**) and positive y-direction (**Figure 6.16 (b)**) respectively. Considering the complex nature of stress evolution in the case of OLVI on a GLARE plate, it is necessary to assess the interfacial delamination at the interfaces.

Figures 6.17-6.19 show the interfacial delamination for various obliquities of impact along x-direction for an initial impact speed of v=10 m/s and only the interfaces where delamination arises are shown. It is seen that at lower values of angle of incidence 0 ° ≤ θ ≤ 15 ° , the nature and size of the interfacial delamination at interfaces 1 and 8 almost remains the same as shown in **Figure 6.17** and **Figure 6.18**, although some minute difference can be seen for interface 5. In accordance with the variation of contact forces with the obliquity, with the further increase in obliquity as the contact forces decrease (**Figure 6.8** and **Figure 6.9**), the extent of delamination also reduces (**Figure 6.19**). No further delamination was observed at higher angles of impact. It is seen that for all the cases, the fibre/metal interfaces are the sites most prone to delamination and the bottom aluminium/ply interface experiences the maximum extent of delamination.

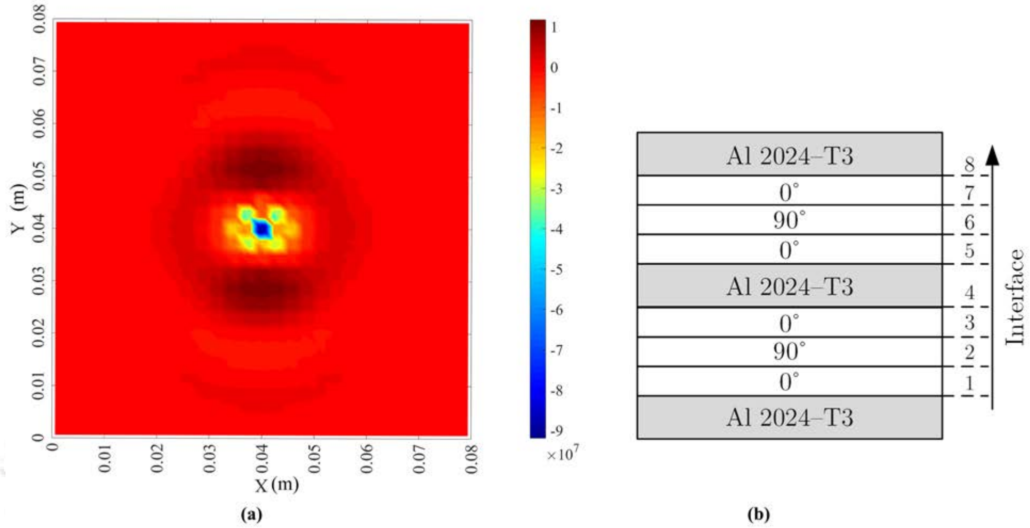

Figure 6.15: (a) σ_y (N/m^2) at interface-8 (Al/composite) at t =15 μs for a normal impact on a clamped (b) GLARE 4-3/2 plate

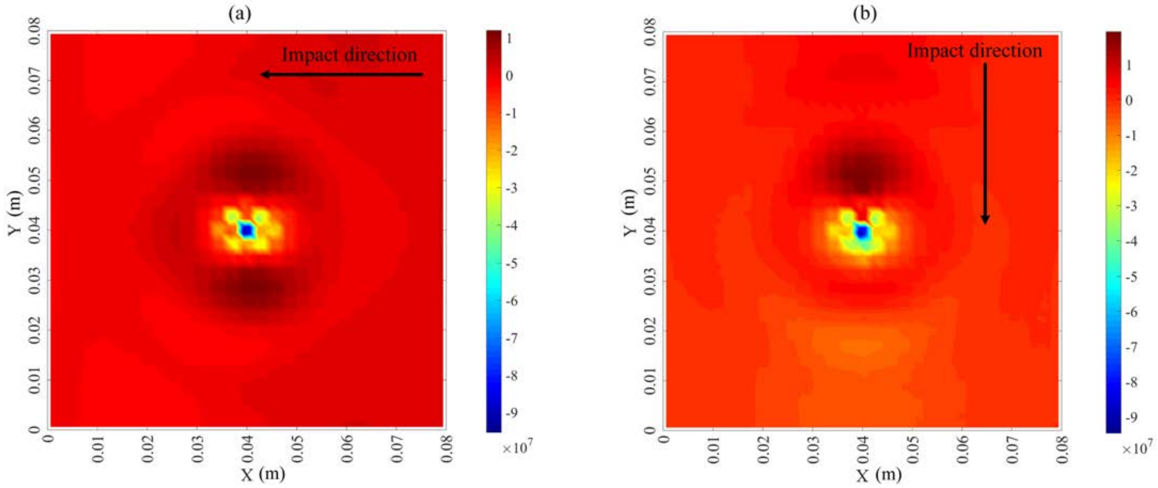

Figure 6.16: σ_y (N/m^2) at interface-8(Al/composite) at t=15 μs for OLVI (θ = 30 $^\circ$) on a clamped GLARE plate (a) impact in x-z plane (b) impact in y-z plane

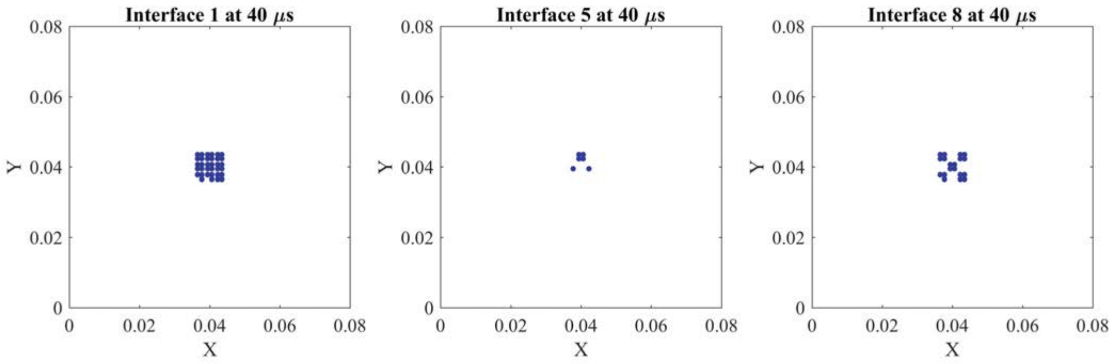

Figure 6.17: Delamination at the interfaces due to OLVI with an initial speed of 10 m/s for θ=0 $^\circ$

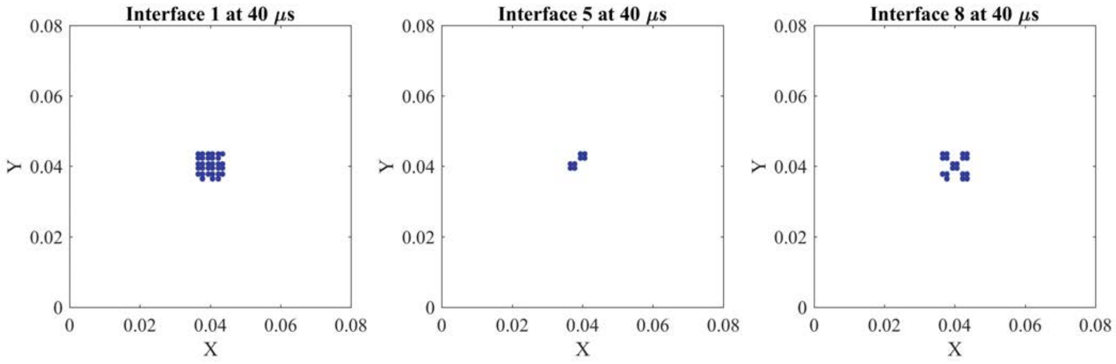

Figure 6.18: Delamination at the interfaces due to OLVI with an initial speed of 10 m/s for θ=15 $^\circ$

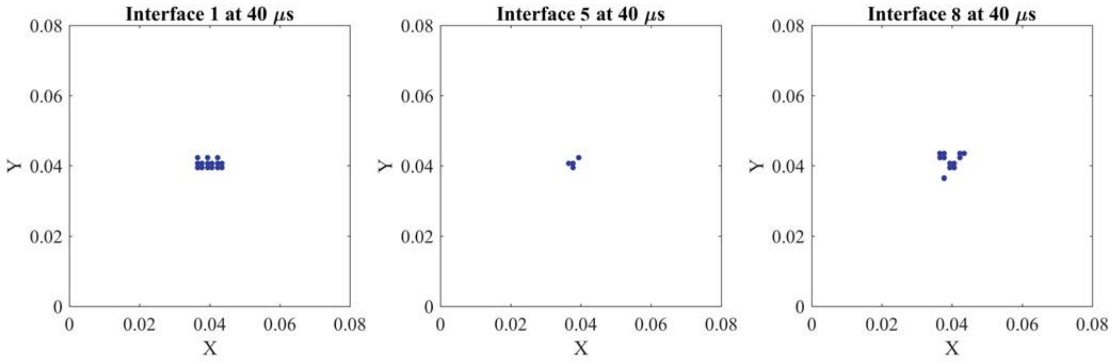

Figure 6.19: Delamination at the interfaces due to OLVI with an initial speed of 10 m/s for θ=30 $^\circ$

In order to study the effect of the trajectory of the impactor on the interfacial delamination, two cases of traversing planes of the impactor have been considered viz. the x-z plane and the y-z plane. **Figure 6.20** and **Figure 6.21** show the extent of delaminations at different interfaces at 40 μs corresponding to two oblique angles viz. $\theta = 15^\circ$ and $\theta = 30^\circ$ respectively for impact in the x-z plane for v_{ni}=10 m/s.

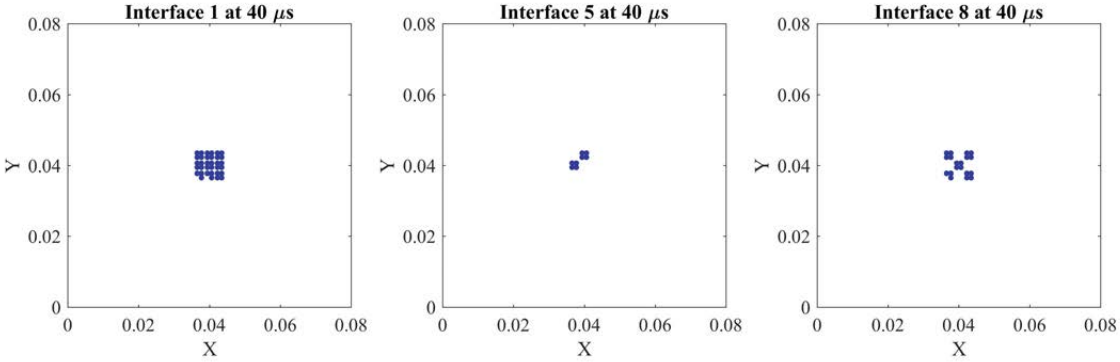

Figure 6.20: Interfacial delamination for OLVI in x-z plane with θ=15 $^\circ$

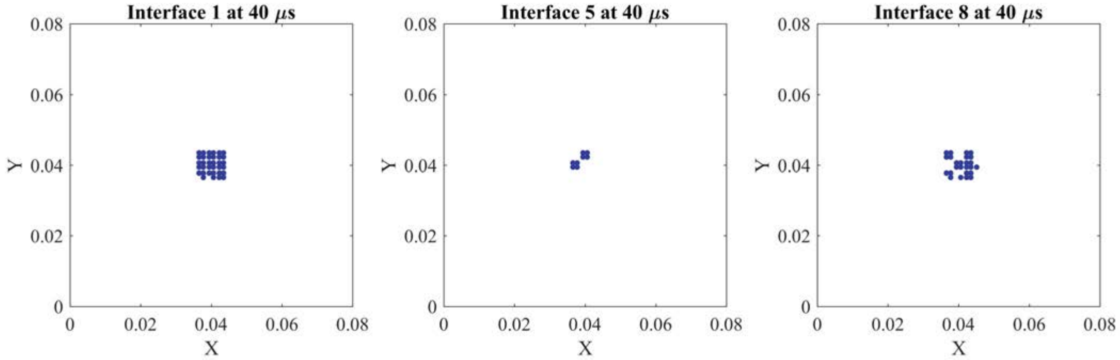

Figure 6.21: Interfacial delamination for OLVI in x-z plane with θ=30 $^\circ$

Figure 6.22 and **Figure 6.23** show the extent of delaminations at different interfaces at 40 μs corresponding to two oblique angles viz. $\theta = 15^\circ$ and $\theta = 30^\circ$ respectively for impact in the y-z plane for v_{ni} =10 m/s. Comparing **Figure 6.20** and **Figure 6.22**, it could be observed that in accordance with the stress profile shown in **Figure 6.16**, for small impact angles $0^\circ \leq \theta \leq 15^\circ$, the delamination at the interfaces remain more or less the same and independent of plane of impact. However, comparing **Figure 6.21** and **Figure 6.23** corresponding to higher oblique angle ($\theta = 30^\circ$), even the delamination at the top (interface-8) and bottom (interface-1) fibre/metal interfaces are markedly different when the plane of impact is y-z compared to those when the plane of impact is x-z. This is due to the dependence of interfacial stresses on the fibre orientation of the lamina below the aluminium layer relative to the plane of impact. Thus, the obliquity of the impact along with the direction of incidence can have significant influence on the delamination at the fibre/metal interface, especially at the immediate interface and in closer proximity to the contact location due to the tangential component of the contact force.

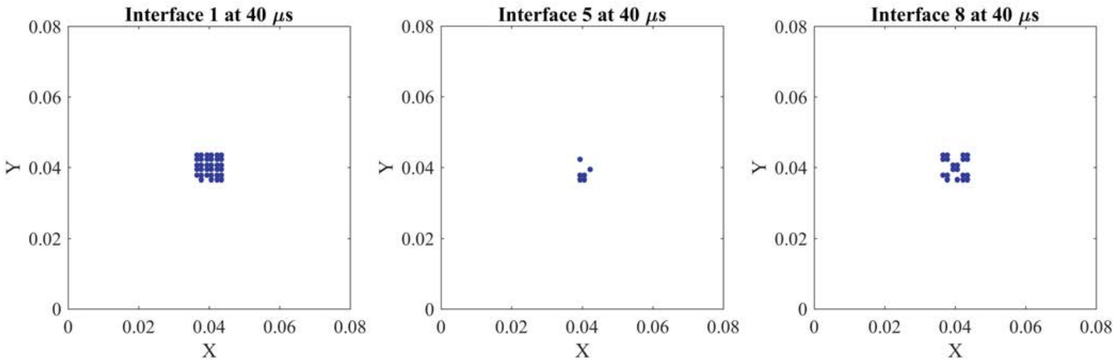

Figure 6.22: Interfacial delamination for OLVI in y-z plane with θ=15 $^\circ$

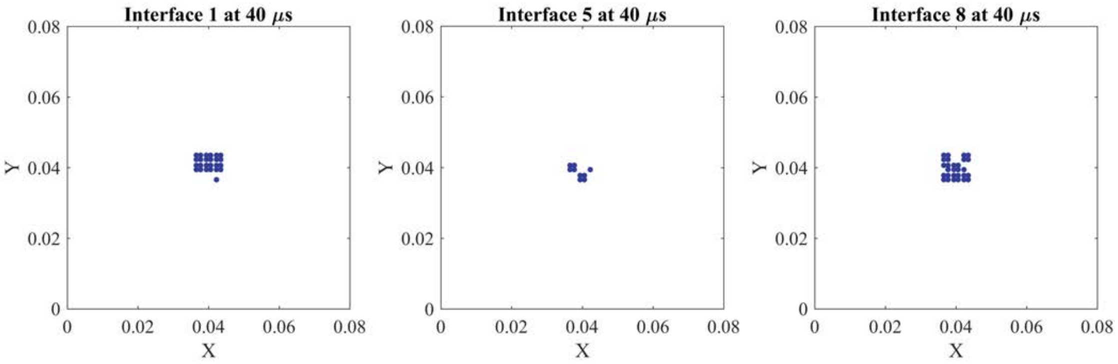

Figure 6.23: Interfacial delamination for OLVI in y-z plane with θ=30 $^\circ$

6.3. Multiple OLVI on GLARE

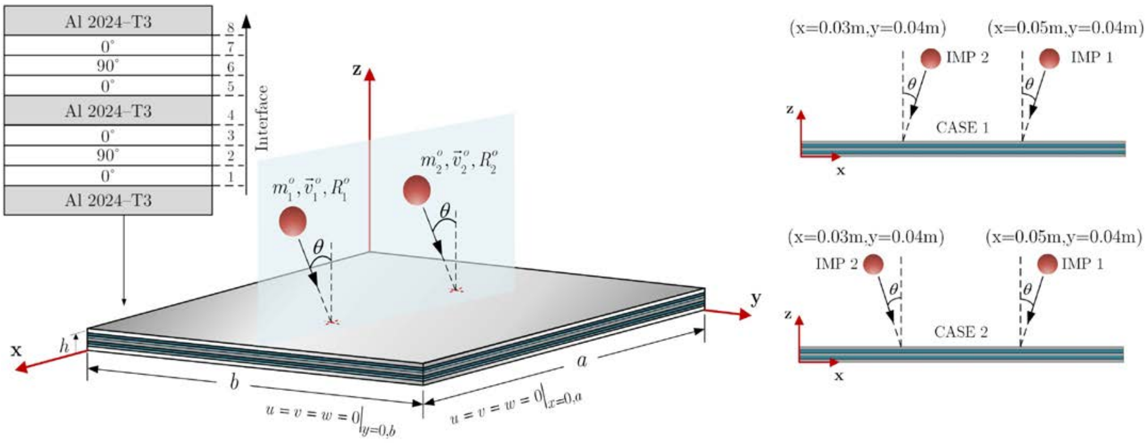

Figure 6.24: Multiple OLVI by spherical impactors

Referring to **Figure 6.24**, the square clamped GLARE 4-3/2 plate of lateral dimensions 0.08 m × 0.08 m is impacted by 5 mm diameter rigid spherical steel impactors at different angles of incidence θ at locations x=0.05 m, y=0.04 m (IMP1) and x=0.03 m, y=0.04 m

(IMP2) with x-z being the plane of impactor motion such that the components of velocity along the normal and tangential direction are v_n^o and v_t^o respectively. The normal component of initial velocity is fixed at 10 m/s throughout the range of obliquities during OLVI on the clamped GLARE plate and the coefficient of friction is μ_f =0.47. The thickness of each aluminium layer is 0.304×10^{-3} m and that of S2-glass/FM94-epoxy lamina is 0.156×10^{-3} m taking the total thickness of the GLARE plate to 1.848×10^{-3} m. The impacts occur simultaneously at different obliquities as per CASE 1 or CASE 2. The obliquity is varied keeping the initial normal component of the velocity fixed at 10 m/s such that it results in a change in the tangential component of the initial velocity only and a direct comparison can be drawn between the tangential response and the normal contact force. Further, the effect of time delay between the impacts are investigated for the change in contact response and the associated delamination at the aluminium/composite interfaces.

6.3.1. Validation of the multiple OLVI model

In case of multiple OLVIs with arbitrary masses and velocities, very few literatures studying impacts occurring at different locations and arbitrary time delays are available. Therefore, an extension of an alternate method is adopted as described by Lam and Sathiyamoorthy [211]. Two separate systems are considered as shown in **Figure 6.25**, where both the GLARE 5-2/1 beams are having uniform cross sections of width 0.01562 m and thickness 0.001562 m with beam in system-1 being half the length of system-2. System-1 represents the symmetric portion of system-2 about its middle with its left end fixed and the other end is defined with symmetric boundary conditions while the 0.1 m long beam in system-2 has both its ends clamped.

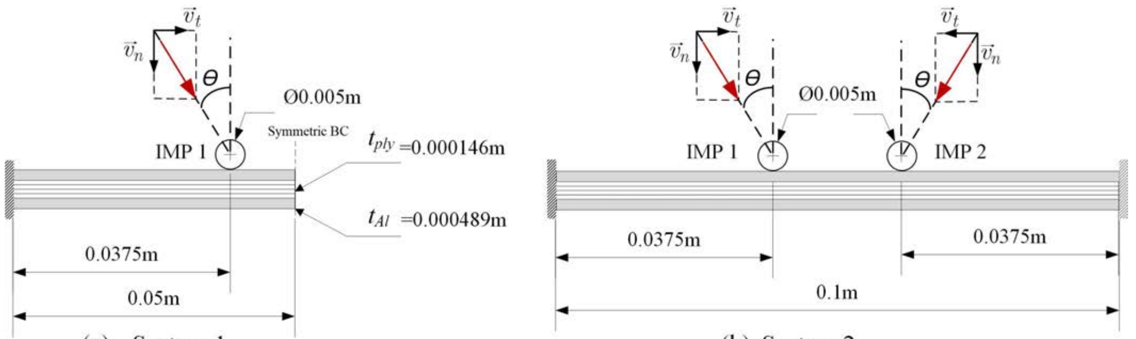

(a) System-1 (b) System-2

Figure 6.25: GLARE beam (a) clamped at one end and subjected to a single OLVI: System-1. (b) clamped at both the ends and subjected to equally offset OLVIs: System-2

The spherical impactors strike the beam having their normal component of velocity as 10 m/s in both the cases as illustrated in **Figure 6.25**. In the present case, the value of Θ is taken as 10° and the contact force responses are compared in **Figure 6.26**. It is seen that the contact force histories are similar for the IMP1 in both the cases and IMP2 in system-2 has its tangential component of the contact force flipped with respect to the tangential component of the contact force of IMP1 because of the direction of the trajectory of the second impactor. The oscillation of the tangential force component is due to the stick-slip phenomenon in a similar manner observed in [162] and this oscillation is cut short when gross slip occurs limited by the condition of $f_T = \mu_f f_N$.

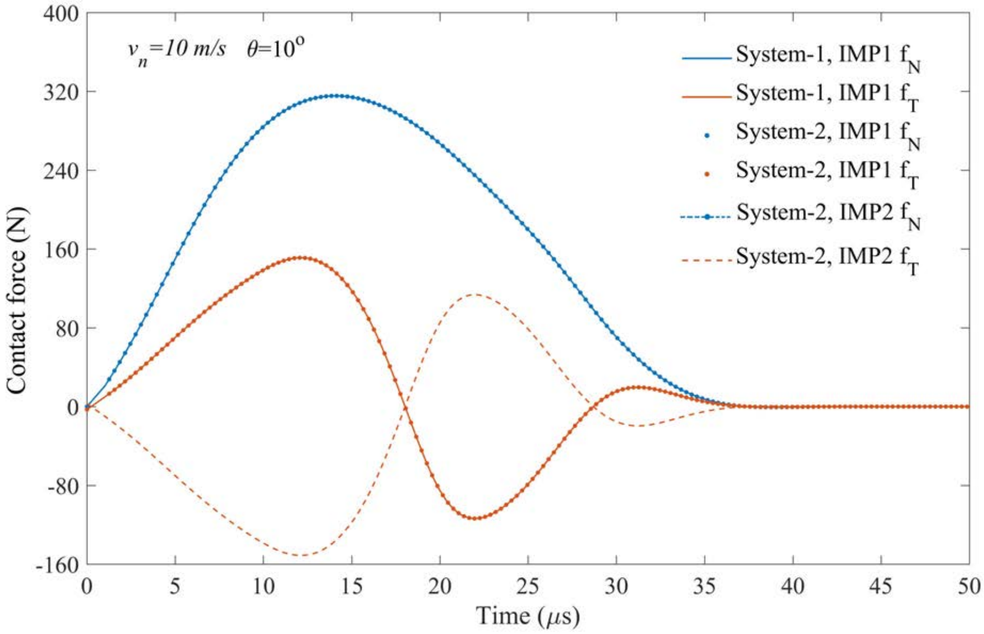

Figure 6.26: Contact force history of system-1 and system-2 for oblique impacts

6.3.2. Simultaneous OLVIs occurring in the same direction

Figure 6.27 and **Figure 6.28** show the variation of the tangential contact force with oblique impact angle and the normal force profile when the impactors strike with the initial normal component of velocity fixed at 10 m/s for IMP1 and IMP2 respectively. The angles of incidence of both the impactors are varied such that the angle of incidence of both the impactors are same for a particular case. It is seen that for the same normal force profile on account of the fixed initial normal component of velocity, the increase in obliquity results in an increase in the peak tangential contact forces in case of both the impactors and the maximum tangential contact force at an instant is limited by $| f_T |= \mu_f f_N$.

For both the impactors impacting simultaneously at symmetric locations, the normal contact force responses are similar. It can be seen that although the trajectories of the impactors are in the same sense, but the symmetricity of the impact in sense of the tangential component of the contact force is not met although the magnitude of the contact forces are identical. The similarity of the tangential component of the contact forces for each of the obliquities considered implies the localised nature of the tangential component of the contact force when impacted by small mass impactors. At lower impacting angles of $\theta \leq 25^\circ$ the tangential contact force reverses direction. This is because initially with increasing obliquity the tangential component of the velocity increases leading to a rise in the tangential contact force while $f_T \leq \mu_f f_N$ and the phenomenon of stick-slip between the impactor and the target is evident causing periodic reversals in the tangential component of the contact force. Moreover, the duration of negative tangential contact force decreases with increasing oblique angle. Further increase in the obliquity results in the peak value of tangential contact force to remain essentially unchanged when $\theta \geq 25^\circ$ and slip occurs throughout the impact regime with $f_T = \mu_f f_N$ when $\theta \geq 45^\circ$.

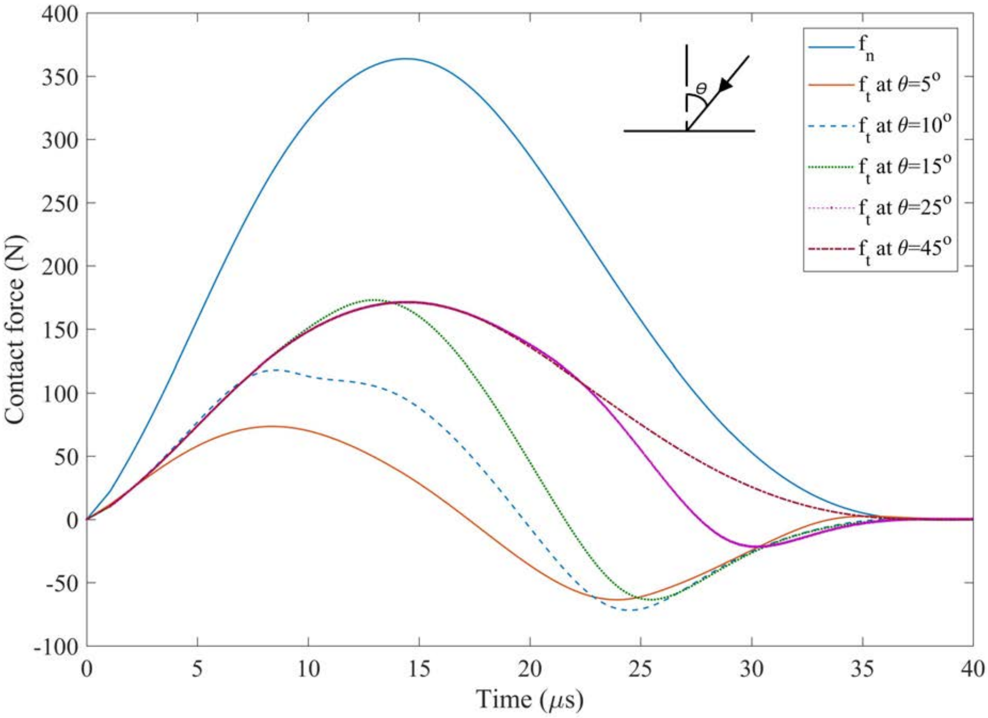

Figure 6.27: OLVI by IMP1 on a clamped GLARE plate at x=0.05 m, y=0.04 m

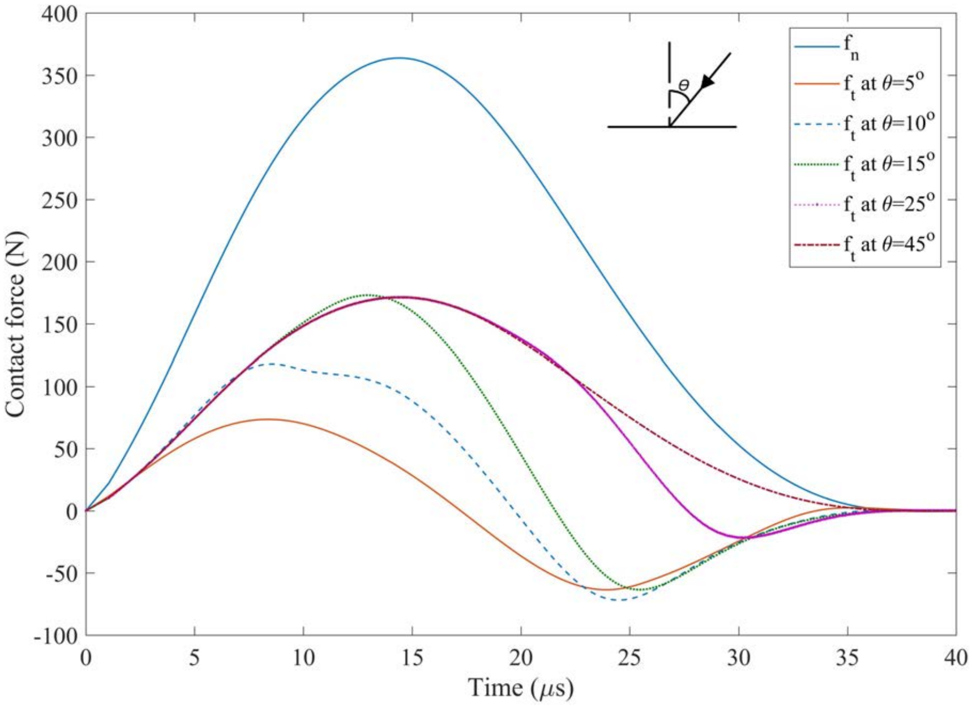

Figure 6.28: OLVI by IMP2 on a clamped GLARE plate at x=0.05 m, y=0.04 m

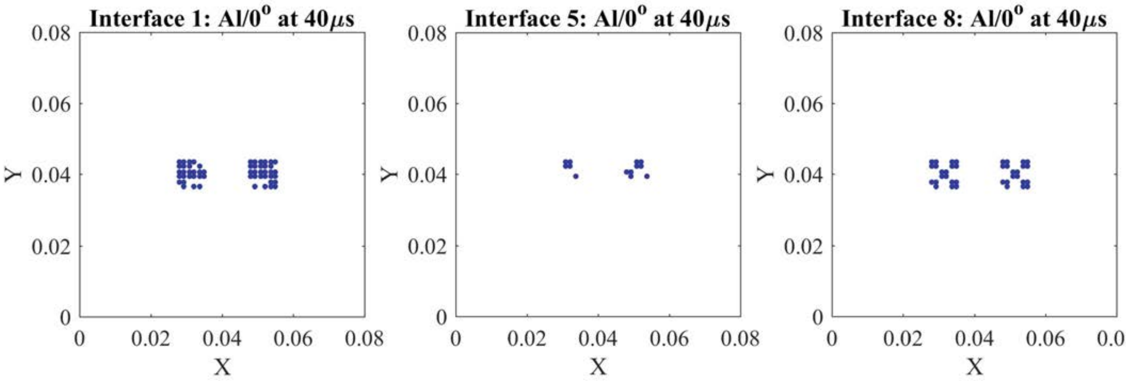

Figure 6.29: Delamination due to OLVIs at the fibre/metal interfaces v_n=10 m/s, θ=5°

In order to assess the delamination at the interfaces due to the different obliquities of the occurring multiple OLVIs along the same direction, the delamination at the metal/composite interfaces and the inner ply interfaces are shown in **Figures 6.29-6.31**. It is seen that at lower obliquities (θ=5°) the delaminations are concentrated near the impact sites and as the obliquity increases the delaminations tend to coalesce at the bottom interface-1. Also, the extent of delamination marginally increases at the top interface-8 with increasing obliquities, and at the inner metal/composite interface-5, the delaminations more or less remain the same. The delamination is seen to be greater for the OLVI when θ=15° compared to the rest of the cases indicating the effect of the tangential contact force reversals which influence the evolution of the interface stresses.

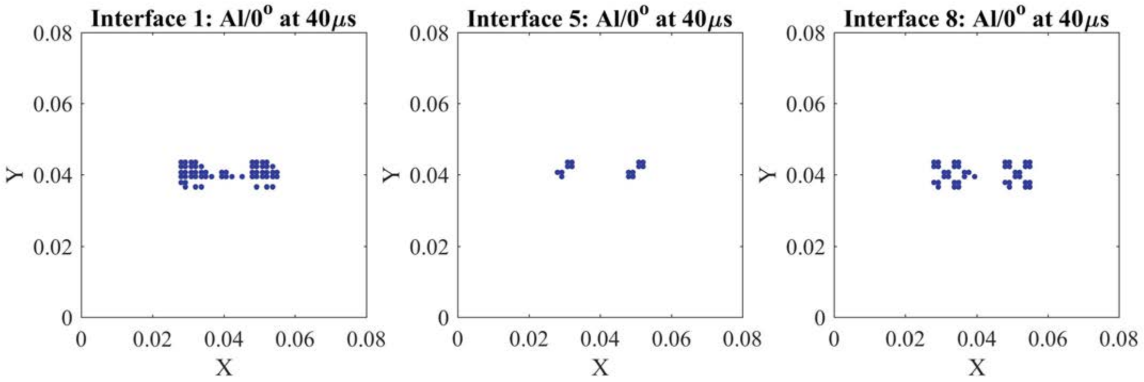

Figure 6.30: Delamination due to OLVIs at the fibre/metal interfaces v_n=10 m/s, θ=15°

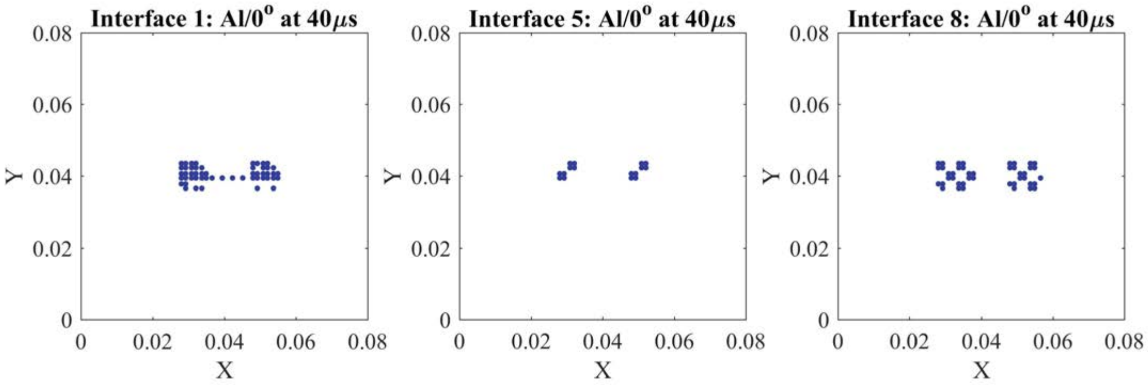

Figure 6.31: Delamination due to OLVIs at the fibre/metal interfaces v_n=10 m/s, θ=45°

6.3.3. Simultaneous OLVIs occurring in opposing directions

In order to study the effect of the trajectories of the impactors on the contact response, the OLVIs occur as per CASE 2 as illustrated in **Figure 6.24**. As can be seen from **Figures 6.32-6.33**, the normal contact force component is same for all the cases because of the impacts at symmetric locations and the peaks attained at all the obliquities are same since the normal component of the velocity is kept fixed at 10 m/s. But a slight difference is seen in the peaks attained by the tangential component of the contact force and the instant of their reversals at lower obliquities (θ=15°). The tangential component of the contact forces for both the impactors are similar in magnitude but due to the trajectory of IMP2 being in the opposing direction, the direction of the tangential contact force is in the opposite sense.

The typical stress profiles of σ_x at the top aluminium/composite ply interface-8 is shown in **Figure 6.34** for the two OLVI cases and as can be seen the stress variations are markedly different for both the cases. This in turn can significantly influence the nature of evolution of the interfacial stresses. It can be inferred from **Figure 6.34**, that the nature of the interfacial stresses are asymmetric when the impacts occur along the same direction and when they occur opposing to each other, the stress contour is seen to be symmetric. This can have significant influence on the delamination at the interfaces of the target.

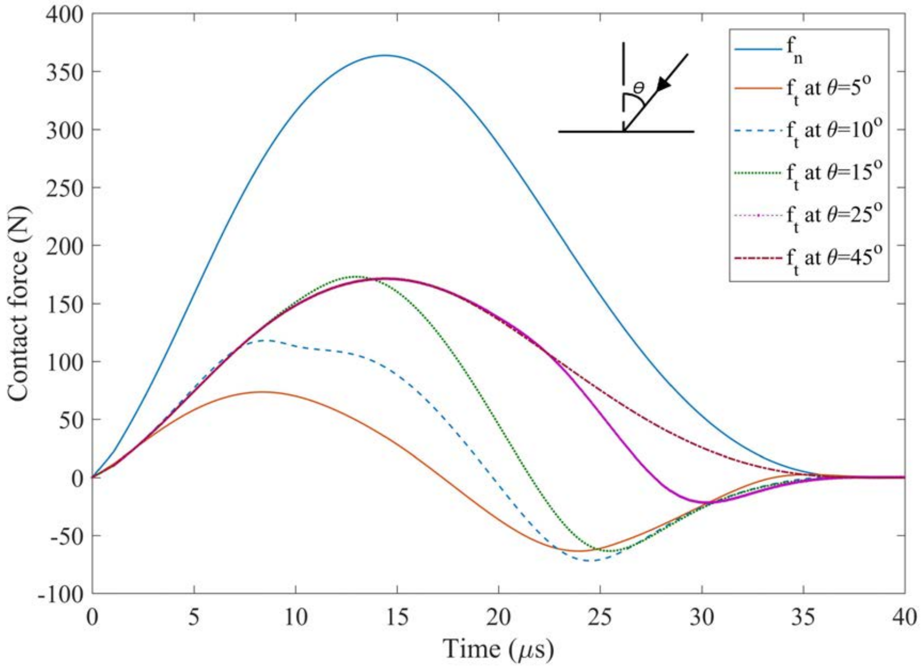

Figure 6.32: OLVI by IMP1 on a clamped GLARE plate at x=0.05 m, y=0.04 m

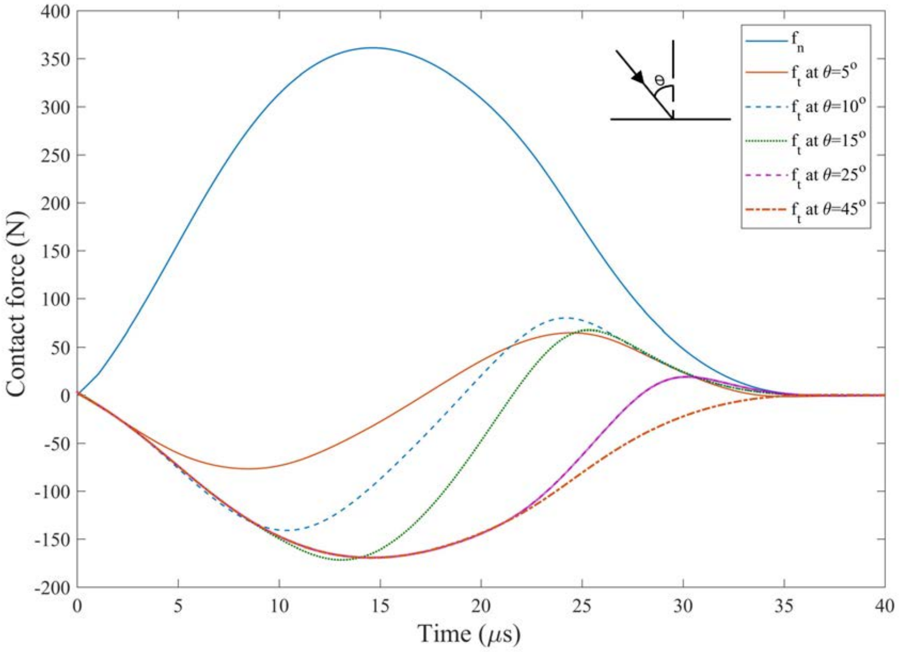

Figure 6.33: OLVI by IMP2 on a clamped GLARE plate at x=0.03 m, y=0.04 m

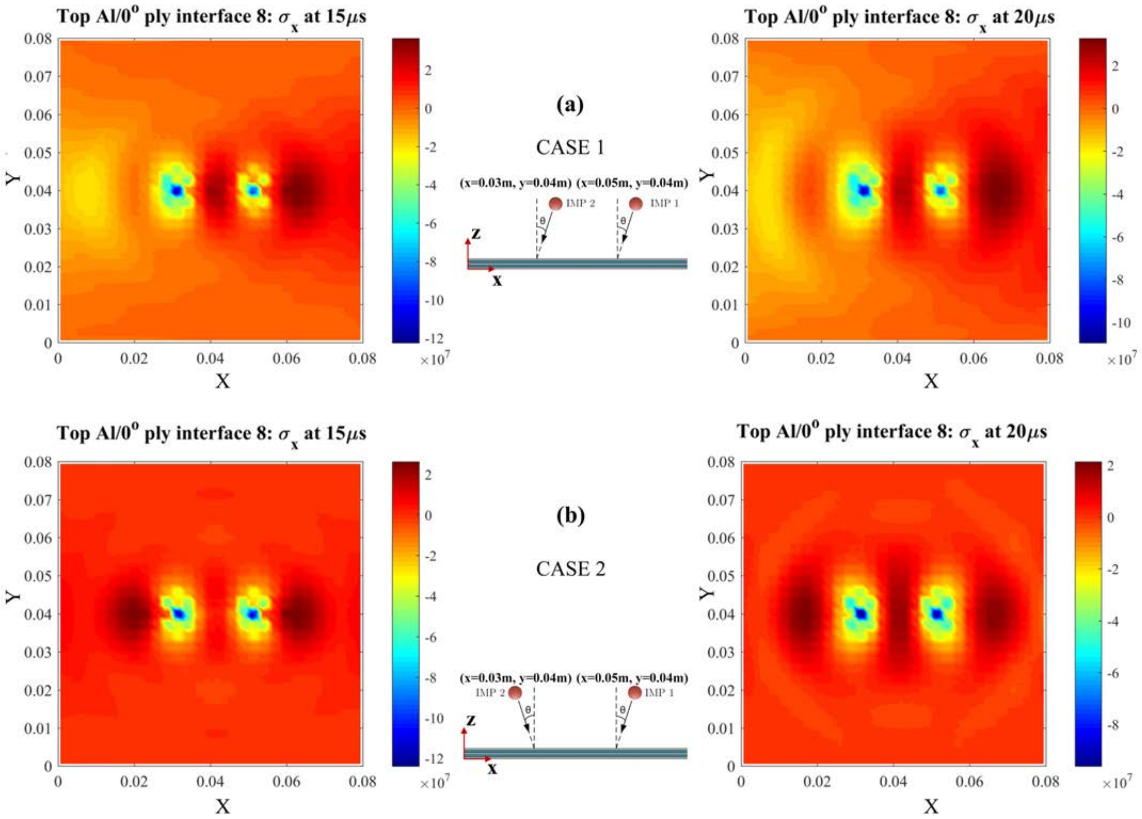

Figure 6.34: σ_x (N/m^2) at interface-8 (Al/composite) for multiple OLVIs (θ=15°) on a clamped GLARE plate for impact in x-z plane (a) same direction (b) opposing direction

Figures 6.35-6.37 show the interfacial delamination at the aluminium/composite interfaces when multiple OLVIs occur such that the two impactor trajectories are in opposite sense to each other. Comparing the delaminations due to the respective multiple OLVIs at a certain angle of impact, it is seen that at θ=5°, the delamination for both the cases (CASE 1 and CASE 2) are similar in nature. But, as the obliquity increases, (θ=15°), the extent of delamination is more at the interfaces (interface-8 and interface-1) for CASE 2 as compared to CASE 1 (refer to **Figures 6.29-6.31** and **Figures 6.35-6.37**). This can be attributed to the nature of evolution in the interfacial stresses as a result of the difference in trajectories of the impacts. The tendency of the delamination is to progress along the fibre direction of the underlying layer as evident at the bottom and top interfaces 1 and 8 and coalesce within the region between the two impact sites. Further, it is seen that the delamination at the inner metal/composite interface is negligible and invariant with the obliquity of the impact, As observed from **Figure 6.37**, for θ=45 °, the upper interface-8 also shows coalescence of the delaminated region between the two impact sites and the extent of delamination is slightly more than the case when θ=15 ° highlighting the effect of obliquity and their relative trajectories during simultaneous OLVIs.

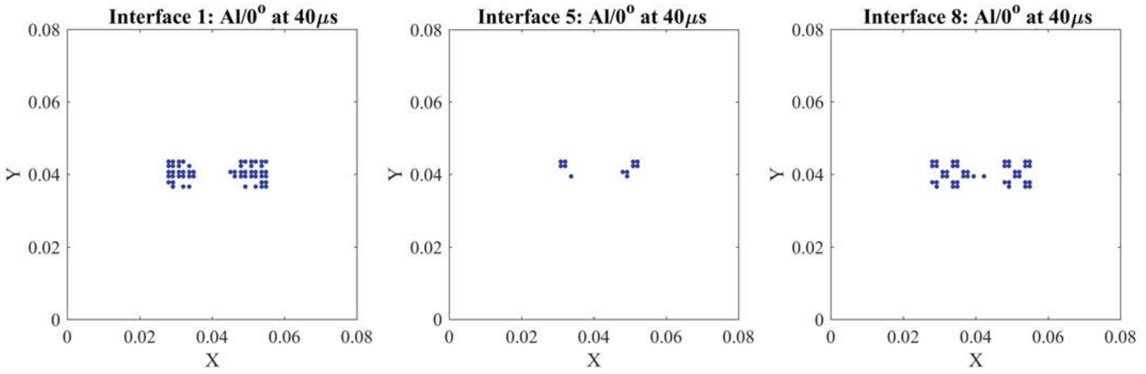

Figure 6.35: Delamination due to OLVIs in opposing directions at the fibre/metal interfaces v_n=10 m/s, θ=5°

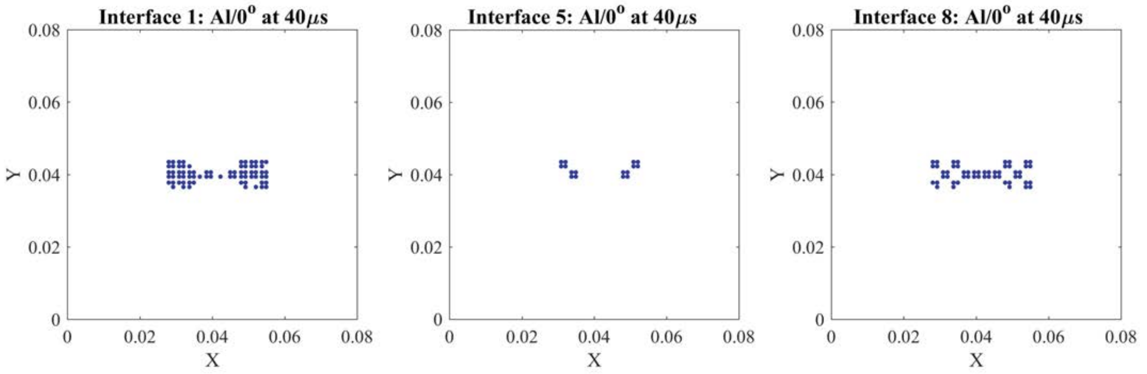

Figure 6.36: Delamination due to OLVIs in opposing directions at the fibre/metal interfaces v_n=10 m/s, θ=15°

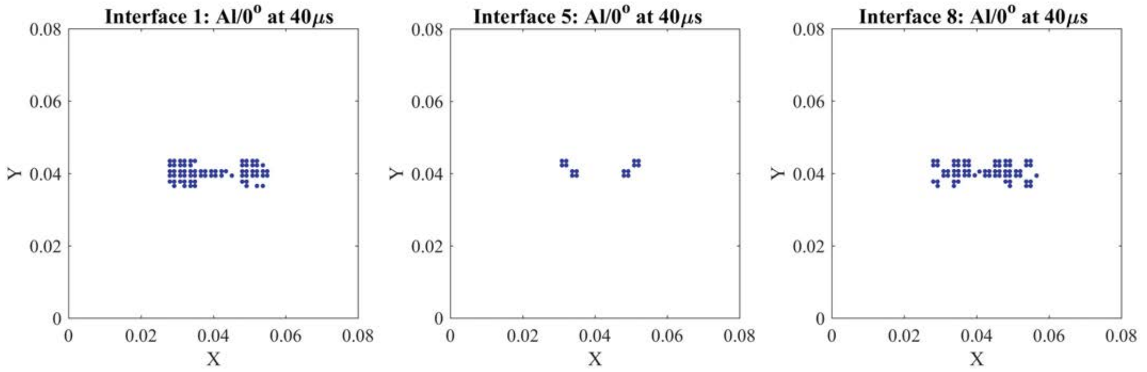

Figure 6.37: Delamination due to OLVIs in opposing directions at the fibre/metal interfaces v_n=10 m/s, θ=45°

6.3.4. Effect of time delay between the OLVIs

In order to study the effect of time delay between the two OLVIs, the contact forces of the two impacts occurring at different obliquities are shown in **Figure 6.38** for a delay of 20μs between them. The impactors strike the clamped GLARE plate as per CASE 2 and the second impactor strikes the impact location in the opposite sense with respect to that of the first impactor. It is seen that the contact force responses are not of same magnitude and the tangential contact forces are flipped with respect to each other because of the trajectories of the impacts. With the increasing obliquity, the tangential contact force peak increases and at higher angles (Θ=45°), there is slip throughout the impact and hence no reversal of the tangential contact force unlike the lower impacting angles where there is a reversal of the tangential contact force. As seen from **Figure 6.38(a)-(b)**, there are instances where the tangential contact forces of both the impactors are in similar phase and such phases where the sense of the tangential contact forces are in the same direction disappear as the obliquity increases (**Figure 6.38(c)-(d)**). It is seen that normal component of the contact force for IMP2 is lower compared to IMP1 in all the cases. This can be attributed to the contact response of the target plate at the impact sites.

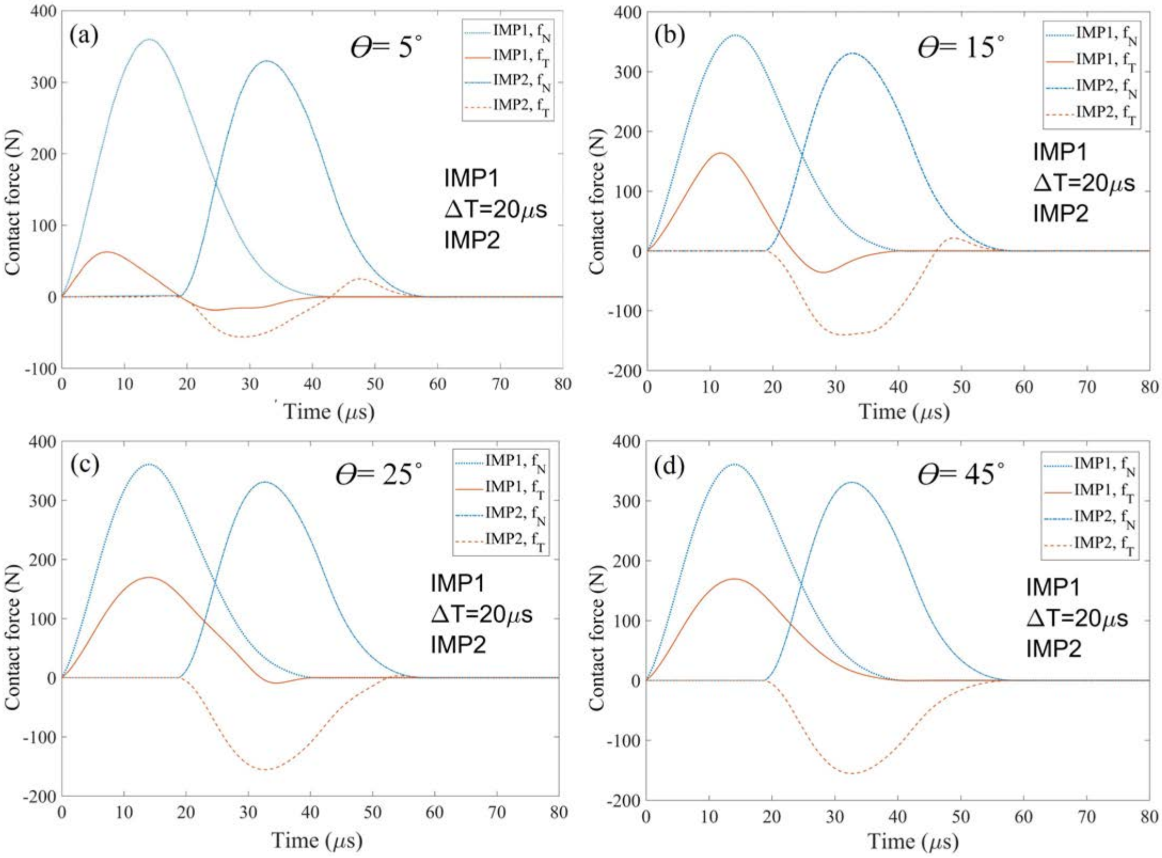

Figure 6.38: Contact force responses for the OLVIs occurring with a time delay of 20μs

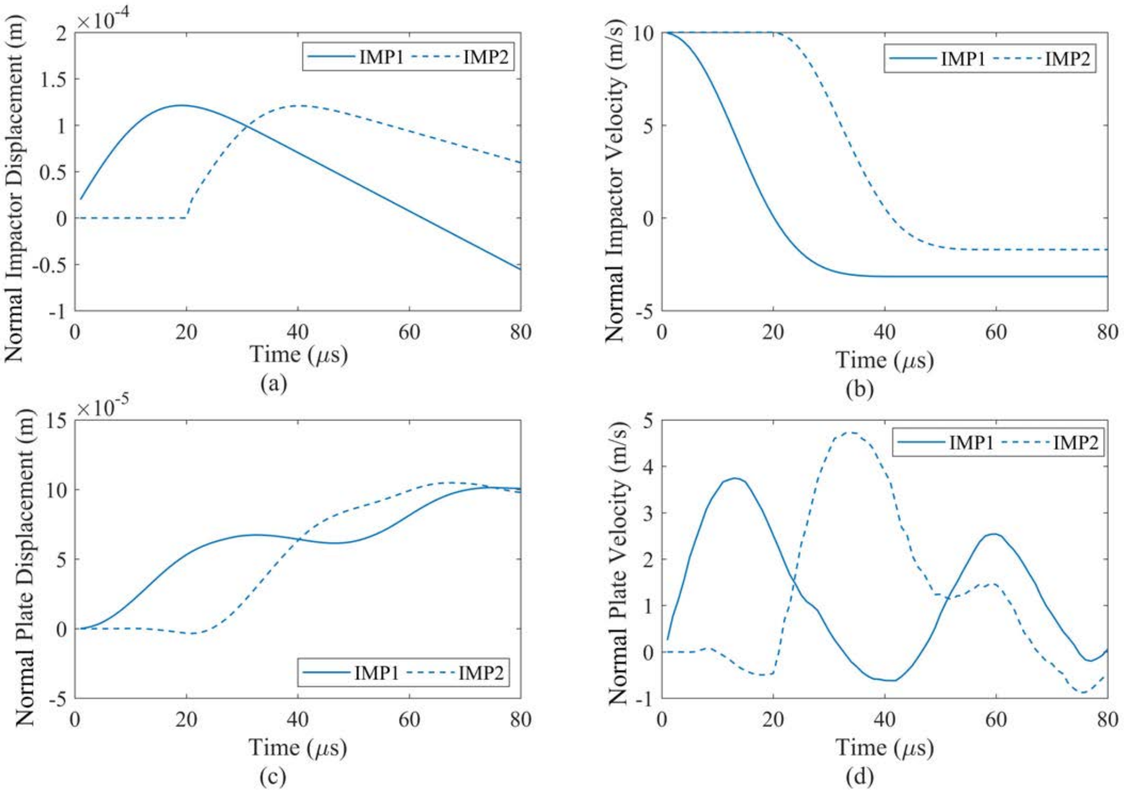

Figure 6.39: Dynamic responses of a clamped GLARE plate for OLVIs at Θ=15°, ΔT=20μs

Figure 6.39 (a)-(d) shows the dynamic responses of the impactor and plate in the normal direction for the OLVIs occurring at obliquities of Θ=15° and v_n=10 m/s when the time interval between the impacts is $20\mu s$. It is seen that the plate velocity at the contact point of IMP2 at $35\mu s$ is in the same direction as the normal velocity of IMP2 (positive) and the plate velocity is increasing while the impactor velocity is reducing. As a result of the initial motion of the plate due to the first impact, the peak contact force attained by the second impactor is comparatively lesser because the motion of both the impactor and the target location are in the same sense and therefore lower instantaneous indentation of the impactor. In contrast, the dynamic responses for simultaneous OLVIs as shown in **Figure 6.40** for Θ=15° and v_n=10 m/s, are symmetric and therefore the contact forces are identical as observed from **Figures 6.32-6.33**. Similar observations can be made for any other obliquity.

From the observed dynamic responses of the impactors and the plate and the differences in the evolution of the contact forces, it can be inferred that the time delay between the successive OLVIs influences the dynamic responses. This is turn can affect the extent of delamination at the interfaces as shown in **Figures 6.41-6.43**. It is seen that with a delay in between the OLVIs, the delamination decreases compared to the interfacial delaminations due to simultaneous OLVIs (**Figures 6.35-6.37**). The delamination is seen to be comparatively

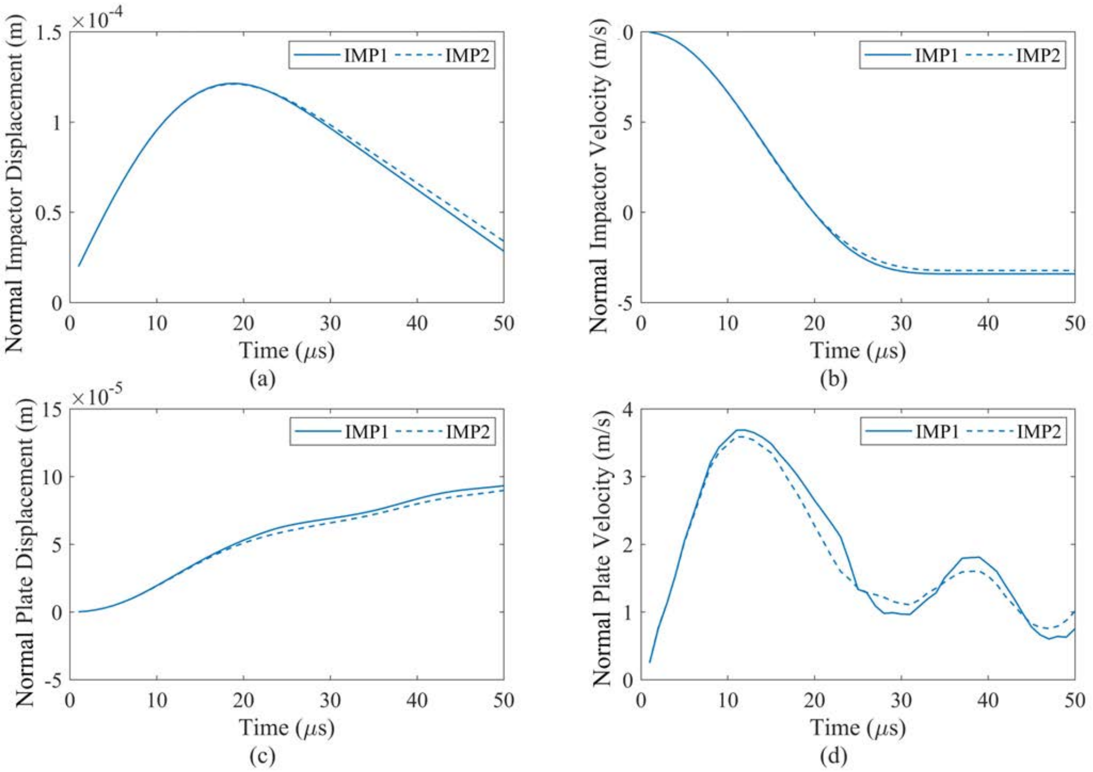

Figure 6.40: Dynamic responses of a clamped GLARE plate for OLVIs at Θ=15°, ΔT=0μs

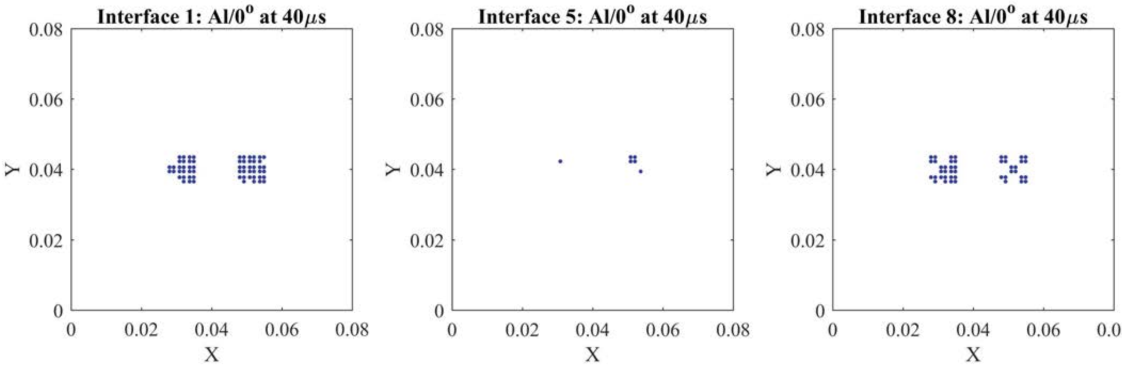

Figure 6.41: Interfacial delamination for OLVIs at Θ=5°, ΔT=20μs

less for the bottom aluminium/composite interface-1 around the location of the second impact. But, the same cannot be stated for the upper interface-8 where a comparatively more delaminated region was observed about the second OLVI site. This may be attributed to the influence of the tangential component of the contact force which influences the interfacial stresses at the upper interface-8 which is in closer proximity. Moreover, the tendency to coalesce gets suppressed at the different obliquities when there is time delay between the impacts. In all the cases, the delamination is seen to increase with increasing obliquity with the least delamination seen when Θ=5°. Furthermore, the delamination at the middle interface-5 is negligible for all the cases compared to the top and bottom interfaces.

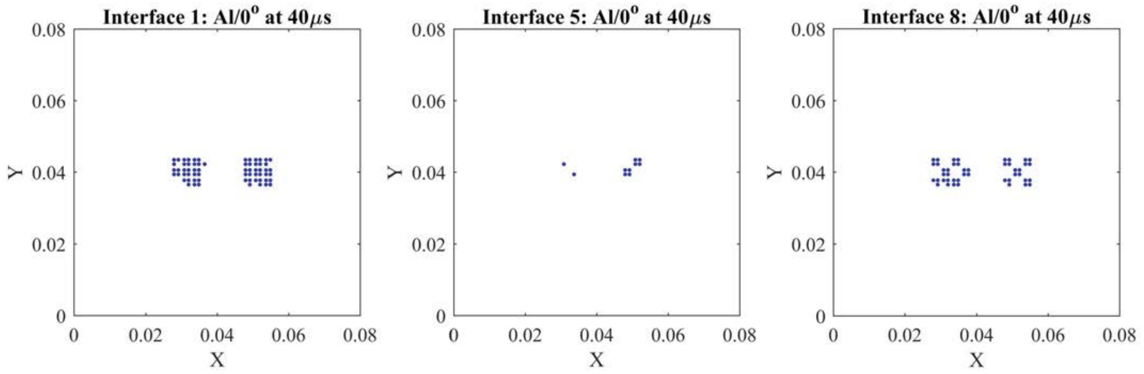

Figure 6.42: Interfacial delamination for OLVIs at Θ=15°, ΔT=20μs

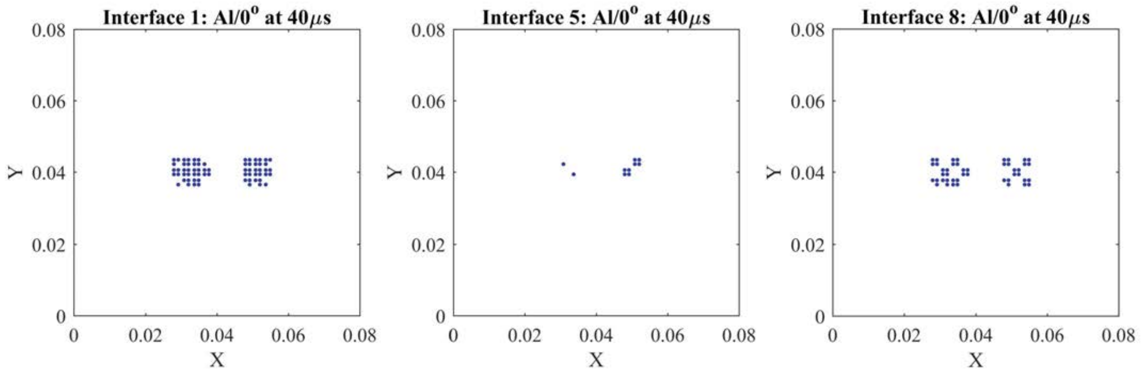

Figure 6.43: Interfacial delamination for OLVIs at Θ=45°, ΔT=20μs

6.3.5. Effect of increasing the impactor radius

In order to study the effect of the impactor radius, 8 mm diameter steel spherical impactors are taken such that the mass of the impactors are also increased due to the increase in their sizes. The clamped GLARE plate is subjected to simultaneous OLVIs as per CASE 2 at different obliquities and the coefficient of friction is kept same at μ_f =0.47. The contact force responses of both the impactors are shown in **Figure 6.44** and **Figure 6.45**. It is seen that with increasing impactor radius (impactor mass) the duration of the impact increases and the peaks attained by the contact forces increase. Although the trend of the evolution of the contact forces remain the same, it can be observed that the reversal of the tangential component of the contact force at lower obliquities ($\Theta \leq 15^\circ$) gets delayed as can be observed by comparing **Figures 6.32-6.33** and **Figures 6.44-6.45**. Furthermore, no reversal of the tangential component of the contact force is seen for Θ = 25° when the impactor radius is increased. This shows that at a particular value of coefficient of friction, increasing the impactor size tends to suppress the reversal of the tangential contact force component. Thus, as the impactor size increases (impactor mass increases) the tendency for gross slip throughout the impact regime increase with no stick-slip phases in between which may be attributed to the increase in inertia of the impactor enabling to overcome the frictional resistance.

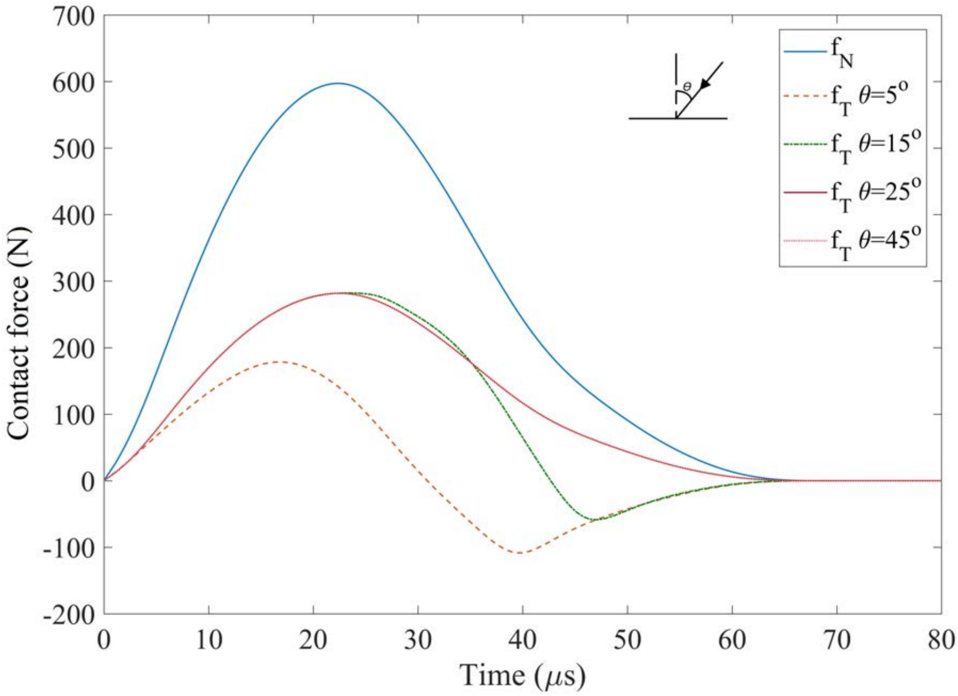

Figure 6.44: OLVI by ϕ8 mm sphere on a clamped GLARE plate at x=0.05 m, y=0.04 m

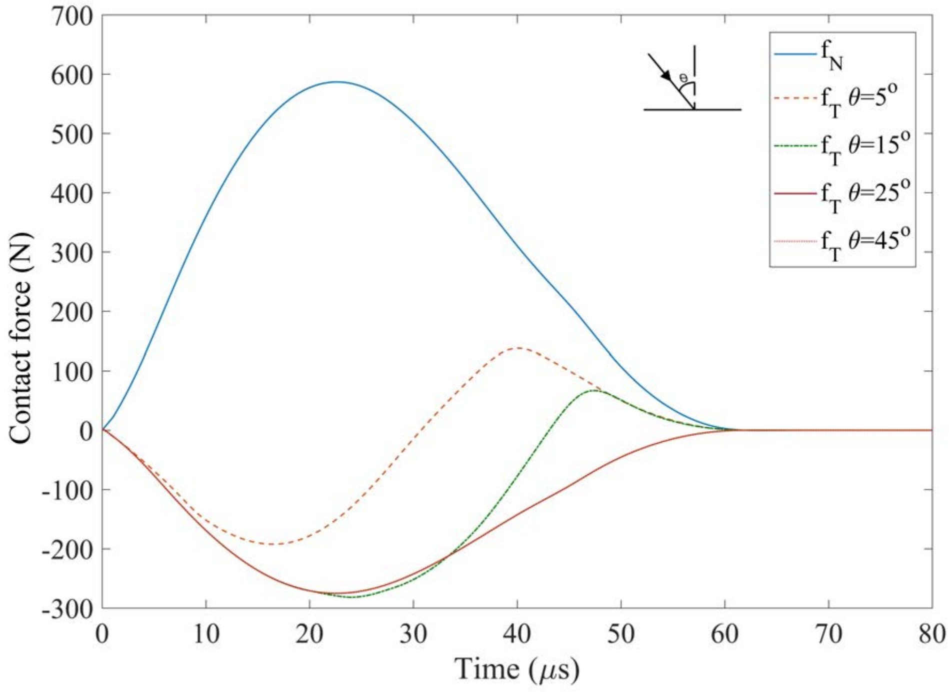

Figure 6.45: OLVI by ϕ8 mm sphere on a clamped GLARE plate at x=0.03 m, y=0.04 m

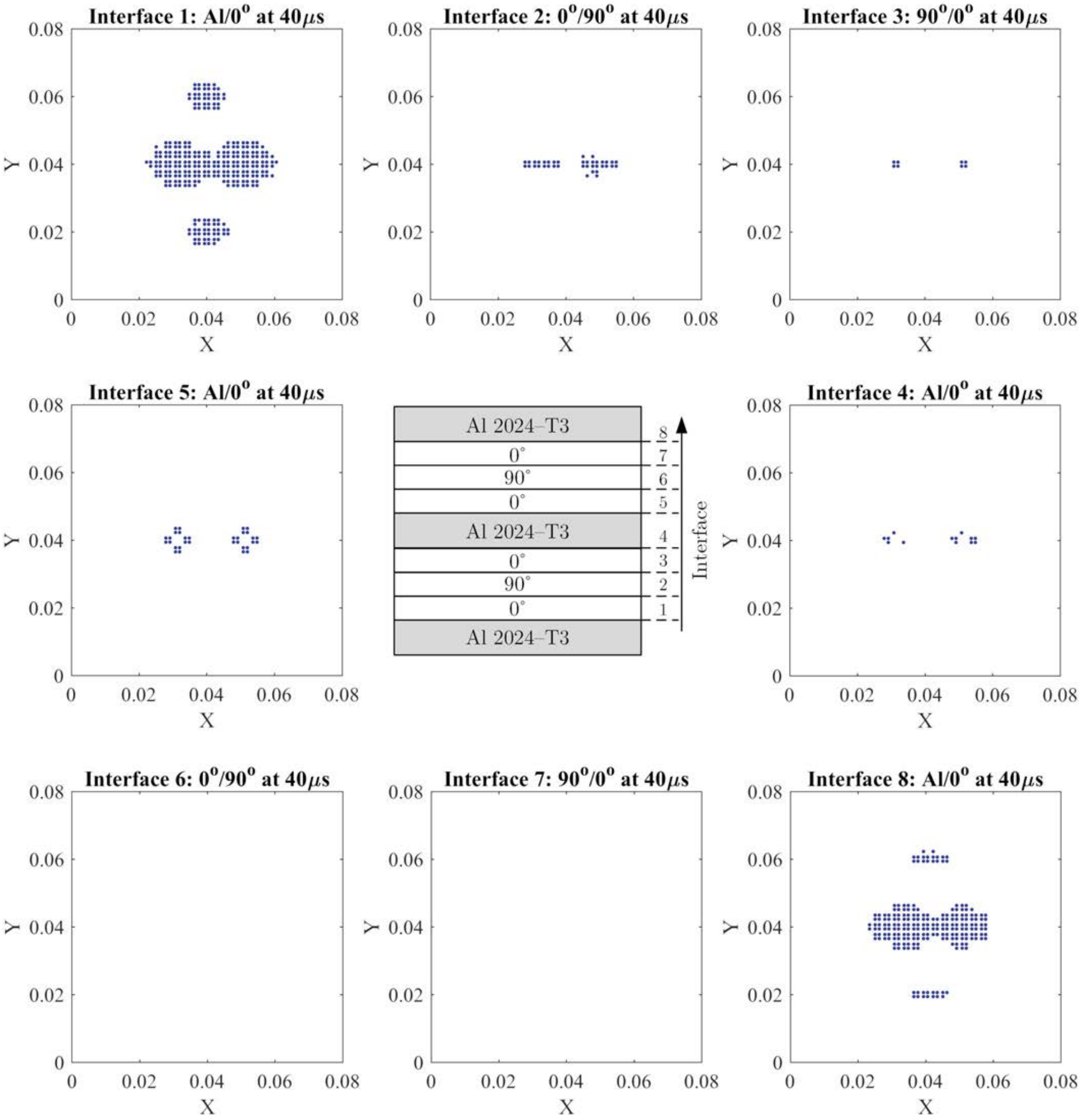

Figure 6.46: Delamination due to OLVIs in opposing directions by ϕ8 mm steel spheres at v_n=10 m/s, θ=5°

The delamination at the interfaces in case of OLVIs by the 8 mm diameter steel spheres are shown in **Figures 6.46-6.48** for the different obliquities. It is observed the delamination at the bottom and top fibre/metal interfaces 1 and 8 coalesce into a single delaminated area due to the increase in the peak load. Also, the inner composite interfaces show some delamination and for $\theta \geq 15^\circ$, the extent of interfacial delamination at the inner composite interfaces becomes marginally more. For θ=5 °, the delamination at the interfaces 1 and 8 is comparatively less and as the obliquity of the impacts increase, the delamination at these interfaces increase, especially at the immediate interface-8, as can be observed from **Figures 6.46-6.48**. For the inner metal/composite interfaces-5, the extent of delamination remains the same and for all the cases and the delamination for the inner interfaces is centred about the impact locations.

The effect of obliquity of the impact is observed at the immediate interfaces near the impact site i.e. the upper interfaces 7 and 8 which show a slight variation in the delamination pattern. In all the cases, the delaminations tend to propagate along the fibre direction of the underlying composite layer. It can be inferred that for the inner interfaces, the normal component of the contact force has a more significant influence on the delamination and their extent is solely due to the peak normal load which may be the reason of their invariance with obliquity of the impact.

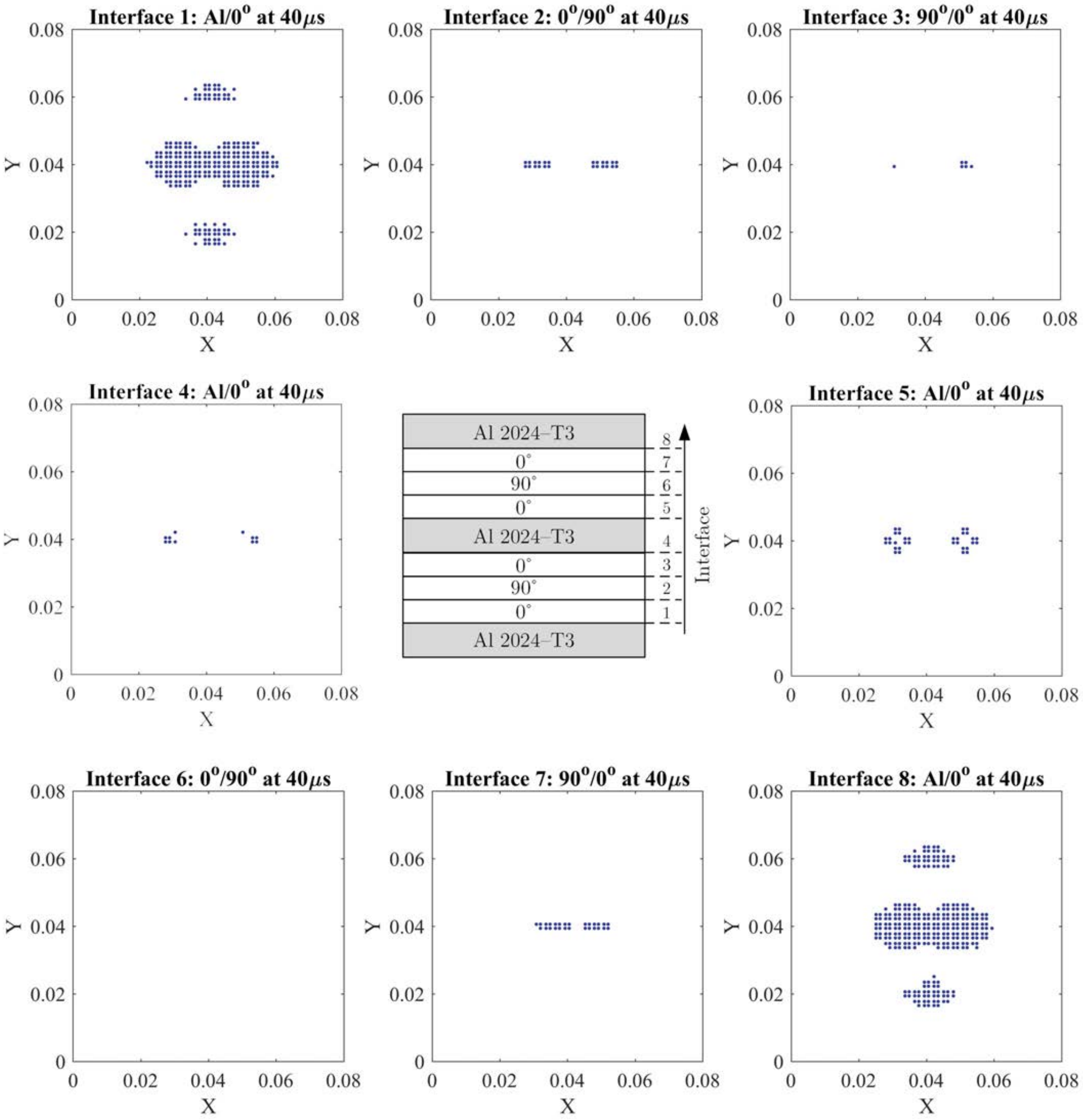

Figure 6.47: Delamination due to OLVIs in opposing directions by ϕ8 mm steel spheres at v_n=10 m/s, θ=15°

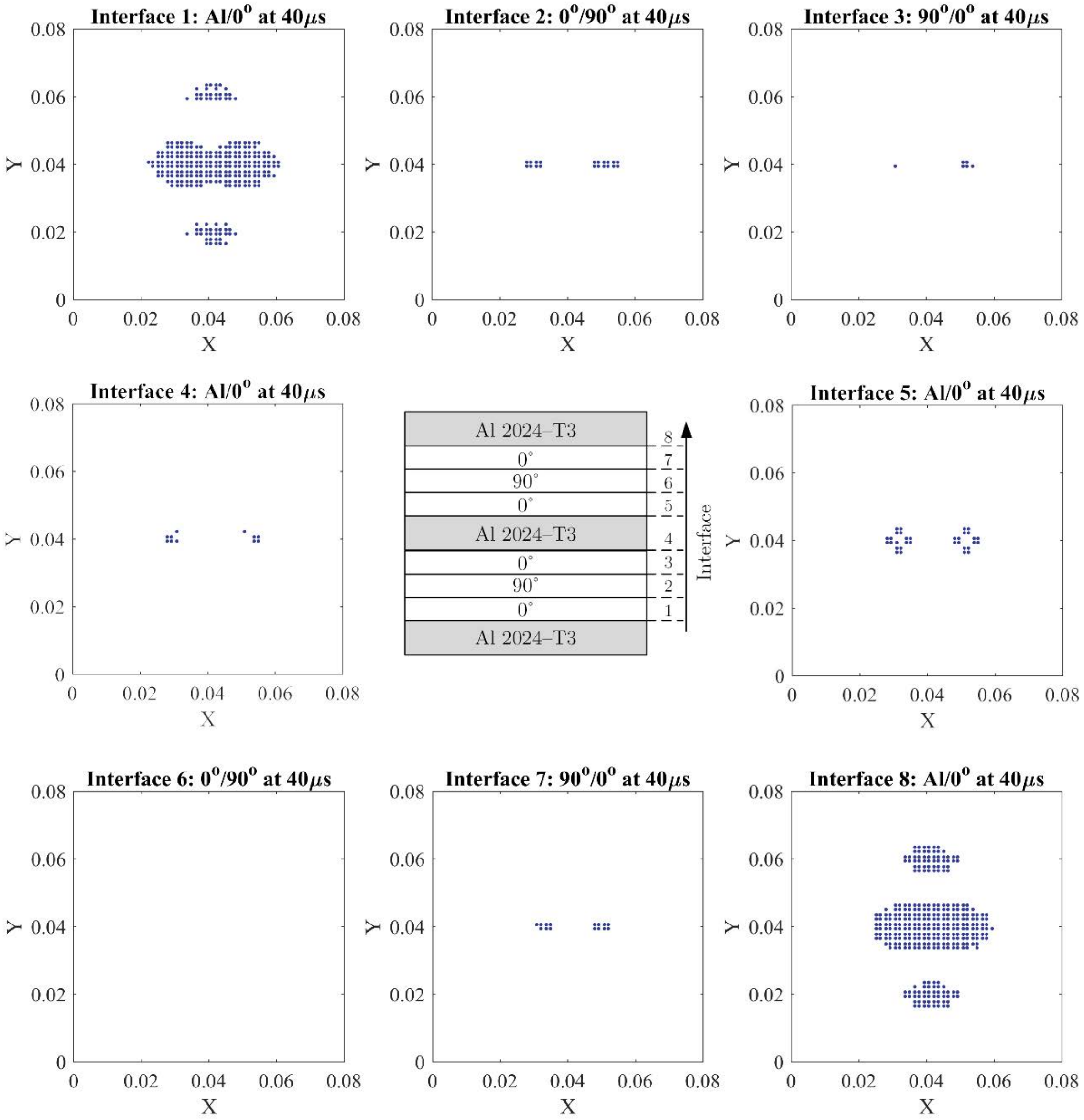

Figure 6.48: Delamination due to OLVIs in opposing directions by $\phi 8$ mm steel spheres at v_n=10m/s, θ=45°

6.4. Summary

The dynamic responses on account of the OLVIs are evaluated using the developed FE code, and the influence of the impactor mass and associated parameters like the coefficient of friction, obliquity of the impact on the contact response and extent of delamination has been investigated. Also, the multiple OLVIs on a GLARE plate has been investigated to observe the effect of time intervals between the impacts along with the obliquity of the impacts. From the observed results, the important conclusions drawn are as follows:

- For an OLVI at a fixed initial speed, the peak attained by the tangential contact force increases up to a certain value of oblique angle beyond which it decreases unlike the normal contact force which monotonically decreases with increasing obliquity.
- The relative tangential displacements are not constant over the contact region and there are instances of sliding between the impactor and the target. This particular stick-slip transitions leads to reversal of the tangential load at lower angles of incidence and as the obliquity increases, there is gross slip throughout the contact regime and no load reversal takes place.
- The overall delamination at the interfaces is primarily influenced by the normal component of the incident velocity which for a given mass of impactor decides the magnitude of the normal contact force.
- At higher obliquities, the tangential component of the contact force influences the delamination at the immediate interface and in closer proximity to the contact location.
- For an impact with fixed initial component of normal velocity, the normal contact force profile is unaffected by obliquity of the impact and only results in the change in tangential contact force which increases with increasing obliquity and its maximum attainable value is limited by the coefficient of friction between the bodies.
- The underlying fibre direction of the metal/composite interface along with its relative orientation to the trajectory of impact influence the extent of the delamination at the interface.
- The coefficient of friction and the contact force reversal in the tangential direction are directly related. With the increasing value of coefficient of friction, the duration of negative tangential force increases for a certain obliquity. However, for a given coefficient of friction, the instant of this reversal is delayed with increasing obliquity and at higher obliquities ($\theta \geq 45^\circ$), reversal is almost negligible.
- The impactor size (mass) at a particular fixed coefficient of friction influences the reversal of the tangential contact force. With increasing impactor mass, the reversal of the tangential contact force gets delayed as the tendency to slip increases.

- In case of multiple OLVIs, the delamination at the fibre-metal interfaces initiate at the contact locations of the two impactors and depending on the magnitude of the contact force they coalesce to a single delaminated area.

- In case of multiple OLVIs, the relative orientation of the trajectory of the impacts influence the size and shape of the delamination the target undergoes.

Chapter 7

GLARE subjected to repeated LVIs

In the present chapter, the repeated LVI on GLARE plates has been investigated for the dynamic responses and associated delamination. For low energy LVIs characterised by surface dents on the outer aluminium layer, by incorporating continuum damage model (CDM) based on Hashin's criteria considering the in-situ 3D stress state, the progression of damage of the internal plies is evaluated. In addition, the effect of repeated impacts on the dynamic response and associated delamination is explored.

7.1. Introduction

In practical scenarios repeated impacts can be common case. A relatable correlation from nature is the repeated loading of the tree bark by a woodpecker which shows the gradual damage the tree bark sustains due the repeated loading at the same site even though the loadings may be intermittent. In a similar manner, such repeated LVIs on GLARE can cause deterioration of the target material with material degradation leading to growth of damage and interfacial delamination thereby necessitating the study of such loading cases considering appropriate material degradation models. In case of the low-energy impacts (LVIs), such repetitive loadings can cause internal damage to the composite plies leading to a loss in target stiffness although at the outer surface, there may only be indentation or dents due to the impact by the rigid projectile. At lower energies, as observed by Bienias et al. [121], in the impact energy range of 1.5 J-2.5 J, delamination is a prevailing form of damage which is also observed at the fibre/metal interfaces. In such LVIs, penetration or cracking of the outer aluminium layer is unlikely but upon repetitive impact, chances are greater that there may be a loss in the plate stiffness due to damage of the inner composite plies leading to further increase in the interfacial delamination. Therefore, it is necessary to investigate the impact responses for such repetitive loading cases where the criticality of the impact cannot be ignored even though the LVIs occur at lower energies resulting in the lack of observable severity of damage in the outer metal layers but increase in the risk of internal damage. Keeping note of the importance for the analysis of repeated LVIs on GLARE at lower energies, the analysis of repeated LVIs is addressed in the present chapter considering a rigid spherical impactor normally impacting a GLARE 5-2/1 target as shown in **Figure 7.1**. The effect of various parameters like the impactor mass and velocity and the division of the impact energy on the dynamic response and its effect on the damage mechanisms of the composite plies are investigated.

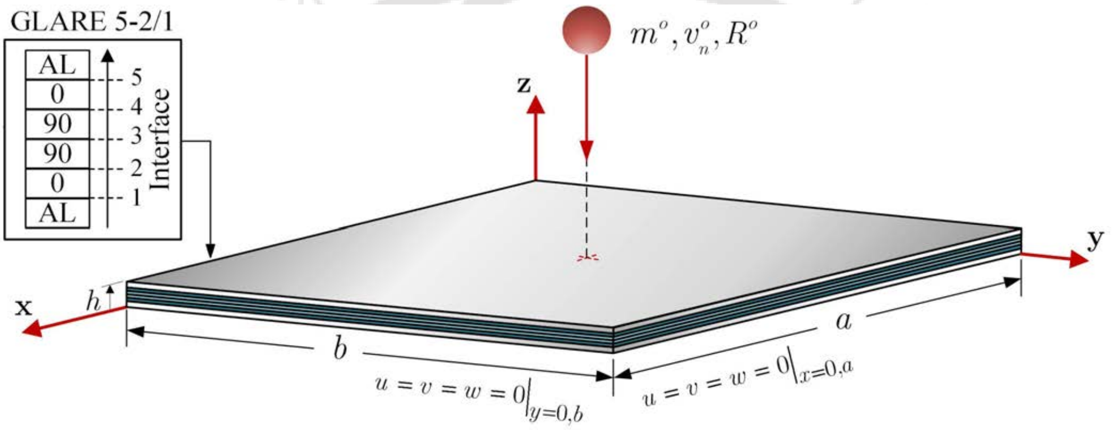

Figure 7.1: Spherical impactor normally striking a clamped GLARE plate

7.2. Problem definition

The present analysis is done on a clamped 0.1 m×0.1 m GLARE 5-2/1 plate with a spherical steel impactor of radius 0.004 m striking it normally at the centre as shown in **Figure 7.1**. The aluminium layers are 0.452 mm thick and the thickness of the S2-glass/epoxy plies are 0.158 mm. **Table 7.1** [45,102,138] lists the material parameters for aluminium alloy, S2-glass/FM94-epoxy laminates, and the steel impactor and **Table 7.2** [204–206] lists the interface strengths. The inner composite plies are checked for damage as per Hashin failure criteria in 3D [180], along with the assessment of the interfacial delamination as discussed in **Section 3.5** of **Chapter 3**. In analysing the different impact cases, the net energy of the impact is kept the same at 2.4 J. The GLARE plate is subjected to two successive LVIs at the same location such that the net sum of the energy of the two impacts remains constant at 2.4 J. The dynamic responses considering different mass impactors are recorded and compared for the different impact cases considered as mentioned in **Table 7.3**.

Table 7.1: Material properties [45,102,138]

Parameter	Notation	Al 2024-T3 alloy	UD S2-glass/FM94-epoxy prepregs	Steel
Density (kg/m^3)	ρ	2780	1980	7800
Poisson's ratio	υ	0.33	$\upsilon_{12}=0.33, \upsilon_{23}=0.33$	
Young's modulus (GPa)	E	72	$E_1=55, E_2=9.5$	200
Shear Modulus (GPa)	G	——	$G_{12}=5.5, G_{23}=3.5$	
Yield strength (MPa)	σ_{ys}	340	——	

Table 7.2: **S**trength parameters [180,204–206]

		S2-glass/FM94-epoxy interfaces	S2-glass/FM94-epoxy and Aluminium 2024-T3
Interface strength	S_n (MPa)	43	40
	S_t (MPa)	50	40
Transverse tensile strength	Y_T (MPa)	50	
Transverse compressive strength	Y_C (MPa)	160	
In-plane shear strength	S_{lt} (MPa)	70	
Longitudinal tensile strength	X_T (MPa)	1900	
Longitudinal compressive strength	X_C (MPa)	550	
Out-of-plane shear strength	S_{23} (MPa)	50	

Table 7.3: Impact event cases

Analysis case	**Impactor parameters**	**1st Impact (J)**	**2nd Impact (J)**	**Total energy (J)**
A Single impact	m= 0.3 kg, v= 4 m/s	2.4	---	2.4
	m= 0.15 kg, v= 5.65 m/s	2.4	---	2.4
B Two impacts with equal energy divisions	m= 0.024 kg, v= 10 m/s	1.2	1.2	2.4
	m= 0.15 kg, v= 4 m/s	1.2	1.2	2.4
	m= 0.3 kg, v= 2.828 m/s	1.2	1.2	2.4
C Two impacts with unequal energy divisions	m= 0.15 kg, v= 3 m/s m= 0.15 kg, v= 4.8 m/s	0.675	1.725	2.4
	m= 0.15 kg, v= 4.8 m/s m= 0.15 kg, v= 3 m/s	1.725	0.675	2.4

7.3. Single impact with net total energy

7.3.1. LVI responses for a single impact

The clamped GLARE plate is subjected to a single impact as per case A, such that each single LVI occurs with the net total energy and the dynamic responses are recorded for LVIs by different mass impactors as shown in **Figure 7.2**. It is seen that the impact duration increases with an increase in the impactor mass. For the same impacting energies of 2.4 J, the peak contact force is relatively higher for the impact by the 0.15 kg impactor as can be seen from **Figure 7.2(a)** and the slope of the drop in the impactor velocity is more in the LVI by the lower mass impactor as can be observed from **Figure 7.2(c)**. This can be attributed to the shorter duration of the impact which results in a more rapid change in the impactor velocity. Furthermore, the drop in the impactor velocity is continuous implying that the contact between the impactor and the target remains throughout the duration of the impact and the end of the contact is marked by a constant velocity slope . The impactor and plate displacements are more or less of the same magnitude as can be seen from **Figure 7.2(b)** and **(d)**.

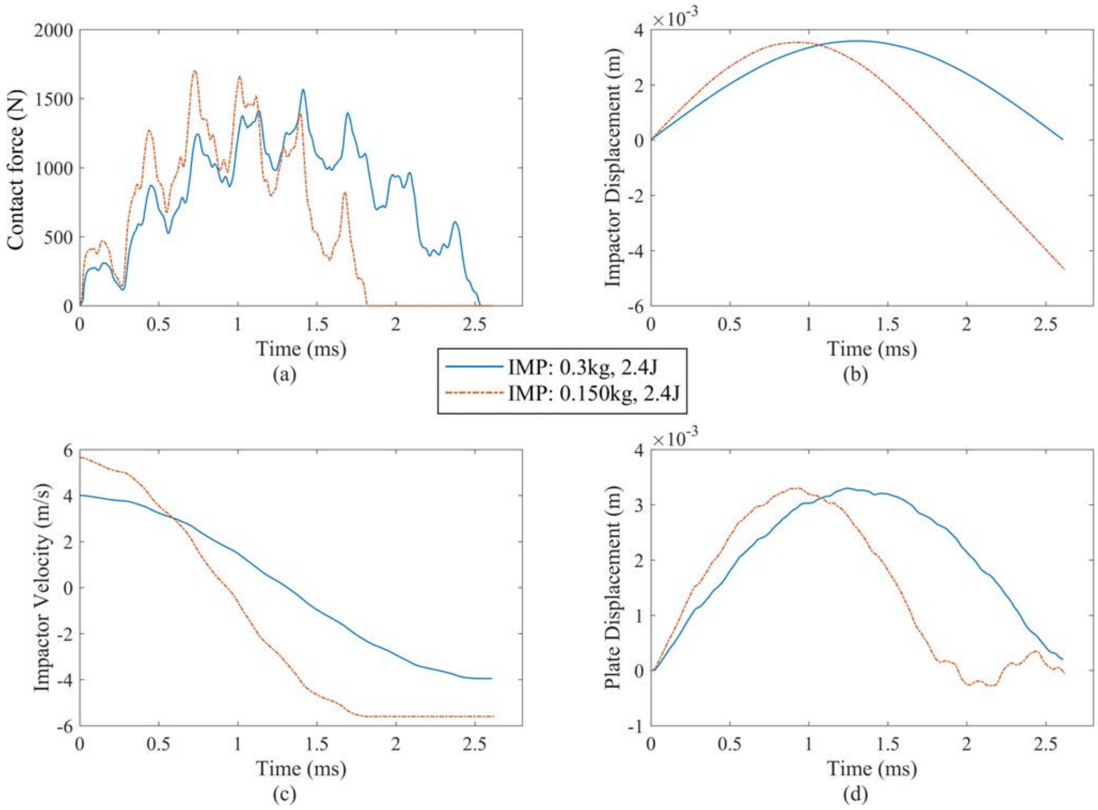

Figure 7.2: LVIs at 2.4J by different mass impactors on a clamped GLARE 5 plate

7.3.2. Composite damage and interfacial delamination

In order to assess the extent of the damage of the inner composite layers and the associated delamination due to the impact by the different mass impactors, the ply damage due to the single LVI at 2.4 J are shown in **Figures 7.3-7.4** and the associated interface delaminations are shown in **Figure 7.5** and **Figure 7.6**. It is seen that the main damage modes of the composite plies are due to the matrix tensile and compressive failure and interfacial delamination between the composite ply interfaces as well as the aluminium/composite interfaces. For both the cases, the 0° plies undergo damage due to the matrix tensile failure and the 90° plies fail by compressive matrix failure. Moreover, the top 0° ply in both the cases show a slight extent of damage due to matrix compression failure, concentrated within the impacting site. This may be attributed to the higher compressive stresses generated during the impact resulting in matrix compressive failure or crushing failure at the impact site. It is seen from **Figures 7.3-7.4** that the matrix tensile failure for the bottom 0° is more compared to the top 0° ply and its extent in case of impact by the 0.15 kg impactor at 2.4 J is comparatively more, whereas for the top 0° ply the extent of matrix tensile failure more or less remains the same.

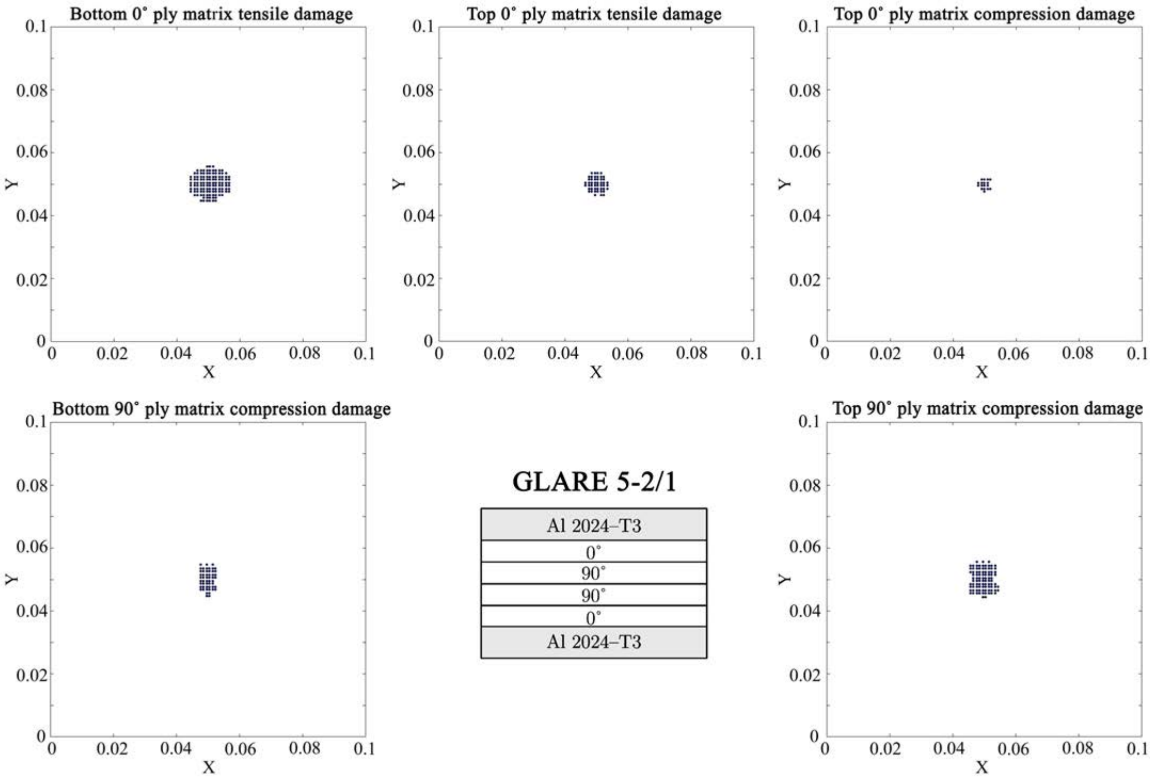

Figure 7.3: Inner composite damage due to LVI by 0.15 kg impactor at 2.4 J

In case of the 90° plies, the top 90° ply undergoes the maximum extent of matrix compression failure and the damage size is seen to be marginally greater for the case of LVI by the 0.3 kg impactor while for the bottom 90° ply, the damage extent more or less remains the same for both the impact cases. These damages incurred by the inner composite layers further expedite the interlaminar delaminations as shown in **Figures 7.5-7.6**. It is seen that the aluminium/composite interfaces suffer the maximum extent of delamination followed by the 0°/90° interface-2. This is because of the mismatch in the material properties and anisotropy of the composite layers. It is seen that the delamination at the interfaces tend to initiate from the impact site and propagate along the fibre direction of the underlying layer. From **Figures 7.5-7.6** it is observed that the extent of delamination is greater for the impact by the 0.15 kg impactor, especially at the interfaces 1 and 2 which is mainly due to tensile failure caused by out-of-plane deformation of the target plate due to the LVI. Therefore, in case of LVIs, the onset of failure is more likely to occur by tensile failure mode accompanied by delamination which are the major damage modes occurring for LVIs at lower energies.

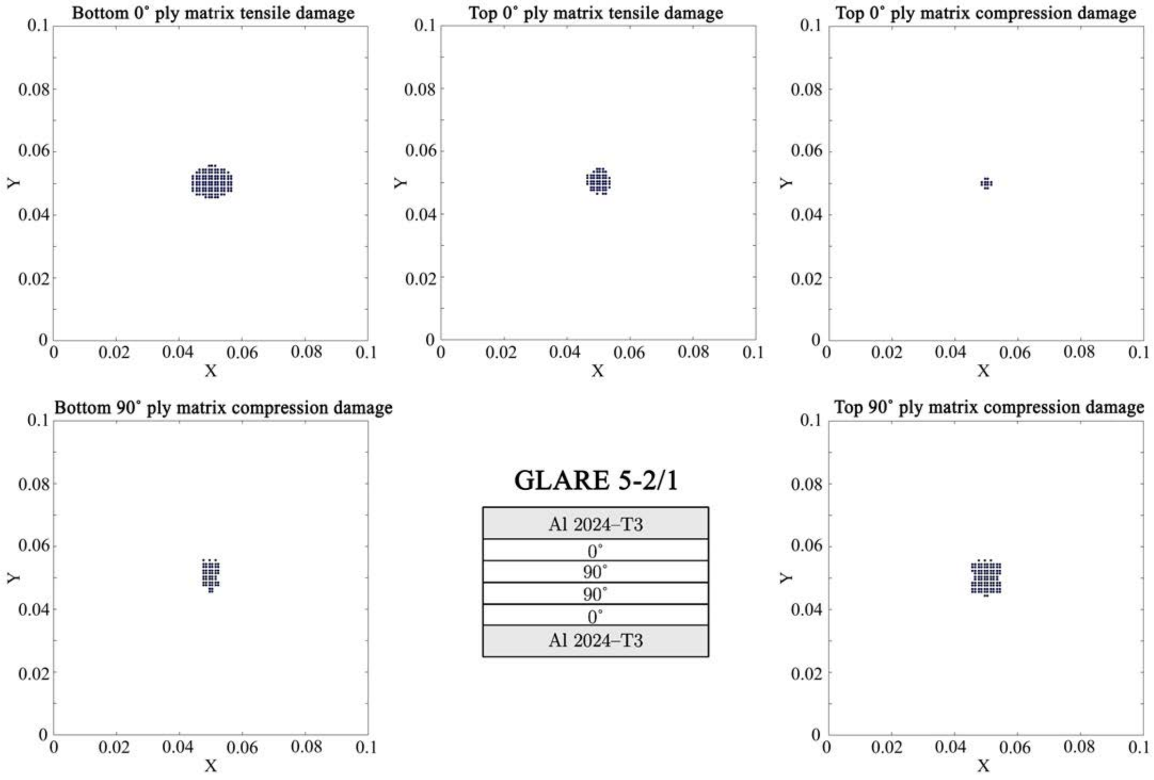

Figure 7.4: Inner composite damage due to LVI by 0.3 kg impactor at 2.4 J

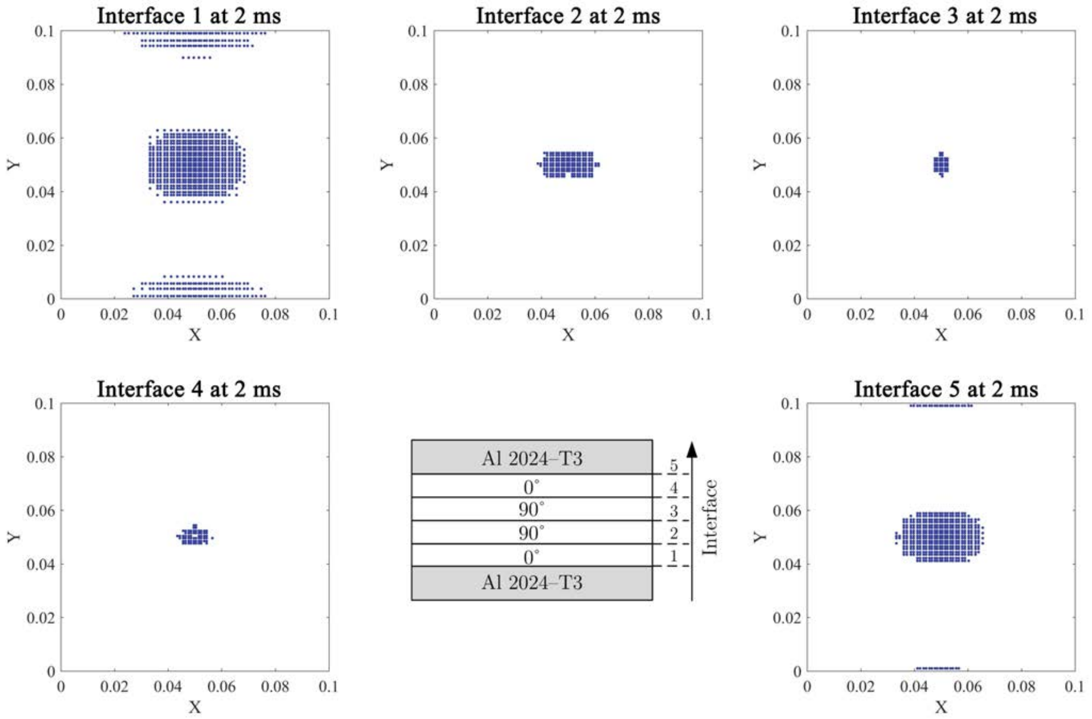

Figure 7.5: Interfacial delamination due to LVI by 0.15 kg impactor at 2.4 J

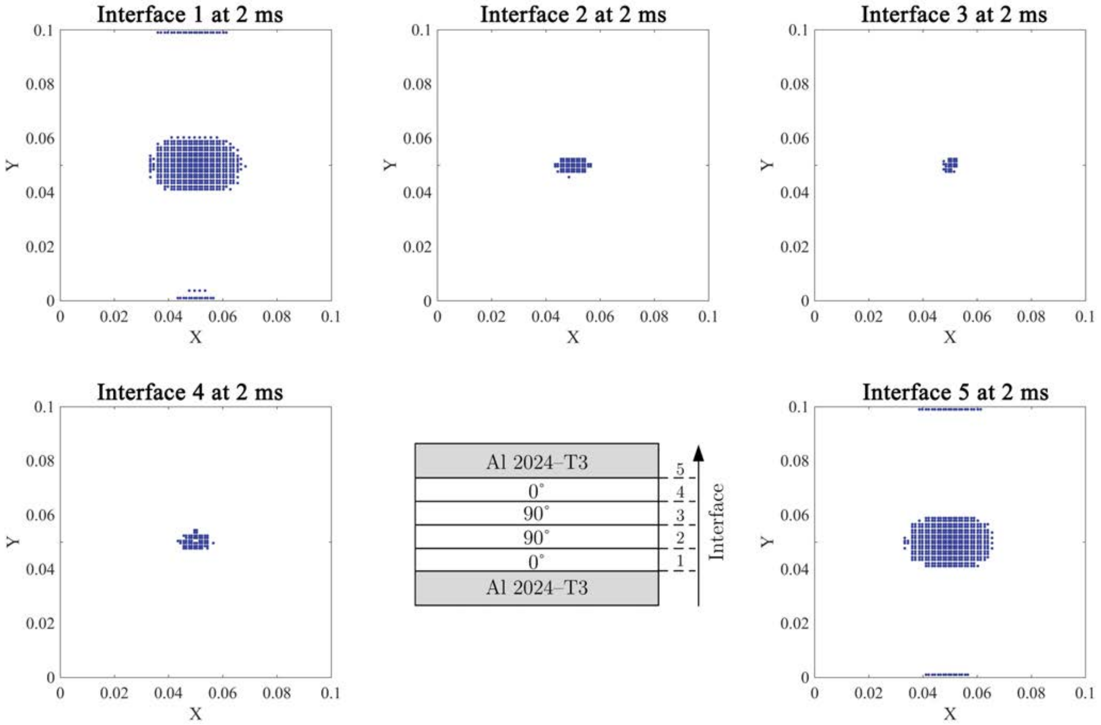

Figure 7.6: Interfacial delamination due to LVI by 0.3 kg impactor at 2.4 J

7.4. Repeated LVIs with equal energy divisions

7.4.1. Effect of impactor mass on the repeated LVIs

In order to understand the effect of repeated LVIs with equal energies on the target GLARE plate, the impact event is divided into two LVI sequences having equal impacting energy of 1.2 J each. As per analysis case B (refer to **Table 7.3**), three different impactors are considered having masses 0.024 kg, 0.15 kg and 0.3 kg respectively and centrally impacting the clamped target and the dynamic responses are shown in **Figure 7.7** and **Figure 7.8**. It is seen that with increase in the impactor mass, the duration of the impact increases and by comparing the contact force responses for the different impactor masses (**Figure 7.7 (a)**, **Figure 7.8 (a)** and **(d)**), it is seen that the peak contact force is the highest for the LVI by the 0.024 kg impactor which is having a higher impacting velocity than the rest two impactors (refer to **Figure 7.7 (b)**, **Figure 7.8 (b)** and **(e)**).

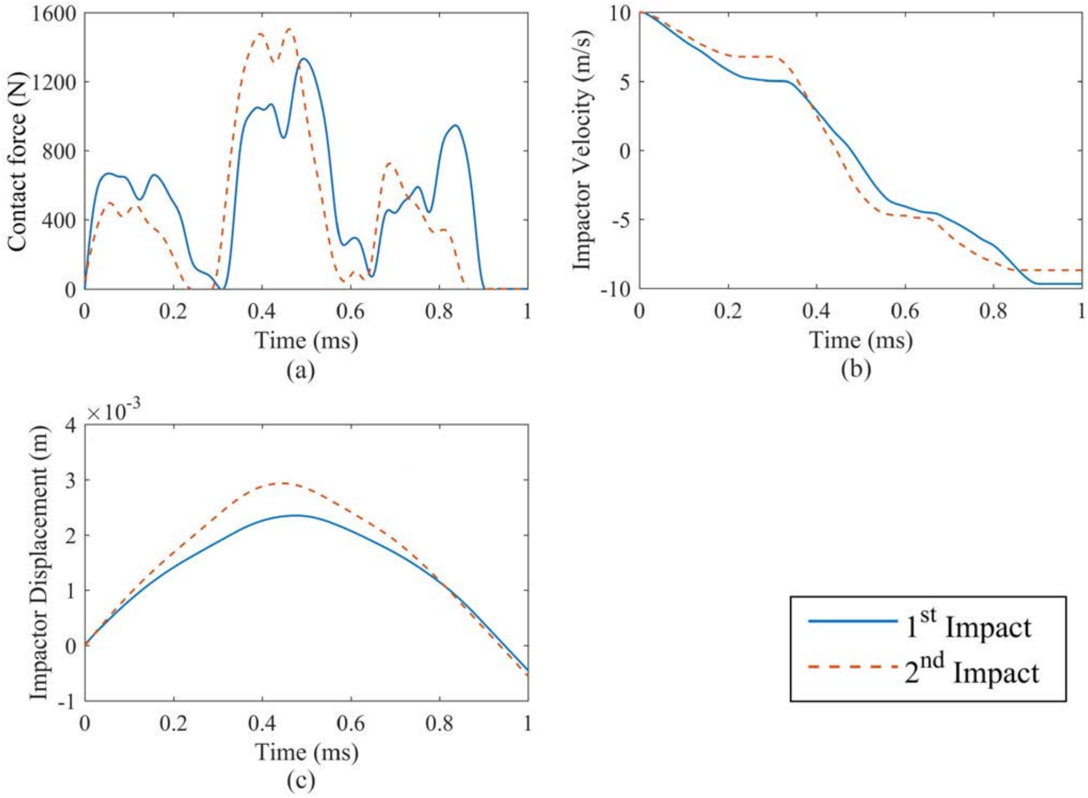

Figure 7.7: Two repeated LVIs with equal energy divisions of 1.2 J by 0.024 kg impactor

After the first impact has occurred, there may be an indentation or dent at the top contacting aluminium surface due to the impact and for the same target, the indentation depth is influenced by the impacting velocity which is evident from the impact responses due to the second LVI by the impactors having different masses. As observed, the peak contact force is relatively higher for the second LVI for all the three impactors impacting at the same energy and the contact force peak for the second impact is comparatively highest for the LVI by the 0.024 kg impactor. Whereas for the higher mass impactor of mass 0.3 kg, the peak contact force during the second impact more or less remains the same. This may be attributed to a greater indentation of the target surface at higher velocities which results in an increase in the local contact stiffness (refer **Section 3.6**). In addition to a rise in the contact force with an increase in the contact stiffness, the contact duration of the second impact slightly reduces as can be observed from **Figures 7.7-7.8**.

Comparing the velocity drops in case of all the three impactors (refer **Figure 7.7(b)** and **Figure 7.8 (b)** and **(e)**), it is seen that during the second impact, the final velocity of the impactors at the end of the impact is less compared to the first impact event implying that the final kinetic energy of the impactor at the conclusion of the second impact is comparatively lower in comparison to the first impact at the same energy. This is more evident for the lower mass 0.024 kg impactor and the least for the 0.3 kg impactor. It may be inferred that this decrease in the final kinetic energy of the impactor is because of the loss in the global plate stiffness as a result of delamination and damage of the inner composite plies on account of the impact which results in an increase in the energy absorbed during the second impact. This degradation of the plate stiffness is not evident from the contact force responses for the different impact cases considered, signifying the localised nature of the contact on the impact force.

In case of the impact by the 0.024 kg mass impactor at a comparatively higher velocity of 10 m/s, the response of the target is more of a wavelike nature compared to the quasi-static response of the target plate in case of impact by the higher mass impactors at lower velocities. As can be seen from the displacement profiles for the different impactors (refer **Figure 7.7(c)** and **Figure 7.8 (c)** and **(f)**) the impactor displacement for the two impact events remain almost the same for LVI by the 0.15 kg and 0.3 kg impactors whereas for the 0.024 kg impactor there is a observable rise in the contact point deflection during the second impact. This is because of the localised response of the plate at higher velocities of impact which tends to cause a more instantaneous deflection of the target near the impact site. On the contrary, in case of LVI by the higher mass impactors at lower velocities the response is also influenced by the global flexural stiffness of the plate since the response tends to be quasi-static causing a global deformation of the pate in addition to the localised deformation at immediate impact site. This global deformation of the target plate leads to a lower indentation at the impact site and hence a smaller increase in the contact stiffness prior to the second impact event leading to a lesser increase in the peak contact force.

Comparing the contact responses of the second impact by the 0.15 kg and 0.3 kg impactor (**Figure 7.8**) to those for the single impacts occurring at 2.4 J (**Figure 7.2**), it is seen that for the 0.3 kg impactor impacting for the second time at 1.2 J, the peak contact force is lower compared to the single 2.4 J impact by the same 0.3 kg impactor. But, for the 0.15 kg impactor, the peak contact force attained during the second impact is closer to the peak contact force for the single 2.4 J impact by the 0.15 kg impactor. The impactor displacement is greater for the for the single 2.4 J impact compared to the repeated impacts occurring at 1.2 J which shows that the impactor momentum has a significant influence on the maximum displacement attained.

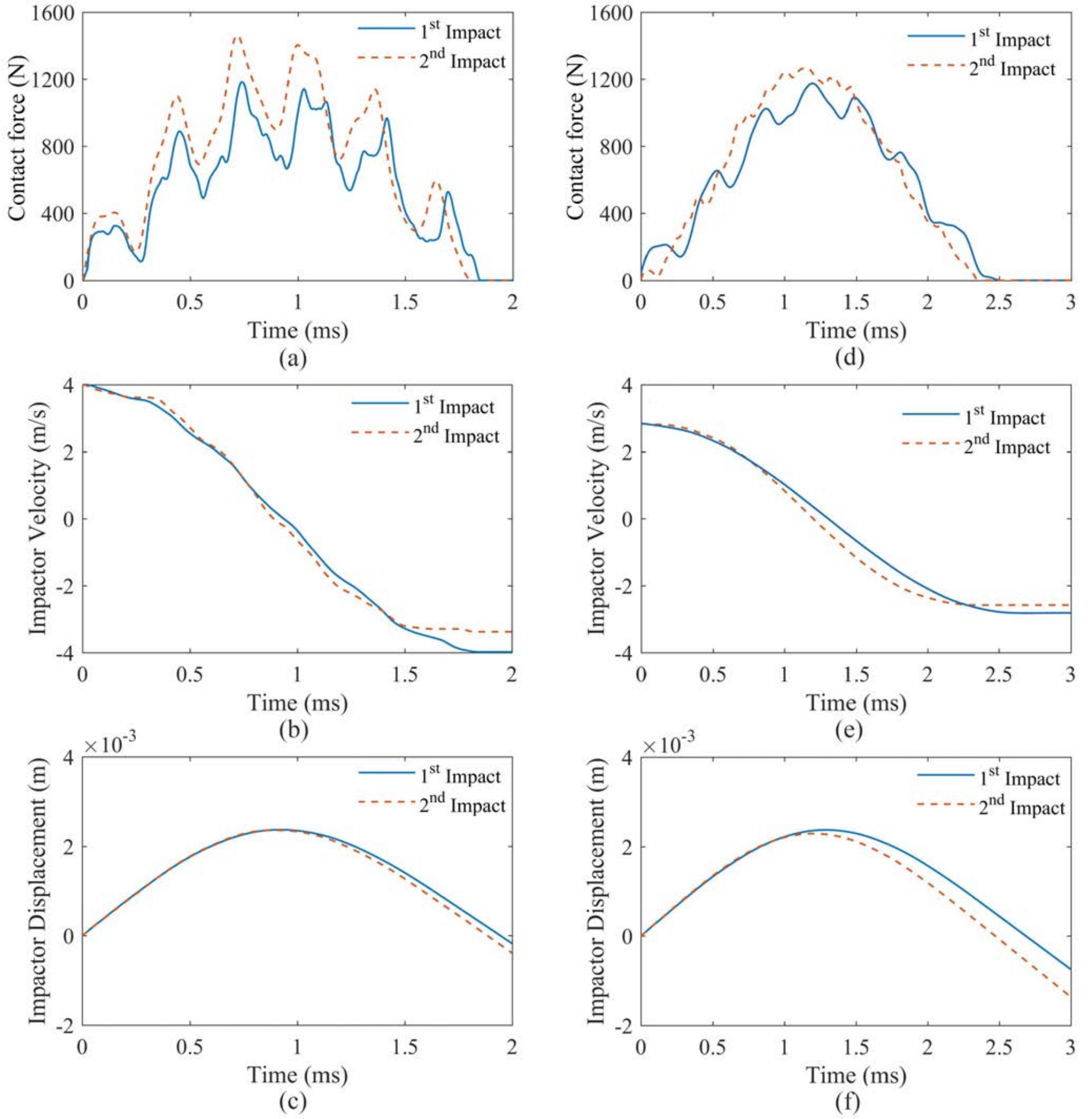

Figure 7.8: Two repeated LVIs with equal energy divisions of 1.2 J by (a)-(c) 0.15 kg impactor and (d)-(f) 0.3 kg impactor

7.4.2. Damage due to repeated LVIs at equal energies

Damage due to repeated impacts on a target can be significant even at lower impact energies where no significant surfacial damage is noticeable. When a structure is subjected to repeated impact, upon initiation of damage, a subsequent impact can significantly increase the extent of damage which can be catastrophic. Therefore, if such impacts occur in a repeating manner, it can cause significant internal damage to the structure. On account of the repeated LVIs by the different impactors at equal energies, the comparisons of the composite damage for the different impactors are shown in **Figures 7.9-7.10** for the first and second LVI events respectively. In addition to the damage incurred by the S2-glass/epoxy plies, delamination at the interfaces is also a prominent damage mode in case of LVI on FMLs. **Figures 7.11-7.12** show the interfacial delamination for the repeated LVIs by the different mass impactors after the the first and second impact.

As observed from **Figure 7.9** and **Figure 7.10**, the damage of the inner composite plies are localised around the impact site and the damage tends to grow with repeated impacts. The bottom 0° ply suffers the maximum extent of damage due to matrix tensile failure followed by the matrix compressive failure of the 90° plies. The extent of damage of the top 90° ply by matrix compressive failure is greater compared to the bottom 90° ply and the extent of damage of the top 0° ply more or less remains the same throughout both the impact events. For all the cases, no fibre failure is seen implying that the major failure mode for impacts at lower energies is by matrix cracking rather than fibre damage.

As discussed in **Section 7.4.1**, the impactor displacement is more or less the same for both the impact events in case of the higher mass impactors whereas a significant rise in the impactor displacement is seen for the impact by the lower mass impactor (refer **Figure 7.7(c)**). This can be justified by the localised response of the target plate rather than the global response as in the case of LVI by the higher mass impactors. Furthermore, with the onset of damage of the composite plies after the first impact, the in-situ plate stiffness tends to decrease due to the degradation of the material stiffness and as a result for the LVI by the 0.024 kg impactor at a higher velocity, the plate deflection is more. This higher deflection of the impactor is not seen for the higher mass impactors although ply damage has occurred near the impact site because of the influence of the global plate stiffness and the boundary conditions due to the quasi-static nature of response.

1st impact by 0.024 kg impactor (1.2 J) | **1st impact by 0.15 kg impactor (1.2 J)** | **1st impact by 0.3 kg impactor (1.2 J)**

(a) Bottom 0° ply matrix tensile damage

(f) Bottom 0° ply matrix tensile damage

(k) Bottom 0° ply matrix tensile damage

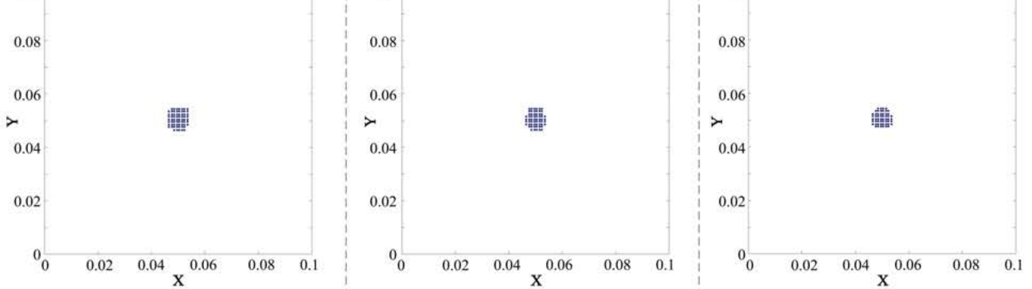

(b) Top 0° ply matrix tensile damage

(g) Top 0° ply matrix tensile damage

(l) Top 0° ply matrix tensile damage

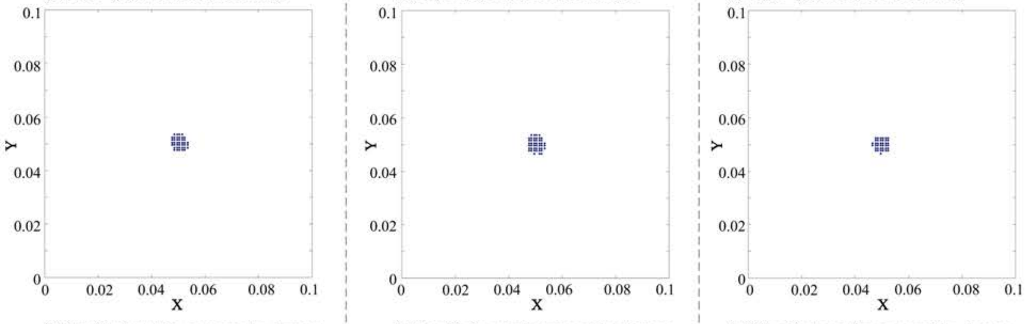

(c) Top 0° ply matrix compression damage

(h) Top 0° ply matrix compression damage

(m) Top 0° ply matrix compression damage

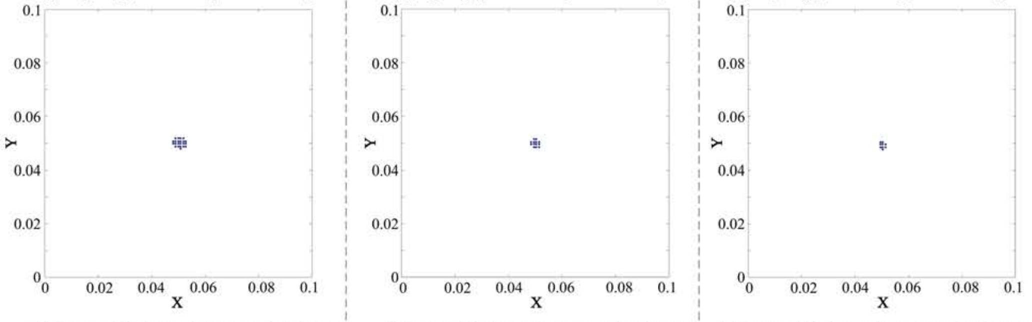

(d) Bottom 90° ply matrix compression damage

(i) Bottom 90° ply matrix compression damage

(n) Bottom 90° ply matrix compression damage

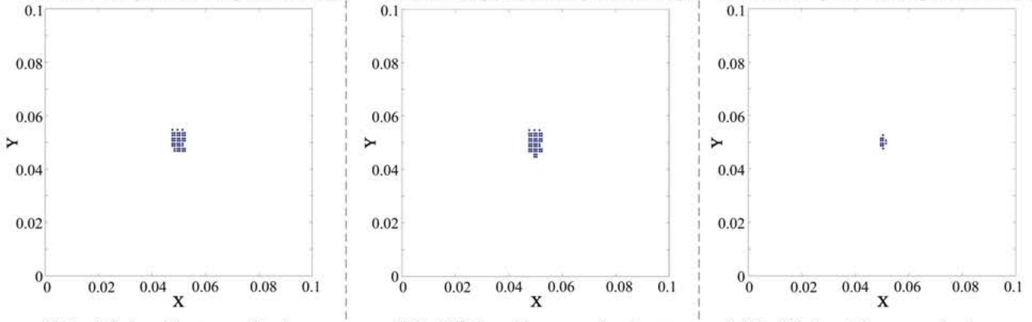

(e) Top 90° ply matrix compression damage

(j) Top 90° ply matrix compression damage

(o) Top 90° ply matrix compression damage

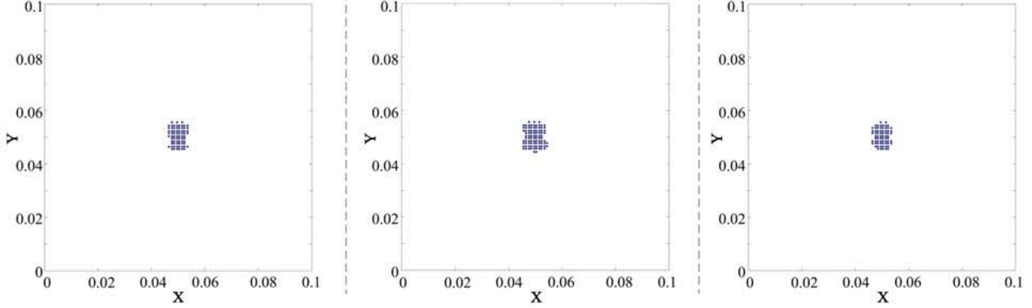

Figure 7.9: S2-glass/epoxy ply damage after the first LVI at 1.2 J

2nd impact by 0.024 kg impactor (1.2 J) | **2nd impact by 0.15 kg impactor (1.2 J)** | **2nd impact by 0.3 kg impactor (1.2 J)**

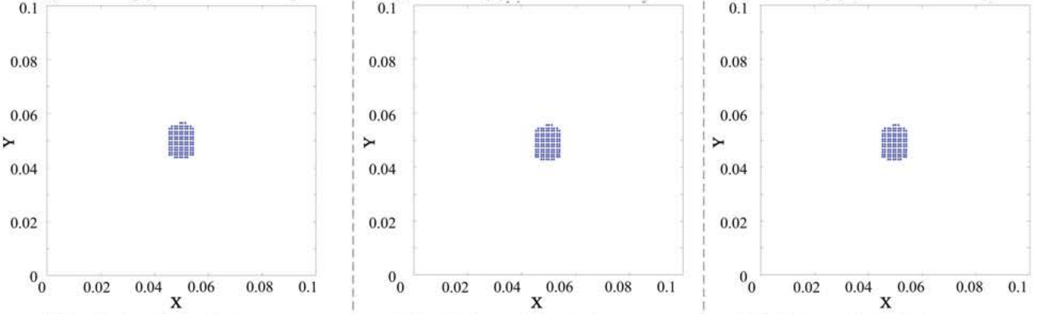
(a) Bottom 0° ply matrix tensile damage
(f) Bottom 0° ply matrix tensile damage
(k) Bottom 0° ply matrix tensile damage

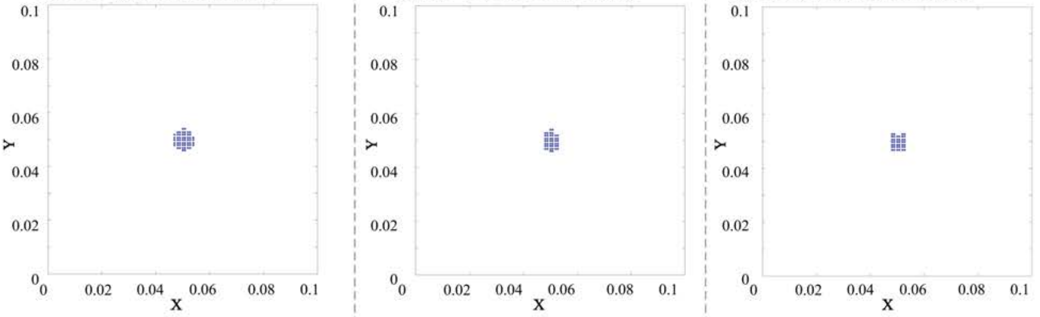
(b) Top 0° ply matrix tensile damage
(g) Top 0° ply matrix tensile damage
(l) Top 0° ply matrix tensile damage

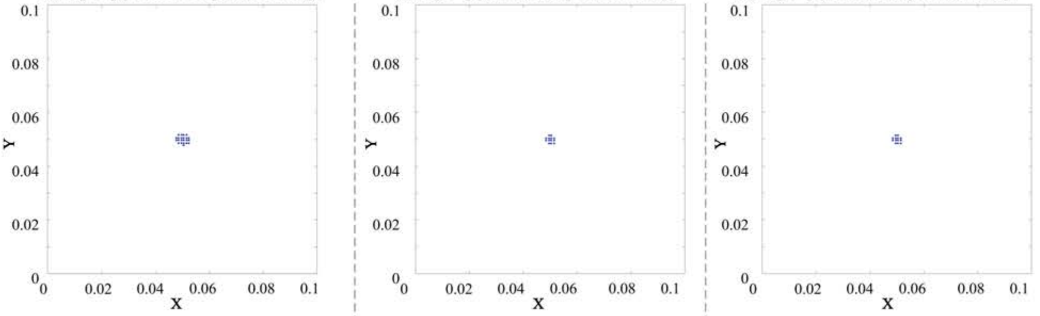
(c) Top 0° ply matrix compression damage
(h) Top 0° ply matrix compression damage
(m) Top 0° ply matrix compression damage

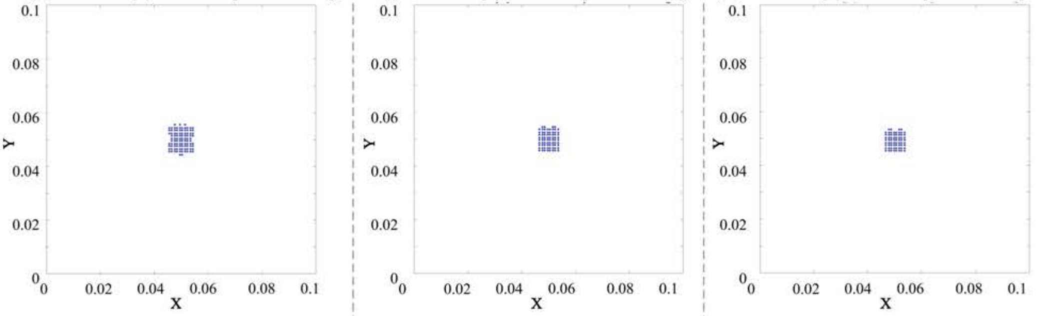
(d) Bottom 90° ply matrix compression damage
(i) Bottom 90° ply matrix compression damage
(n) Bottom 90° ply matrix compression damage

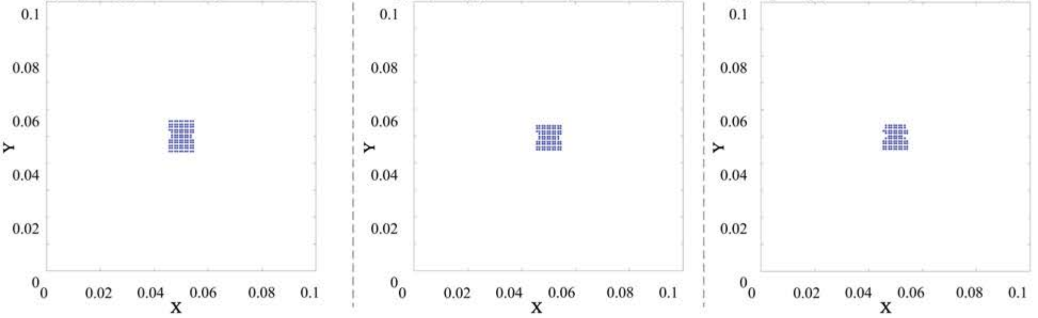
(e) Top 90° ply matrix compression damage
(j) Top 90° ply matrix compression damage
(o) Top 90° ply matrix compression damage

Figure 7.10: S2-glass/epoxy ply damage after the second LVI at 1.2 J

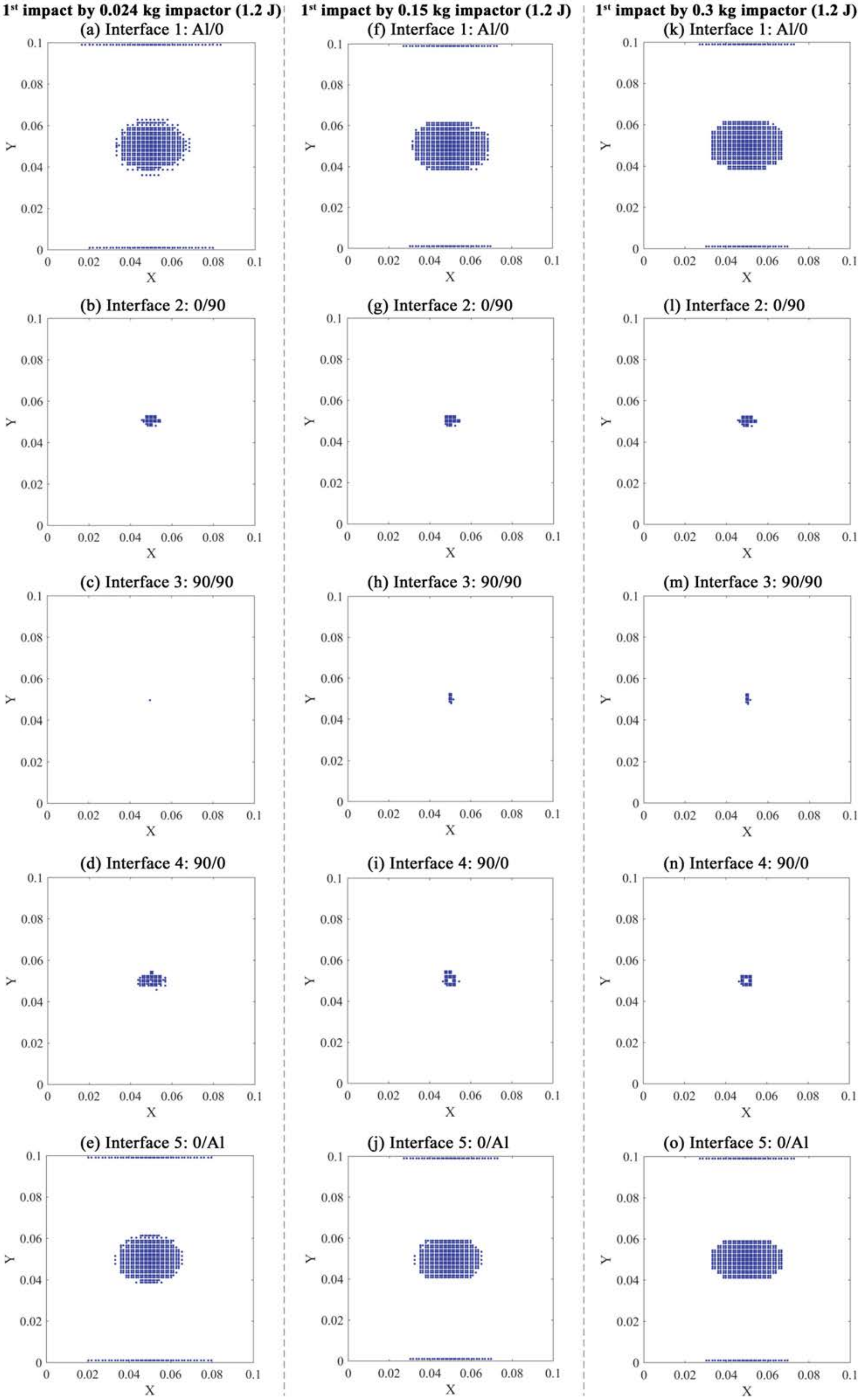

Figure 7.11: Interfacial delamination after the first LVI at 1.2 J

2nd impact by 0.024 kg impactor (1.2 J) **2nd impact by 0.15 kg impactor (1.2 J)** **2nd impact by 0.3 kg impactor (1.2 J)**

(a) Interface 1: Al/0 (f) Interface 1: Al/0 (k) Interface 1: Al/0

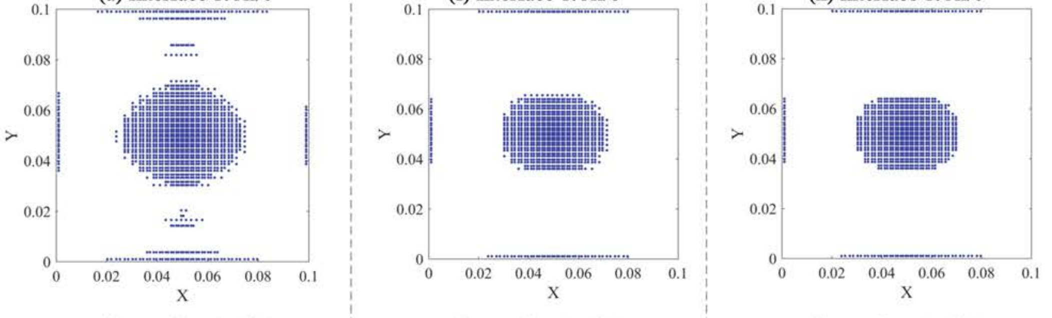

(b) Interface 2: 0/90 (g) Interface 2: 0/90 (l) Interface 2: 0/90

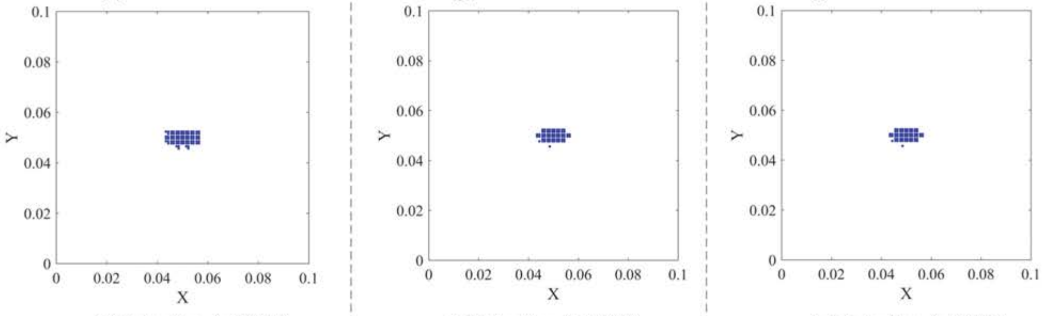

(c) Interface 3: 90/90 (h) Interface 3: 90/90 (m) Interface 3: 90/90

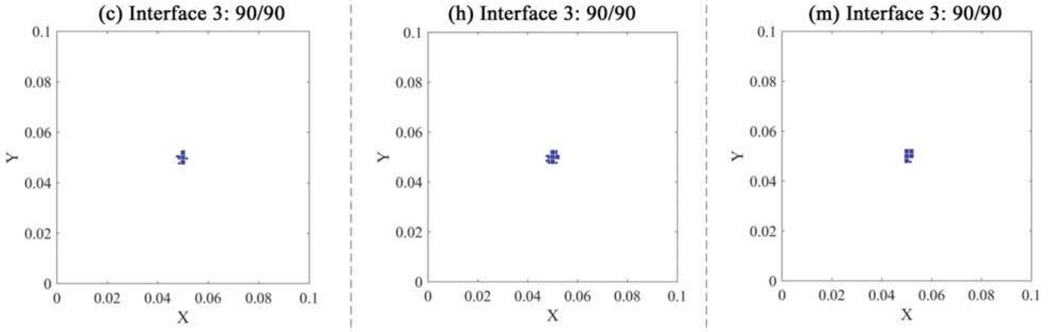

(d) Interface 4: 90/0 (i) Interface 4: 90/0 (n) Interface 4: 90/0

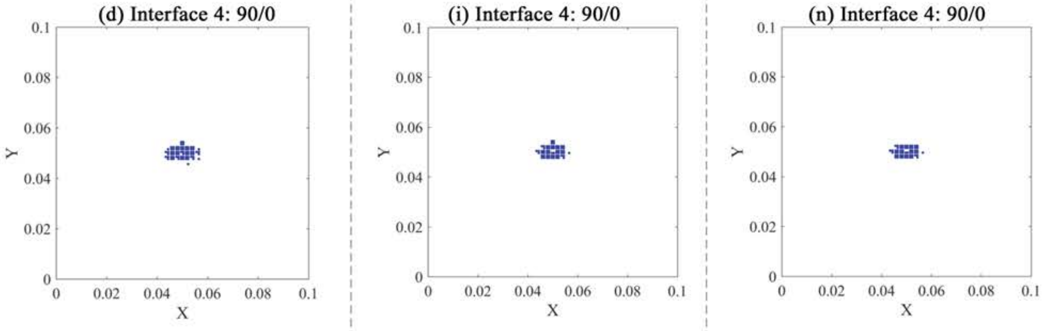

(e) Interface 5: 0/Al (j) Interface 5: 0/Al (o) Interface 5: 0/Al

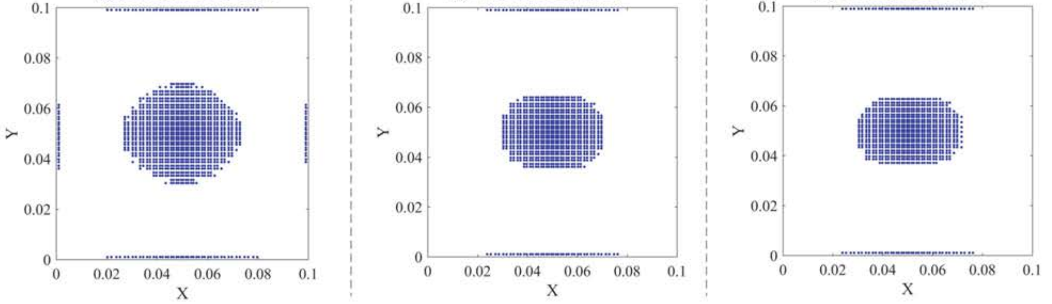

Figure 7.12: Interfacial delamination after the second LVI at 1.2 J

From the delamination at the interfaces as seen in **Figure 7.11** and **Figure 7.12** after the first and second impact, it can be inferred that the delamination tends to easily initiate near the impact site and the extent of delamination is more at the aluminium/composite interfaces and least at interface-3 (90°/90°). Moreover, the 0°/90° interfaces 2 and 4 show some extent of delamination due to the anisotropy between the layers and they are of comparable magnitude. It is seen that with the onset of the first impact, the delamination grows at the aluminium/composite interfaces and its extent is greater for the bottom interface-1 indicating the tensile failure of the bottom interface due to the out-of-plane loading. For the rest of the composite ply interfaces, there is a marginal rise in the extent of delamination after the second impact and in all the cases the delamination tends to grow along the underlying fibre direction. For the metal/composite interfaces this directional propagation of the delamination is more prominent for LVI by the higher mass impactors whereas for the lower mass impactor, the delamination tends to spread in a more circular profile from the impact site.

From the damage profiles of the target GLARE plate due to repetitive loading (**Figure 7.9-Figure 7.12**), it is evident that an impactor having lower mass can cause more damage compared to higher mass impactor impacting at the same energy. Therefore, repetitive loading by small mass impactors can prove to be more critical and proper safety measures needs to be implemented for small mass impacts and critical inspection of the damage needs to be done. Comparing the damage of the inner composite plies due to the repeated LVI by the 0.15 kg and 0.3 kg impactor (**Figure 7.10**) to those for the single impacts occurring at 2.4 J (**Figure 7.3-Figure 7.4**), it is seen that the final extent of damage is similar in both the cases and failure by tensile matrix damage of the bottom 0° ply is only marginally more for the single impacts at 2.4 J in case of both the impactors. Further, from **Figure 7.5-Figure 7.6** and **Figure 7.12**, it could be inferred that the extent of delamination is more for the repeated impacts, each occurring at 1.2 J compared to the single impact occurring at 2.4 J highlighting the critical nature of the repetitive LVIs on GLARE and laminated structures in general. For all the impactor masses considered, the damage caused by the repetitive impact by the 0.024 kg impactor is the most and also causes a greater extent of interfacial delamination compared to the single LVIs occurring at 2.4 J.

7.5. Repeated LVIs with unequal energy divisions

In case of repeated LVIs with unequal energies, the order of the impacting energies and the sequence in which they occur may also affect the dynamic responses and the associated damage the target sustains. To see the effect of the division in the impacting energy during repeated LVIs, two impact events are considered as per analysis case C (refer **Table 7.3**) and the impact responses are shown in **Figure 7.13**. The energy divisions are such that the net impacting energy for each case is the same at 2.4 J.

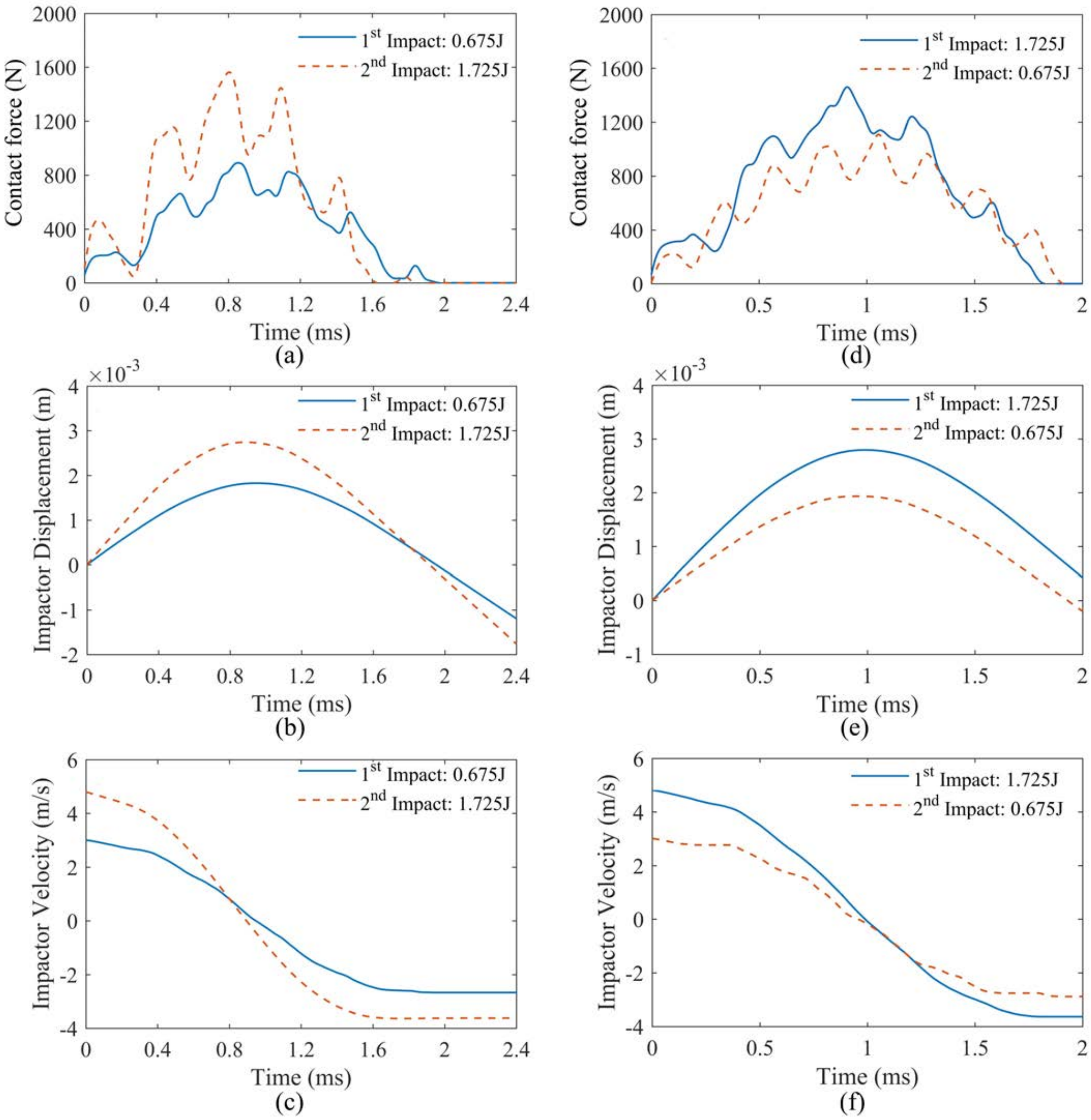

Figure 7.13: Repeated LVIs by 0.150 kg impactor with unequal energy divisions

In case of the first impact occurring at a lower energy (0.675 J) compared to the second (1.725 J), no significant changes are observed other than the lower peaks attained by the contact force and impactor displacement for the first impact compared to that of the second impact which is of generic inference (**Figure 7.13 (a)-(c)**). But on reversing the order of the impacting energies a slight change can be observed for the peak contact force during the second impact occurring at lower energy (refer **Figure 7.13 (d)**). This is because when the first impact occurs at higher energy marked by a higher peak contact force, there is relatively a greater indentation of the target resulting in an increase in the local contact stiffness which leads to a slight rise in the peak contact force during the second impact. As observed from **Figure 7.13 (b)-(c)** and **(e)-(f)**, the impactor displacement and velocity more or less remains the same in both instances. Therefore the energy divisions can significantly affect the extent of damage the target sustains as discussed in the next subsection.

7.5.1. Damage due to repeated LVIs at unequal energies

The repeated LVIs occurring at unequal energy divisions can influence the damage magnitudes although the net energy of the impact events remains the same at 2.4 J. **Figure 7.14 (a)-(e)** show the inner composite damages after the first impact occurs at a lower energy (0.675 J) and **Figure 7.14 (f)-(j)** show the same after the second impact occurs at a higher energy (1.725 J). For the case when the order of theses impacts are changed, only the damage case after the first impact is shown (**Figure 7.14 (k)-(o)**) since no further progression in damage or delamination is seen for the impact occurring at lower energy. The same is done for the delamination plots shown in **Figure 7.15 (a)-(o)** considering the different order of the impacting energies.

From **Figure 7.14**, it is seen that when the first impact is at 0.675 J, the extent of damage is small with only the bottom 0° ply failing by matrix tensile mode and the top 90 ° ply failing by matrix compressive failure mode and the rest of the plies showing negligible damage. Also, the damage is closely confined within the impact site. With the onset of the second impact at 1.725 J, the damage is seen to grow in the composite plies with the maximum extent of damage being due to the matrix tensile failure of the bottom 0° ply. The 90 ° plies also show a growth in their damage due to matrix tensile failure with the extent of damage being larger for the top 90 ° ply and the top 0 ° ply also shows failure by matrix tension. In addition, a small extent of damage due to matrix compression failure is seen in the top 0° ply concentrated within the impact location which may be attributed to the crushing mode of failure of the matrix due to the higher compressive stresses generated at the impact site during the peak load.

Now, for the case when the order of the impacting energies are reversed (**Figure 7.14 (k)-(o)**), considerable damage is incurred after the first impact and no further increase in the damage of the composite plies are seen for the second impact at 0.675 J. Further, comparing **Figure 7.14 (f)** and **(k)**, the damage due to matrix tensile failure for the bottom 0 ° ply is seen to be relatively more for the case when the higher energy impact follows the lower energy impact. This is because of the onset of degradation of the stiffness of the plies at the damaged location during the first impact which further expedite the tendency affinity for the damage

1st impact at 0.675 J **2nd impact at 1.725 J** **1st impact at 1.725 J and 2nd impact at 0.675 J**

(a) Bottom 0° ply matrix tensile damage (f) Bottom 0° ply matrix tensile damage (k) Bottom 0° ply matrix tensile damage

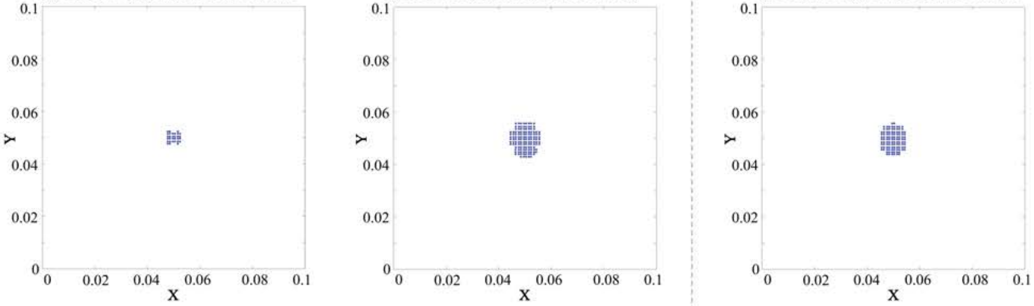

(b) Top 0° ply matrix tensile damage (g) Top 0° ply matrix tensile damage (l) Top 0° ply matrix tensile damage

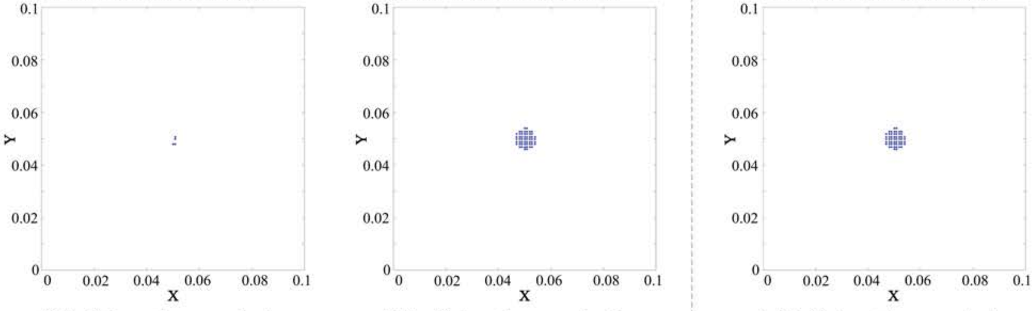

(c) Top 0° ply matrix compression damage (h) Top 0° ply matrix compression damage (m) Top 0° ply matrix compression damage

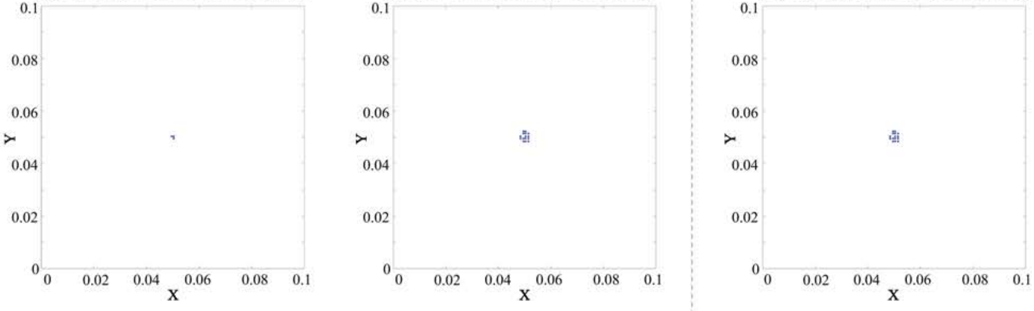

(d) Bottom 90° ply matrix compression damage (i) Bottom 90° ply matrix compression damage (n) Bottom 90° ply matrix compression damage

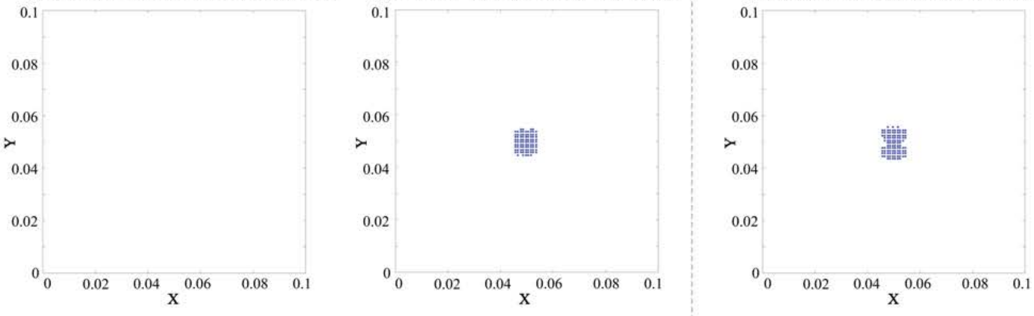

(e) Top 90° ply matrix compression damage (j) Top 90° ply matrix compression damage (o) Top 90° ply matrix compression damage

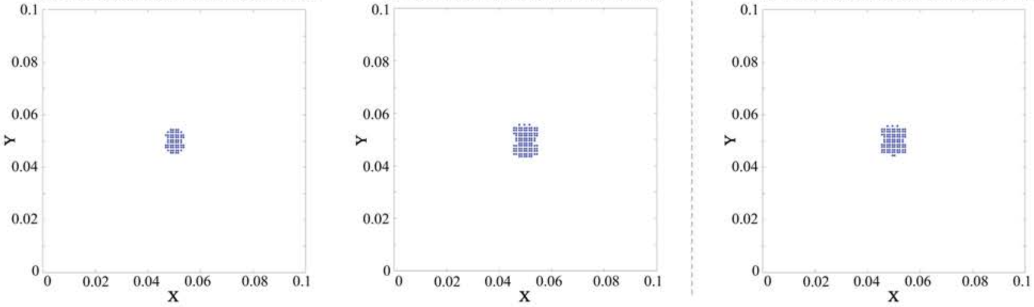

Figure 7.14: Composite damage due to LVI by 0.15 kg impactor at unequal energy divisions

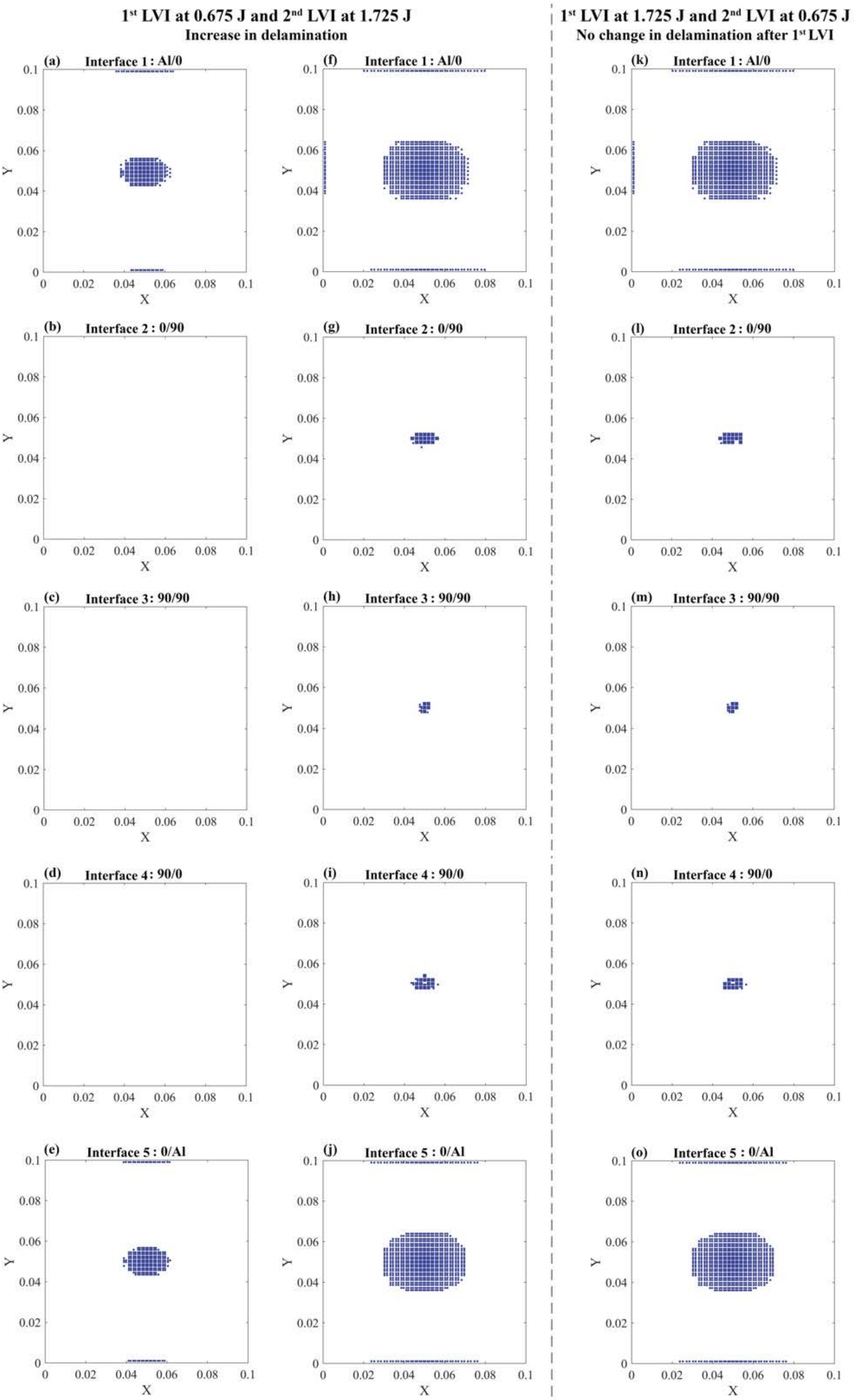

Figure 7.15: Interfacial delamination due to repeated LVIs at unequal energies

to progress upon subsequent impacts. A similar observation was be made for the top 90° ply which fail by matrix compressive failure (**Figure 7.14 (e)** and **(o)**) although the difference is negligible while for rest of the plies the damage extent more or less remains the same. Therefore it can be concluded that the tendency of the damage by matrix tensile failure due to repeated impacts is higher, especially for the bottom 0° ply and the order of the impacts can also influence the damage extent of the inner composite plies.

Figure 7.15 (a)-(j) show the delamination due to the repeated impacts occurring first with a lower energy (0.675 J) followed by the higher energy (1.725 J) and **Figure 7.15 (k)-(o)** show the delamination when the order is reversed with the 0.675 J impact occurring latter. For the latter case, the delamination at the interfaces remain the same and no increase in the delaminated area is seen for the subsequent 0.675 J impact. Further, it is seen that the final extent of delamination at the interfaces for both the cases are similar and is seen to progress along the fibre direction of the underlying layer for all cases. The aluminium/composite interfaces experience the maximum extent of delamination followed by the 0°/90° interfaces because of the mismatch in the material properties and anisotropy of the composite layers. In case of the 0.675 J impact occurring first where negligible composite damage was seen, the delamination is seen to initiate only at the aluminium/composite interfaces (**Figure 7.14**) and upon subsequent impact it spread at the other composite interfaces. This shows that the delamination damage mode initiates with the onset of impact at the aluminium/composite interfaces. Moreover, the delamination engulfs the damage regions and have a higher affinity to spread outward as can be seen comparing **Figure 7.14** and **Figure 7.15** indicating that the failure by delamination is more prominent for impacts occurring at lower energies.

7.6. Summary

Repeated LVI response of a GLARE 5-2/1 plate has been studied and compared to to a signle impact occuring at the same net total energy. The dynamic responses on account of the repeated LVIs are evaluated using the developed FE code and the impact responses and associated damage for the internal composite plies are evaluated considering 3D Hashin damage criteria. The influence of the impactor mass and the division of the impacting energy on the dynamic responses and damage of the composite plies are investigated. Based on the results pertaining to different cases the following important conclusions can be drawn:

- For LVIs occurring at lower energies (0.5 J-2.5 J), matrix cracking and delamination are the critical damage modes. The interfacial delamination is likely to grow between the composite plies due to repetitive LVIs although the extent of the damage depends on the energy of the impact.

- In case of repetitive loading, the impact energy division also influence the contact responses as well as the initiation of the damage of the composite plies. For all the energy divisions considered and the sequence of their occurrence, the delamination at the aluminium/composite interface occur in in all the cases considered making them the most critical sites.
- The influence of the impactor velocity on the indentation of the outer aluminium layer on account of LVI is greater compared to the impactor mass. A smaller mass impactor having higher velocity will cause a greater indentation compared to a heavier impactor having equivalent momentum.
- For the repeated impacts occurring on GLARE at lower energies, the progression of failure can be demarcated into initial plastic deformation of the outer aluminium layer in the form of dent/indentation, followed by the delamination between the aluminium/composite interfaces and matrix cracking and delamination of the inner composite plies. The outer aluminium layers play a significant role in limiting the damage of the inner composite plies.
- In case of the repeated LVIs occurring at equal energies, the indentation at the impact site significantly influence the peak contact force response as well as the contact duration of the second impact. Because of the elastic-plastic behaviour of the outer aluminium layer, the first impact creates a permanent indentation at the impact location. This increase in the area of contact between the impactor and the target results in an increase in the local contact stiffness. Therefore, the peak contact force in case of the second impact with the same equal energy is higher.
- A higher contact force peak for the second impact does not signify the target to be undamaged. This increase in the contact force peak is solely due to the localised geometrical change between the target and the impactor. But with the onset of the first impact itself, interfacial delamination and inner composite damage are observed leading to in-situ degradation of the flexural stiffness of the target.
- The delamination at the interfaces tend to progress along the fibre direction of the underlying layer. For a repetitive LVI by a lower mass impactor, the extent of delamination is higher compared to a heavier impactor impacting with the same energy divisions. This makes the repetitive LVI by lower mass impactors more critical.

Chapter 8

Conclusion and scope for future work

The main inferences drawn from the analysis of LVI of GLARE which can further contribute to the understanding of their impact characteristics are discussed in the present chapter. Summarising the work done in this dissertation, the chapter proceeds to present the general conclusions followed by the specific conclusions and possible scope for future work.

8.1. Concluding summary

The critical investigation for the impact behaviour of GLARE is necessary due their site specific applications like the aircraft fuselage and wings which are prone to impact. Although GLARE have superior impact characteristics, extensive studies regarding their impact behaviour is still an important area of exploration because of the complex damage modes associated in such hybrid structures, especially when subjected to arbitrary LVIs due to the hidden nature of the damage. In addition, the complex nature of the contact and the associated response of the target subjected to LVIs at different trajectories of incidence further necessitated the need to explore such LVIs which is still not explored much. In the present work, a 3D FE code using layered solid elements have been developed to analyse the LVI of GLARE by incorporating the Newmark-β method and Newton-Raphson scheme for the dynamic impact analysis. The LVI by arbitrary masses at arbitrary velocities and different trajectory of impact are analysed by considering a Hertzian contact model [189] for the normal impact component of the impact and a tangential contact model based on the works of Mindlin and Deresiewicz [176,177] for the tangential component of the impact. The effect of various geometrical parameters of the impactor and the GLARE plate viz. the impactor shape and size, plate size and stacking configurations have been studied. Based on the results obtained from the present study, the general and specific important conclusions drawn are outlined in the following sub-sections.

8.2. General conclusions

The general conclusions drawn from the present work are as follows:

- The developed 3D finite element code can be used to analyse both normal and oblique LVIs by arbitrary mass impactors and to estimate the associated damage induced in the target.
- The outer aluminium layers has significant effect on the peak values attained by the contact force and displacement of the impactor and target plate as well as the associated interfacial delamination.
- Low-velocity impacts are more critical in the sense that these impacts can cause considerable sub-surface damage although at the visible surface the indication of damage is negligible.
- The aluminium/composite interfaces are the most critical sites for delamination followed by the 0°/90° interfaces.
- In case of the inner interfaces, the delamination is generally located around the impact region and for all the cases, the direction of the delamination is influenced by the fibre orientation of the underlying layer.
- Stacking sequence affects the extent of delamination at the interfaces. Compared to a GLARE 4-3/2 plate, a GLARE 5-2/1 plate with $[Al/0°/90°]_S$ configuration experiences lesser extent of delamination for the same impact parameters.

8.3. Specific conclusions

8.3.1. Influence of impactor and plate parameters on the normal LVI response of GLARE

- Ratio of the impactor mass to the plate mass significantly influences the contact impact response of GLARE, both in terms of magnitude and duration of the contact force. Consequently, the evolution of the interfacial stresses varies with different impactor to plate mass ratios resulting in a change in the delamination at the interfaces.
- It is the relative inertia of the impactor and the plate which influences the nature of the dynamic response due to LVI rather than the mass of the impactor or the

target alone. In view of this, the use of hybrid configurations considering lighter Kevlar-49/epoxy layers was observed to improve the impact characteristics.

- For similar impacting energies, the LVI by a smaller mass impactor causes more damage compared to that caused by a larger mass impactor. For the LVI by a larger mass impactor, the delamination region at the aluminium/composite interfaces is confined within the impact location, unlike the smaller mass impacts.
- Geometric parameters of the impactor also influence the extent of delamination. In case of a cylindrical LVI, the effect of contact length is more pronounced compared to that of cylinder radius.

8.3.2. Effect of cut-outs on the LVI response of GLARE

- Closer is the impact site to the open hole, more is the damage caused due to delamination. Furthermore, an increase in contact force accelerates the delamination around the hole at the fibre/metal interfaces compared to that near the impact locations. Thus, area around the hole is more prone to delamination.
- Relative to the GLARE plate dimension, for holes having diameters below a critical minimum, the position of the holes have minor effect on the dynamic response. However, the same is not true for the extent of interfacial delamination at the fibre/metal interfaces. Therefore, the pitch between the holes is an important factor that needs to be considered while making cut-outs on a GLARE laminate.
- The hole shape and their orientation relative to the fibre direction of the underlying ply influences the delamination at the aluminium/glass-epoxy interfaces and also around the hole periphery.

8.3.3. Oblique LVIs on GLARE

- For an OLVI at a fixed initial speed, the peak attained by the tangential contact force increases up to a certain value of oblique angle beyond which it decreases unlike the normal contact force which monotonically decreases with increasing obliquity.
- The stick-slip transitions in case of an OLVI, leads to reversal of the tangential load at lower angles of incidence and as the obliquity increases, there is gross slip throughout the contact regime and no load reversal takes place.
- For an impact with fixed initial component of normal velocity, the normal contact force profile is unaffected by obliquity of the impact and only results in the change in tangential contact force which increases with increasing obliquity and its

maximum attainable value is limited by the coefficient of friction between the impactor and the target.

- With the increasing value of coefficient of friction, the duration of negative tangential force increases for a certain obliquity. However, for a given coefficient of friction, the instant of this reversal is delayed with increasing obliquity and at higher obliquities ($\theta \geq 45^\circ$), reversal is almost negligible.
- For a given coefficient of friction, the impactor size influences the reversal of the tangential contact force. With increasing impactor size, the reversal of the tangential contact force gets delayed as the tendency to slip increases.
- At higher obliquities, the tangential component of the contact force influences the delamination at the immediate interface and in closer proximity to the contact location.
- The fibre orientation of the underlying lamina at the metal/composite interface and the relative orientation to the trajectory of impact influence the delamination at higher obliquities of impact.

8.3.4. Multiple LVIs on GLARE

- The magnitude and evolution of the contact force for the second impact is influenced by the time interval between the two impacts and also by the location of the impacts.
- The relative position of the two impactors significantly influences the progression and extent of delamination.
- In estimating the extent of delamination, particularly at the fibre/metal interfaces, the time delay between successive LVIs has a significant influence on whether the delaminations remain as discrete patches or coalesce into a single delaminated area. With increasing magnitude of the contact force, the tendency to coalesce increases.
- In case of multiple OLVIs, the relative trajectories of the impacts influence the size and shape of the interfacial delamination.
- The presence of discontinuities in the form of holes in the target plate causes the delaminations to initiate more easily around the periphery of the hole and upon multiple impacts the delaminations tend to coalesce.

8.3.5. Repeated LVIs on GLARE

- In the case of repetitive loading, the impact energy division and their order of occurrence influence the contact responses as well as the initiation of damage.

- The influence of the impactor velocity on the indentation of the outer aluminium layer is more than that of the impactor mass.
- For the repeated impacts occurring on GLARE at lower energies, the progression of failure can be demarcated into initial plastic deformation of the outer aluminium layer in the form of dent/indentation. This is followed by the delamination between the aluminium/composite interfaces, matrix cracking and delamination of the inner composite plies. The outer aluminium layers play a significant role in limiting the damage to the inner composite plies.
- A higher contact force peak for the second impact does not signify the target to be undamaged. This increase in the contact force peak is solely due to the localised geometrical change between the target and the impactor. But, with the onset of the first impact itself, interfacial delamination and damage in the composite plies are observed leading to in-situ degradation of the flexural stiffness of the target.

8.4. Major contributions

- The present work on the impact analysis of GLARE gives a comprehensive insight into the modelling and analysis of impact at arbitrary trajectories for any arbitrary impactor mass.
- The contact impact modelling incorporates the adjustment of the contact stiffness based on the impactor to GLARE plate mass ratio which is an important aspect in evaluating the impact behaviour of a target having any arbitrary layup and impacted by varied mass impactors, necessary for accurately estimating the damage evolution under low velocity impact.

8.5. Scope for future work

The work done in the present research is limited to the LVI regime and certain aspects can be explored for future research as follows:

- The material parameters are considered to be temperature independent even though the temperature fluctuations can be prominent in aerospace applications. The temperature dependent modelling of the target can be an important area for exploring the LVI responses since local temperature rise at the impact site can occur for impacts at higher velocities which can affect the stiffness and strength properties.

- In the present research and in most of the research in literature, the target is considered mostly as a flat plate. But in real scenarios like in case of the aircraft fuselage and wings, the structure is curved. Investigations exploring the dynamic impact behaviour of curved GLARE structures are required.

- Besides the analysis of LVI on GLARE, other FMLs can be considered taking other constituent materials like steel or magnesium. Also, composite layups containing different material combinations can be considered such as Kevlar-49 layers along with carbon or glass/epoxy plies and checked for impact performances. Although an effort has been made in the present work investigating the hybridisation of the inner layers with Kevlar-49 layers and evaluating their impact characteristics, further studies can be done focusing on optimising such layups.

- The material properties of the individual composite plies along the thickness are considered to be uniform on account of which the potentiality of the initiation of delamination at the interface of differently oriented plies increases. The composite plies can be functionally graded to mitigate the discontinuities at the interfaces. The effect of functional gradation in the mechanical properties of the inner composite plies on the impact response and associated damage can be explored.

- The experimental investigations for oblique low-velocity impact on GLARE can be an interesting prospect.

References

[1] Yang J-M, Hahn TH, Seo H, Chang P-Y, Yeh P-C. Damage Tolerance and Durability of Fiber-Metal Laminates for Aircraft Structures. 2010.

[2] Airbus. A350 Less Operating Cost. More Capabilities. n.d. https://aircraft.airbus.com/en/aircraft/a350/a350-less-operating-cost-more-capabilities.

[3] Soutis C. Carbon fiber reinforced plastics in aircraft construction. Mater Sci Eng A 2005;412:171–6. https://doi.org/https://doi.org/10.1016/j.msea.2005.08.064.

[4] Whitney JM. Issues in compression loading in composite structures. Util. Adv. Compos. Mil. Aircraft, AGARD-R-785, USA: AGARD; 1992, p. 1–1 to 1–5.

[5] Green S. Aspects of Compression in Aerospace Composites-Future Requirements. Util. Adv. Compos. Mil. Aircraft, AGARD-R-785, USA: AGARD; 1992, p. 4–1 to 4–13.

[6] Laliberte JF, Poon C, Straznicky P V, Fahr a. Applications of fiber-metal laminates. Polym Compos 2000;21:558–67. https://doi.org/10.1002/pc.10211.

[7] Alderliesten R, Rans C, Benedictus R. The applicability of magnesium based Fibre Metal Laminates in aerospace structures. Compos Sci Technol 2008;68:2983–93. https://doi.org/10.1016/j.compscitech.2008.06.017.

[8] Asundi A, Choi AYN. Fiber metal laminates: An advanced material for future aircraft. J Mater Process Technol 1997;63:384–94. https://doi.org/10.1016/S0924-0136(96)02652-0.

[9] Vogelesang LB, Gunnink JW. ARALL: A materials challenge for the next generation of aircraft. Mater Des 1986;7:287–300. https://doi.org/10.1016/0261-3069(86)90098-1.

[10] Vogelesang LB, Gunnink JW, Chen D, Roebroeks GHJJ, Vlot A. New Developments in ARALL Laminates. 16th Congr Int Counc Aeronaut Sci 1988;1:1615–33.

[11] Botelho EC, Silva RA, Pardini LC, Rezende MC. A review on the development and properties of continuous fiber/epoxy/aluminum hybrid composites for aircraft structures. Mater Res 2006;9:247–56. https://doi.org/10.1590/S1516-14392006000300002.

[12] Pan Y, Wu X, Huang Z, Wu G, Sun S, Ye H, et al. Composites : Part A A new approach to enhancing interlaminar strength and galvanic corrosion resistance of CFRP / Mg laminates. Compos Part A 2018;105:78–86. https://doi.org/10.1016/j.compositesa.2017.11.009.

[13] Hamill L, Hofmann DC, Nutt S. Galvanic Corrosion and Mechanical Behavior of Fiber Metal Laminates of Metallic Glass and Carbon Fiber Composites. Adv Eng Mater 2018;20:1700711. https://doi.org/https://doi.org/10.1002/adem.201700711.

[14] Song SH, Byun YS, Ku TW, Song WJ, Kim J, Kang BS. Experimental and numerical investigation on impact performance of carbon reinforced aluminum laminates. J Mater Sci Technol 2010;26:327–32. https://doi.org/10.1016/S1005-0302(10)60053-9.

[15] Vlot A. Glare History of the Development of a New Aircraft Material. Springer Dordrecht; 2001. https://doi.org/https://doi.org/10.1007/0-306-48398-X.

[16] Vermeeren CAJR. An Historic Overview of the Development of Fibre Metal Laminates. Appl Compos Mater 2003;10:189–205. https://doi.org/10.1023/A:1025533701806.

[17] Gunnink JW, Vlot A, De Vries TJ, Van Der Hoeven W. Glare technology development 1997-2000. Appl Compos Mater 2002;9:201–19. https://doi.org/10.1023/A:1016006314630.

[18] Wu G, Yang J-M. The Mechanical Behaviour of GLARE Laminates for Aircraft Structures. Jom 2005;57:72–9.

[19] Vermeeren C, editor. Around Glare: A New Aircraft Material in Context. Kluwer ACademic Publishers; 2002. https://doi.org/10.1007/0-306-48385-8.

[20] Roebroeks GHJJ. Fibre-metal laminates: Recent developments and applications. Int J Fatigue 1994;16:33–42. https://doi.org/https://doi.org/10.1016/0142-1123(94)90443-X.

[21] Vlot A, editor. Fibre Metal Laminates: An Introduction. 1st ed. Springer; 2001. https://doi.org/10.1007/978-94-010-0995-9.

[22] Assler H, Telgkamp J. Design of Aircraft Structures under Special Consideration of NDT. 9th Eur. Conf. NDT, Berlin, Germany: 2006.

[23] AIRBUS. Fast #48. Airbus Technical Magazine-Flight Airworthiness Support Technology. Airbus 2011:47.

[24] Navarro A, Levin A. Boeing 737 Passenger Jet Damaged in Possible Midair Drone Hit. Bloomberg 2018.

[25] Takeda S, Minakuchi S, Okabe Y, Takeda N. Delamination monitoring of laminated composites subjected to low-velocity impact using small-diameter FBG sensors. Compos Part A Appl Sci Manuf 2005;36:903–8. https://doi.org/10.1016/j.compositesa.2004.12.005.

[26] Chai GB, Manikandan P. Low velocity impact response of fibre-metal laminates – A review. Compos Struct 2014;107:363–81. https://doi.org/https://doi.org/10.1016/j.compstruct.2013.08.003.

[27] Vlot A. Impact properties of Fibre Metal Laminates. Compos Eng 1993;3:911–27. https://doi.org/10.1016/0961-9526(93)90001-Z.

[28] Tan CY, Akil HM. Impact response of fiber metal laminate sandwich composite structure with polypropylene honeycomb core. Compos Part B Eng 2012;43:1433–8. https://doi.org/10.1016/j.compositesb.2011.08.036.

[29] Chen Q, Guan Z, Li Z, Ji Z, Zhuo Y. Experimental investigation on impact performances of GLARE laminates. Chinese J Aeronaut 2015;28:1784–92. https://doi.org/10.1016/j.cja.2015.07.002.

[30] Dolbeer RA, Wright SE, Weller JR, Anderson AL, Begier MJ. Wildlife strikes to civil aircraft in the United States 1990–2014. vol. 21. 2015.

https://doi.org/10.13140/RG.2.1.2370.6649.

[31] Vlot A. Impact loading on fibre metal laminates. Int J Impact Eng 1996;18:291–307. https://doi.org/10.1016/0734-743X(96)89050-6.

[32] Abrate S. Impact on laminated composite materials. Appl Mech Rev 1991;44:155–90. https://doi.org/10.1115/1.3119500.

[33] Abrate S. Impact on Laminated Composites: Recent Advances. Appl Mech Rev 1994;47:517–44. https://doi.org/10.1115/1.3111065.

[34] Cantwell WJ, Morton J. The impact resistance of composite materials - a review. Composites 1991;22:347–62. https://doi.org/10.1016/0010-4361(91)90549-V.

[35] Richardson MOW, Wisheart MJ. Review of low-velocity impact properties of composite materials. Compos Part A Appl Sci Manuf 1996;27:1123–31. https://doi.org/10.1016/1359-835X(96)00074-7.

[36] Morinière FD, Alderliesten RC, Benedictus R. Low-velocity impact energy partition in GLARE. Mech Mater 2013;66:59–68. https://doi.org/10.1016/j.mechmat.2013.06.007.

[37] Bikakis GSE. Simulation of the dynamic response of GLARE plates subjected to low velocity impact using a linearized spring–mass model. Aerosp Sci Technol 2017;64:24–30. https://doi.org/10.1016/j.ast.2017.01.013.

[38] Zarei H, Fallah M, Minak G, Bisadi H, Daneshmehr A. Low velocity impact analysis of Fiber Metal Laminates (FMLs) in thermal environments with various boundary conditions. Compos Struct 2016;149:170–83. https://doi.org/https://doi.org/10.1016/j.compstruct.2016.04.036.

[39] Santiago RC, Cantwell WJ, Jones N, Alves M. The modelling of impact loading on thermoplastic fibre-metal laminates. Compos Struct 2018;189:228–38. https://doi.org/10.1016/j.compstruct.2018.01.052.

[40] Kakati S, Chakraborty D. Delamination in GLARE laminates under low velocity impact. Compos Struct 2020;240:112083. https://doi.org/10.1016/j.compstruct.2020.112083.

[41] Sadighi M, Pärnänen T, Alderliesten RC, Sayeaftabi M, Benedictus R. Experimental and numerical investigation of metal type and thickness effects on the impact resistance of fiber metal laminates. Appl Compos Mater 2012;19:545–59. https://doi.org/10.1007/s10443-011-9235-6.

[42] Abrate S. Modeling of impacts on composite structures. Compos Struct 2001;51:129–38. https://doi.org/10.1016/S0263-8223(00)00138-0.

[43] Mohamed GFA, Soutis C, Hodzic A. Blast resistance and damage modelling of fibre metal laminates to blast loads. Appl Compos Mater 2012;19:619–36. https://doi.org/10.1007/s10443-011-9225-8.

[44] Fan J, Cantwell WJ, Guan ZW. The low-velocity impact response of fiber-metal laminates. J Reinf Plast Compos 2011;30:26–35. https://doi.org/10.1177/0731684410386133.

[45] Seyed Yaghoubi A, Liaw B. Thickness influence on ballistic impact behaviors of GLARE 5 fiber-metal laminated beams: Experimental and numerical studies. Compos Struct 2012;94:2585–98. https://doi.org/10.1016/j.compstruct.2012.03.004.

[46] Yungwirth CJ, O'Connor J, Zakraysek A, Deshpande VS, Wadley HNG. Explorations of hybrid sandwich panel concepts for projectile impact mitigation. J Am Ceram Soc 2011;94:s62–75. https://doi.org/10.1111/j.1551-2916.2011.04501.x.

[47] Jakubczak P, Podolak P. The issue of CAI assessment of Fibre Metal Laminates. Compos Struct 2022;281:114959. https://doi.org/10.1016/j.compstruct.2021.114959.

[48] Hoo Fatt MS, Lin C, Revilock DM, Hopkins DA. Ballistic impact of GLARE™ fiber-metal laminates. Compos Struct 2003;61:73–88. https://doi.org/10.1016/S0263-8223(03)00036-9.

[49] Sun CT, Dicken A, Wu HF. Characterization of impact damage in ARALL laminates. Compos Sci Technol 1993;49:139–44. https://doi.org/10.1016/0266-3538(93)90053-J.

[50] Vlot A. Impact properties of fibre metal laminates. Compos Eng 1993;3:911–27. https://doi.org/https://doi.org/10.1016/0961-9526(93)90001-Z.

[51] Mosse L, Cantwell WJ, Cardew-Hall MJ, Compston P, Kalyanasundaram S. A Study of the Effect of Process Variables on the Stamp Forming of Rectangular Cups Using Fibre-Metal Laminate Systems. Adv Mater Res 2005;6–8:649–56. https://doi.org/10.4028/www.scientific.net/AMR.6-8.649.

[52] Lee M, Kim S, Lim O, Kang C. Effect of process parameters on epoxy flow behavior and formability with CR340 / CFRP composites by different laminating in deep drawing process. Procedia Eng 2014;81:1627–32. https://doi.org/10.1016/j.proeng.2014.10.202.

[53] Lambert M, Schneider E. Shielding against space debris. A comparison between different shields: The effect of materials on their performances. Int J Impact Eng 1995;17:477–85. https://doi.org/10.1016/0734-743X(95)99872-O.

[54] Dhaliwal GS, Newaz GM. Compression after impact characteristics of carbon fiber reinforced aluminum laminates. Compos Struct 2017;160:1212–24. https://doi.org/10.1016/j.compstruct.2016.11.015.

[55] Chandrasekar M, Ishak MR, Jawaid M, Leman Z, Sapuan SM. An experimental review on the mechanical properties and hygrothermal behaviour of fibre metal laminates. J Reinf Plast Compos 2017;36:72–82. https://doi.org/10.1177/0731684416668260.

[56] Yu GC, Wu LZ, Ma L, Xiong J. Low velocity impact of carbon fiber aluminum laminates. Compos Struct 2015;119:757–66. https://doi.org/10.1016/j.compstruct.2014.09.054.

[57] Cortés P, Cantwell WJ. The fracture properties of a fibre-metal laminate based on magnesium alloy. Compos Part B Eng 2005;37:163–70. https://doi.org/10.1016/j.compositesb.2005.06.002.

[58] Asaee Z, Taheri F. Experimental and numerical investigation into the influence of stacking sequence on the low-velocity impact response of new 3D FMLs. Compos Struct

2016;140:136–46. https://doi.org/10.1016/j.compstruct.2015.12.015.

[59] Wilk MS, Sliwa RE. The influence of features of aluminium alloys 2024, 6061 and 7075 on the properties of glare-type composites. Arch Metall Mater 2015;60:3101–8. https://doi.org/10.1515/amm-2015-0496.

[60] Vo TP, Guan ZW, Cantwell WJ, Schleyer GK. Modelling of the low-impulse blast behaviour of fibre-metal laminates based on different aluminium alloys. Compos Part B Eng 2013;44:141–51. https://doi.org/10.1016/j.compositesb.2012.06.013.

[61] Pan Y, Wu G, Cheng X, Zhang Z, Li M, Ji S, et al. Galvanic corrosion behaviour of carbon fibre reinforced polymer/magnesium alloys coupling. Corros Sci 2015;98:672–7. https://doi.org/10.1016/j.corsci.2015.06.024.

[62] Nakatani H, Kosaka T, Osaka K, Sawada Y. Damage characterization of titanium/GFRP hybrid laminates subjected to low-velocity impact. Compos Part A Appl Sci Manuf 2011;42:772–81. https://doi.org/10.1016/j.compositesa.2011.03.005.

[63] Nakatani H, Kosaka T, Oki J, Osaka K, Sawada Y. Damage evalution of Ti/GFRP laminates under low-energy impact loading. ICCM Int Conf Compos Mater 2009.

[64] Li X, Zhang X, Guo Y, Shim VPW, Yang J, Chai GB. Influence of fiber type on the impact response of titanium-based fiber-metal laminates. Int J Impact Eng 2018;114:32–42. https://doi.org/10.1016/j.ijimpeng.2017.12.011.

[65] Jakubczak P. The impact behaviour of hybrid titanium glass laminates—Experimental and numerical approach. Int J Mech Sci 2019;159:58–73. https://doi.org/10.1016/j.ijmecsci.2019.05.035.

[66] Cortes P, Cantwell WJ. The impact properties of high-temperature fiber-metal laminates. J Compos Mater 2007;41:613–32. https://doi.org/10.1177/0021998306065291.

[67] Liu Y, Liaw B. Effects of constituents and lay-up configuration on drop-weight tests of fiber-metal laminates. Appl Compos Mater 2010;17:43–62. https://doi.org/10.1007/s10443-009-9119-1.

[68] Vlot A. Low-velocity impact loading on fibre reinforced aluminium laminates (ARALL and GLARE) and other aircraft sheet materials. 1993.

[69] Alberto M. Introduction of Fibre-Reinforced Polymers − Polymers and Composites: Concepts, Properties and Processes. In: Masuelli M, editor. Fiber Reinf. Polym. - Technol. Appl. Concr. Repair, Rijeka: InTech; 2013, p. Ch. 1. https://doi.org/10.5772/54629.

[70] Soutis C. Fibre reinforced composites in aircraft construction. Prog Aerosp Sci 2005;41:143–51. https://doi.org/10.1016/j.paerosci.2005.02.004.

[71] Adams DF, Miller AK. An analysis of the impact behavior of hybrid composite materials. Mater Sci Eng 1975;19:245–60. https://doi.org/10.1016/0025-5416(75)90112-3.

[72] Jones FR, Huff NT. High Strength Glasses. Handb. Tensile Prop. Text. Tech. Fibres,

2009.

[73] Smith JC, Mccrackin FL, Schiefer HF. Stress-strain relationships in yarns subjected to rapid impact loading: 5. Wave propagation in long textile yarns impacted transversely. J Res Natl Bur Stand (1934) 1958;60:517. https://doi.org/10.6028/jres.060.052.

[74] Component Form and Manufacture. Compos. Mater. Aircr. Struct. Third Ed., American Institute of Aeronautics and Astronautics, Inc.; 2016, p. 153–226. https://doi.org/doi:10.2514/5.9781624103261.0153.0226.

[75] Lv L, Gu B. Transverse impact damage and energy absorption of three-dimensional orthogonal hybrid woven composite: Experimental and FEM simulation. J Compos Mater 2008;42:1763–86. https://doi.org/10.1177/0021998308093718.

[76] Moon FC, Broutman LJ. Wave propagation and impact in composite materials. Compos Mater 1975;7:259–332.

[77] Smith JC, McCrackin FL, Schiefer HF, Stone WK, Towne KM. Stress-strain relationships in yarns subjected to rapid impact loading: 4. Transverse impact tests. J Res Natl Bur Stand (1934) 1956;57:83. https://doi.org/10.6028/jres.057.009.

[78] Ye L, Mai YW, Su Z. Composites technologies for 2020. Compos Technol 2020 2004:1–1096. https://doi.org/10.1533/9781845690625.

[79] Hasan KMF, Horváth PG, Alpár T. Potential fabric-reinforced composites: a comprehensive review. J Mater Sci 2021;56:14381–415. https://doi.org/10.1007/s10853-021-06177-6.

[80] Beaumont PWR, Riewald PG, Zweben C. Methods for improving the impact resistance of composite materials. ASTM Spec Tech Publ 1975:134–58. https://doi.org/10.1520/STP33154S.

[81] Billon HH, Robinson DJ. Models for the ballistic impact of fabric armour. Int J Impact Eng 2001;25:411–22. https://doi.org/10.1016/S0734-743X(00)00049-X.

[82] Zhou Y, Chen X, Wells G. Influence of yarn gripping on the ballistic performance of woven fabrics from ultra-high molecular weight polyethylene fibre. Compos Part B Eng 2014;62:198–204. https://doi.org/10.1016/j.compositesb.2014.02.022.

[83] Carr DJ. Failure mechanisms of yarns subjected to ballistic impact. J Mater Sci Lett 1999;18:585–8. https://doi.org/10.1023/A:1006655301587.

[84] Reyes G, Sharma U. Modeling and damage repair of woven thermoplastic composites subjected to low velocity impact. Compos Struct 2010;92:523–31. https://doi.org/10.1016/j.compstruct.2009.08.038.

[85] Nash NH, Young TM, Mcgrail PT, Stanley WF. Inclusion of a thermoplastic phase to improve impact and post-impact performances of carbon fi bre reinforced thermosetting composites — A review. JMADE 2015;85:582–97. https://doi.org/10.1016/j.matdes.2015.07.001.

[86] Yaghoubi AS, Liaw B. Influences of thickness and stacking sequence on ballistic impact behaviors of GLARE 5 FML plates: Part I-experimental studies. J Compos Mater

2014;48:2011–21. https://doi.org/10.1177/0021998313494097.

[87] Yaghoubi AS, Liaw B. Influences of thickness and stacking sequence on ballistic impact behaviors of GLARE 5 FML plates: Part II - Numerical studies. J Compos Mater 2014;48:2363–74. https://doi.org/10.1177/0021998313498104.

[88] Seyed Yaghoubi A, Liu Y, Liaw B. Stacking sequence and geometrical effects on low-velocity impact behaviors of GLARE 5 (3/2) fiber-metal laminates. J Thermoplast Compos Mater 2012;25:223–47. https://doi.org/10.1177/0892705711408165.

[89] Hitchen SA, Kemp RMJ. The effect of stacking sequence on impact damage in a carbon fibre/epoxy composite. Composites 1995;26:207–14. https://doi.org/10.1016/0010-4361(95)91384-H.

[90] Kaware K, Kotambkar M. Low velocity impact response and influence of parameters to improve the damage resistance of composite structures/materials: a critical review. Int J Crashworthiness 2021:1–25. https://doi.org/10.1080/13588265.2021.1914985.

[91] Seyed Yaghoubi A, Liaw B. Effect of lay-up orientation on ballistic impact behaviors of GLARE 5 FML beams. Int J Impact Eng 2013;54:138–48. https://doi.org/10.1016/j.ijimpeng.2012.10.007.

[92] Bikakis GSE, Karaiskos E, Sideridis EP. Low-velocity impact response of fiber-metal laminates consisting of different standard GLARE grades. J Reinf Plast Compos 2016;35:1029–40. https://doi.org/10.1177/0731684416633770.

[93] Wang HR, Long SC, Zhang XQ, Yao XH. Study on the delamination behavior of thick composite laminates under low-energy impact. Compos Struct 2018;184:461–73. https://doi.org/10.1016/j.compstruct.2017.09.083.

[94] Khoramishad H, Bagheri Tofighi M. Effects of mechanical and geometrical properties of adhesive and metal layers on low-velocity impact behavior of metal laminate structures. J Adhes Sci Technol 2015;29:592–608. https://doi.org/10.1080/01694243.2014.999610.

[95] Laliberté J, Straznicky P V., Poon C. Impact Damage in Fiber Metal Laminates, Part 1: Experiment. AIAA J 2005;43:2445–53. https://doi.org/10.2514/1.15159.

[96] Morinière FD, Alderliesten RC, Sadighi M, Benedictus R. An integrated study on the low-velocity impact response of the GLARE fibre-metal laminate. Compos Struct 2013;100:89–103. https://doi.org/10.1016/j.compstruct.2012.12.016.

[97] Vlot A, Krull M. Impact damage resistance of various fibre metal laminates. J Phys IV JP 1997;7. https://doi.org/10.1051/jp4:19973176.

[98] Zhu S, Chai GB. Low-velocity impact response of fibre-metal laminates - Experimental and finite element analysis. Compos Sci Technol 2012;72:1793–802. https://doi.org/10.1016/j.compscitech.2012.07.016.

[99] Khoramishad H, Bagheri Tofighi M, Khodaei M. Effect of Stacking Sequence on Low-Velocity Impact Behavior of Metal Laminates. Phys Mesomech 2018;21:140–9. https://doi.org/10.1134/S1029959918020078.

[100] Laliberté JF, Straznicky P V, Poon C. Impact Damage in Fiber Metal Laminates, Part 1: Experiment. AIAA J 2005;43:2445–53. https://doi.org/10.2514/1.15159.

[101] Vlot A. Impact tests on aluminium 2024 T3, aramid and glass reinforced aluminium laminates and thermoplastic composites. TU Delft; 1987.

[102] Seyed Yaghoubi A, Liu Y, Liaw B. Low-Velocity Impact on GLARE 5 Fiber-Metal Laminates: Influences of Specimen Thickness and Impactor Mass. J Aerosp Eng 2012;25:409–20. https://doi.org/10.1061/(ASCE)AS.1943-5525.0000134.

[103] Fan J, Guan ZW, Cantwell WJ. Numerical modelling of perforation failure in fibre metal laminates subjected to low velocity impact loading. Compos Struct 2011;93:2430–6. https://doi.org/10.1016/j.compstruct.2011.04.008.

[104] Rajkumar GR, Krishna M, Narasimhamurthy HN, Keshavamurthy YC, Nataraj JR. Investigation of Tensile and Bending Behavior of Aluminum based Hybrid Fiber Metal Laminates. Procedia Mater Sci 2014;5:60–8. https://doi.org/10.1016/j.mspro.2014.07.242.

[105] Dadej K, Surowska B, Bieniaś J. Isostrain elastoplastic model for prediction of static strength and fatigue life of fiber metal laminates. Int J Fatigue 2018;110:31–41. https://doi.org/10.1016/j.ijfatigue.2018.01.009.

[106] Singh TJ, Samanta S. Characterization of Kevlar Fiber and Its Composites: A Review. Mater Today Proc 2015;2:1381–7. https://doi.org/10.1016/j.matpr.2015.07.057.

[107] Sikarwar RS, Rajput NS, Velmurugan R, Naik S. FE Analysis of Impact on Kevlar/Epoxy Laminates with Different Orientations and Thicknesses. Mater Today Proc 2017;4:2599–607. https://doi.org/10.1016/j.matpr.2017.02.114.

[108] Dorey G, Sidey GR, Hutchings J. Impact properties of carbon fibre/Kevlar 49 fibre hydrid composites. Composites 1978;9:25–32. https://doi.org/10.1016/0010-4361(78)90514-1.

[109] Ramadhan AA, Abu Talib AR, Mohd Rafie AS, Zahari R. High velocity impact response of Kevlar-29/epoxy and 6061-T6 aluminum laminated panels. Mater Des 2013;43:307–21. https://doi.org/10.1016/j.matdes.2012.06.034.

[110] Zhou Y, Wang Y, Mallick PK. An experimental study on the tensile behavior of Kevlar fiber reinforced aluminum laminates at high strain rates. Mater Sci Eng A 2004;381:355–62. https://doi.org/10.1016/j.msea.2004.04.027.

[111] Megeri S, Naik GN. Numerical studies of the low velocity impact behaviour on hybrid fiber metal laminates. Mater Today Proc 2021;44:1860–4. https://doi.org/10.1016/j.matpr.2020.12.030.

[112] Dadej K, Bienias J, Surowska B. On the effect of glass and carbon fiber hybridization in fiber metal laminates: Analytical, numerical and experimental investigation. Compos Struct 2019;220:250–60. https://doi.org/10.1016/j.compstruct.2019.03.051.

[113] Cantwell WJ. Geometrical effects in the low velocity impact response of GFRP. Compos Sci Technol 2007;67:1900–8. https://doi.org/10.1016/j.compscitech.2006.10.015.

[114] Fan J, Cantwell WJ, Guan ZW. The low-velocity impact response of fiber-metal laminates. J Reinf Plast Compos 2011;30:26–35. https://doi.org/10.1177/0731684410386133.

[115] Laliberté J, Straznicky P V., Poon C. Impact Damage in Fiber Metal Laminates, Part 1: Experiment. AIAA J 2008;43:2445–53. https://doi.org/10.2514/1.15159.

[116] Cantwell WJ, Morton J. Impact perforation of carbon fibre reinforced plastic. Compos Sci Technol 1990;38:119–41. https://doi.org/10.1016/0266-3538(90)90002-M.

[117] Olsson R. Mass criterion for wave controlled impact response of composite plates. Compos Part A Appl Sci Manuf 2000;31:879–87. https://doi.org/https://doi.org/10.1016/S1359-835X(00)00020-8.

[118] Liu Y, Yaghoubi AS, Liaw B. Low-velocity impact study on GLARE FMLs using various indenters. J Aerosp Eng 2014;27:325–35. https://doi.org/10.1061/(ASCE)AS.1943-5525.0000250.

[119] Morinière FD, Alderliesten RC, Benedictus R. Modelling of impact damage and dynamics in fibre-metal laminates - A review. Int J Impact Eng 2014;67:27–38. https://doi.org/10.1016/j.ijimpeng.2014.01.004.

[120] Sevkat E, Liaw B, Delale F. Drop-weight impact response of hybrid composites impacted by impactor of various geometries. Mater Des 2013;52:67–77. https://doi.org/10.1016/j.matdes.2013.05.016.

[121] Bieniaś J, Jakubczak P, Surowska B, Dragan K. Low-energy impact behaviour and damage characterization of carbon fibre reinforced polymer and aluminium hybrid laminates. Arch Civ Mech Eng 2015;15:925–32. https://doi.org/10.1016/j.acme.2014.09.007.

[122] Mueller RPG. An experimental and analytical investigatin on the fatigue behaviour of fuselage riveted lap joints. Delft University of Technology, 1995.

[123] Santos RAM, Reis PNB, Santos MJ, Coelho CACP. Effect of distance between impact point and hole position on the impact fatigue strength of composite laminates. Compos Struct 2017;168:33–9. https://doi.org/10.1016/j.compstruct.2017.02.045.

[124] Ortiz de Mendibil I, Aretxabaleta L, Sarrionandia M, Mateos M, Aurrekoetxea J. Impact behaviour of glass fibre-reinforced epoxy/aluminium fibre metal laminate manufactured by Vacuum Assisted Resin Transfer Moulding. Compos Struct 2016;140:118–24. https://doi.org/10.1016/j.compstruct.2015.12.026.

[125] Jain NK, Mittal ND. Finite element analysis for stress concentration and deflection in isotropic, orthotropic and laminated composite plates with central circular hole under transverse static loading. Mater Sci Eng A 2008;498:115–24. https://doi.org/10.1016/j.msea.2008.04.078.

[126] Khalili SMR, Malekzadeh K, Davar A, Mahajan P. Dynamic response of pre-stressed fibre metal laminate (FML) circular cylindrical shells subjected to lateral pressure pulse loads. Compos Struct 2010;92:1308–17. https://doi.org/10.1016/j.compstruct.2009.11.012.

[127] Vlot A. Impact tests on fibre metal laminates under a tensile load. 1993.

[128] Homan JJ. Fatigue initiation in fibre metal laminates. Int J Fatigue 2006;28:366–74. https://doi.org/10.1016/j.ijfatigue.2005.07.030.

[129] Vlot A, Van Ingen JW. Delamination Resistance of Post-Stretched Fibre Metal Laminates. J Compos Mater 1998;32:1784–805. https://doi.org/10.1177/002199839803201903.

[130] Roeder BA, Sun CT. Dynamic penetration of alumina/aluminum laminates: Experiments and modeling. Int J Impact Eng 2001;25:169–85. https://doi.org/10.1016/S0734-743X(00)00031-2.

[131] Badawy AAM. Impact behavior of glass fibers reinforced composite laminates at different temperatures. Ain Shams Eng J 2012;3:105–11. https://doi.org/10.1016/j.asej.2012.01.001.

[132] Hirai Y, Hamada H, Kim JK. Impact response of woven glass-fabric composites - I. Effect of fibre surface treatment. Compos Sci Technol 1998;58:91–104. https://doi.org/10.1016/S0266-3538(97)00111-5.

[133] Chow ZP, Ahmad Z, Wong KJ. Temperature effects on the low-velocity impact of FML panels: Experimental and numerical analyses. Int J Impact Eng 2022;172:104403. https://doi.org/10.1016/j.ijimpeng.2022.104403.

[134] Shi Y, Swait T, Soutis C. Modelling damage evolution in composite laminates subjected to low velocity impact. Compos Struct 2012;94:2902–13. https://doi.org/10.1016/j.compstruct.2012.03.039.

[135] González E V., Maimí P, Camanho PP, Turon A, Mayugo JA. Simulation of drop-weight impact and compression after impact tests on composite laminates. Compos Struct 2012;94:3364–78. https://doi.org/10.1016/j.compstruct.2012.05.015.

[136] Minak G, Ghelli D. Influence of diameter and boundary conditions on low velocity impact response of CFRP circular laminated plates. Compos Part B Eng 2008;39:962–72. https://doi.org/10.1016/j.compositesb.2008.01.001.

[137] Tsartsaris N, Meo M, Dolce F, Polimeno U, Guida M, Marulo F. Low-velocity impact behavior of fiber metal laminates. J Compos Mater 2011;45:803–14. https://doi.org/10.1177/0021998310376108.

[138] Seo H, Hundley J, Hahn HT, Yang J-MM. Numerical Simulation of Glass-Fiber-Reinforced Aluminum Laminates with Diverse Impact Damage. AIAA J 2010;48:676–87. https://doi.org/10.2514/1.45551.

[139] Fan J, Guan ZW, Cantwell WJ. Numerical modelling of perforation failure in fibre metal laminates subjected to low velocity impact loading. Compos Struct 2011;93:2430–6. https://doi.org/10.1016/j.compstruct.2011.04.008.

[140] Ming L, Pantalé O. An efficient and robust VUMAT implementation of elastoplastic constitutive laws in Abaqus/Explicit finite element code. Mech Ind 2018;19. https://doi.org/10.1051/meca/2018021.

[141] Azhdari S, Fakhreddini-Najafabadi S, Taheri-Behrooz F. An experimental and numerical investigation on low velocity impact response of GLAREs. Compos Struct 2021;271:114123. https://doi.org/10.1016/j.compstruct.2021.114123.

[142] Xiao-Yu S, Jian-Xin T, Zheng H, Xuan G. A study on the failure mechanisms of composite laminates simultaneously impacted by two projectiles. Adv Compos Lett 2018;27:96–107. https://doi.org/10.1177/096369351802700302.

[143] Alabbad M, Vel SS, Lopez-Anido RA. Computational model for predicting the low-velocity impact resistance and tolerance of composite laminates. Compos Part B Eng 2022;244:110187. https://doi.org/10.1016/j.compositesb.2022.110187.

[144] Zhang J, Wang Y, Wen Y, Dai X, Zhao Y, Fang G. Energy dissipation mechanism of fiber metal laminate under low-velocity impact. Thin-Walled Struct 2023;183:110355. https://doi.org/10.1016/j.tws.2022.110355.

[145] Yao L, Sun G, He W, Meng X, Xie D. Investigation on impact behavior of FMLs under multiple impacts with the same total energy: Experimental characterization and numerical simulation. Compos Struct 2019;226. https://doi.org/10.1016/j.compstruct.2019.111218.

[146] Hu H, Wei Q, Liu B, Liu Y, Hu N, Ma Q, et al. Progressive Damage Behaviour Analysis and Comparison with 2D/3D Hashin Failure Models on Carbon Fibre–Reinforced Aluminium Laminates. Polymers (Basel) 2022;14. https://doi.org/10.3390/polym14142946.

[147] Zhou J, Liu B, Wang S. Finite element analysis on impact response and damage mechanism of composite laminates under single and repeated low-velocity impact. Aerosp Sci Technol 2022;129:107810. https://doi.org/10.1016/j.ast.2022.107810.

[148] Podolak P, Jakubczak P. Influence of constitutive metal model on the numerical prediction of the impact behaviour of titanium-based Fibre Metal Laminates 2022;169. https://doi.org/10.1016/j.ijimpeng.2022.104342.

[149] Hasan MZ. Interface failure of heated GLARE™ fiber-metal laminates under bird strike. Aerospace 2020;7. https://doi.org/10.3390/aerospace7030028.

[150] Wang Z, Zhao J. Low velocity impact response of GLARE laminates based on a new efficient implementation of Puck's criterion. Thin-Walled Struct 2019;144:106321. https://doi.org/10.1016/j.tws.2019.106321.

[151] Wang ZW, Zhao JP, Zhang X. Finite element analysis of composite laminates subjected to low-velocity impact based on multiple failure criteria. Mater Res Express 2018;5:65320. https://doi.org/10.1088/2053-1591/aacca3.

[152] Zhou J, Wen P, Wang S. Numerical investigation on the repeated low-velocity impact behavior of composite laminates. Compos Part B Eng 2020;185:107771. https://doi.org/10.1016/j.compositesb.2020.107771.

[153] Yaghoubi AS, Liu YX, Liaw BM. Drop-Weight Impact Studies of GLARE 5 Fiber-Metal Laminates BT - Experimental and Applied Mechanics, Volume 6. In: Proulx T, editor., New York, NY: Springer New York; 2011, p. 267–79.

[154] Ramkumar RL, Chen PC. Low-velocity impact response of laminated plates. AIAA J 1983;21:1448–52. https://doi.org/10.2514/3.8266.

[155] Shivakumar KN, Elber W, Illg W. Prediction of low-velocity impact damage in thin circular laminates. AIAA J 1985;23:442–9. https://doi.org/10.2514/3.8933.

[156] Pang SS, Zhao Y, Yang C, Griffin SA. Impact response of composite laminates with a hemispherical indenter. Polym Eng Sci 1991;31:1461–6. https://doi.org/10.1002/pen.760312004.

[157] Pierson MO, Vaziri R. Analytical solution for low-velocity impact response of composite plates. AIAA J 1996;34:1633–40. https://doi.org/10.2514/3.13282.

[158] Caprino G, Lopresto V, Iaccarino P. A simple mechanistic model to predict the macroscopic response of fibreglass-aluminium laminates under low-velocity impact. Compos Part A Appl Sci Manuf 2007;38:290–300. https://doi.org/10.1016/j.compositesa.2006.04.005.

[159] Payeganeh GH, Ashenai Ghasemi F, Malekzadeh K. Dynamic response of fiber-metal laminates (FMLs) subjected to low-velocity impact. Thin-Walled Struct 2010;48:62–70. https://doi.org/10.1016/j.tws.2009.07.005.

[160] Choi IH, Lim CH. Low-velocity impact analysis of composite laminates using linearized contact law. Compos Struct 2004;66:125–32. https://doi.org/10.1016/j.compstruct.2004.04.030.

[161] Asaee Z, Taheri F. A practical analytical model for predicting the low-velocity impact response of 3D-fiber metal laminates. Mech Adv Mater Struct 2018;0:1–14. https://doi.org/10.1080/15376494.2018.1472328.

[162] Maw N, Barber JR, Fawcett JN. The oblique impact of elastic spheres. Wear 1976;38:101–14. https://doi.org/10.1016/0043-1648(76)90201-5.

[163] Thornton C. A note on the effect of initial particle spin on the rebound behaviour of oblique particle impacts. Powder Technol 2009;192:152–6. https://doi.org/10.1016/j.powtec.2008.12.015.

[164] Wu CY, Thornton C, Li LY. A semi-analytical model for oblique impacts of elastoplastic spheres. Proc R Soc A Math Phys Eng Sci 2009;465:937–60. https://doi.org/10.1098/rspa.2008.0221.

[165] Thornton C, Cummins SJ, Cleary PW. An investigation of the comparative behaviour of alternative contact force models during elastic collisions. Powder Technol 2011;210:189–97. https://doi.org/10.1016/j.powtec.2011.01.013.

[166] Stronge WJ. Oblique elastic-plastic impact between rough cylinders in plane strain. Int J Eng Sci 1999;37:97–122.

[167] Jäger J. Elastic contact of equal spheres under oblique forces. Arch Appl Mech 1993;63:402–12. https://doi.org/10.1007/BF00805740.

[168] Zhikharev M V., Kudryavtsev OA, Pavlovskaya MS. Experimental and numerical study of the behavior of a Glass Fiber Reinforced Plastic plate under oblique impact.

J Compos Mater 2021;55:1167–78. https://doi.org/10.1177/0021998320965663.

[169] Neogi S Das, Karmakar A, Chakravorty D. Finite Element Analysis of Laminated Composite Skewed Hypar Shell Roof under Oblique Impact with Friction 2017:314–22.

[170] Patil S, Mallikarjuna Reddy D. Study of oblique low velocity impact on composite plate. Mater Today Proc 2020. https://doi.org/10.1016/j.matpr.2020.03.125.

[171] Yao L, Yu H, Wang C, He W. Numerical and experimental investigation on the oblique successive impact behavior and accumulated damage characteristics of fiber metal laminates. Thin-Walled Struct 2021;166:108033. https://doi.org/10.1016/j.tws.2021.108033.

[172] Mao Y, Hong L, Ai S, Fu H, Chen C. Dynamic response and damage analysis of fiber-reinforced composite laminated plates under low-velocity oblique impact. Nonlinear Dyn 2017;87:1511–30. https://doi.org/10.1007/s11071-016-3130-5.

[173] Neogi S Das, Karmakar A, Chakravorty D. Finite Element Analysis of Laminated Composite Skewed Hypar Shell Roof Under Oblique Impact with Friction. Procedia Eng 2017;173:314–22. https://doi.org/https://doi.org/10.1016/j.proeng.2016.12.023.

[174] Mindlin RD, Deresiewicz H. Elastic spheres in contact under varying oblique forces. J Appl Mech 1953;20:327–44.

[175] Johnson KL. Line loading of an elastic half-space. 2013. https://doi.org/10.1017/cbo9781139171731.003.

[176] Thornton C, Yin KK. Impact of elastic spheres with and without adhesion. Powder Technol 1991;65:153–66. https://doi.org/10.1016/0032-5910(91)80178-L.

[177] Thornton C, Cummins SJ, Cleary PW. An investigation of the comparative behaviour of alternative contact force models during inelastic collisions. Powder Technol 2013;233:30–46. https://doi.org/10.1016/j.powtec.2012.08.012.

[178] Bikakis GSE. Finite element and analytical modeling to predict the frictional oblique indentation response of GLARE fiber-metal laminates. J Reinf Plast Compos 2017;36:797–807. https://doi.org/10.1177/0731684417690928.

[179] Heydari-Meybodi M, Mohammadkhani H, Bagheri MR. Oblique Low-Velocity Impact on Fiber-Metal Laminates. Appl Compos Mater 2017;24:611–23. https://doi.org/10.1007/s10443-016-9530-3.

[180] Li L, Sun L, Wang T, Kang N, Cao W. Repeated low-velocity impact response and damage mechanism of glass fiber aluminium laminates. Aerosp Sci Technol 2019;84:995–1010. https://doi.org/10.1016/j.ast.2018.11.038.

[181] Kaw AK. Mechanics of Composite Materials, Second Edition. CRC Press; 2005.

[182] Zienkiewicz OC. The finite element method in engineering science / [by] O. C. Zienkiewicz. London ; New York: McGraw-Hill; 1971.

[183] Wilson EL, Taylor RL, Doherty WP, Ghaboussi J. Incompatible Displacement models. In: Fenves SJ, Perrone N, Robinson AR, Schnobrich W, editors. Numer. Comput. Methods Struct. Mech., Academic Press; 1973, p. 43–57.

[184] Jones R, Callinan R, Teh KK, Brown KC. Analysis of multi-layer laminates using three-dimensional super-elements. Int J Numer Methods Eng 1984;20:583–7. https://doi.org/10.1002/nme.1620200316.

[185] Bathe KJ. Finite element procedures. K.J. Bathe; 2014.

[186] Wu H-YT, Chang F-K, Wu T, Wu H-YT, Chang F-K. Transient dynamic analysis of laminated composite plates subjected to transverse impact. Comput Struct 1989;31:453–66. https://doi.org/https://doi.org/10.1016/0045-7949(89)90393-3.

[187] Christoforou AP, Yigit AS. Impact of Composite Structures—The Momentum Balance Method. J Compos Mater 1996;30:1068–87. https://doi.org/10.1177/002199839603001001.

[188] Menčík J, Munz D, Quandt E, Weppelmann ER, Swain M V. Determination of elastic modulus of thin layers using nanoindentation. J Mater Res 1997;12:2475–84. https://doi.org/DOI: 10.1557/JMR.1997.0327.

[189] Choi HY, Chang F-K. A Model for Predicting Damage in Graphite/Epoxy Laminated Composites Resulting from Low-Velocity Point Impact. J Compos Mater 1992;26:2134–69. https://doi.org/10.1177/002199839202601408.

[190] Shi X, Polycarpou AA. Measurement and modeling of normal contact stiffness and contact damping at the meso scale. J Vib Acoust Trans ASME 2005;127:52–60. https://doi.org/10.1115/1.1857920.

[191] Bucinell RB, Nuismer RJ, Koury JL. Response of Composite Plates to Quasi-Static Impact Events. In: O'Brien TK, editor. Compos. Mater. Fatigue Fract. (Third Vol., West Conshohocken, PA: ASTM International; 1991, p. 528–49. https://doi.org/10.1520/STP17735S.

[192] Jhonson KL. Contact Mechanics. Cambridge: Cambridge University Press; 1985. https://doi.org/10.1002/cncr.30378.

[193] Olsson R. Impact response of composite laminates: A guide to closed form solutions. 1993.

[194] THORNTON C, RANDALL CW. Applications of Theoretical Contact Mechanics to Solid Particle System Simulation. In: Satake M, Jenkins JTBT-S in AM, editors. Micromechanics Granul. Mater., vol. 20, Elsevier; 1988, p. 133–42. https://doi.org/https://doi.org/10.1016/B978-0-444-70523-5.50023-0.

[195] Kosarev OI. Contact deformation and compression of cylinders. Russ Eng Res 2011;31:107–12. https://doi.org/10.3103/S1068798X11020122.

[196] Norden BN. On the compression of a cylinder in contact with a plane surface. Interag Rep 1973:73--243. https://doi.org/https://doi.org/10.6028/NBS.IR.73-243.

[197] Hinton E. Local and Global Smoothing of Discontinuous Finite Element Functions. Int J 1974;8:461–80.

[198] Joshi R, Pal P, Duggal SK. Ply-by-ply failure analysis of laminates using finite element method. Eur J Mech A/Solids 2020;81:103964.

https://doi.org/10.1016/j.euromechsol.2020.103964.

[199] Rathbone D, Marigo M, Dini D, van Wachem B. An accurate force-displacement law for the modelling of elastic-plastic contacts in discrete element simulations. Powder Technol 2015;282:2–9. https://doi.org/10.1016/j.powtec.2014.12.055.

[200] Big-Alabo A, Harrison P, Cartmell MP. Contact model for elastoplastic analysis of half-space indentation by a spherical impactor. Comput Struct 2015;151:20–9. https://doi.org/10.1016/j.compstruc.2015.01.005.

[201] Olsson R. Engineering Method for Prediction of Impact Response and Damage in Sandwich Panels. J Sandw Struct Mater 2002;4:3–29. https://doi.org/10.1106/109963602023192.

[202] Bienias J, Jakubczak P, Dadej K. Low-velocity impact resistance of aluminium glass laminates - Experimental and numerical investigation. Compos Struct 2016;152:339–48. https://doi.org/10.1016/j.compstruct.2016.05.056.

[203] Christoforou AP, Yigit AS. Transient response of a composite beam subject to elasto-plastic impact. Compos Eng 1995;5:459–70. https://doi.org/10.1016/0961-9526(95)00018-I.

[204] Ikegami K, Takeshita T, Matsuo K, Sugibayashi T. Strength of adhesively bonded scarf joints between glass fibre-reinforced plastics and metals. Int J Adhes Adhes 1990;10:199–206. https://doi.org/10.1016/0143-7496(90)90104-6.

[205] Khan SH, Sharma AP, Kitey R, Parameswaran V. Effect of metal layer placement on the damage and energy absorption mechanisms in aluminium/glass fibre laminates. Int J Impact Eng 2018;119:14–25. https://doi.org/10.1016/j.ijimpeng.2018.04.011.

[206] Solvay Adhesive Materials. Technical Data Sheet FM ® 94 Film Adhesive. 2017.

[207] Kasavajhala ARM, Gu L. Fracture analysis of Kevlar-49/epoxy and e-glass/epoxy doublers for reinforcement of cracked aluminum plates. Compos Struct 2011;93:2090–5. https://doi.org/10.1016/j.compstruct.2011.02.012.

[208] Jones MLC. The Basic Ply Properties of a Kevlar 49/Epoxy Resin Composite System 1983:38.

[209] Tsamasphyros GJ, Bikakis GS. Quasi-static response of circular glare plates subjected to low velocity impact. Mech Adv Mater Struct 2014;21:39–46. https://doi.org/10.1080/15376494.2012.677104.

[210] Kakati S, Chakraborty D. Delamination in GLARE laminates under low velocity impact. Compos Struct 2020;240:112083. https://doi.org/https://doi.org/10.1016/j.compstruct.2020.112083.

[211] Lam KY, Sathiyamoorthy TS. Response of composite beam under low-velocity impact of multiple masses. Compos Struct 1999;44:205–20. https://doi.org/10.1016/S0263-8223(99)80000-2.

[212] Zarei H, Brugo T, Belcari J, Bisadi H, Minak G, Zucchelli A. Low velocity impact damage assessment of GLARE fiber-metal laminates interleaved by Nylon 6,6

nanofiber mats. Compos Struct 2017;167:123–31. https://doi.org/https://doi.org/10.1016/j.compstruct.2017.01.079.

[213] Liu Y, Yaghoubi AS, Liaw B. Low-Velocity Impact Study on GLARE FMLs Using Various Indenters. J Aerosp Eng 2012;27:325–35. https://doi.org/10.1061/(asce)as.1943-5525.0000250.

[214] Thornton C, Cummins SJ, Cleary PW. On elastic-plastic normal contact force models, with and without adhesion. Powder Technol 2017;315:339–46. https://doi.org/10.1016/j.powtec.2017.04.008.

[215] Wu CY, Thornton C, Li LY. Coefficients of restitution for elastoplastic oblique impacts. Adv Powder Technol 2003;14:435–48. https://doi.org/10.1163/156855203769710663.

[216] Maw N, Barber JR, Fawcett JN. The Role of Elastic Tangential Compliance in Oblique Impact. J Lubr Technol 1981;103:74–80. https://doi.org/10.1115/1.3251617.

List of publications

Journal publications

1. Kakati S, Chakraborty D. Delamination in GLARE laminates under low velocity impact. Compos Struct 2020;240:112083. https://doi.org/10.1016/j.compstruct.2020.112083.
2. Kakati S, Chakraborty D. Cylindrical Impacts on GLARE 5 Plates with Open Hole. Appl Compos Mater 2021. https://doi.org/10.1007/s10443-021-09999-4.
3. Kakati S, Chakraborty D. Influence of impactor mass on the low energy impact response of thin GLARE plates. Mech Adv Mater Struct 2022:1–15. https://doi.org/10.1080/15376494.2022.2134529.
4. Kakati S, Chakraborty D. Delamination in GLARE laminates subjected to oblique low velocity impact considering friction. Eur J Mech / A Solids 2023;97:104817. https://doi.org/10.1016/j.euromechsol.2022.104817.
5. Kakati S, Chakraborty D. Effect of Impact Energy Divisions for Repeated Low - Velocity Impacts by Varied Masses on GLARE. Iran J Sci Technol Trans Mech Eng 2023. https://doi.org/10.1007/s40997-023-00726-x.
6. Kakati S, Chakraborty D. Low velocity impact on fibre metal laminates: A review. J Compos Mater 2023. https://doi.org/10.1177/00219983231212544.

Conferences

- Kakati S, Chakraborty D. Effect of hybridisation on low velocity impact of GLARE laminates. ICCS24 (2021), Faculty of Engineering, University of Porto, Portugal.
- Kakati S, Chakraborty D. Effect of open holes on the delamination of a GLARE plate subjected to low velocity impact. IMPLAST-2022, Mater Today Proc 2023. https://doi.org/10.1016/j.matpr.2023.03.169.
- Kakati S, Chakraborty D. Impact response of a GLARE 5 plate with open holes subjected to low-velocity cylindrical impact. SICE 2022, Department of Mechanical and Aerospace Engineering, IIT Hyderabad.
- Kakati S, Chakraborty D. Effect of hybridization of a GLARE plate with central cut-out subjected to offset low velocity impact. VETOMAC 2022, Institute of Engineering, Pulchowk Campus, Nepal.

- Kakati S, Chakraborty D. Low velocity impact response of GLARE laminates under multiple spherical impacts. 8th Asian Conference on Mechanics of Functional Materials and Structures (ACMFMS-2022), IIT Guwahati.


भारतीय प्रौद्योगिकी संस्थान गुवाहाटी
Indian Institute of Technology Guwahati